

# UC San Diego

## UC San Diego Electronic Theses and Dissertations

### Title

Interfacially driven flows: from electrohydrodynamics to active interfaces

### Permalink

<https://escholarship.org/uc/item/01q1r7jd>

### Author

Firouznia, Mohammadhossein

### Publication Date

2023

Peer reviewed|Thesis/dissertation

UNIVERSITY OF CALIFORNIA SAN DIEGO

Interfacially driven flows: from electrohydrodynamics to active interfaces

A dissertation submitted in partial satisfaction of the  
requirements for the degree Doctor of Philosophy

in

Engineering Sciences (Mechanical Engineering)

by

Mohammadhossein Firouznia

Committee in charge:

Professor David Saintillan, Chair  
Professor Bo Li  
Professor Stefan G. Llewellyn Smith  
Professor Padmini Rangamani  
Professor William R. Young

2023

Copyright

Mohammadhossein Firouznia, 2023

All rights reserved.

The Dissertation of Mohammadhossein Firouznia is approved, and it is acceptable in quality and form for publication on microfilm and electronically.

University of California San Diego

2023

## DEDICATION

To my parents, for their boundless love and unwavering support.

In fond remembrance of my beloved grandmother, Aziz.

## EPIGRAPH

صوفی نشود صافی تا در نلشد جامی  
بسیار سفر باید تا پخته شود خامی  
نو مید نباید بود از روشنی بامی  
گرچه شب مشتاقان تاریک بود اما  
در کام ننگان رو گرمی طلبی کامی  
سعدی به لب دریا در دانه کجایابی  
سعدی شیرازی

Many journeys must one undertake ere immaturity matures.  
Not until the chalice is drained, the Sufi becomes pure.

Though night be dim for those in love's yearning quest;  
Despair must not arise from rooftop's radiant crest.

Saadi, where by the sea will you locate a pearl so fine?  
In the realm of whales, venture forth if treasure's what you pine.

*Saadi Shirazi*

To all journeys within, and in the world beyond. . .

## TABLE OF CONTENTS

Dissertation Approval Page .....	iii
Dedication .....	iv
Epigraph .....	v
Table of Contents .....	vi
List of Figures .....	ix
List of Tables .....	xv
Acknowledgements .....	xvi
Vita .....	xx
Abstract of the Dissertation .....	xxi
Chapter 1    Interfacially driven flows .....	1
1.1    Electrohydrodynamics .....	2
1.1.1    From electrokinetic theories to leaky dielectric model .....	4
1.1.2    Leaky dielectric model .....	5
1.2    Active surfaces .....	9
1.2.1    Hydrodynamics of interfacial active nematics .....	11
Chapter 2    Boundary integral method .....	16
2.1    Laplace’s equation .....	17
2.2    Stokes equation .....	18
Chapter 3    Electrohydrodynamic instabilities in viscous films .....	23
3.1    Introduction .....	24
3.2    Problem definition and governing equations .....	26
3.3    Non-dimensionalization .....	29
3.4    Linear stability analysis .....	32
3.4.1    Theoretical formulation .....	32
3.5    Numerical simulations .....	37
3.5.1    Boundary element method .....	38
3.5.2    Results and discussion .....	42
3.6    Concluding remarks .....	48
3.7    Acknowledgements .....	50
Chapter 4    Electrohydrodynamic interfacial instabilities in convergent flows .....	51
4.1    Introduction .....	52
4.2    Problem definition and governing equations .....	54

4.3	Non-dimensionalization . . . . .	59
4.4	Local linear stability theory . . . . .	61
4.5	Boundary element method and numerical stability . . . . .	63
	4.5.1 Boundary element method . . . . .	64
	4.5.2 Numerical linear stability analysis . . . . .	66
4.6	Results and discussion . . . . .	68
	4.6.1 Effect of tangential electric field . . . . .	68
	4.6.2 Effect of stagnation-point flow . . . . .	72
	4.6.3 Combined effects of electric field and flow . . . . .	74
	4.6.4 Mechanisms of charge transport in the dominant mode of instability . . . . .	78
4.7	Relevance to the equatorial streaming instability . . . . .	81
4.8	Conclusions . . . . .	83
4.9	Acknowledgements . . . . .	84
Chapter 5	Electrohydrodynamic flows in viscous drops . . . . .	85
5.1	Introduction . . . . .	86
5.2	Problem definition . . . . .	89
	5.2.1 Governing equations . . . . .	89
	5.2.2 Non-dimensionalization . . . . .	92
	5.2.3 Boundary integral formulation . . . . .	93
5.3	Numerical methods . . . . .	95
	5.3.1 Surface representation . . . . .	97
	5.3.2 Aliasing errors . . . . .	99
	5.3.3 Numerical integration . . . . .	100
	5.3.4 Incompressibility and charge neutrality . . . . .	102
	5.3.5 Reparametrization . . . . .	102
	5.3.6 Convergence analysis and time step restriction . . . . .	106
5.4	Numerical results . . . . .	108
	5.4.1 Axisymmetric regime . . . . .	108
	5.4.2 Quincke regime . . . . .	109
	5.4.3 Low-viscosity drops . . . . .	111
5.5	Conclusions . . . . .	115
5.6	Acknowledgements . . . . .	116
Chapter 6	Viscous drops with interfacial nematic activity . . . . .	117
6.1	Introduction . . . . .	118
6.2	Problem definition and governing equations . . . . .	119
6.3	Non-dimensional groups . . . . .	122
6.4	Methods . . . . .	123
	6.4.1 Boundary integral method . . . . .	123
	6.4.2 Identification of topological defects . . . . .	126
	6.4.3 Braiding dynamics of topological defects . . . . .	128
6.5	Results and discussion . . . . .	131
	6.5.1 Small deformations . . . . .	131

6.5.2	Finite deformations .....	136
6.6	Conclusions .....	140
6.7	Acknowledgements .....	141
Chapter 7	Conclusions and directions for future work .....	142
7.1	Conclusions .....	142
7.2	Directions for future work .....	144
Appendix A	Electrified liquid films .....	147
A.1	Linear stability analysis .....	147
A.2	Fastest growing mode .....	149
A.3	Nonlinear regime .....	150
Appendix B	Differential geometry of curved surfaces .....	153
Appendix C	Active drops .....	156
C.1	Simulation parameters .....	156
C.2	Defect dynamics in spherical active drops .....	156
C.3	Energy conservation in a an active drop .....	159
C.4	Active drops under finite deformations .....	161
Bibliography	.....	163

## LIST OF FIGURES

Figure 1.1.	Two immiscible fluid layers are subject to an external uniform electric field $\mathbf{E}_0$ and a background velocity field $\mathbf{u}_0(\mathbf{x})$ . . . . .	6
Figure 1.2.	An active interface, denoted by $\partial V$ , separates two fluid layers, $V_1$ and $V_2$ . The director field $\mathbf{n}(\mathbf{x})$ describes the average orientation of the nematic particles at every point on the interface. . . . .	12
Figure 1.3.	The induced flow by a nematic particle with (a) extensile ( $\xi < 0$ ), and (b) contractile ( $\xi > 0$ ) activity. . . . .	14
Figure 3.1.	Problem definition: a liquid film suspended between two infinite immiscible liquid layers is subject to a perpendicular electric field $\mathbf{E}_\infty$ . . . . .	26
Figure 3.2.	Streamlines of the flow in the two dominant modes of linear instability: (a) in-phase (sinuous) mode when $R = 2$ , (b) antiphase (varicose) mode when $R = 0.5$ . Other parameters are $(Q, \lambda, Ca_E, Re_E) = (1, 1, 10, 1)$ in both systems. The blue region illustrates a typical shape of the film in the . . . . .	34
Figure 3.3.	Growth rate versus wavenumber in the dominant modes of linear instability for $(R, Q, \lambda) = (0.5, 1, 1)$ : (a) effect of electric capillary number when $Re_E = 1$ . Inset shows the unstable wavenumbers. (b) Effect of electric Reynolds number when $Ca_E = 10$ . . . . .	36
Figure 3.4.	Wavenumber $k_{marg}$ corresponding to marginally stable perturbations ( $\sigma = 0$ ) in different modes of instability as a function of: (a) electric capillary number, and (b) electric Reynolds number for two different systems with $R = 0.5$ and $R = 2$ while $(Q, \lambda) = (1, 1)$ . $Re_E = 1$ in (a) and $Ca_E = 10$ in (b). . . . .	37
Figure 3.5.	Maximum growth rate in each mode of instability as a function of: (a) electric capillary number, and (b) electric Reynolds number for two different systems with $R = 0.5$ and $R = 2$ while $(Q, \lambda) = (1, 1)$ . $Re_E = 1$ in (a) and $Ca_E = 10$ in (b) (identical systems studied in Fig. 3.4). . . . .	38
Figure 3.6.	Maximum growth rate in each mode of instability as a function of: (a) viscosity ratio $\lambda$ for two different systems with $R = 0.5$ and $R = 2$ , (b) conductivity ratio $R$ , and (c) permittivity ratio $Q$ . The permittivity ratio is set to $Q = 1$ in (a,b), the conductivity ratio is $R = 1$ in (c) and $\lambda = 1$ in (b,c). . . . .	39
Figure 3.7.	Evolution of the shape of both interfaces (left column) and their charge distributions (right column) in different modes of instability: (a,b) antiphase mode for system <b>S1</b> , (c,d) in-phase mode for system <b>S2</b> . Each snapshot is color-coded based on the time it was taken (from red at $t = 0$ to blue). . . . .	43

Figure 3.8.	Growth rate $s$ as a function of wavenumber $k$ in the dominant mode of instability obtained via numerical simulations (NS) and linear stability analysis (LSA) for <b>S1</b> in (a), and <b>S2</b> in (b). In these simulations, the size of the domain is set to $L_p = 4\pi k_{max}^{-1}$ , which is twice the wavelength associated	44
Figure 3.9.	Snapshots of the tip-streaming jets (left column) formed on the upper interface during antiphase instability with different: (a) permittivity ratios in system <b>S4</b> , (b) conductivity ratios in system <b>S3</b> , and (c) viscosity ratios in system <b>S5</b> . Deformation parameter is $\mathcal{D} = 5$ for all cases except for $R = 5$	45
Figure 3.10.	Snapshots of the films during in-phase mode instability with different: (a) permittivity ratios in system <b>S4</b> , (b) conductivity ratios in system <b>S6</b> , (c) viscosity ratios in system <b>S7</b> . For the cases with inward jets, the minimum thickness of the film is $d = 0.2$ , or one tenth of the equilibrium thickness.	48
Figure 4.1.	An oblate drop under a uniform electric field: (a) the quadrupolar EHD flow from the poles to the equator. (b) convergent streamlines and tangential electric field in the vicinity of the stagnation line. ....	53
Figure 4.2.	Problem definition: two immiscible fluid layers are subject to a tangential electric field $\mathbf{E}_0$ and to a planar extensional flow $\mathbf{u}^\infty(\mathbf{x})$ , with a stagnation point located at the origin $O$ on the interface. ....	54
Figure 4.3.	Streamlines of the various background flows used in this study: (a) linear planar extensional flow, (b) periodic Taylor-Green vortex, (c) periodic array of anti-parallel point forces separated by $d$ and $L_p$ along the $z$ - and $x$ -directions, respectively. The origin is marked with a “+”, the positions of	58
Figure 4.4.	Effect of tangential electric field: dominant eigenmodes of (a) deformation $\hat{\xi}$ , and (b) interfacial charge $\hat{q}$ , obtained via Num-LSA for $(R, Q, \lambda, Re_E, Ca_E) = (2, 3, 1, 1, 15.92)$ . The corresponding growth rate values are $(s_1, s_2, s_3, s_4) = (0.111, 0.098, 0.085, 0.073)$ . (c, d) Time evolution of the interface shape	70
Figure 4.5.	Growth rate $s$ as a function of $Ca_E$ obtained by Num-LSA, LT and TS for $(R, Q, \lambda, Re_E) = (2, 3, 1, 1)$ . Inset shows the decay of the numerical error $\mathcal{E}$ with the grid size $N$ for $Ca_E = 7.96$ . ....	70
Figure 4.6.	Effect of applied stagnation-point flow: (a) dominant eigenmodes of deformation $\hat{\xi}$ obtained via Num-LSA for a system with $(\lambda, Ca) = (1, 6)$ . The corresponding growth rates are $(s_1^*, s_2^*, s_3^*, s_4^*) = (0.851, 0.650, 0.517, 0.393)$ . (b) Time evolution of the interface shape in a transient simulation with an	73

Figure 4.7.	Combined effects of electric field and flow: (a, b) dominant eigenmodes of deformation $\hat{\xi}$ and interfacial charge $\hat{q}$ for a system with $(R, Q, \lambda, Ca_E, Re_E, \hat{A}) = (2, 3, 1, 15.92, 1, 0.177)$ . (c, d) Time evolution of the interface shape and charge distribution in a transient simulation with initial condition given	75
Figure 4.8.	Maximum growth rate as a function of local strain rate $\hat{A}$ in a system with $(R, Q, \lambda, Re_E, Ca_E) = (2, 3, 1, 1, 15.92)$ . The blue and red curves show results of Num-LSA with and without charge convection, while the light and dark green curves show the predictions of LT with and without charge	77
Figure 4.9.	Maximum growth rate as a function of: (a) conductivity ratio $R$ with $Q = 3$ , and (b) permittivity ratio $Q$ with $R = 2$ . The remaining parameters are $(\lambda, Re_E, Ca_E, \hat{A}) = (1, 1, 15.92, 0.1)$ in both cases. Inset in (a) shows a longer range for the vertical axis, highlighting additional stable eigenmodes.	78
Figure 4.10.	(a) Ohmic flux and convective flux, defined in equations (4.60)–(4.61), in the dominant mode of instability for a system with $(R, Q, Ca_E, Re_E, \hat{A}) = (2, 3, 15.92, 1, 0.177)$ . (b) Ohmic flux in the dominant mode of instability for two different values of $\hat{A}$ , with and without charge convection. . . . .	79
Figure 4.11.	(a) Eigenmodes of charge $\hat{q}$ , interfacial deflection $\hat{\xi}$ , and horizontal component of the unit normal vector $\hat{n}_x$ in the dominant mode of instability for a system with $(R, Q, \lambda, Re_E, \hat{A}, Ca_E) = (2, 3, 1, 1, 0.177, 15.92)$ . (b) Resulting Ohmic currents induced by perturbations in the charge distribution	80
Figure 4.12.	Growth rate $s$ as a function of $Ca_E$ obtained via Num-LSA and LT for a system with $(R, Q) = (31.4, 0.6)$ characteristic of the EHD flow in a droplet. $Re_E$ and $\hat{A}$ are linearly proportional to $Ca_E$ in that case, and the blue marker $(\lambda, Re_E, \hat{A}, Ca_E) = (1, 4.37, 1.19, 1.45)$ is the reference point . . . .	81
Figure 5.1.	Problem definition: a leaky dielectric drop with $(\sigma^-, \epsilon^-, \mu^-)$ is suspended in another leaky dielectric fluid with $(\sigma^+, \epsilon^+, \mu^+)$ and subject to an external electric field $\mathbf{E}_\infty$ . The drop deforms and diverges from its initially spherical shape. . . . .	89
Figure 5.2.	Error in the mean curvature as a function of the number of modes used in the upsampled $P$ -space. Two ellipsoids with $l/b = 5$ (prolate) and $l/b = 0.2$ (oblate) are investigated, representing the typical shapes of a drop due to EHD flows with large deformations. $\mathbf{H}^*$ is the mean curvature . . . .	100
Figure 5.3.	(a) Large deformations and strong flow degrade the grid when a drop of system <b>S5</b> is subject to $(Ca_E, Ma) = (0.35, 5.75)$ without reparametrization. (b) Using reparametrization for the same system maintains the quality of the grid towards the steady state ( $P_{\text{cutoff}} = 0.2, \tau = 1.0$ ). Both simulations .	106

Figure 5.4.	(a) Numerical convergence for drop shape, charge density distribution, and the velocity field. The numerical solution with $N^* = 32$ is considered as the reference. The plot shows the relative error for each field, defined in Eq. (5.53), as a function of grid resolution $N$ . (b) Critically stable time . . .	107
Figure 5.5.	Axisymmetric regime: evolution of a drop of system <b>S2</b> subject to a uniform electric field with $Ca_E = 0.2$ ( $N = 8$ , $M = 3N$ ). Colors show the interfacial charge density $q$ , while arrows show the interfacial fluid velocity. Also see the corresponding video in the Supplemental Material. . . . .	109
Figure 5.6.	Steady drop deformation as a function of electric capillary number $Ca_E$ for systems <b>S1</b> in (a) and <b>S2</b> in (b). Results from our spectral boundary integral method (SBIM) are compared with the experimental data (EXP) of [141], along with axisymmetric and three-dimensional boundary integral	110
Figure 5.7.	Quincke regime: spontaneous rotation and tilt of a drop of system <b>S3</b> subject to an applied electric field with $E_\infty/E_c = 1$ and $Ca_{MW} = 1.32$ ( $N = 10$ , $M = 3N$ ). The tilt angle $\alpha$ is measured from the initial orientation of the drop as depicted. See the Supplemental Material for the corresponding	111
Figure 5.8.	Steady tilt angle $\alpha$ (a), and deformation $\mathcal{D}$ (b) as functions of the applied electric field $E_\infty/E_c$ for different values of $Ca_{MW}$ (different $r_0$ ) for system <b>S3</b> . The solid black line in (a) shows the tilt angle $\beta$ of a rigid sphere. Filled markers in (b) show cases where Quincke electrorotation occurs. We used	112
Figure 5.9.	Charge dynamics in a low-viscosity drop of <b>S4</b> with $(Ca_E, Ma) = (0.3, 1.43)$ : steady-state velocity and charge density fields in the presence of charge convection (a), and with no convection (b), and the corresponding charge profiles along the direction of the applied electric field (c). We used . . . . .	113
Figure 5.10.	WSH convergence study on a drop of <b>S4</b> with $(Ca_E, Ma) = (1.0, 0.43)$ : (a) Error in the steady-state charge density distribution as a function of mesh resolution $N$ for a fixed value of $\delta = 10^{-3}$ ( $N^* = 42$ ). Open markers correspond to cases with ringing artifacts. (b) Error in the steady-state . . .	114
Figure 6.1.	A viscous drop with interfacial nematic activity. The director field $\mathbf{n}$ represents the average orientation of the nematic particles at every point on the interface. . . . .	120
Figure 6.2.	(a) Initial configuration depicting the director field and the surface distribution of the scalar order parameter. (b) The spatial arrangement of four defects positioned at the vertices of a symmetric tetrahedron. . . . .	125

Figure 6.3.	(a) Trajectories of three defects in the $X - Y$ plane over time $t$ on an active drop with $(Ca, Pe, l_c) = (0.01, 0.2, 0.16)$ . At any given time, the reference defect is positioned at the north pole of the sphere which corresponds to $ \mathbf{X}  \rightarrow \infty$ . (b) The projection of particle trajectories . . . . .	130
Figure 6.4.	(a) The arrangements of defects oscillates between tetrahedral (left) and planar (right) configurations. (b) The average angle $\alpha$ over time for a system with $(Ca, Pe, l_c) = (0.01, 1.2, 0.32)$ , illustrating the oscillatory behavior between $120^\circ$ (red) in the planar configuration, and $109.5^\circ$ (blue) in the . .	132
Figure 6.5.	Diagram of (a) the golden braid $\mathbf{b}_1$ , and (b) the silver braid $\mathbf{b}_2$ . . . . .	134
Figure 6.6.	(a) Finite-Time Braiding Exponent (FTBE) of defect trajectories, and (b) the average active power $\bar{P}_a$ of a spherical active drop as a function of $Pe$ and $l_c$ . The markers (golden, silver, and mix) represent different dynamical phases characterized by distinct braiding patterns. The capillary number is	135
Figure 6.7.	Defect trajectories in active drops with golden (left), silver (middle), and mix (right) braiding patterns, at different values of $Pe$ . The initial positions of defects are indicated by circular markers. The time interval between the first and last data points is set to $\Delta t = 50/f_1$ , where $f_1$ corresponds to the .	136
Figure 6.8.	Chaotic regime: snapshots of the director field (first row) and the scalar order parameter represented as the colormap, along with the corresponding interfacial velocity field (second row). The simulations is conducted for a system with $(Ca, l_c, Pe) = (0.5, 0.16, 10)$ . . . . .	137
Figure 6.9.	Time-average translational velocity as a function of $Pe$ , under finite deformations: (a) $Ca = 0.5$ , and (b) $Ca = 0.3$ . Blue and brown lines correspond to $l_c = 0.16$ and $0.32$ , respectively. Filled markers indicate cases where more than four defects were observed during the evolution of the active. . .	138
Figure 6.10.	Shape-shifting active drop: snapshots of the director field (first row) and the scalar order parameter represented as the colormap, along with the corresponding interfacial velocity field (second row). The simulations is conducted for a system with $(Ca, l_c, Pe) = (0.5, 0.32, 5)$ . . . . .	139
Figure A.1.	Fastest-growing wavenumber in each mode of instability as a function of: (a) electric capillary number, and (b) electric Reynolds number for two different systems with $R = 0.5$ and $R = 2$ with $(Q, \lambda) = (1, 1)$ . $Re_E = 1$ in (a) and $Ca_E = 10$ in (b). . . . .	149

Figure A.2.	Fastest-growing wavenumber in each mode of instability as a function of: (a) viscosity ratio $\lambda$ for two different systems with $R = 0.5$ and $R = 2$ , (b) conductivity ratio $R$ , and (c) permittivity ratio $Q$ . The permittivity ratio is set to $Q = 1$ in (a,b), the conductivity ratio is $R = 1$ in (c) and $\lambda = 1$ in (b,c).	149
Figure A.3.	Evolution of the tip streaming jets during antiphase instability as a function of: (a,b) permittivity ratio in system <b>S4</b> , (c,d) conductivity ratio in system <b>S3</b> , and (e,f) viscosity ratio in system <b>S5</b> . Left and right columns show the evolution of the tip curvature and vertical tip velocity, respectively. . . . .	151
Figure A.4.	Evolution of the inward and outward jets during in-phase instability as a function of: (a,b) permittivity ratio in system <b>S4</b> , (c,d) conductivity ratio in system <b>S6</b> , and (e,f) viscosity ratio in system <b>S7</b> . Left and right columns show the evolution of the tip curvature and vertical tip velocity, respectively.	152
Figure C.1.	(a) Zero-mean oscillations of the average angle, $\beta = \alpha - \langle \alpha \rangle_t$ (in degrees $^\circ$ ), for an active drop with $(Ca, l_c, Pe) = (0.01, 0.16, 0.3)$ . Only 38% of the time series is displayed for better visualization. (b) Corresponding FFT spectrum displaying a single peak frequency $f_1$ , indicated by a triangle. . .	157
Figure C.2.	(a) Zero-mean oscillations of the average angle, $\beta = \alpha - \langle \alpha \rangle_t$ (in degrees $^\circ$ ), for an active drop with $(Ca, l_c, Pe) = (0.01, 0.16, 0.75)$ . Only 46% of the time series is displayed for better visualization. (b) The corresponding FFT spectrum displays two peaks, indicated by red ( $f_1$ ) and green ( $f_2$ ) triangles.	157
Figure C.3.	(a) Zero-mean oscillations of the average angle, $\beta = \alpha - \langle \alpha \rangle_t$ (in degrees $^\circ$ ), for an active drop with $(Ca, l_c, Pe) = (0.01, 0.16, 3)$ . Only 47% of the time series is displayed for better visualization. (b) The corresponding FFT spectrum showing a range of important time scales. The most dominant . .	158
Figure C.4.	The first and second most dominant frequencies ( $f_1$ and $f_2$ ) derived from the FFT analysis of the average angle $\alpha$ as a function of $Pe$ and $l_c$ , for an active drop with $Ca = 0.01$ . Each marker represents a distinct dynamical phase characterized by a specific braiding pattern: golden (triangle), silver	158
Figure C.5.	An immersed drop with interfacial activity. . . . .	159
Figure C.6.	Snapshots of an active drop displaying chaotic behavior under a strong activity and finite deformations. In this regime, new pairs of $\pm 1/2$ defects are continuously created and annihilated. The director field is depicted along with the scalar order parameter as the colormap for an active drop . .	162

## LIST OF TABLES

Table 3.1.	Different systems studied using numerical simulations and their dimensionless parameters. ....	42
Table 5.1.	Systems studied using simulations and their dimensional and dimensionless parameters. We use $\mu^+ = 0.69 \text{ Pas}$ , $\gamma = 4.5 \text{ mNm}^{-1}$ , $\sigma^0 = 10^{-11} \text{ Sm}^{-1}$ , and $\epsilon^0 = 8.8542 \times 10^{-12} \text{ Fm}^{-1}$ denotes the permittivity of vacuum. ....	108
Table C.1.	Non-dimensional parameters used in the simulations of active drops. ....	156

## ACKNOWLEDGEMENTS

The completion of this dissertation would have not been possible without the invaluable patience, support, and guidance of my advisor, David Saintillan. David is an exemplary scientist and mentor, whom I feel very lucky to have worked with. He provided me with valuable resources and encouraged me to tackle fundamental scientific problems. I appreciate the confidence and latitude he gave me to pursue diverse research paths while making sure I don't lose sight of the bigger picture. David is also an excellent teacher and I owe a big part of what I know in fluid mechanics to him. I am deeply grateful for his unwavering support, constant encouragement, and steadfast commitment to upholding the highest standards in scientific research.

I have been fortunate to work in collaboration with exceptional individuals across various projects. I worked closely with Petia Vlahovska and Michael Miksis from Northwestern University on problems involving electrohydrodynamic flows. I am grateful for all the meetings and insightful conversations we had which was a great learning experience for me. I am also thankful for their generous support in different stages of my career. In a separate project that I found immensely enjoyable, I had the pleasure of working with Spencer Bryngelson from the Georgia Institute of Technology on spectral boundary integral methods. This project was an amazing opportunity for me to deepen my understanding of advanced numerical techniques. Spencer's generosity in sharing his expertise, codes, and resources significantly enriched this learning journey, for which I am genuinely thankful.

I am also greatly thankful to my PhD Committee: Stefan Llewellyn Smith for meticulously proof-reading my dissertation, career advice, and his excellent lectures on advanced mathematics and asymptotics, Padmini Rangamani for her constant support for my work and valuable feedback, William Young for his insightful comments and his wonderful lectures on PDEs—especially the ones on the mathematics of shocks that I enjoyed the most— and Bo Li, for his valuable comments and support. Their perspectives and input greatly contributed to enhancing the quality of this work.

I owe my interest in physics and mathematics to a number of incredible teachers from

elementary school to high school and undergraduate studies. Notably, the methodical approaches of Mr. Masouminejad and Mr. Ramezankhani in teaching physics and mathematics have ignited my curiosity and significantly shaped my scientific perspective.

Joining U.C. San Diego for PhD has been a profoundly transformative experience in my life, and I couldn't be happier about it. This is largely attributed to the members of the Saintillan group. First, I would like to thank Achal, not only for the many tips on coding in Fortran and other software skills that I learned from him, but also for lots of fun lunch/dinners, science and non-science conversations, and side-conference activities. I should thank Brato for all the conversations we had about science and soccer, as well as career advice that I cherish deeply. Sharing the office with Akhil for almost a year was a delightful experience, filled lots of fun conversations about work as well as fun activities and gatherings. I should thank Arijit for lots of helpful discussions, especially those on differential geometry. Tanumoy, the moments we spent together during lunch breaks and coffee sessions, discussing both scientific and life matters, have been wonderful. I thank Yuzhu for the amazing discussions we had on a range of topics including nematodynamics on curved surfaces. A special appreciation goes to Cuncheng for introducing me to computational geometry and computer graphics and for letting me use his workstation to finish my simulations on time before my defense. Also, I would like to thank Luca, Chenji, and Pedro, for a cherished time spent together in the lab, as well as other social settings. I want to emphasize that each of my group mates has contributed to both my personal and professional growth during my time at U.C. San Diego, and for that I am thankful. Beyond our group, I want to extend my gratitude to Maria, Mayte, Kyle, Nate, Ali, Chris, and Aravind, who have played a vital role in keeping the biomechanics corridor lively and dynamic.

I would like to thank the administrative team of the Mechanical and Aerospace Engineering Department: Lusia Veksler, Krista Meinke, Brittany Noris, Regina Ready, and Estella Mercado. Their diligent efforts ensured everything was done in a timely and organized manner.

Meeting new friends at U.C. San Diego has truly enriched the past years with shared joy. My heartfelt thanks go to Cathleen, Jennifer, Jack, Lysha, and Adithan for the memorable

moments we've shared, and for being there to support one another during challenging times. I am also grateful for my many friends from high school, Tehran Polytechnic, and Ohio University: Parham, Mohsen, Mohammadreza, Larousse, Andrea, Ali, Mohammad, Rose, Mehdi, Taghi, Sobhan, Hadi, Maryam, Moein, Iman, Rasoul, Kiana, and Saeed. Despite being apart, their presence and bonds remain invaluable to me. Finally, many thanks to Brianna for her care, support, and inspiration over the last few years.

My parents and my family hold a special place in my heart. Their sacrifices, limitless love, and unwavering support have significantly shaped who I am today. Serving as my first teacher, my mother took on the role of homeschooling during our frequent relocations. I have fond memories of her patiently explaining the concept of proportionality, a topic I struggled to grasp at that time. My father's influence ingrained within me the pursuit of excellence and the importance of upholding principles. To my sisters, Zahra and Sarah, your steadfast love and unwavering belief in me are truly invaluable. My achievements are deeply indebted to my beloved family.

Finally, I would like to acknowledge the contributions of various researchers and authors to different chapters of this dissertation.

Chapter 3 is primarily based on the material published in *Physical Review Fluids*, authored by Mohammadhossein Firouznia and David Saintillan [58]. The dissertation author served as the primary researcher and author of this paper.

Chapter 4 is primarily based on the material published in *Journal of Fluid Mechanics*, authored by Mohammadhossein Firouznia, Michael J. Miksis, Petia M. Vlahovska and David Saintillan [57]. The dissertation author was the primary researcher and author of this paper and performed numerical simulations and worked on theoretical modeling.

Chapter 5 is primarily based on the material published in *Journal of Computational Physics*, authored by Mohammadhossein Firouznia, Spencer H. Bryngelson and David Saintillan [56]. The dissertation author was the primary researcher and author of this paper.

Chapter 6 is a manuscript in preparation authored by Mohammadhossein Firouznia and

David Saintillan. The dissertation author was the primary researcher and author of this paper.

## VITA

- 2008-2012 B.S in Mechanical Engineering  
Amirkabir University of Technology (Tehran Polytechnic), Tehran (Iran)
- 2014-2017 M.S in Mechanical Engineering  
Ohio University, Athens, Ohio
- 2018-2023 PhD in Engineering Sciences (Mechanical Engineering)  
University of California San Diego

## ABSTRACT OF THE DISSERTATION

Interfacially driven flows: from electrohydrodynamics to active interfaces

by

Mohammadhossein Firouznia

Doctor of Philosophy in Engineering Sciences (Mechanical Engineering)

University of California San Diego, 2023

Professor David Saintillan, Chair

Interfacially driven flows are ubiquitous in biological processes and engineering applications. In these systems, the interface separating adjacent fluid phases is subject to mechanical stresses that drive the fluid into motion and cause deformations. The origin of interfacial stresses may vary from one physical system to another. In some cases, such as in electrohydrodynamic flows, an external electric field induces interfacial stresses that drag the fluid into motion. Alternatively, in active matter systems, an internal mechanism converts chemical energy into mechanical work and drives the system out of equilibrium. The main challenge in studying these systems lies in unraveling the complex interplay between the bulk flow, nonlinear transport on the interface, and interface mechanics, which collectively give rise to intricate dynamical behaviors.

We develop robust theoretical and computational frameworks to address these challenges. In the first part of this thesis, we employ analytical and numerical analyses to study different canonical electrohydrodynamic problems. The interfacial charge dynamics is modeled by considering different transport mechanisms including Ohmic conduction, advection by the flow, and finite charge relaxation. Using this model, we identify different modes of instability and explore how the non-equilibrium evolution of flow and interfacial charge dynamics lead to nonlinear phenomena observed in experiments, such as tip streaming in liquid films, Quincke rotation in drops, tip formation, and the growth of charge density shocks in stratified systems.

Furthermore, our investigation extends to biological surfaces that exhibit in-plane order, such as nematic or polar, and are driven internally by microscopic chemical reactions. We study morphological dynamics in a freely-suspended viscous drop with surface nematic activity, which serves as a simplified model for understanding self-organized behaviors in active living systems such as cells. We demonstrate how the coupling of flow, nematic activity, and interface mechanics can induce symmetry-breaking instabilities and spontaneous deformations in active drops, consistent with experimental observations. Diverse dynamical behaviors are observed, from periodic braiding motion of topological defects to chaotic creation and annihilation of defects under high activity levels. Our study provides valuable insights into emergent dynamics in biological and biomimetic systems involving active fluid surfaces.

# Chapter 1

## Interfacially driven flows

A diverse range of engineering and natural processes involves flows of different fluid phases interacting with one another. In these systems, two immiscible fluids are separated by a deformable interface. In various applications, the interface hosts a variable quantity that is transported by the flow, as well as other mechanisms like diffusion. Examples include electrical charges [103, 193], concentration of surfactants [94, 168, 173], proteins or any other chemical species [83, 9]. In all of the examples mentioned above, the surface distribution of a scalar variable is of interest. However, the mathematical representation of the system can be generalized to encompass cases where a tensor field (of different orders) defined at each point on the interface, is transported by the flow, along with other mechanisms. This representation has been used to describe the evolution of biological fluid interfaces that exhibit different forms of in-plane order such as nematic or polar order [106, 78, 87]. The interplay between the flow, mechanics of the interface, and the transport of the surface variable gives rise to rich dynamical behavior in these systems.

Of interest to us are systems where the flow emerges due to mechanical stresses applied at the interface. The mechanism responsible for interfacial stresses could vary from one physical system to another. In some cases, such as in electrohydrodynamic (EHD) flows, an external electric field induces interfacial stresses that drag the fluid into motion. Alternatively, in active systems, an internal mechanism transforms chemical energy into mechanical work and drives

the system out of equilibrium. The intricate interplay between the bulk flow in each fluid phase, nonlinear transport on the interface, and the mechanics of the deforming interface leads to complex dynamical behaviors in these systems, thereby rendering theoretical and computational analysis inherently challenging. In this work, we develop theoretical and computational frameworks to study interfacial flows that are driven whether externally or internally, due to the stresses applied at the interface.

In Sec. 1.1, we discuss electrohydrodynamic flows in weakly conducting fluids and introduce the leaky dielectric model (LDM) that serves as the theoretical foundation for Ch. 3, 4, and 5. Next, in Sec. 1.2 we discuss the theory of active liquid crystals (ALC) that is used to study the self-organized behavior of viscous drops with surface nematic activity in Ch. 6.

## **1.1 Electrohydrodynamics**

Electrohydrodynamics (EHD) is the study of electrically induced flows that mainly involve weakly conducting fluids and solids. Despite similarities between EHD and electrokinetics (EK), both fields have advanced almost independently, as they focus on different types of fluids and interfaces. From classic works in colloid science [4, 99] to more recent developments in microfluidics [13], EK studies are predominantly concentrated on charged fluids, specifically liquid electrolytes that give rise to neutral dipolar interfaces called electric double layers [12]. On the other hand, the field of EHD is focused on weakly conducting neutral fluids [103, 143]. Examples of such fluids include silicone oil, castor oil and vegetable oil. Following the leaky dielectric assumption, the effects of diffuse charge layers are neglected, and the dynamics is primarily dictated by the forces acting upon interfacial polarization charges by the electric field. Recently, there have been some efforts to reconcile EHD and EK theories, which will be discussed in Sec. 1.1.1.

In his seminal work, Taylor pioneered the field of EHD in 1966 where he predicted and

visualized the quadrupolar flows inside and outside of a drop that is subject to a uniform electric field [176]. In the limit of weak electric fields, he determined that the direction of the flow, and the shape of the drop are affected by the material properties in the drop and the suspending phase. In 1969, Melcher and Taylor formally defined the field of electrohydrodynamics in a review article [103]. The development of EHD has led to a variety of engineering applications including those in jet printing [121], cooling of microelectronics [7, 135, 38], microfabrication [31, 146, 147, 96, 111, 199], and other microfluidic devices that improve mixing and droplet formation [202, 162]. In addition, EHD phenomena such as electrophoresis (EP) and dielectrophoresis (DEP) have been employed to manipulate particles [198, 120, 122], and sort cells [80].

In this work, we study interfacial instabilities in different EHD systems that are motivated by experimental observations and engineering applications. In Ch. 3, we consider a film of a leaky dielectric that is suspended in another leaky dielectric fluid while subject to a uniform electric field. In addition to its fundamental importance as a canonical problem in EHD systems, this configuration mimicks microfluidic applications where EHD instabilities are employed to create prescribed patterns, enhance mixing between two immiscible phases, or to generate drops of a certain size. We identify the main modes of instability using linear stability analysis. In each mode, we explore the nonlinear regime of evolution following the onset of instability via boundary element simulations. We demonstrate that the interplay of the flow, charge dynamics, and capillary effects gives rise to nonlinear phenomena in this regime, such as tip streaming jets and pinching into droplets.

The electric-field induced flows in a drop have been a long-standing subject of investigation in the field of electrohydrodynamics, garnering significant attention from researchers. Taylor's seminal study [176] was followed by a subsequent body of works studying the dynamics of the system under stronger electric fields. Recent experimental observations show that oblate drops may undergo equatorial streaming under strong electric fields [20]. In this configuration, the equator is the stagnation line of the flow and the electric field is locally tangent to the interface

at the equator. Inspired by the experimental observations, we study interfacial instabilities that occur when a planar interface is subject to a tangential electric field and a stagnation point flow in Ch. 4. Our study integrates local theoretical analysis with numerical normal-mode linear stability analysis, uncovering the crucial role of charge convection in influencing the dynamics of the system. Through stability analyses along with numerical simulations far from the equilibrium, we provide valuable insights into the underlying mechanisms that drive EHD equatorial streaming in droplets. Specifically, we demonstrate that the interplay between the flow and charge dynamics leads to the emergence of a convergent line instability and the generation of pronounced charge gradients at the equatorial region.

In Ch. 5, we develop a spectral boundary integral method for simulating EHD flows in a droplet, under a uniform electric field. Using a comprehensive charge transport model that incorporates charge relaxation, Ohmic conduction, and surface charge convection, we account for various electric field strengths. All physical quantities, including the shape of the droplet and interfacial charge density, are represented using spherical harmonic expansions. The adoption of a spectral representation offers exponential accuracy and allows for a non-dissipative dealiasing method, which ensures numerical stability. We validate our methodology and simulations by comparing our results against experimental data and analytical predictions in the axisymmetric Taylor and Quincke electrorotation regimes. This serves as an assessment of the accuracy and reliability of our method. In the case of low-viscosity droplets, strong charge convection leads to steep interfacial charge gradients near the equatorial region of the droplet. However, this can introduce numerical artifacts known as ringing. To address this issue, we employ a weighted spherical harmonic expansion approach, which enables convergent solutions.

### **1.1.1 From electrokinetic theories to leaky dielectric model**

In leaky dielectric materials, the ion dissociation in the presence of an electric field is weak. Therefore, the effect of diffuse Debye layers is negligible in these systems. Consequently,

the fluid motion occurs as a result of the coupling between the electric and the hydrodynamic stresses at the interface. It has been shown by Schnitzer and Yariv that the Taylor–Melcher leaky dielectric model (LDM) can be derived asymptotically from electrokinetic models in the double limit of strong electric fields and thin Debye layers [148, 112, 11]. Two fundamental parameters determining this asymptotic limit are the dimensionless Debye thickness  $\delta = \delta_D/a$ , and  $\beta = aE_0/\varphi^*$  which is the ratio of the applied field voltage (applied electric field  $E_0$  times the characteristic length  $a$ ) to the thermal voltage  $\varphi^* = k_B T/e$  is the thermal voltage. Schnitzer and Yariv derived the effective LDM in the leading-order in the limit  $1 \ll \beta \ll \delta^{-1}$  by matching asymptotic expansions in the inner and outer regions of  $O(\delta)$  and  $O(1)$  thickness, respectively.

In the case of millimeter-sized drops, Saville provided the characteristic value for Debye thickness in leaky dielectric liquids as  $\delta_D \sim 10^{-7}$  m which results in  $\delta \sim 10^{-4}$  [143]. Considering an approximate thermal voltage of  $\varphi^* \approx 25$  mV at room temperature, and an external electric field of magnitude  $E_0 \sim 10^3$  V cm<sup>-1</sup> (typical in experiments) yields an applied voltage ratio of  $\beta \sim 10^3$  [141, 20]. Therefore, the asymptotic limit  $1 \ll \beta \ll \delta^{-1}$  holds in our systems of interest, and the use of Taylor–Melcher leaky dielectric model is justified.

### 1.1.2 Leaky dielectric model

In this section, we present the Melcher–Taylor leaky dielectric model (LDM) for a model system [103]. We assume that two immiscible fluid phases occupying volumes  $V_1$  and  $V_2$  are separated by an interface  $\partial V$  as shown schematically in Fig.1.1. The shape of  $\partial V$  can be expressed by  $z = \xi(x, t)$  in two dimensions (or  $z = \xi(x, y, t)$  in three dimensions), and has unit normal  $\mathbf{n}$  pointing from fluid 1 into fluid 2. A background velocity field  $\mathbf{u}_0(\mathbf{x})$  is applied to the system along with a uniform external electric field  $\mathbf{E}_0$ . Under this static applied electric field, the magnetic  $\mathbf{B}$  and electric fields  $\mathbf{E}$  are decoupled in the Maxwell’s equations [81, 143]. In the absence of an external magnetic field, the magnetic field is zero everywhere in space  $\mathbf{B}(\mathbf{x}) = \mathbf{0}$ ,  $\mathbf{x} \in V_{1,2}, \partial V$ . Therefore, according to Maxwell-Faraday equation, the electric field is irrotational:

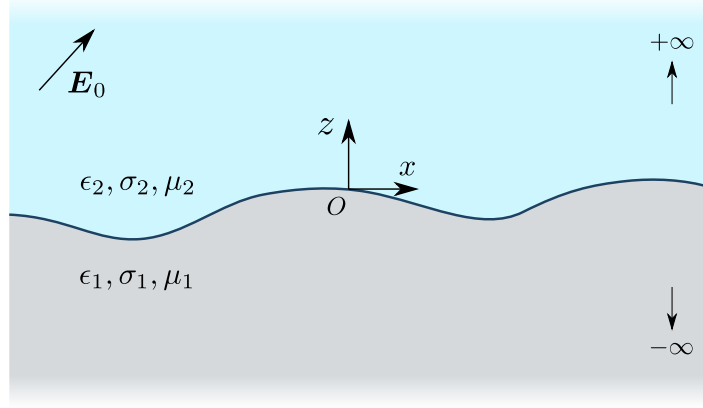


**Figure 1.1.** Two immiscible fluid layers are subject to an external uniform electric field  $\mathbf{E}_0$  and a background velocity field  $\mathbf{u}_0(\mathbf{x})$ .

$$\nabla \times \mathbf{E} = 0, \quad \mathbf{x} \in V_{1,2}, \partial V. \quad (1.1)$$

The Gauss' law relates the charge density  $q$  to the electric displacement field  $\mathbf{D} = \epsilon \mathbf{E}$ :

$$\nabla \cdot \mathbf{D}(\mathbf{x}) = q(\mathbf{x}), \quad \mathbf{x} \in V_{1,2}. \quad (1.2)$$

Following the leaky dielectric assumption for the fluids, the polarization charges appear only on the interface  $\partial V$ . In other words, the bulk of fluids remain electro-neutral,  $q(\mathbf{x}) = 0$ ,  $\mathbf{x} \in V_{1,2}$ . Considering the relationship  $\mathbf{E} = -\nabla \varphi$ , it follows that the electric potential  $\varphi$  is harmonic in both phases:

$$\nabla^2 \varphi = 0, \quad \mathbf{x} \in V_{1,2}. \quad (1.3)$$

The material properties including electric permittivities, electric conductivities, and viscosities are denoted by  $(\epsilon_1, \sigma_1, \mu_1)$  and  $(\epsilon_2, \sigma_2, \mu_2)$  in each fluid, respectively. Far away from the interface, the electric field approaches the applied uniform field:

$$\mathbf{E}(\mathbf{x}) \rightarrow \mathbf{E}_0, \quad \text{as } |y| \rightarrow \infty. \quad (1.4)$$

Across the interface, the tangential component of the electric field remains continuous while its normal component suffers a jump, due to the mismatch in electrical properties on both sides:

$$\mathbf{n} \times \llbracket \mathbf{E} \rrbracket = \mathbf{0}, \quad \mathbf{x} \in \partial V. \quad (1.5)$$

As a result, a surface charge density develops on the interface:

$$q(\mathbf{x}) = \mathbf{n} \cdot \llbracket \epsilon \mathbf{E} \rrbracket, \quad \mathbf{x} \in \partial V. \quad (1.6)$$

Equation (1.6) can be derived by applying the Gauss' law on a pill-box enclosing a portion of the interface and using the divergence theorem. (1.5) can be obtained similarly from (1.1). A new notation is introduced in (1.5) and (1.6) that we refer to as the jump operator. It is defined as the difference in any field variable  $g(\mathbf{x})$  on both sides of the interface,  $\llbracket g(\mathbf{x}) \rrbracket := g_2(\mathbf{x}) - g_1(\mathbf{x})$ . The evolution of the surface charge density is determined by balancing different interfacial charge fluxes in the system, and by taking into account finite charge relaxation:

$$\partial_t q + \mathbf{n} \cdot \llbracket \sigma \mathbf{E} \rrbracket + \nabla_s \cdot (q \mathbf{u}) = 0, \quad \mathbf{x} \in \partial V, \quad (1.7)$$

where  $\nabla_s = (\mathbf{I} - \mathbf{nn}) \cdot \nabla$  is the surface gradient operator.  $\mathbf{n} \cdot \llbracket \sigma \mathbf{E} \rrbracket$  is the net Ohmic flux from the bulk of the fluids while  $\nabla_s \cdot (q \mathbf{u})$  represents the surface charge convection by the flow.

Next, we investigate the fluid motion and its subsequent coupling with the electric problem. Neglecting the effects of inertia and gravity, the fluid motion is governed by the Stokes equations in both layers:

$$\mu_1 \nabla^2 \mathbf{u}_1 - \nabla p_1 = \mathbf{0}, \quad \nabla \cdot \mathbf{u}_1 = 0, \quad \mathbf{x} \in V_1, \quad (1.8)$$

$$\mu_2 \nabla^2 \mathbf{u}_2 - \nabla p_2 = \mathbf{0}, \quad \nabla \cdot \mathbf{u}_2 = 0, \quad \mathbf{x} \in V_2. \quad (1.9)$$

The velocity is continuous across the interface, and approaches the background velocity field far

away from the interface:

$$\llbracket \mathbf{u}(\mathbf{x}) \rrbracket = \mathbf{0}, \quad \mathbf{x} \in \partial V, \quad (1.10)$$

$$\mathbf{u}(\mathbf{x}) \rightarrow \mathbf{u}_0(\mathbf{x}), \quad \text{as } |y| \rightarrow \infty. \quad (1.11)$$

The interfacial force balance requires that the jump in electric and hydrodynamic tractions across the interface balance surface tension forces:

$$\llbracket \mathbf{f}^H \rrbracket + \llbracket \mathbf{f}^E \rrbracket = \gamma(\nabla_s \cdot \mathbf{n})\mathbf{n}, \quad \mathbf{x} \in \partial V, \quad (1.12)$$

where  $\gamma$  denotes the surface tension between the two liquids, and it is assumed to be constant along  $\partial V$ . Hydrodynamic and electric tractions can be expressed in terms of the Newtonian and Maxwell stress tensors, respectively:

$$\mathbf{f}^H = \mathbf{n} \cdot \mathbf{T}^H, \quad \mathbf{T}^H = -p\mathbf{I} + \mu(\nabla\mathbf{u} + \nabla\mathbf{u}^T), \quad (1.13)$$

$$\mathbf{f}^E = \mathbf{n} \cdot \mathbf{T}^E, \quad \mathbf{T}^E = \epsilon \left( \mathbf{E}\mathbf{E} - \frac{1}{2}E^2\mathbf{I} \right). \quad (1.14)$$

The electric traction can alternatively be expressed in terms of its tangential and normal components:

$$\mathbf{f}^E = \llbracket \epsilon E^n \rrbracket \mathbf{E}^t + \frac{1}{2} \llbracket \epsilon (E^{n2} - E^{t2}) \rrbracket \mathbf{n} = q\mathbf{E}^t + \llbracket p^E \rrbracket \mathbf{n}. \quad (1.15)$$

The effect of the tangential electric field on the interfacial charge distribution is captured by the first term on the right-hand side. The second term in (1.15) captures normal electric stresses and can be interpreted as the jump in an electric pressure [90]. It is important to highlight that the nonlinear coupling between the electric field and fluid flow arises from the charge conservation equation (1.7), and the dynamic boundary condition (1.12), leading to an intricate interplay between the electric field and the fluid flow in the system. We employ a similar approach, as discussed above, to investigate EHD flows in the subsequent chapters of this study.

## 1.2 Active surfaces

In a wide range of biological systems, different fluid phases are interacting with one another via a soft interface. These biological surfaces are typically driven by microscopic chemical reactions. Furthermore, they often exhibit a form of in-plane order (such as nematic or polar) that enables extensive hydrodynamic interactions and self-organized phenomena. The intricate interplay between surface mechanics, chemical activity, in-plane hydrodynamic interactions, and fluid flow results in complex dynamics that are crucial in various biological processes in cells and tissues. The mechanical properties of cells and tissues are primarily governed by actomyosin networks. Actin filaments are semiflexible polymers that constantly undergo polymerization and depolymerization, and characterized by a persistence length of approximately  $10 - 15\mu\text{m}$  [139]. Given their typical length, thermal fluctuations do not strongly distort their overall shape. However, the bending modulus of these filaments is small enough that bending contributes to their mechanical response. Actin filaments form crosslinked networks that display active properties, setting them apart from passive semiflexible networks. Within these complex meshworks, molecular motors called Myosin generate contractile stresses by exerting force on actin filaments in opposing directions. To capture the behavior of actomyosin networks, coarse-grained models have been developed, treating them as continuous *active gels* that experience internal stresses that arise from the activity [89, 130, 109, 140, 3]. These models have been successful in describing the prominent physical behavior of various biological processes, ranging from the subcellular to the supracellular level.

Cellular morphology is primarily governed by cellular mechanical properties and the cell's physical interaction with its environment. Most cell deformations are primarily governed by modulating the physical properties of the cell surface, which are predominantly determined by the cellular cortex [29]. The cortex refers to a thin, interconnected actomyosin network

positioned directly beneath the plasma membrane of animal cells. Due to its attachment to the cell membrane, the cortex plays a crucial role in regulating the shape of the cell. Recently, there has been a growing interest in understanding various functions of the cortex in cellular processes. Coarse-grained models have proven successful in explaining a range of biophysical phenomena such as cell migration [75], polarization [102, 67, 27], bleb expansion [187], and cell deformations during cytokinesis [149, 108, 36].

At larger scales, collections of cells often demonstrate geometrically ordered patterns and share characteristic features of active gels. Examples include, bacterial colonies [43], and tissues [145]. It has been observed that epithelial tissues exhibit elastic behavior over short time scales, and fluid-like behavior over long times [130]. Morphogenesis of tissues involves the contraction of actomyosin networks, which generate forces. The attachment of actin networks to cell-cell junctions allows for the transmission of forces between cells, leading to deformations and shape adjustments in individual cells, contributing to tissue remodeling and the shaping of different organisms. In recent years, researchers have utilized coarse-grained models for tissues based on the active gel formalism in various theoretical and computational studies [78, 106, 153, 87]. These studies provided valuable insights into the main mechanisms involved in morphogenesis, such as apical constriction [101, 170].

Soft active materials have been constructed by drawing inspiration from the biological systems discussed above [86, 73, 196]. In their pioneering study, Keber and colleagues encapsulated a film of microtubules and kinesin motors on the inner surface of a lipid vesicle, resulting in a shape-shifting structure [86]. Their work inspired further investigations into the interplay between orientational order, activity-induced flow, and substrate geometry [206, 155]. These studies have provided a deeper understanding of the emergent behavior in these soft active materials.

In this work, we are focused on investigating soft active surfaces characterized by in-plane nematic order. Experimental observations have shown that the cortex exhibits nematic order and self-induced flows during the last stages of cytokinesis [197, 134, 167]. Nematic order has

also been observed in tissues composed of cells with elongated shapes [144, 72, 46]. These observations highlight the prevalence of nematic order in various biological and biomimetic systems, and serve as a motivation for our study in Ch.6 on viscous drops with surface nematic activity. In the next step, we discuss the hydrodynamic equations for an interfacial film of active nematic material in Sec 1.2.1 .

### 1.2.1 Hydrodynamics of interfacial active nematics

In this section, we present a hydrodynamic theory for an interfacial film of active nematic materials. Similar to Sec. 1.1.2, we consider two immiscible fluid phases occupying volumes  $V_1$  and  $V_2$ . These fluids are separated by an interface  $\partial V$  as shown schematically in Fig. 1.2. The shape of  $\partial V$  is defined by a smooth surface  $\mathbf{r} = \mathbf{r}(s^1, s^2)$  embedded in  $\mathbb{R}^3$  and parameterized by coordinates  $(s^1, s^2)$ . Tangent vectors  $\mathbf{g}_i = \partial_i \mathbf{r}$  ( $i = 1, 2$ ) along with the unit normal vector  $\mathbf{v} = (\mathbf{g}_1 \times \mathbf{g}_2) / |\mathbf{g}_1 \times \mathbf{g}_2|$  form a local coordinate system with the surface metric tensor given by  $g_{ij} = \mathbf{g}_i \cdot \mathbf{g}_j$ . The notations used for differential geometry are summarized in the appendix B. A monolayer of active nematic particles is constrained to the interface and their activity drives the system out of equilibrium by inducing flows in  $V_1$  and  $V_2$ , and by causing deformations to the interface. We use a coarse-grained representation of the nematic field using  $\mathbf{Q}$  tensor:

$$\mathbf{Q} = Q^{ij} \mathbf{g}_i \mathbf{g}_j \quad \text{where} \quad Q^{ij} = S(n^i n^j - g^{ij}/2). \quad (1.16)$$

$\mathbf{n} = n^i \mathbf{g}_i$  denotes the local average nematic director such that  $n^i n_i = 1$ , and  $S$  ( $0 \leq S \leq 1$ ) is the scalar order parameter showing the strength of local alignment in the nematic monolayer. According to (1.16),  $\mathbf{Q}$  is symmetric, trace-free and resides only on the surface,  $\mathbf{Q} \cdot \mathbf{v} = \mathbf{0}$ . It is also important to note that the two states characterized by  $\mathbf{n}$  and  $-\mathbf{n}$  are equivalent, due to nematic symmetry. Using  $\mathbf{Q}$  tensor which is quadratic in  $\mathbf{n}$ , we ensure that the nematic symmetry is reflected in all governing equations.

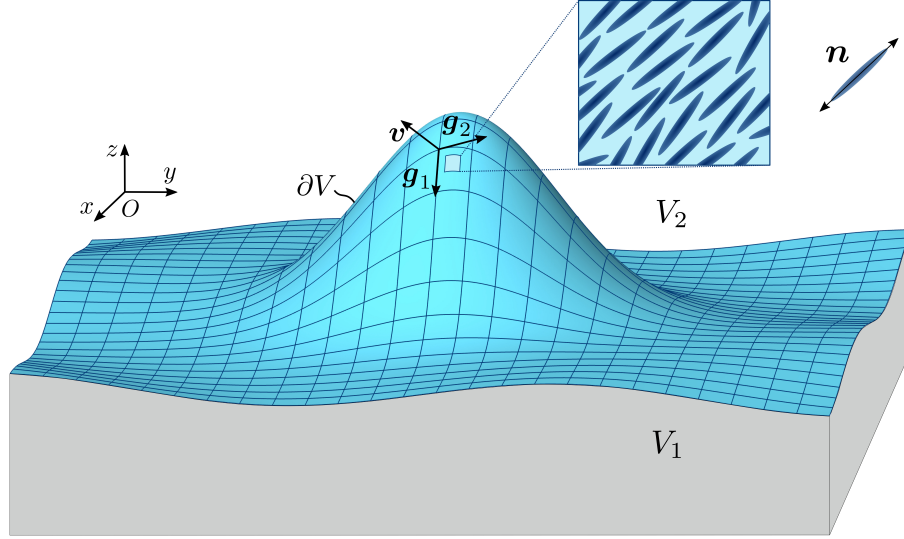


**Figure 1.2.** An active interface, denoted by  $\partial V$ , separates two fluid layers,  $V_1$  and  $V_2$ . The director field  $\mathbf{n}(\mathbf{x})$  describes the average orientation of the nematic particles at every point on the interface.

The evolution of the nematic tensor is described by the hydrodynamic equations of an active nematic. In this study, we use a theoretical model that is consistent with that of Giomi et al. in [66, 123] and Salbreux et al. in [140]. Accordingly, the evolution of the nematic field is influenced by advection, rotation, and alignment by the flow, as well as orientational relaxation:

$$D_t Q^{ij} = \frac{1}{\Gamma} H^{ij} + \zeta \tilde{U}^{ij}, \quad \mathbf{x} \in \partial V. \quad (1.17)$$

The term on the left-hand side denotes a co-rotational material derivative that embodies the advection and rotation of the nematic field by the flow:

$$D_t Q^{ij} = \partial_t Q^{ij} + u^k \nabla_k Q^{ij} + u_n (C_k^j Q^{ik} + C_k^i Q^{kj}) + w_n (\epsilon^{ik} Q_k^j + \epsilon^{jk} Q_k^i). \quad (1.18)$$

In the equation above,  $\nabla_k$  is the covariant derivative with respect to  $s^k$ . The curvature tensor is given by  $C_{ij} = -\partial_j \partial_i \mathbf{r} \cdot \mathbf{n}$ .  $w_n = \frac{1}{2} \epsilon^{ij} \nabla_i u_j$  is the normal vorticity, and  $\epsilon^{ij} = \mathbf{v} \cdot (\mathbf{g}^i \times \mathbf{g}^j)$  is the Levi-Civita tensor. In Eq. (1.17), the first term on the right-hand side models the orientational

relaxation governed by the molecular tensor  $H^{ij} = -\delta F / \delta Q^{ij}$ . Here,  $\Gamma$  denotes the rotational viscosity. The free energy  $F$  is expressed as:

$$F = \frac{1}{2} \int_{\partial V} dA \left( k_s [d Q_{ij} Q^{ij} + c (Q_{ij} Q^{ij})^2] + k_e [\nabla_i Q_{jk} \nabla^i Q^{jk}] \right), \quad (1.19)$$

by accounting for short-range and elastic interactions in the nematic monolayer [116, 88].  $k_s$  and  $k_e$  are steric and elastic phenomenological constants and  $d = (a + \frac{b}{3}S + \frac{c}{6}S^2)$ , where  $a$ ,  $b$  and  $c$  are normalized thermotropic parameters [42]. We assume that the characteristic length of an individual nematic particle is relatively small compared to the characteristic radius of curvature. Therefore, we do not consider any explicit coupling with the extrinsic curvature and the nematic tensor in Eq. (1.19). Effectively, short-range terms prevent the free energy from vanishing, while the elastic terms penalize the gradients of the nematic tensor. The interplay between these two effects gives rise to the characteristic coherence length  $l_c = \sqrt{k_e/k_s}$ . The coherence length represents the distance over which a topological defect influences the surrounding nematic field.

The alignment of the nematic field by the flow is captured by the term  $\zeta \tilde{U}^{ij}$  in Equation (1.17). Here,  $\zeta$  represents the flow alignment parameter, and  $\tilde{U}^{ij}$  corresponds to the trace-less part of the strain-rate tensor:

$$\tilde{U}^{ij} = U^{ij} - \frac{1}{2} U^k_k g^{ij}, \quad U^{ij} = \frac{1}{2} (\nabla^i u^j + \nabla^j u^i) + C^{ij} u_n. \quad (1.20)$$

We note that the velocity vector can be decomposed into tangential and normal components as  $\mathbf{u} = u^i \mathbf{g}_i + u_n \mathbf{v}$  at any point on the interface.

Nematic particles exert active stress  $\mathbf{T}^a = \xi \mathbf{Q}$  on their surrounding which drags the fluid into motion and causes deformations. The constant  $\xi$  represents the biochemical activity level and  $\xi < 0$  ( $\xi > 0$ ) in the case of extensile (contractile) activity. Fig. 1.3 shows the typical flow induced under extensile and contractile activity. In the absence of inertia, the local force balance

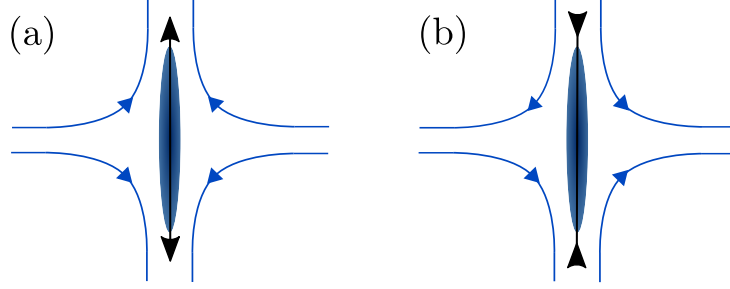


**Figure 1.3.** The induced flow by a nematic particle with (a) extensile ( $\xi < 0$ ), and (b) contractile ( $\xi > 0$ ) activity.

along the tangential and normal directions reads

$$f^{H,j} + \xi \nabla_i Q^{ij} = 0, \quad \mathbf{x} \in \partial V, \quad (1.21)$$

$$f_n^H - \gamma C_k^k - \xi C_{ij} Q^{ij} = 0, \quad \mathbf{x} \in \partial V, \quad (1.22)$$

where  $\gamma$  is the surface tension, and the mean curvature is given by  $H = \frac{1}{2} C_k^k$ . In (1.21) and (1.22),  $\mathbf{f}^H = \mathbf{v} \cdot \llbracket \mathbf{T}^H \rrbracket$  represents the jump in the hydrodynamic traction across the interface, and  $\mathbf{T}^H = -p\mathbf{I} + \mu(\nabla\mathbf{u} + \nabla\mathbf{u}^T)$  is the Newtonian stress tensor.

Finally, the dynamics of the interface is coupled to the bulk flow. We follow a similar approach as discussed in Sec. 1.1.2 for EHD systems. Neglecting inertial effects and gravity, the flow is governed by Stokes and continuity equations in  $V_1$  and  $V_2$ :

$$\mu_1 \nabla^2 \mathbf{u}_1 - \nabla p_1 = \mathbf{0}, \quad \nabla \cdot \mathbf{u}_1 = 0, \quad \mathbf{x} \in V_1, \quad (1.23)$$

$$\mu_2 \nabla^2 \mathbf{u}_2 - \nabla p_2 = \mathbf{0}, \quad \nabla \cdot \mathbf{u}_2 = 0, \quad \mathbf{x} \in V_2. \quad (1.24)$$

The velocity vector remains continuous across the interface and vanishes far from it.

$$\llbracket \mathbf{u}(\mathbf{x}) \rrbracket = \mathbf{0}, \quad \mathbf{x} \in \partial V, \quad (1.25)$$

$$\mathbf{u}(\mathbf{x}) \rightarrow \mathbf{0}, \quad \text{as } |z| \rightarrow \infty. \quad (1.26)$$

The coupling between the surface mechanics, the evolution of the interfacial nematic monolayer, and the bulk flow yields a complex dynamical behavior. In Ch. 6, we adopt a similar approach as discussed above, to analyze self-organized phenomena in viscous drops that possess interfacial nematic activity.

## Chapter 2

# Boundary integral method

The boundary integral method is a powerful computational technique utilized in various scientific and engineering applications to tackle problems governed by elliptic partial differential equations. This method excels by reducing the dimensionality of the problems at hand, enabling efficient and accurate solutions for partial differential equations in complex and evolving geometries where conventional methods are inefficient or unreliable. Notably, the boundary integral method is applicable in electromagnetic and potential problems governed by Laplace's equation, low-Reynolds-number hydrodynamic problems governed by Stokes equations, biomolecular electrostatic problems governed by Poisson-Boltzmann equation, and problems in linear elasticity governed by Navier's equation.

In this study, our primary focus is on Laplace's and Stokes equations that are coupled in EHD systems. In the case of active systems, the flow within the bulk is governed by the Stokes equation. We derive the boundary integral equations for Laplace's and Stokes equations and discuss their properties in this chapter. For more detailed derivations, in-depth discussions, and different applications of the boundary integral method, the works of Pozrikidis [125, 126] offer extensive resources on the subject matter.

## 2.1 Laplace's equation

A Green's function represents the solution of a PDE in the presence of a singularity. Therefore, the Green's function satisfies the PDE everywhere in space except at the singular point  $\mathbf{x} = \mathbf{x}_0$ . In the following, we discuss the Green's function for Laplace's equation in two and three dimensions .

The singularly forced Laplace equation reads:

$$\nabla^2 G(\mathbf{x}, \mathbf{x}_0) + \delta_d(\mathbf{x} - \mathbf{x}_0) = 0, \quad d \in \{2, 3\}, \quad (2.1)$$

where different values of  $d$  corresponds to two, and three dimensions. The second term in (2.1) is the Dirac's delta function representing the singularity located at  $\mathbf{x} = \mathbf{x}_0$ . Solving (2.1) by inspection or using Fourier transform, we obtain:

$$G(\mathbf{x}, \mathbf{x}_0) = -\frac{1}{2\pi} \ln r, \quad \text{for } d = 2, \quad (2.2)$$

$$G(\mathbf{x}, \mathbf{x}_0) = \frac{1}{4\pi r}, \quad \text{for } d = 3, \quad (2.3)$$

where  $r = |\mathbf{x} - \mathbf{x}_0|$  is the distance between the field point  $\mathbf{x}$  and the singular point  $\mathbf{x}_0$ . Equations (2.2) and (2.3) are also known as free-space Green's functions and correspond to infinite solution domains in the absence of any interior boundaries. According to (2.2) and (2.3), it is evident that  $G(\mathbf{x}, \mathbf{x}_0) = G(\mathbf{x}_0, \mathbf{x})$ .

Green's second identity states that the following relation holds between two functions  $f(\mathbf{x})$  and  $\varphi(\mathbf{x})$  that are twice-differentiable:

$$f \nabla^2 \varphi - \varphi \nabla^2 f = \nabla \cdot (f \nabla \varphi - \varphi \nabla f). \quad (2.4)$$

Let us assume that  $\varphi$  is harmonic. Without loss of generality, we consider the case of  $d = 3$  in the following discussion. Substituting  $f(\mathbf{x})$  by the Green's function  $G(\mathbf{x}, \mathbf{x}_0)$ , and using (2.1), we

get:

$$\varphi(\mathbf{x}) \delta_3(\mathbf{x} - \mathbf{x}_0) = \nabla \cdot (G(\mathbf{x}, \mathbf{x}_0) \nabla \varphi(\mathbf{x}) - \varphi(\mathbf{x}) \nabla G(\mathbf{x}, \mathbf{x}_0)). \quad (2.5)$$

Next, we integrate Eq.(2.5) over the volume  $V$  enclosed by boundary  $\partial V$ . After using the integral property of the delta function and the divergence theorem, we obtain the following integral equation:

$$\begin{aligned} \varphi(\mathbf{x}_0) = & - \int_{\partial V} G(\mathbf{x}, \mathbf{x}_0) [\mathbf{n}(\mathbf{x}) \cdot \nabla \varphi(\mathbf{x})] dS(\mathbf{x}) \\ & + \int_{\partial V} \varphi(\mathbf{x}) [\mathbf{n}(\mathbf{x}) \cdot \nabla G(\mathbf{x}, \mathbf{x}_0)] dS(\mathbf{x}), \quad \mathbf{x}_0 \in V, \end{aligned} \quad (2.6)$$

where  $\mathbf{n}(\mathbf{x})$  is the unit normal vector pointing into  $V$ . The first and second integrals on the right-hand side of (2.6) represent boundary distributions of point-sources and point-source dipoles, known as *single-layer potential* and *double-layer potential*, respectively. The equation above holds when the evaluation point  $\mathbf{x}_0$  is located in  $V$ . When the evaluation point  $\mathbf{x}_0$  approaches the boundary  $\partial V$ , careful evaluation reveals that the single-layer potential remains continuous, while the double-layer potential experiences a jump. By accounting for this discontinuity and utilizing integral identities, we arrive at the following integral equation:

$$\begin{aligned} \varphi(\mathbf{x}_0) = & -2 \int_{\partial V} G(\mathbf{x}, \mathbf{x}_0) [\mathbf{n}(\mathbf{x}) \cdot \nabla \varphi(\mathbf{x})] dS(\mathbf{x}) \\ & + 2 \int_{\partial V}^{PV} \varphi(\mathbf{x}) [\mathbf{n}(\mathbf{x}) \cdot \nabla G(\mathbf{x}, \mathbf{x}_0)] dS(\mathbf{x}), \quad \mathbf{x}_0 \in \partial V, \end{aligned} \quad (2.7)$$

where the evaluation point is located on the boundary, and  $PV$  denotes the principal-value integral.

## 2.2 Stokes equation

In this section, we follow a similar approach to the one used for the Laplace's equation in the previous section. Let us consider the flow due to a point force located at  $\mathbf{x} = \mathbf{x}_0$ . The Stokes

equation is given by:

$$\nabla \cdot \boldsymbol{\sigma} + \delta_d(\mathbf{x} - \mathbf{x}_0) \mathbf{b} = -\nabla p + \mu \nabla^2 \mathbf{u} + \delta_d(\mathbf{x} - \mathbf{x}_0) \mathbf{b} = \mathbf{0}, \quad d \in \{2, 3\}, \quad (2.8)$$

where  $\mathbf{b}$  is a constant vector characterizing the strength and direction of the point force, and  $\boldsymbol{\sigma} = -\nabla p + \mu(\nabla \mathbf{u} + \nabla \mathbf{u}^T)$  is the Newtonian hydrodynamic stress tensor. The Green's function for Stokes equation provides an incompressible velocity field  $\nabla \cdot \mathbf{u} = 0$ , and pressure that satisfy (2.8). It is convenient to express the solution in the following form, using index notation:

$$u_i(\mathbf{x}) = \frac{1}{2^d \pi \mu} \mathcal{G}_{ij}(\mathbf{x}, \mathbf{x}_0) b_j, \quad d \in \{2, 3\}, \quad (2.9)$$

$$p(\mathbf{x}) = \frac{1}{2^d \pi} \mathcal{P}_j(\mathbf{x}, \mathbf{x}_0) b_j, \quad (2.10)$$

$$\sigma_{ij}(\mathbf{x}) = \frac{1}{2^d \pi} \mathcal{T}_{ikj}(\mathbf{x}, \mathbf{x}_0) b_k. \quad (2.11)$$

The solution to (2.8) is given by

$$\mathcal{G}_{ij}(\mathbf{x}, \mathbf{x}_0) = \delta_{ij} \ln r + \frac{r_i r_j}{r^2}, \quad (2.12)$$

$$\mathcal{P}_i(\mathbf{x}, \mathbf{x}_0) = 2 \frac{r_i}{r^2}, \quad (2.13)$$

$$\mathcal{T}_{ijk}(\mathbf{x}, \mathbf{x}_0) = -4 \frac{r_i r_j r_k}{r^4}, \quad (2.14)$$

in two dimensions  $d = 2$ , and by

$$\mathcal{G}_{ij}(\mathbf{x}, \mathbf{x}_0) = \frac{\delta_{ij}}{r} + \frac{r_i r_j}{r^3}, \quad (2.15)$$

$$\mathcal{P}_i(\mathbf{x}, \mathbf{x}_0) = 2 \frac{r_i}{r^3}, \quad (2.16)$$

$$\mathcal{T}_{ijk}(\mathbf{x}, \mathbf{x}_0) = -6 \frac{r_i r_j r_k}{r^5}, \quad (2.17)$$

in three dimensions  $d = 3$ . In the equations above,  $\mathbf{r} = \mathbf{x} - \mathbf{x}_0$  represents the vector difference between the field point  $\mathbf{x}$  and the singular point  $\mathbf{x}_0$ , while  $r = |\mathbf{x} - \mathbf{x}_0|$  denotes the distance between them. The tensors  $\mathcal{G}$  and  $\mathcal{T}$  are commonly known as the *Stokeslet* (or the *Oseen-Burgers tensor*) and the *stresslet*, respectively. We highlight two important properties of the Green's function for velocity. First, it satisfies the incompressibility condition, which is expressed as:

$$\frac{\partial \mathcal{G}_{ij}}{\partial x_i}(\mathbf{x}, \mathbf{x}_0) = 0. \quad (2.18)$$

Secondly, it has the following symmetry property:

$$\mathcal{G}_{ij}(\mathbf{x}, \mathbf{x}_0) = \mathcal{G}_{ji}(\mathbf{x}_0, \mathbf{x}). \quad (2.19)$$

In addition, the symmetry of the hydrodynamic stress tensor requires that:

$$\mathcal{T}_{ijk}(\mathbf{x}, \mathbf{x}_0) = \mathcal{T}_{kji}(\mathbf{x}, \mathbf{x}_0). \quad (2.20)$$

In order to recast the Stokes equation into the form of boundary integrals, we use Lorentz reciprocal theorem which serves as the counterpart of Green's second identity used in the previous section. Without loss of generality, we proceed with the derivation for the case of three dimensions,  $d = 3$ . Let us consider two solutions of the Stokes equation for the same fluid, in the control volume  $V$  enclosed by the boundary  $\partial V$ , and denoted as  $u_i, \sigma_{ij}$  and  $u'_i, \sigma'_{ij}$ . According to the Lorentz reciprocal theorem, the following relation exists between these two solutions:

$$\frac{\partial}{\partial x_j} (u'_i \sigma_{ij} - u_i \sigma'_{ij}) = 0. \quad (2.21)$$

Integrating (2.21) over the control volume and applying the divergence theorem, we obtain:

$$\int_{\partial V} \left[ u'_i(\mathbf{x}) \sigma_{ij}(\mathbf{x}) - u_i(\mathbf{x}) \sigma'_{ij}(\mathbf{x}) \right] n_j(\mathbf{x}) dS(\mathbf{x}) = 0. \quad (2.22)$$

where  $\mathbf{n}$  is the unit normal vector pointing into the control volume  $V$ . Next, we substitute (2.9) and (2.11) into the equation above. If the singular point is outside of the control volume,  $\mathbf{x}_0 \notin V$  the function inside the bracket is regular. Therefore, using the divergence theorem, we obtain:

$$\int_{\partial V} [\mathcal{G}_{ij}(\mathbf{x}, \mathbf{x}_0) \sigma_{ik}(\mathbf{x}) - \mu u_i(\mathbf{x}) \mathcal{T}_{ijk}(\mathbf{x}, \mathbf{x}_0)] n_k dS(\mathbf{x}) = 0. \quad (2.23)$$

However, when  $\mathbf{x}_0 \in V$  the function inside the bracket in (2.23) is singular at  $\mathbf{x} = \mathbf{x}_0$ . To handle this singularity, we consider a spherical volume  $V_\epsilon$  with radius  $\epsilon$ , centered at  $\mathbf{x} = \mathbf{x}_0$ . By doing so, we convert (2.23) to the following regular integral over the reduced volume,  $V - V_\epsilon$ :

$$\int_{\partial V \cup \partial V_\epsilon} [\mathcal{G}_{ij}(\mathbf{x}, \mathbf{x}_0) \sigma_{ik}(\mathbf{x}) - \mu u_i(\mathbf{x}) \mathcal{T}_{ijk}(\mathbf{x}, \mathbf{x}_0)] n_k dS(\mathbf{x}) = 0. \quad (2.24)$$

In the limit of  $\epsilon \rightarrow 0$ , it can be shown that the boundary integral over  $\partial V_\epsilon$  is equal to  $8\pi\mu u_j(\mathbf{x}_0)$  [125]. Therefore, we obtain the Stokes boundary integral equation as:

$$u_j(\mathbf{x}_0) = -\frac{1}{8\pi\mu} \int_{\partial V} \mathcal{G}_{ij}(\mathbf{x}, \mathbf{x}_0) f_k(\mathbf{x}) dS(\mathbf{x}) + \frac{1}{8\pi} \int_{\partial V} u_i(\mathbf{x}) \mathcal{T}_{ijk}(\mathbf{x}, \mathbf{x}_0) n_k dS(\mathbf{x}), \quad \mathbf{x}_0 \in V. \quad (2.25)$$

where  $f_k = \sigma_{jk} n_k$  is the hydrodynamic traction. Physically, the first integral on the right-hand side of (2.25) represents the flow due to a boundary distribution of point forces, known as the *single-layer potential*. The second integral however, represents the flow due to a distribution of point-force dipoles on the boundary and is called the *double-layer potential*. As the evaluation point  $\mathbf{x}_0$  approaches the boundary, the double-layer potential exhibits a jump. By accounting for this jump and utilizing integral identities, we derive the following boundary integral equation

when the evaluation point is precisely located on the boundary,  $\mathbf{x}_0 \in \partial V$  [125]:

$$u_j(\mathbf{x}_0) = -\frac{1}{4\pi\mu} \int_{\partial V} \mathcal{G}_{ij}(\mathbf{x}, \mathbf{x}_0) f_k(\mathbf{x}) dS(\mathbf{x}) + \frac{1}{4\pi} \int_{\partial V}^{PV} u_i(\mathbf{x}) \mathcal{T}_{ijk}(\mathbf{x}, \mathbf{x}_0) n_k dS(\mathbf{x}), \quad \mathbf{x}_0 \in \partial V, \quad (2.26)$$

where  $PV$  denotes the principal-value.

The Laplace's and Stokes boundary integral equations presented in equations (2.7) and (2.26) can be numerically solved through various techniques such as discretizing the boundary into elements or employing spectral methods. The primary advantage of boundary integral methods lies in their ability to reduce the solution space by one dimension. Rather than solving the governing equations within the entire physical domain  $V$ , as done in finite element or finite difference methods, boundary integral methods focus solely on solving the equations on the boundary  $\partial V$ . This reduction in dimensionality significantly improves the computational efficiency.

Boundary integral methods particularly excel in cases involving linear, elliptic, and homogeneous partial differential equations governing boundary value problems. For such problems, boundary integral methods offer superior performance compared to conventional methods like finite element and finite difference approaches. However, the discretization of boundary integral equations results in dense linear systems that require iterative solvers. Additionally, since the boundary integral method is derived using fundamental singularity solutions, the resulting integrals may be singular. These singularities must be treated either analytically or numerically to ensure accurate and convergent numerical solutions.

## Chapter 3

# Electrohydrodynamic instabilities in viscous films

Electrohydrodynamic instabilities of fluid-fluid interfaces can be exploited in various microfluidic applications in order to enhance mixing, replicate well-controlled patterns or generate drops of a particular size. In this work, we study the stability and dynamics of a system of three superimposed layers of two immiscible fluids subject to a normal electric field. Following the Taylor-Melcher leaky dielectric model, the bulk remains electroneutral while a net charge accumulates on the interfaces. The interfacial charge dynamics is captured by a conservation equation accounting for Ohmic conduction, advection by the flow and finite charge relaxation. Using this model, we perform a linear stability analysis and identify different modes of instability, and we characterize the behavior of the system as a function of the relevant dimensionless groups in each mode. Further, we perform numerical simulations using the boundary element method in order to study the effect of nonlinearities on long-time interfacial dynamics. We demonstrate how the coupling of flow and surface charge transport in different modes of instability can give rise to nonlinear phenomena such as tip streaming or pinching of the film into droplets.

## 3.1 Introduction

The interface between two immiscible fluids can become unstable under the effect of an imposed electric field. In weakly conducting dielectrics, ion dissociation in the presence of an electric field is negligible, and therefore, diffuse Debye layers are absent in these systems where the fluid motion occurs as a result of the coupling between the electric and the hydrodynamic stresses at the interface. Following the Taylor-Melcher leaky dielectric model, the bulk of the fluid is assumed electroneutral and all free charges are concentrated on the interfaces separating the fluid volumes with different electrical properties [103, 143]. The electric field acting on the interfacial charge creates electric stresses along the normal and tangential directions, which cause deformation and drag the fluid into motion. Surface tension acts mainly as a stabilizing effect, trying to restore the equilibrium interfacial shape.

In their pioneering works, Taylor and McEwan [178] and Melcher and coworkers [104, 105] studied the effect of an electric field on the stability of fluid-fluid interfaces and provided analytical solutions in different limits. Their analyses were followed by an extensive body of research aiming to obtain more accurate analytical solutions [119, 95, 190], to provide numerical solutions for large deformations [179, 33] and to study more complex configurations such as multi-layer systems [107, 124, 156, 202, 204]. Of interest to us here is to understand the stability and dynamics of a system of superimposed fluid layers under the effect of an external electric field. Apart from its fundamental importance, there has been a renewed interest in this topic in recent years due to engineering applications where these electrohydrodynamic (EHD) instabilities have been exploited to develop techniques by which well-controlled patterns can be replicated on free surfaces, such as polymeric films or fluid layers flowing in microfluidic channels. In one of these techniques, EHD instabilities are employed to create fine periodic patterns in polymeric layers confined between a substrate and a mask [31, 146, 147, 96, 111]. A summary of these applications is reviewed in [199]. Theoretical analyses and numerical simulations have been employed to study the behavior of these systems under the following

assumptions: (i) in the limit of zero inertia [179, 35, 190], (ii) in the limit of instantaneous charge relaxation where the charge is mainly transported via Ohmic current [179, 204], and (iii) using the lubrication approximation for thin films [124, 156, 179, 95].

More recently, EHD instabilities have been used in microfluidic devices to enhance mixing, or to generate droplets of a certain size. Zahn and Reddy [202] developed a microfluidic mixer where two streams of immiscible fluids are mixed in a microchannel by applying an external field. Zhang *et al.* [204] used transfer relations to study two- and trilayer systems in a variety of configurations such as unbounded geometries and channel flows, and provided analytical solutions in different limits of the Reynolds number. They recovered the previous analytical results of [107, 119] for trilayer systems, and those of [190] for two-layers systems as special cases of their model. Considering the limit of instantaneous charge relaxation, they observed two modes of instability which they referred to as “kink” and “sausage”.

In this work, we study the stability and dynamics of a freely suspended viscous film that is subject to a perpendicular external electric field. We use a charge transport model that incorporates finite charge relaxation, interfacial charge convection as well as Ohmic conduction from the bulk. This enables us to characterize the effect of charge convection on the behavior of the system, which is especially important under strong electric fields. We present the governing equations in Sec. 3.2 and their non-dimensionalization in Sec. 3.3. Next, we conduct a linear stability analysis in Sec. 3.4 where we study the effect of the non-dimensional parameters governing the system on the fastest growing mode at the onset of instability. To supplement our theory, we employ boundary element simulations in Sec. 3.5 to explore how the development of the flow and charge dynamics far from equilibrium gives rise to nonlinear phenomena such as tip streaming or pinching into droplets. Finally, we conclude and discuss the potential extensions to the present work in Sec. 3.6.

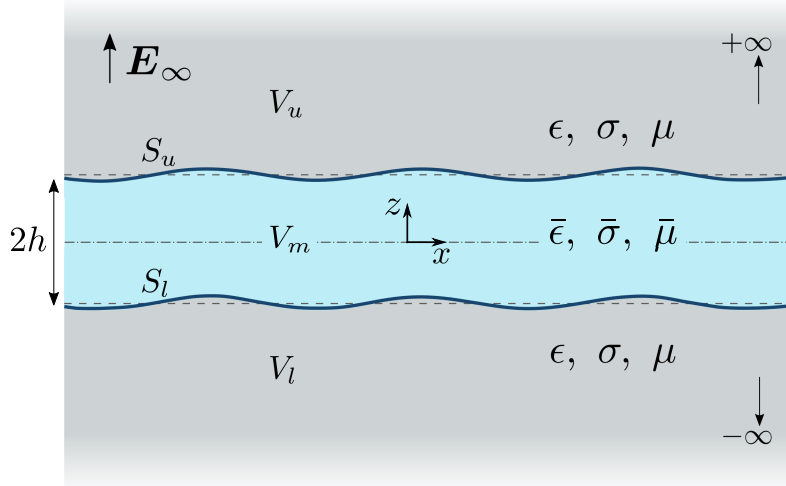


**Figure 3.1.** Problem definition: a liquid film suspended between two infinite immiscible liquid layers is subject to a perpendicular electric field  $\mathbf{E}_\infty$ .

## 3.2 Problem definition and governing equations

We study electrohydrodynamic instabilities that arise at the interfaces of a neutrally buoyant liquid film that is suspended in another liquid and subject to a uniform electric field along the perpendicular direction  $\mathbf{E}_\infty = E_\infty \hat{\mathbf{e}}_z$ . The liquid film occupying volume  $V_m$  is surrounded by the upper layer  $V_u$  from above, and by the lower layer  $V_l$  from below as depicted in Fig. 3.1. The subscripts  $l$ ,  $m$  and  $u$  correspond to the lower, middle and upper layers, respectively. The interfaces separating the three liquid layers are denoted by  $S_l$  and  $S_u$ . At equilibrium, the system is at rest, both interfaces are flat and coincide with the planes  $z = \pm h$ . We consider two-dimensional dynamics in the  $(x, z)$  plane. The shape of each interface is parametrized as  $z = \xi_{l,u}(x, t)$ , with unit normal  $\mathbf{n}$  pointing from the film into the suspending liquid.

The two phases are immiscible leaky dielectric Newtonian fluids with constant material properties. The electric permittivities, electric conductivities and viscosities are denoted by  $(\bar{\epsilon}, \bar{\sigma}, \bar{\mu})$  in the film and by  $(\epsilon, \sigma, \mu)$  in the suspending liquid. Following the Taylor-Melcher leaky dielectric model [103], the bulk is assumed to be electroneutral while any net charge in the system is concentrated on the interfaces between the two liquids. Consequently, the electric

potential is harmonic in all layers:

$$\nabla^2 \varphi_j(\mathbf{x}) = 0, \quad \mathbf{x} \in V_j, \quad j \in \{l, m, u\}. \quad (3.1)$$

Far from the film, the electric field  $\mathbf{E} = -\nabla\varphi$  approaches the applied uniform field:

$$\mathbf{E} \rightarrow \mathbf{E}_\infty = E_\infty \hat{\mathbf{e}}_z, \quad \text{as } z \rightarrow \pm\infty. \quad (3.2)$$

Across the interface, the tangential component of the electric field remains continuous while its normal component undergoes a jump due to the mismatch in electrical properties on both sides:

$$\mathbf{n} \times \llbracket \mathbf{E} \rrbracket = \mathbf{0}, \quad \mathbf{x} \in S_j, \quad j \in \{l, u\}. \quad (3.3)$$

As a result, a surface charge density  $q(\mathbf{x})$  develops on each interface and is given by Gauss's law:

$$q_i(\mathbf{x}) = \mathbf{n} \cdot \llbracket \epsilon \mathbf{E} \rrbracket, \quad \mathbf{x} \in S_i, \quad i \in \{l, u\}. \quad (3.4)$$

The jump operator introduced above is defined as the subtraction of any field variable on both sides of each interface,  $\llbracket \mathcal{F}(\mathbf{x}) \rrbracket = \mathcal{F}_{l,u}(\mathbf{x}) - \mathcal{F}_m(\mathbf{x})$ . The evolution of the surface charge density is described by a charge conservation equation accounting for finite charge relaxation, Ohmic conduction from the bulk and charge convection by the induced velocity:

$$\partial_t q_i + \mathbf{n} \cdot \llbracket \sigma \mathbf{E} \rrbracket + \nabla_s \cdot (q\mathbf{u})_i = 0, \quad \mathbf{x} \in S_i, \quad i \in \{l, u\}, \quad (3.5)$$

where  $\nabla_s = (\mathbf{I} - \mathbf{nn}) \cdot \nabla$  is the surface gradient operator.

Neglecting the effects of inertia and gravity, the fluid motion is governed by the Stokes

equations in all layers:

$$\bar{\mu}\nabla^2\mathbf{u}_m - \nabla p_m = \mathbf{0}, \quad \nabla \cdot \mathbf{u}_m = 0, \quad \mathbf{x} \in V_m, \quad (3.6)$$

$$\mu\nabla^2\mathbf{u}_j - \nabla p_j = \mathbf{0}, \quad \nabla \cdot \mathbf{u}_j = 0, \quad \mathbf{x} \in V_j, \quad j \in \{l, u\}. \quad (3.7)$$

The velocity is continuous across the interfaces, and vanishes far away from the film:

$$\llbracket \mathbf{u}(\mathbf{x}) \rrbracket = \mathbf{0}, \quad \mathbf{x} \in S_{l,u}, \quad (3.8)$$

$$\mathbf{u}(\mathbf{x}) \rightarrow \mathbf{0}, \quad \text{as } z \rightarrow \pm\infty. \quad (3.9)$$

In the absence of Marangoni effects, the jump in electric and hydrodynamic tractions across each interface is balanced by surface tension forces:

$$\llbracket \mathbf{f}^H \rrbracket + \llbracket \mathbf{f}^E \rrbracket = \gamma(\nabla_s \cdot \mathbf{n})\mathbf{n}, \quad \mathbf{x} \in S_{l,u}, \quad (3.10)$$

where  $\gamma$  denotes the surface tension between the two liquids, assumed to be constant. Hydrodynamic and electric tractions can be expressed in terms of the Newtonian and Maxwell stress tensors, respectively:

$$\mathbf{f}^H = \mathbf{n} \cdot \mathbf{T}^H, \quad \mathbf{T}^H = -p\mathbf{I} + \mu(\nabla\mathbf{u} + \nabla\mathbf{u}^T), \quad (3.11)$$

$$\mathbf{f}^E = \mathbf{n} \cdot \mathbf{T}^E, \quad \mathbf{T}^E = \epsilon\left(\mathbf{E}\mathbf{E} - \frac{1}{2}E^2\mathbf{I}\right). \quad (3.12)$$

The electric traction can alternatively be expressed in terms of its tangential and normal components:

$$\mathbf{f}^E = \llbracket \epsilon E^n \rrbracket \mathbf{E}_t + \frac{1}{2} \llbracket \epsilon(E^{n2} - E^{t2}) \rrbracket \mathbf{n} = q\mathbf{E}_t + \llbracket p^E \rrbracket \mathbf{n}. \quad (3.13)$$

The effect of the tangential electric field on the interfacial charge distribution is captured by the first term on the right-hand side. The second term captures normal electric stresses and can be

interpreted as the jump in an electric pressure [90].

Finally, the interfaces evolve and deform under the local velocity field as material surfaces. Defining the functions  $g_{l,u}(\mathbf{x}, t) = z - \xi_{l,u}(x, t)$ , the kinematic boundary conditions read:

$$\frac{Dg_j}{Dt} = 0, \quad \mathbf{x} \in S_j, \quad j \in \{l, u\}, \quad (3.14)$$

leading to the conditions

$$\partial_t \xi_j = -u \partial_x \xi_j + w, \quad \mathbf{x} \in S_j, \quad j \in \{l, u\}, \quad (3.15)$$

where  $\mathbf{u} = (u, w)$  are the velocity components. Also, the outward unit normal vectors to each interface can be written as  $\mathbf{n}_u = (\nabla g / |\nabla g|)_u$  and  $\mathbf{n}_l = -(\nabla g / |\nabla g|)_l$ .

### 3.3 Non-dimensionalization

For the system of governing equations presented above, dimensional analysis yields five non-dimensional groups, three of which characterize the mismatch in physical properties between the film and the suspending liquid:

$$R = \frac{\sigma}{\bar{\sigma}}, \quad Q = \frac{\bar{\epsilon}}{\epsilon}, \quad \lambda = \frac{\bar{\mu}}{\mu}. \quad (3.16)$$

A system with  $\lambda > 1$  corresponds to a film that is more viscous than the suspending liquid, and vice versa. The limit  $\lambda \rightarrow \infty$  describes a rigid film, while  $\lambda \rightarrow 0$  is relevant to describe a gas film suspended in a liquid.

The other two non-dimensional groups can be obtained as the ratios of different times scales in the problem. First, we note that the conduction response of each liquid layer is characterized by the charge relaxation time scale, which is the time required for the free charge in

the bulk to relax:

$$\tau_c = \frac{\epsilon}{\sigma}, \quad \bar{\tau}_c = \frac{\bar{\epsilon}}{\bar{\sigma}}, \quad (3.17)$$

as can be deduced from Eqs. (3.4) and (3.5). The product  $RQ = \bar{\tau}_c/\tau_c$  is the ratio of the charge relaxation time scales in both liquids. For instance, in the case  $RQ < 1$  conduction occurs at a faster rate in the film. Under an applied electric field, free charges in the bulk start to move towards the interfaces, resulting in the polarization of the film. This occurs on a time scale comparable to the Maxwell-Wagner relaxation time:

$$\tau_{MW} = \frac{\bar{\epsilon} + 2\epsilon}{\bar{\sigma} + 2\sigma} = \frac{\tau_c}{\alpha}, \quad \text{where} \quad \alpha = \frac{1 + 2R}{R(Q + 2)}. \quad (3.18)$$

Following the accumulation of charge on the interfaces, the fluid is dragged into motion due to the force exerted by the electric field. This electrohydrodynamic flow deforms the interfaces on a time scale that is proportional to the inverse shear rate of the driving electric stress:

$$\tau_{EHD} = \frac{\mu(1 + \lambda)}{\epsilon E_\infty^2}. \quad (3.19)$$

In response, the interfacial tension acts as a restoring effect trying to minimize the surface area. The deformed interface recovers its equilibrium flat shape on the capillary time scale defined as:

$$\tau_\gamma = \frac{\mu(1 + \lambda)h}{\gamma}. \quad (3.20)$$

By comparing  $\tau_c$ ,  $\tau_{EHD}$  and  $\tau_\gamma$ , we can construct two additional non-dimensional groups. First, we define the electric capillary number as the ratio of the capillary time scale over the electrohydrodynamic flow time scale:

$$Ca_E = \frac{\tau_\gamma}{\tau_{EHD}} = \frac{\epsilon E_\infty^2 h}{\gamma}. \quad (3.21)$$

According to Eq. (3.21), the stronger the applied electric field the larger the electric capillary number. Moreover, the ratio of the charge relaxation time scale to the flow time scale defines the electric Reynolds number:

$$Re_E = \frac{\tau_c}{\tau_{EHD}} = \frac{\epsilon^2 E_\infty^2}{\mu(1+\lambda)\sigma}, \quad (3.22)$$

which characterizes the importance of charge convection versus conduction, two mechanisms responsible for the evolution of the interfacial charge distribution.

We scale the governing equations and boundary conditions using time scale  $\tau_{MW}$ , length scale  $h$ , pressure scale  $\epsilon E_\infty^2$ , velocity scale  $h\tau_{EHD}^{-1}$ , and characteristic electric potential  $hE_\infty$ . The dimensionless momentum equations read:

$$\nabla^2 \mathbf{u}_m - (1 + \lambda^{-1}) \nabla p_m = 0, \quad \mathbf{x} \in V_m, \quad (3.23)$$

$$\nabla^2 \mathbf{u}_j - (1 + \lambda) \nabla p_j = 0, \quad \mathbf{x} \in V_j, \quad j \in \{l, u\}. \quad (3.24)$$

The charge conservation equations become:

$$\alpha \partial_t q_j + \mathbf{n} \cdot [\mathbf{E}_j - R^{-1} \mathbf{E}_m] + Re_E \nabla_s \cdot (q \mathbf{u})_j = 0, \quad \mathbf{x} \in S_j, \quad j \in \{l, u\} \quad (3.25)$$

where

$$q_j = \mathbf{n} \cdot [\mathbf{E}_j - Q \mathbf{E}_m], \quad \mathbf{x} \in S_j, \quad j \in \{l, u\}. \quad (3.26)$$

The stress balance at the interfaces yields:

$$\begin{aligned} & \mathbf{n} \cdot \left[ -p_j \mathbf{I} + (1 + \lambda)^{-1} (\nabla \mathbf{u}_j + \nabla \mathbf{u}_j^T) + p_m \mathbf{I} - (1 + \lambda^{-1})^{-1} (\nabla \mathbf{u}_m + \nabla \mathbf{u}_m^T) \right] \\ & + \mathbf{n} \cdot \left[ (\mathbf{E}_j \mathbf{E}_j - \frac{1}{2} E_j^2 \mathbf{I}) - Q (\mathbf{E}_m \mathbf{E}_m - \frac{1}{2} E_m^2 \mathbf{I}) \right] = Ca_E^{-1} (\nabla_s \cdot \mathbf{n}) \mathbf{n}, \quad \mathbf{x} \in S_j, \quad j \in \{l, u\}. \end{aligned} \quad (3.27)$$

Finally, the kinematic boundary conditions become:

$$\alpha \partial_t \xi_j = Re_E (w - u \partial_x \xi_j), \quad \mathbf{x} \in S_j, \quad j \in \{l, u\}. \quad (3.28)$$

The remaining governing equations and boundary conditions in (3.1)–(3.3), (3.8) and (3.9) remain unchanged in their non-dimensional form, and hence are not repeated here for brevity. In the remainder of the paper, all equations and variables are presented in non-dimensional form.

## 3.4 Linear stability analysis

### 3.4.1 Theoretical formulation

In this section, we perform a linear stability analysis to study the dynamic behavior of the system at short times as a function of the governing parameters. We note that the system is stable in the absence of the electric field due to the effect of surface tension. In the base state (tilded variables), all liquid layers are at rest, both interfaces have flat shapes,  $\tilde{\xi}_u = -\tilde{\xi}_l = 1$ , and the interfacial charges are  $\tilde{q}_u = -\tilde{q}_l = 1 - RQ$ . The applied electric field induces pressure jumps  $\tilde{p}_u - \tilde{p}_m = \tilde{p}_l - \tilde{p}_m = (1 - QR^2)/2$  across the interfaces due to the mismatch in electrical properties between the film and the suspending liquid. We consider infinitesimal perturbations (primed variables) applied to the base state variables:

$$\xi_l = -1 + \varepsilon\xi'_l, \quad \xi_u = 1 + \varepsilon\xi'_u, \quad q_l = \tilde{q}_l + \varepsilon q'_l, \quad q_u = \tilde{q}_u + \varepsilon q'_u, \quad (3.29)$$

$$\varphi_j = \tilde{\varphi}_j + \varepsilon\varphi'_j, \quad \mathbf{u}_j = \tilde{\mathbf{u}}_j + \varepsilon\mathbf{u}'_j, \quad p_j = \tilde{p}_j + \varepsilon p'_j, \quad j \in \{l, m, u\}. \quad (3.30)$$

Next, we substitute Eqs. (3.29) and (3.30) into the governing equations and boundary conditions and linearize with respect to  $\varepsilon$ . The governing equations for the electric potential, velocity and pressure are:

$$\nabla^2 \varphi'_j(\mathbf{x}) = 0, \quad \mathbf{x} \in V_j, \quad j \in \{l, m, u\}, \quad (3.31)$$

$$\nabla^2 \mathbf{u}'_m - (1 + \lambda^{-1}) \nabla p'_m = \mathbf{0}, \quad \mathbf{x} \in V_m, \quad (3.32)$$

$$\nabla^2 \mathbf{u}'_j - (1 + \lambda) \nabla p'_j = \mathbf{0}, \quad \mathbf{x} \in V_j, \quad j \in \{l, u\}. \quad (3.33)$$

with jump conditions  $[[u']] = [[w']] = 0$  and  $\hat{\mathbf{e}}_z \times [[\mathbf{E}']] + \mathbf{n}' \times [[\tilde{\mathbf{E}}]] = \mathbf{0}$ . The stress balance at the linearized location of the upper interface  $z = 1$  yields

$$(1 - QR^2)\partial_x \xi'_u = (1 + \lambda^{-1})^{-1} (\partial_z u'_m + \partial_x w'_m) - (1 + \lambda)^{-1} (\partial_z u'_u + \partial_x w'_u) + \partial_x \varphi'_u - RQ\partial_x \varphi'_m, \quad (3.34)$$

$$Ca_E^{-1}\partial_{xx}\xi'_u = 2(1 + \lambda^{-1})^{-1}\partial_z w'_m - 2(1 + \lambda)^{-1}\partial_z w'_u + p'_u - p'_m + \partial_z \varphi'_u - RQ\partial_z \varphi'_m, \quad (3.35)$$

along the  $x$  and  $z$  directions, respectively. The kinematic boundary condition, charge conservation equation and Gauss's law read:

$$\alpha \partial_t \xi'_u = Re_E w'_u, \quad (3.36)$$

$$\alpha \partial_t q'_u = [\partial_z \varphi'_u - R^{-1} \partial_z \varphi'_m] + Re_E (1 - RQ) \partial_z w'_u, \quad (3.37)$$

$$q'_u = Q \partial_z \varphi'_m - \partial_z \varphi'_u. \quad (3.38)$$

Similarly, the linearized boundary conditions on the lower interface  $z = -1$  are:

$$(1 - QR^2)\partial_x \xi'_l = (1 + \lambda^{-1})^{-1} (\partial_z u'_m + \partial_x w'_m) - (1 + \lambda)^{-1} (\partial_z u'_l + \partial_x w'_l) + \partial_x \varphi'_l - RQ\partial_x \varphi'_m, \quad (3.39)$$

$$Ca_E^{-1}\partial_{xx}\xi'_l = 2(1 + \lambda)^{-1}\partial_z w'_l - 2(1 + \lambda^{-1})^{-1}\partial_z w'_m + p'_m - p'_l + RQ\partial_z \varphi'_m - \partial_z \varphi'_l, \quad (3.40)$$

$$\alpha \partial_t \xi'_l = Re_E w'_l, \quad (3.41)$$

$$\alpha \partial_t q'_l = [R^{-1} \partial_z \varphi'_m - \partial_z \varphi'_l] - Re_E (1 - RQ) \partial_z w'_l, \quad (3.42)$$

$$q'_l = \partial_z \varphi'_l - Q \partial_z \varphi'_m. \quad (3.43)$$

Next, we seek normal-mode solutions of the form  $\varphi'(x, z, t) = \Re\{\hat{\varphi}(z) \exp(st + ikx)\}$ , with similar expressions for all the variables. We perform a temporal stability analysis, in which the wavenumber  $k$  of the perturbation is real-value and the corresponding growth rate  $s$  can in general be complex. Substituting the normal-mode solutions into the governing equations, we obtain a coupled system of differential equations for the normal-mode amplitude functions such as  $\hat{\varphi}(z)$  (see appendix A.1 for details of the equations). Applying the boundary conditions along

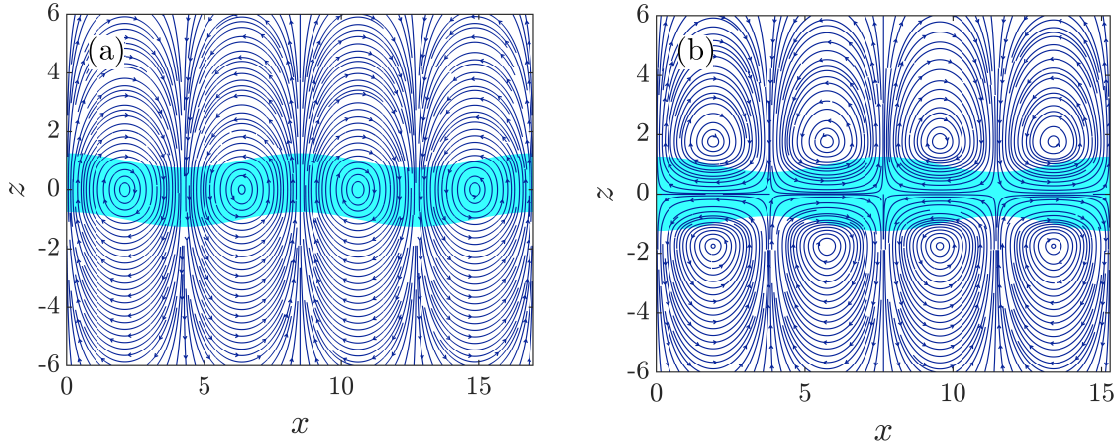


**Figure 3.2.** Streamlines of the flow in the two dominant modes of linear instability: (a) in-phase (sinuous) mode when  $R = 2$ , (b) antiphase (varicose) mode when  $R = 0.5$ . Other parameters are  $(Q, \lambda, Ca_E, Re_E) = (1, 1, 10, 1)$  in both systems. The blue region illustrates a typical shape of the film in the dominant mode.

with the decay properties as  $z \rightarrow \pm\infty$  results in an algebraic system for the unknown coefficients. Finally, we obtain a biquadratic dispersion relation by setting the determinant of the algebraic system to zero.

Employing a more comprehensive charge transport model compared to the previous studies [204, 95] results in a larger number of parameters. Therefore, the eigenvalue problem is solved numerically for every  $k$ , and the effect of each parameter on the stability of the system is characterized. Using our methodology for the case of two semi-infinite fluid layers as well as three-layer channel flow, we recover the analytical results of [204] in the limit of instantaneous charge relaxation, where the charge is transported only via Ohmic conduction.

The linear stability analysis (LSA) yields two types of eigenmodes. Given that the dispersion equation is biquadratic in  $s$ , there are two solution branches associated with each mode (for a total of four eigenvalues), one of which is dominant. In the first mode, the instability is characterized by the growth of in-phase (sinuous) perturbations for the two interfaces ( $\xi_u = \xi_l + 2$ ). In the second mode, however, antiphase (varicose) perturbations are the most unstable ( $\xi_u = -\xi_l$ ). Figure 3.2 shows the flow induced in each mode of instability along with the typical shapes of the film.

The effect of the external electric field is characterized by both the electric capillary number and the electric Reynolds number. Figure 3.3 shows the growth rate as a function of wavenumber  $k$  in each mode of instability for different values of  $Ca_E$  and  $Re_E$ . For a given pair of leaky dielectric liquids, the electric capillary number  $Ca_E$  characterizes the strength of the electric stresses versus surface tension effects. According to Fig. 3.3(a), the system is unstable at low wavenumbers over a finite range of  $k$ , and increasing  $Ca_E$  destabilizes the system by increasing the maximum growth rate as well as the width of the unstable range. The effect of surface tension becomes stronger for large values of  $k$  until it stabilizes the system for  $k > k_{marg} > 0$  where  $k_{marg}$  is the wavenumber associated with the marginal stability ( $s_{marg} = 0$ ). The electric Reynolds number plays a critical role in determining the charge transport regime and consequently the dynamics of the system. As  $Re_E$  increases, the dominant mode of charge transport switches from Ohmic conduction to charge convection on the interface. According to Fig. 3.3(b), increasing  $Re_E$  not only destabilizes the system, but can also alter the dominant mode of instability. Fig. 3.4 shows  $k_{marg}$  as a function of  $Ca_E$  and  $Re_E$  for two model systems with different dominant unstable modes. According to Fig. 3.4,  $k_{marg}$  is identical between the two modes for large values of  $Ca_E$  and  $Re$ . Moreover,  $k_{marg}$  increases as a function of  $Ca_E$  and grows linearly when  $Ca_E \gg 1$ .

The fate of the system following the onset of instability is determined by the dynamical behavior in the fastest growing mode. The maximum growth rate and the corresponding wavenumber in each mode are denoted respectively as  $s_{max}$  and  $k_{max}$ . We studied the effect of each non-dimensional group on the maximum growth rate in Figs. 3.5 and 3.6 (for more information on  $k_{max}$  see appendix A.2). Information about the fastest growing mode is of practical importance for engineering applications where electrohydrodynamic instabilities may be utilized to generate interfacial patterns with a prescribed length scale [31, 111, 202]. When  $RQ < 1$  ( $\bar{\tau}_c < \tau_c$ ), the charge is provided to the interface at a faster rate in the film than in the bulk. Therefore, the interfacial charge is predominantly provided from the film, and the dipole moment is aligned with the external electric field. Conversely, when  $RQ > 1$ , the suspending

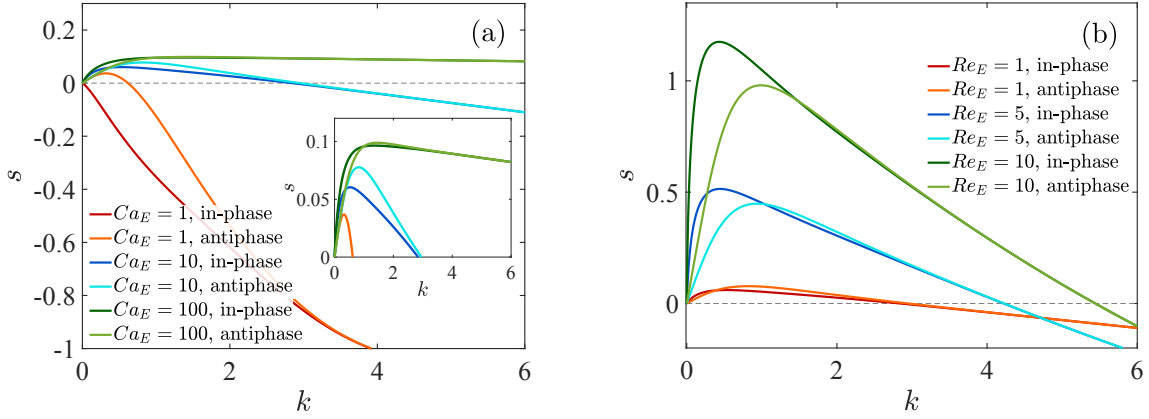


**Figure 3.3.** Growth rate versus wavenumber in the dominant modes of linear instability for  $(R, Q, \lambda) = (0.5, 1, 1)$ : (a) effect of electric capillary number when  $Re_E = 1$ . Inset shows the unstable wavenumbers. (b) Effect of electric Reynolds number when  $Ca_E = 10$ .

liquid is more conducting and the dipole moment is anti-parallel to the applied electric field. Since displacing the dipole moment by deforming the interface results in a destabilizing torque, the system is inherently more unstable in this configuration. This is confirmed in Figs. 3.5 and 3.6(a) when comparing the maximum growth rates between two model systems with  $RQ = 2$  and 0.5. We note the two systems are comprised of identical leaky dielectric liquids that are arranged in an opposite order in the film and the suspending phase ( $R_1 = R_2^{-1}$ ). According to Fig. 3.5(a), the maximum growth rate in each mode increases with  $Ca_E$  until it plateaus at  $Ca_E \gg 1$ . Figure 3.5(b) shows the maximum growth rate as a function of  $Re_E$  for two different configurations. Increasing the electric Reynolds number has a destabilizing effect in both cases. Additionally, the mode of instability (in-phase vs antiphase) can switch as a function of electric Reynolds number. The maximum growth rate is found to scale linearly with  $Re_E$  in both limits of  $Re_E \gg 1$  and  $Re_E \ll 1$ .

The effect of the ratios of material properties is considered in more detail in Fig. 3.6. We observe in Fig. 3.6(a) that a large viscosity ratio (more viscous film) is unfavorable for stability regardless of the configuration. Moreover, the dominant mode of stability switches from antiphase to in-phase when going from small to large values of  $\lambda$ . Figures 3.6(b) and (c) characterize the effect of conductivity ratio  $R$  and permittivity ratio  $Q$  on the stability of the system, while all other

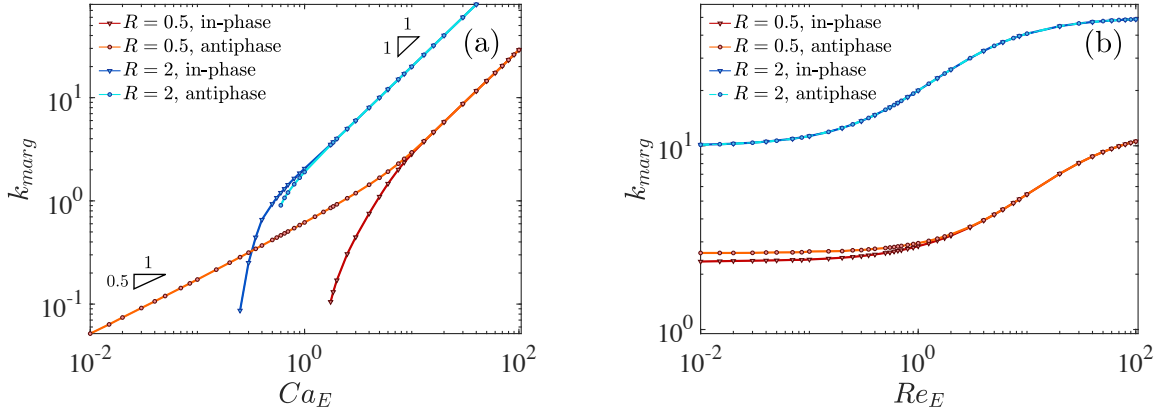


**Figure 3.4.** Wavenumber  $k_{marg}$  corresponding to marginally stable perturbations ( $\sigma = 0$ ) in different modes of instability as a function of: (a) electric capillary number, and (b) electric Reynolds number for two different systems with  $R = 0.5$  and  $R = 2$  while  $(Q, \lambda) = (1, 1)$ .  $Re_E = 1$  in (a) and  $Ca_E = 10$  in (b).

material properties are kept the same between the fluid layers. The larger growth rates observed at large values of  $R$  and  $Q$  confirm our expectation that  $RQ > 1$  ( $\bar{\tau}_c > \tau_c$ ) corresponds to a system that is more electrically unstable. According to Fig. 3.6(c), the maximum growth rate is independent of the permittivity ratio when  $Q \ll 1$  and the mode of instability changes from antiphase to in-phase going from  $Q < 1$  to  $Q > 1$ . We also note that the system becomes stable as  $RQ$  approaches 1 in both Fig. 3.6(b) and (c) since  $RQ = 1$  corresponds to a non-polarizing system in the electric field.

### 3.5 Numerical simulations

In this section, we complement the linear stability analysis of Sec. 3.4 with numerical simulations. We present a numerical method in Sec. 3.5.1 for the nonlinear solution of the system of governing equations (3.23)–(3.28) based on the boundary integral equation for Laplace and Stokes equations in a periodic domain of period  $L_p$  along the  $x$ -direction. The size of the domain is chosen based on the wavenumber associated with the fastest growing mode obtained via linear stability analysis:  $L_p = 2\pi k_{max}^{-1}$ . These simulations provide us with insight into the dynamical behavior of the system beyond the linear regime of instability. Our methodology shares

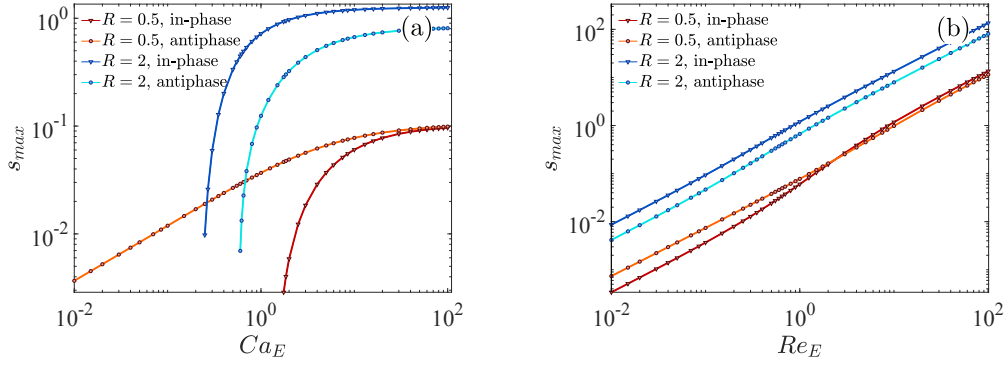


**Figure 3.5.** Maximum growth rate in each mode of instability as a function of: (a) electric capillary number, and (b) electric Reynolds number for two different systems with  $R = 0.5$  and  $R = 2$  while  $(Q, \lambda) = (1, 1)$ .  $Re_E = 1$  in (a) and  $Ca_E = 10$  in (b) (identical systems studied in Fig. 3.4).

similarities with that of [39, 40, 57] for interfaces separating two liquid layers. We implement adaptive grid refinement to handle large local deformations, curvature and charge gradients in the nonlinear regime of growth. Results are presented in Sec. 3.5.2 where we compare the predictions from the linear theory (LSA) of Sec. 3.4 and from numerical simulations (NS). Nonlinear dynamics are also explored in transient simulations far past the onset of instabilities, where the interplay between charge dynamics and fluid flow gives rise to nonlinear phenomena such as tip streaming and pinching into drops.

### 3.5.1 Boundary element method

Laplace's equation (3.1) for the electric potential can be reformulated as a single-layer integral equation [157, 10, 90]:

$$\varphi_{l,m,u}(\mathbf{x}_0) = -\mathbf{x}_0 \cdot \mathbf{E}_\infty - \int_S \mathbf{n} \cdot \llbracket \nabla \varphi(\mathbf{x}) \rrbracket \mathcal{G}^P(\mathbf{x}_0; \mathbf{x}) d\ell(\mathbf{x}), \quad \text{for } \mathbf{x}_0 \in V, S, \quad (3.44)$$

where  $V = V_l \cup V_m \cup V_u$ ,  $S = S_l \cup S_u$ , and  $\ell(\mathbf{x})$  denotes arclength along the interfaces. The evaluation point  $\mathbf{x}_0$  can be anywhere in space while the integration point  $\mathbf{x}$  lies on one of the two

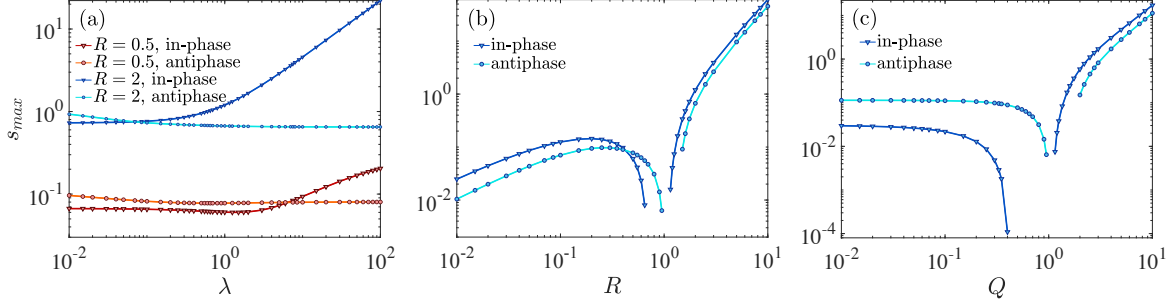


**Figure 3.6.** Maximum growth rate in each mode of instability as a function of: (a) viscosity ratio  $\lambda$  for two different systems with  $R = 0.5$  and  $R = 2$ , (b) conductivity ratio  $R$ , and (c) permittivity ratio  $Q$ . The permittivity ratio is set to  $Q = 1$  in (a,b), the conductivity ratio is  $R = 1$  in (c) and  $\lambda = 1$  in (b,c). In all systems  $(Ca_E, Re_E) = (10, 1)$ .

interfaces. The periodic Green's function for Laplace's equation  $\mathcal{G}^P$  represents the potential due to a periodic array of point sources separated by distance  $L_p$  along the  $x$  axis [127, 126]:

$$\mathcal{G}^P(\mathbf{x}; \mathbf{x}_0) = -\frac{1}{4\pi} \ln \left[ 2 \left\{ \cosh [k_p(y - y_0)] - \cos [k_p(x - x_0)] \right\} \right], \quad (3.45)$$

where  $k_p = 2\pi/L_p$  is the wavenumber associated with the geometrical periodicity. Taking the gradient of Eq. (3.44) with respect to  $\mathbf{x}_0$ , we obtain an integral equation for the electric field:

$$\mathbf{E}_{l,m,u}(\mathbf{x}_0) = \mathbf{E}_\infty - \int_S \llbracket E^n(\mathbf{x}) \rrbracket \nabla_0 \mathcal{G}^P d\ell(\mathbf{x}), \quad \text{for } \mathbf{x}_0 \in V. \quad (3.46)$$

The derivative of the Green's function undergoes a discontinuity across each interface [127].

Therefore, we express the electric field on either side of each interface as:

$$\mathbf{E}_{l,u}(\mathbf{x}_0) = \mathbf{E}_\infty - \int_S \llbracket E^n(\mathbf{x}) \rrbracket \nabla_0 \mathcal{G}^P d\ell(\mathbf{x}) + \frac{1}{2} \llbracket E^n(\mathbf{x}_0) \rrbracket \mathbf{n}(\mathbf{x}_0), \quad \text{for } \mathbf{x}_0 \in S, \quad (3.47)$$

$$\mathbf{E}_m(\mathbf{x}_0) = \mathbf{E}_\infty - \int_S \llbracket E^n(\mathbf{x}) \rrbracket \nabla_0 \mathcal{G}^P d\ell(\mathbf{x}) - \frac{1}{2} \llbracket E^n(\mathbf{x}_0) \rrbracket \mathbf{n}(\mathbf{x}_0), \quad \text{for } \mathbf{x}_0 \in S. \quad (3.48)$$

The second terms on the right-hand side of (3.47) and (3.48) denote the principal-value integral where the evaluation point is located precisely on the interfaces. The singularity in Eqs. (3.47) and (3.48) can be removed by taking a dot product with the normal vector  $\mathbf{n}(\mathbf{x}_0)$ . Finally, we obtain the following equation after combining the results with Gauss's law Eq. (3.26):

$$\oint_S \llbracket E^n(\mathbf{x}) \rrbracket [\mathbf{n}(\mathbf{x}_0) \cdot \nabla_0 \mathcal{G}^P] d\ell(\mathbf{x}) - \frac{1+Q}{2(1-Q)} \llbracket E^n(\mathbf{x}_0) \rrbracket = E_\infty^n(\mathbf{x}_0) - \frac{q(\mathbf{x}_0)}{1-Q}, \quad \text{for } \mathbf{x}_0 \in S, \quad (3.49)$$

which is an integral equation for  $\llbracket E^n \rrbracket$  as a function of the charge distribution. Subsequently, we determine the normal component of the electric field at each interface based on Gauss's law:

$$E_{l,u}^n = \frac{q - Q \llbracket E^n \rrbracket}{1 - Q}, \quad E_m^n = \frac{q - \llbracket E^n \rrbracket}{1 - Q}. \quad (3.50)$$

The electric potential is obtained via (3.44) in the next step. This allows us to obtain the tangential component of the electric field by numerically differentiating the electric potential along  $S$ . This way, we avoid using (3.47) and (3.48), which are singular and require further treatment [150]. Having both components of the electric field at the interface, we can find the jump in electric tractions  $\llbracket \mathbf{f}^E \rrbracket$  from (3.13). The jump in the hydrodynamic tractions can then be obtained using the interfacial stress balance (3.10). Finally, the interfacial velocity is determined using the Stokes boundary integral equation, in its dimensionless form [133, 125]:

$$\begin{aligned} \mathbf{u}(\mathbf{x}_0) = & -\frac{1}{2\pi} \int_S \llbracket \mathbf{f}^H(\mathbf{x}) \rrbracket \cdot \mathbf{G}^P(\mathbf{x}; \mathbf{x}_0) d\ell(\mathbf{x}) \\ & + \frac{1-\lambda}{2\pi(1+\lambda)} \int_S \mathbf{u}(\mathbf{x}) \cdot \mathbf{T}^P(\mathbf{x}; \mathbf{x}_0) \cdot \mathbf{n}(\mathbf{x}) d\ell(\mathbf{x}), \quad \text{for } \mathbf{x}_0 \in S, \end{aligned} \quad (3.51)$$

where  $\mathbf{G}^P$  is the singly periodic Green's function describing the flow due to a periodic array of point forces separated by the distance  $L_p$  along the  $x$  direction, and  $\mathbf{T}^P$  is the corresponding stress tensor [125]. Equation (3.51), which is a Fredholm integral equation of the second kind for  $\mathbf{u}$ , yields a dense linear system after discretization. The linear algebraic system is solved

iteratively using a GMRES method [138, 59], and the interfacial velocity is used to update the charge distribution and the shape of each interface via the kinematic boundary conditions. The numerical algorithm during one time step of the simulations can be summarized as follows:

- (I) Calculate  $[[E^n]]$ ,  $E_{l,u}^n$  and  $E_m^n$  for the given charge distribution  $q(\mathbf{x})$ , by solving the integral equation (3.49) along with (3.50).
- (II) Compute the electric potential on each interface using (3.44).
- (III) Differentiate the surface potential numerically along each interface in order to obtain the tangential electric field  $\mathbf{E}^t = -\nabla_s \varphi$ .
- (IV) Knowing both components of the electric field on each interface, evaluate the jump in electric tractions  $[[\mathbf{f}^E]]$  via (3.13) and use it to determine the jump in hydrodynamic tractions  $[[\mathbf{f}^H]]$  via (3.10).
- (V) Solve for the interfacial velocity by inverting the discretized Stokes boundary integral equation (3.51).
- (VI) Update the charge distribution by integrating (3.25) explicitly in time using a second-order Runge-Kutta scheme.
- (VII) Advance the position of both interfaces by advecting the grid using the normal component of the interfacial velocity:  $\dot{\mathbf{x}}_i(t) = (\mathbf{u} \cdot \mathbf{n})\mathbf{n}$ .
- (VIII) Refine the grid locally if either the local curvature, element length or magnitude of the charge gradient exceed certain thresholds.

We use piecewise cubic spline interpolation to represent the shape of the interface with continuous slope and curvature from one element to another. This provides an easy and accurate way to compute the geometrical properties such as curvature, normal and tangent vectors. In case either the mean curvature, the length or the magnitude of the charge gradient in an element

exceeds the predefined thresholds, that element is divided into two new elements. The position of the new node along with other variables such as velocity and charge density are evaluated using spline interpolation. The use of adaptive grid refinement significantly improved the performance of our numerical scheme in handling large local deformations and charge gradients in the nonlinear regime. Nonetheless, the number of new elements is only a fraction of total elements in each iteration. Excessive grid refinement can result in spurious oscillations in the spline representation and excite numerical instabilities [41].

### 3.5.2 Results and discussion

The list of systems considered in our simulations is provided in Table 5.1 along with the corresponding parameter values. We first consider in Fig. 3.7 two representative cases, *S1* and *S2*, that exhibit antiphase and in-phase instabilities, respectively. Initially, both interfaces are uncharged and their flat shapes are perturbed by the dominant mode of instability given by LSA with a small amplitude. The film polarizes mainly via Ohmic conduction at short times, and the charge distribution first increases uniformly on both interfaces as shown in Fig. 3.7(b,d). Meanwhile, perturbations of shape and charge start to grow as predicted by LSA. The growth rates obtained in our simulations are in a close agreement with the theoretical values from LSA as shown in Fig. 3.8. Following the onset of instability, as the induced flow becomes

**Table 3.1.** Different systems studied using numerical simulations and their dimensionless parameters.

system	$R$	$Q$	$\lambda$	$Ca_E$	$Re_E$
<i>S1</i>	0.5	1	1	10	1
<i>S2</i>	2	1	1	10	1
<i>S3</i>	–	0.1	1	10	1
<i>S4</i>	1	–	1	10	1
<i>S5</i>	0.5	1	–	10	1
<i>S6</i>	–	1	1	10	1
<i>S7</i>	2	1	–	10	1

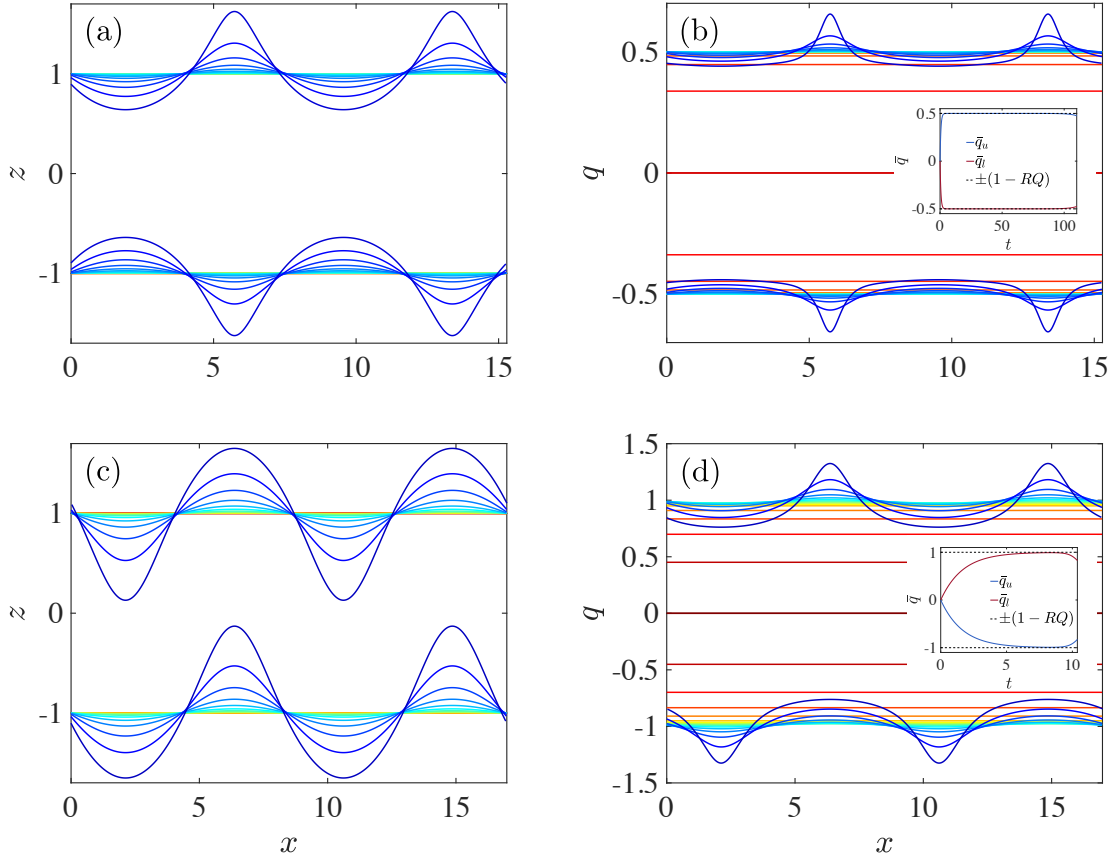


**Figure 3.7.** Evolution of the shape of both interfaces (left column) and their charge distributions (right column) in different modes of instability: (a,b) antiphase mode for system  $S1$ , (c,d) in-phase mode for system  $S2$ . Each snapshot is color-coded based on the time it was taken (from red at  $t = 0$  to blue). Insets in (b,d) show the average charge densities  $\bar{q}$  on each interface as a function of time. In the insets, blue and red curves show the transient average charge on the upper and lower interface, respectively, while the dashed lines show the steady interfacial charges in the base state.

stronger, the effect of charge convection becomes more significant. The accumulation of charge on certain points on each interface results in large local electric stresses exerted by the applied electric field, which further deforms the interface as shown in Fig. 3.7(a,c). While the charge and shape perturbations are sinusoidal at short times in agreement with the linear theory, they depart from perfect sine waves as nonlinear effects start becoming important. Nevertheless, the underlying symmetry between the two interfaces is maintained in the non-linear regime, with  $\xi_u(x) = -\xi_l(x + \Lambda/2)$  for in-phase modes and  $\xi_u(x) = -\xi_l(x)$  for anti-phase modes, where

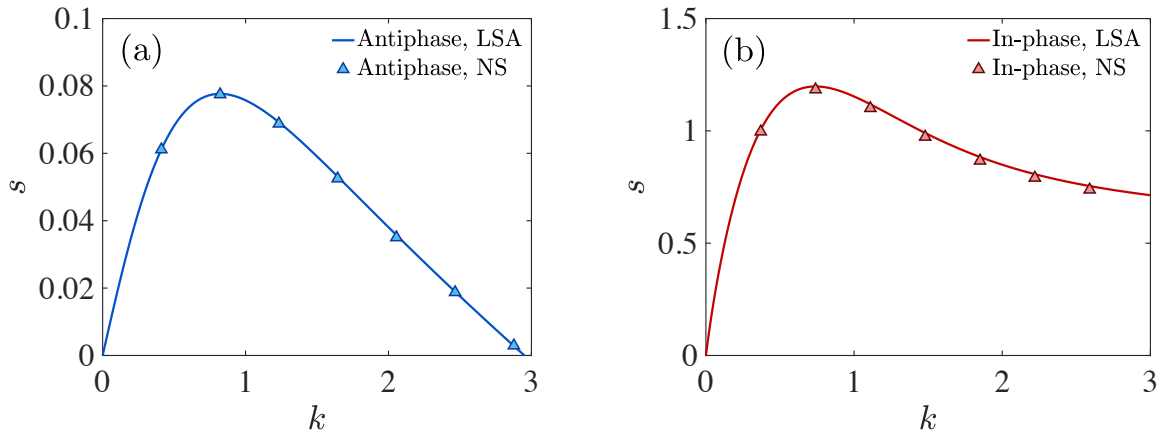


**Figure 3.8.** Growth rate  $s$  as a function of wavenumber  $k$  in the dominant mode of instability obtained via numerical simulations (NS) and linear stability analysis (LSA) for  $SI$  in (a), and  $S2$  in (b). In these simulations, the size of the domain is set to  $L_p = 4\pi k_{max}^{-1}$ , which is twice the wavelength associated with the fastest growing mode.

$\Lambda = 2\pi/k$  is the wavelength of the initial perturbation.

Further development of the flow and charge dynamics in the antiphase mode gives rise to the formation of pointed conical structures on each interface, which may eventually turn into tip streaming jets intruding the suspending phase. Initially, as new charges are brought to the tip via Ohmic conduction, the electrostatic pressure  $p_E$  increases thus accelerating the fluid along the normal direction. The tip curvature increases as a result, leading to larger capillary pressures. The time scale of the induced EHD flow continues to decrease until it eventually becomes comparable and finally smaller than the charge relaxation time  $\tau_c$ . Consequently, the dominant mode of charge transport switches from Ohmic conduction to charge convection. Finally, the intruding jet becomes smoother on the tip and the structure begins to diverge from its conical geometry. It is evident from Figs. 3.9(e,f) that the tip curvature and velocity increase simultaneously until they peak and start to decrease following the emergence of tip formation.

Tip streaming has also been observed in other configurations when leaky dielectric films or drops are subject to sufficiently strong electric fields [33, 34]. Previous studies suggest that tip streaming is a local phenomenon and is nearly independent of the boundary conditions and global scales in the problem such as the thickness of the film and the strength of the electric field

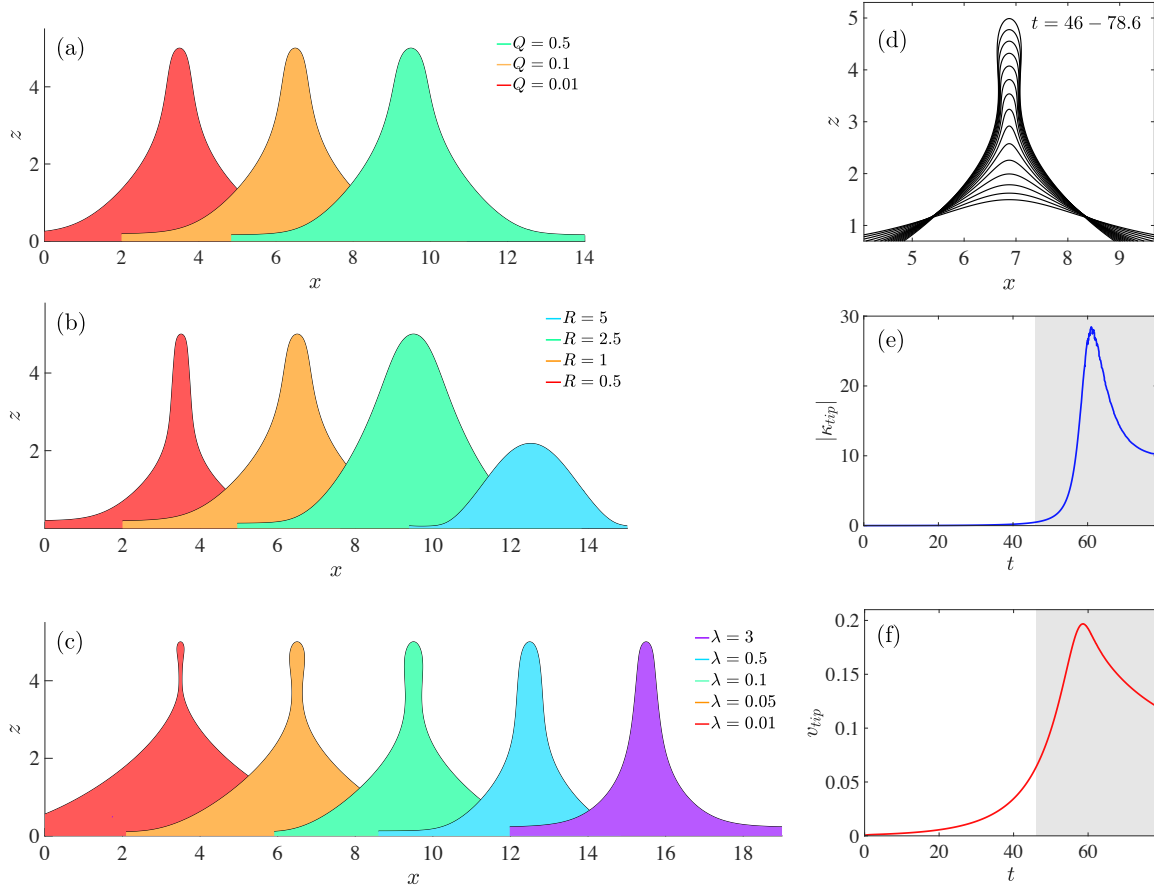


**Figure 3.9.** Snapshots of the tip-streaming jets (left column) formed on the upper interface during antiphase instability with different: (a) permittivity ratios in system **S4**, (b) conductivity ratios in system **S3**, and (c) viscosity ratios in system **S5**. Deformation parameter is  $\mathcal{D} = 5$  for all cases except for  $R = 5$  in (b), where the minimum thickness of the film reached the local grid size at  $\mathcal{D} = 2.18$  (disintegration from the base). The evolution of (d) the jet profile, (e) tip curvature, and (f) the vertical tip velocity is shown in the right column for system **S5** when  $\lambda = 0.1$ . Shaded regions in (e,f) correspond to the time interval shown in (d). Also see videos in the Supplemental Material.

[61, 30, 33, 34]. Accordingly, dimensional analysis for our system suggests that

$$\frac{z^* \mu}{\gamma \tau_c} = F(t^*/\tau_c, R, Q, \lambda) \quad (3.52)$$

where  $z^*$  is any spatial feature of the tip streaming jet such as thickness of the neck and  $F$  is a dimensionless function of  $t^*/\tau_c, R, Q$ , and  $\lambda$ . Note that  $z^*$  and  $t^*$  are in dimensional form. Consequently, the jet structure and its dynamics depend on  $R, Q$  and  $\lambda$ . Figure 3.9(a-c) provides a shape diagram of the tip streaming jets and illustrates how the mismatch in material properties affects the resulting morphologies. Snapshots of the jet profiles are shown at a fixed value of the deformation parameter  $\mathcal{D}$ , which we define as the maximum vertical deflection along the film normalized by the initial half thickness:

$$\mathcal{D} = \max \left| \frac{z}{h} \right|, \quad \text{for all } \mathbf{x} \in S. \quad (3.53)$$

Note that our boundary element simulations are unable to capture topological changes occurring during breakup into droplets. Instead, if the thickness of the film or jet decreases below the local grid size, we denote this as a disintegration event. We predict two disintegration scenarios based on our results: pinching into droplets from the tip such as in system **S5** when  $\lambda = 0.01$ , and breakup from the base of the jets such as in figure **S4** when  $R = 2.5$ . A strong thinning at the base of the jet inhibits larger vertical deformations in some cases such as in **S4** when  $R = 5$ . The simulations in Fig. 3.9 are initiated from the base state with a small imposed perturbation given by the dominant unstable eigenmode obtained via LSA. More information on the time evolution of the tip streaming jets shown in Fig. 3.9 is included in appendix A.3. See Supplemental Material for videos showing the evolution of the film and the emergence of tip streaming jets in different systems with antiphase instability.

A fundamental challenge for the numerical simulations of tip streaming is the large discrepancy in the length scales present in the problem. The computational domain needs to be

large enough so that the dynamics associated with small wavenumbers are accurately captured. This increases the computational cost for a given global grid resolution. In addition, in order to capture the large local deformations during tip streaming, a high local resolution must also be maintained throughout the simulations. Employing adaptive grid refinement allows us to address this challenge. Finally, we note that despite some similar features, the tip streaming observed here differs from the conic cusping singularity observed in inviscid perfect conducting or perfect dielectric liquids where the tip curvature diverges in a finite time [208, 209]. The presence of tangential electric stresses in leaky dielectric liquids is the main difference between the two types of EHD instabilities.

During the in-phase mode instability, the system undergoes a different dynamics as a result of the coupling between the flow and charge evolution. We observe two main dynamical behaviors in these systems as we show in Fig. 3.10, where the initial conditions were chosen in a similar way as in Fig. 3.9. In systems where the equilibrium electric stresses are compressive on the film ( $RQ > 1$ ), further development of the flow and charge dynamics results in the formation of conic structures that intrude the film. These inward jets exhibit a similar evolution pattern to the ones observed in Fig. 3.9(e,f) during tip streaming. The curvature and velocity at the tip of these inward jets increase until they peak and start to decrease as they approach the other interface (Fig. A.4). The film may breakup into droplets when these inward jets reach the other interface. On the other hand, in cases where the equilibrium electric stresses are extensional ( $RQ < 1$ ), the system develops jets that are flowing outward from the film. Generally, the dynamics in this mode is dominated by strong local effects in the nonlinear regime, which is analogous to the antiphase mode. Therefore, we can infer that the same dimensional analysis holds for the evolution of the resulting structures in this mode. Figure 3.10 shows how the mismatch in material properties affects the behavior of the system and the resulting structures during in-phase instabilities. More information on the time evolution of these systems is included in appendix A.3. Videos of simulations for different systems undergoing in-phase instability with emerging inward and outward jets are included in the Supplemental Material.

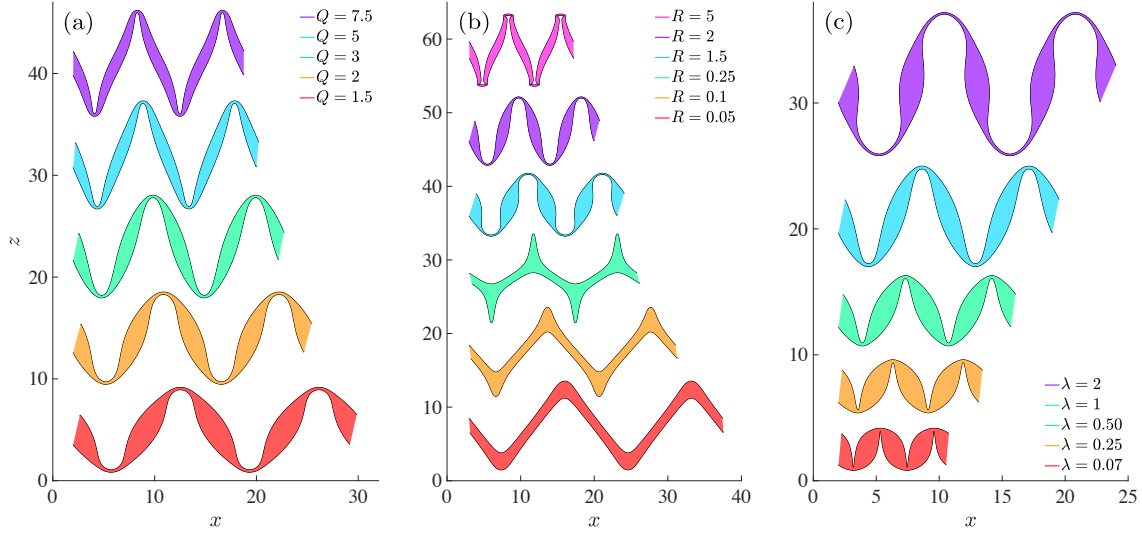


**Figure 3.10.** Snapshots of the films during in-phase mode instability with different: (a) permittivity ratios in system **S4**, (b) conductivity ratios in system **S6**, (c) viscosity ratios in system **S7**. For the cases with inward jets, the minimum thickness of the film is  $d = 0.2$ , or one tenth of the equilibrium thickness.  $\mathcal{D} = 5$  for outward jets. Also see videos in the Supplemental Material.

### 3.6 Concluding remarks

We have presented a theoretical and numerical model in two dimensions to study the dynamics of a suspended viscous film that is subject to a perpendicular electric field. We performed a linear stability analysis using a charge transport model that accounts for Ohmic conduction, charge convection and finite charge relaxation, which was shown to recover the previous results of Zhang *et al.* [204] in the limit of instantaneous charge relaxation. Two main modes of instability were identified, which are referred to as *in-phase* and *antiphase* modes. The system exhibits different dynamical behaviors in each mode. We characterized the effect of the relevant non-dimensional groups on the stability of the system in each mode. Our results suggest that interfacial charge convection by the flow, which had been neglected in previous related studies in the literature [204, 202, 107], plays an important role in determining the dynamics of the system. Besides its destabilizing effect, it was shown that charge convection can also alter the

dominant mode of instability.

Our theoretical analysis was complemented by numerical simulations using the boundary element method so as to explore the dynamics of the system far from equilibrium. We demonstrated how the coupling of flow and interfacial charge dynamics in the antiphase mode gives rise to strongly nonlinear effects such as the formation of tip streaming jets that are intruding the suspending phase. During the in-phase mode, however, the system can undergo various nonlinear routes depending on the type of electric stresses in the base state. In cases where the equilibrium electric stresses are compressive on film, we observed the emergence of inwards jets that are drawn towards the film on each interface. Conversely, if the equilibrium electric stresses are extensional, the system was shown to develop conical jets that are flowing outward from the film. Strong local effects are a key common feature between the two modes during their non-linear regime of growth. Finally, we characterized the effect of different controlling parameters on the dynamical behavior of the system and the resulting structures in the non-linear regime. In an experiment, we expect a range of wavenumbers to be excited simultaneously due to the randomness in the initial perturbation, which may result in nonlinear behaviors that differ from those observed in Figs. 3.9 and 3.10. Nevertheless, the fastest growing mode predicted by LSA is expected to be dominant and our results are locally valid for the most critical mode.

The present study casts new light on the dynamics of suspended viscous films under applied electric fields, where the interplay between electric, hydrodynamic and capillary forces can result in a plethora of dynamical behaviors. Our knowledge on the fastest growing modes along with the additional insight into the nonlinear behavior of the system should be of great use for engineering applications where EHD instabilities are exploited to create patterns or structures with prescribed morphologies and length scales. Since the mentioned nonlinear phenomena such as tip streaming are inherently three dimensional, extending this work to describe three-dimensional pattern formation would be of interest, as would including the effects of fluid inertia, which may play a role during regimes of rapid nonlinear growth.

### **3.7 Acknowledgements**

Chapter 3 is primarily based on the material published in *Physical Review Fluids*, authored by Mohammadhossein Firouznia and David Saintillan [58]. The dissertation author served as the primary researcher and author of this paper.

The authors thank Petia Vlahovska and Michael Miksis for useful conversations, and gratefully acknowledge funding from National Science Foundation Grant CBET-1705377.

## Chapter 4

# Electrohydrodynamic interfacial instabilities in convergent flows

The interface between two immiscible fluids can become unstable under the effect of an imposed tangential electric field along with a stagnation point flow. This canonical situation, which arises in a wide range of electrohydrodynamic systems including at the equator of electrified droplets, can result in unstable interface deflections where the perturbed interface gets drawn along the extensional axis of the flow while experiencing strong charge build-up. Here, we present analytical and numerical analyses of the stability of a planar interface separating two immiscible fluid layers subject to a tangential electric field and a stagnation point flow. The interfacial charge dynamics is captured by a conservation equation accounting for Ohmic conduction, advection by the flow and finite charge relaxation. Using this model, we perform a local linear stability analysis in the vicinity of the stagnation point to study the behavior of the system in terms of the relevant dimensionless groups of the problem. The local theory is complemented with a numerical normal-mode linear stability analysis based on the full system of equations and boundary conditions using the boundary element method. Our analysis demonstrates the subtle interplay of charge convection and conduction on the dynamics of the system, which oppose one another in the dominant unstable eigenmode. Finally, numerical simulations of the full nonlinear problem demonstrate how the coupling of flow and interfacial charge dynamics can give rise to nonlinear phenomena such as tip formation and the growth of charge density shocks.

## 4.1 Introduction

A century ago, Zeleny photographed instabilities of electrified interfaces, sparking interest into understanding the phenomenon [203]. The mechanisms of interface destabilization by electric fields have been studied in the pioneering works of [175], [178] and Melcher and coworkers [104, 105], followed by an extensive body of research aimed at gaining more detailed fundamental understanding and at exploiting electrohydrodynamic instabilities in novel applications [103, 143, 199, 70, 6, 52, 8, 62, 118, 193].

Interfaces polarize in applied electric fields. Free charges brought by conduction accumulate at the boundary between phases and the electric field acting on this induced charge creates shear stresses that drag the fluids into motion [103]. In the case of a drop in a uniform electric field, the classic small-deformation analysis by [176] showed that the resulting electrohydrodynamic (EHD) flow consists of two toroidal vortices inside and a stresslet-quadrupole flow outside the drop. Depending on the electric properties of the fluids, the surface flow is directed either to the poles or the equator. The latter case is shown in figure 4.1(a). In strong fields, however, this flow undergoes a plethora of instabilities that may result in drop break-up [175, 188, 157, 84, 90]. Droplet disintegration can proceed in various patterns depending on fluid properties. In the case of the pole-convergent flow, the drop can develop conical tips that emit jets, which subsequently break up into droplets [33, 34, 110, 151]. In the case of the equator-converging flow, the drop either dimples at the poles and breaks into a torus, or deforms into a pancake-like lenticular shape with a sharp edge emitting rings encircling the drop [20, 194].

While EHD streaming from Taylor cones has been extensively studied [33, 34, 77, 63], the mechanisms underlying the equatorial streaming remain an open question. Noting the similarity between the EHD tip-streaming and the tip-streaming in flow focusing [6, 64, 5], [20] speculated,

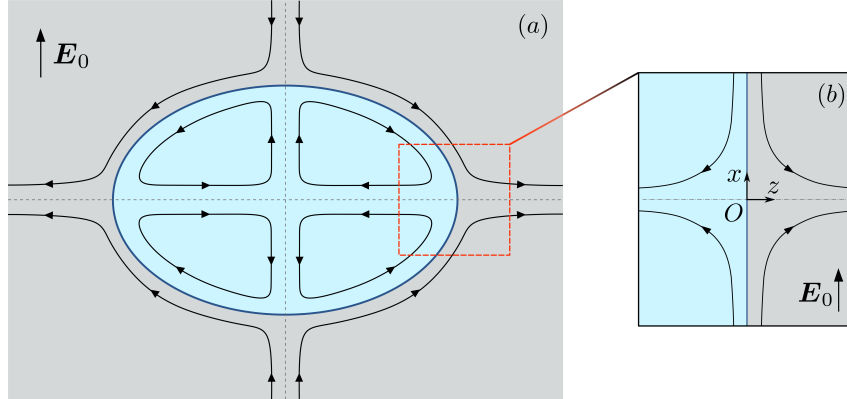


**Figure 4.1.** An oblate drop under a uniform electric field: (a) the quadrupolar EHD flow from the poles to the equator. (b) convergent streamlines and tangential electric field in the vicinity of the stagnation line.

in the original paper that reported the phenomenon, that the EHD equatorial streaming arises from an interfacial instability due to a convergent flow [189, 129, 16]. Near a stagnation point, a perturbation of the interface may get drawn by the flow and grow into a fluid filament if viscous stresses overcome interfacial tension. Unlike flow focusing, however, EHD streaming involves both flow and electric field. In EHD tip streaming, the electric field is initially normal to the interface at the stagnation point, while in EHD equatorial streaming, the applied field is parallel to the interface at the stagnation line.

In this work, we analyze the effect of an electric field on the convergent flow instability in a configuration mimicking the EHD equatorial streaming as depicted in figure 4.1(b).

We develop a two-dimensional model to study the dynamics of a system of two superimposed layers of fluids subject to a tangential electric field and a stagnation point flow. The convergent flow and the electric field are assumed to be independently applied, unlike the equatorial EHD instability, where the flow is generated by the electric field. Despite this simplification, the analysis provides valuable insights into mechanisms responsible for the EHD equatorial streaming such as the evolution of the convergent line instability and the emergence of charge shocks. We present the governing equations in Sec. 4.2 and their non-dimensionalization in Sec. 4.3. We develop a local linear stability theory in Sec. 4.4. To supplement our theory, we

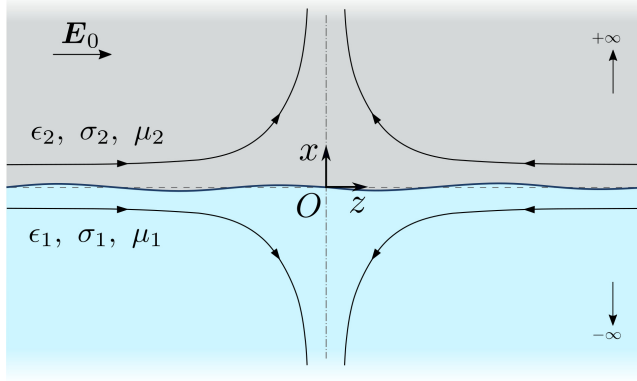


**Figure 4.2.** Problem definition: two immiscible fluid layers are subject to a tangential electric field  $\mathbf{E}_0$  and to a planar extensional flow  $\mathbf{u}^\infty(\mathbf{x})$ , with a stagnation point located at the origin  $O$  on the interface.

employ the boundary element method, outlined in Sec. 4.5, to perform numerical simulations as well as a numerical linear stability analysis. We compare the results from the local theory, numerical linear stability analysis and transient simulations in Sec. 4.6. Finally, we conclude and discuss potential extensions of this work in Sec. 4.8.

## 4.2 Problem definition and governing equations

We study electrohydrodynamic instabilities that arise at the interface  $S$  between two immiscible fluids under the combined effects of a tangential electric field  $\mathbf{E}_0$  and of an imposed stagnation point flow  $\mathbf{u}^\infty(\mathbf{x})$ , to be specified more precisely later. The two layers are labeled 1 and 2 as depicted in figure 4.2, with fluid 1 occupying the lower half space. The applied electric field is uniform along the  $x$  direction, and the stagnation point is located on the interface at the origin  $O$  of the coordinate system. At equilibrium, the interface is uncharged and flat and coincides with the plane  $z = 0$ , and we consider two-dimensional dynamics in the  $(x, z)$  plane. The shape of the deformed interface is parametrized as  $z = \xi(x, t)$ , and has unit normal  $\mathbf{n}$  pointing from fluid 1 into fluid 2.

Both fluids are leaky dielectrics with electric conductivity  $\sigma$ , electric permittivity  $\epsilon$ , and

dynamic viscosity  $\mu$ . While we formulate the governing equations to allow for distinct viscosities, all the results presented in Sec. 4.6 will be for equiviscous fluids. Under the Taylor–Melcher leaky dielectric model [103], any net charge in the system occurs at the location of the interface while the bulk of the fluids remains electroneutral. The Taylor–Melcher leaky dielectric model can be formally derived from more detailed electrokinetic models based on the Poisson–Nernst–Planck equations in the limit of strong electric fields and under the assumption of thin Debye layers [148, 112]. As an example, these assumptions are valid for millimeter-sized drops of leaky dielectric liquids subject to electric fields of magnitude  $E_0 \sim 10^3 \text{ V cm}^{-1}$  according to [143]. Under these assumptions, the electric potential is harmonic in both fluids:

$$\nabla^2 \varphi = 0, \quad \mathbf{x} \in V_{1,2}. \quad (4.1)$$

Far from the interface, the electric field  $\mathbf{E} = -\nabla\varphi$  tends to the applied uniform field:

$$\mathbf{E} \rightarrow \mathbf{E}_0 = E_0 \hat{\mathbf{e}}_x, \quad \text{as } z \rightarrow \pm\infty. \quad (4.2)$$

Across the interface, its tangential component is continuous while a jump can arise in the normal direction due to the mismatch in electrical properties:

$$\mathbf{n} \times \llbracket \mathbf{E} \rrbracket = \mathbf{0}, \quad \mathbf{x} \in S. \quad (4.3)$$

We have introduced the notation  $\llbracket \mathcal{F} \rrbracket = \mathcal{F}_2 - \mathcal{F}_1$  for the jump of any variable  $\mathcal{F}$  defined on both sides of the interface. A surface charge density develops at the interface following Gauss’s law:

$$q(\mathbf{x}, t) = \mathbf{n} \cdot \llbracket \epsilon \mathbf{E} \rrbracket, \quad \mathbf{x} \in S. \quad (4.4)$$

This surface charge density satisfies a conservation equation accounting for finite charge relaxation,

Ohmic conduction from the bulk and charge convection by the flow:

$$\partial_t q + \mathbf{n} \cdot \llbracket \sigma \mathbf{E} \rrbracket + \nabla_s \cdot (q\mathbf{u}) = 0, \quad \mathbf{x} \in S, \quad (4.5)$$

where  $\nabla_s = (\mathbf{I} - \mathbf{nn}) \cdot \nabla$  is the surface gradient operator and  $\mathbf{u}$  is the total fluid velocity.

Neglecting the effects of inertia and gravity, the velocity field and its corresponding pressure field satisfy the Stokes equations in both fluids:

$$-\nabla p + \mu \nabla^2 \mathbf{u} = \mathbf{0}, \quad \nabla \cdot \mathbf{u} = 0, \quad \mathbf{x} \in V_{1,2}. \quad (4.6)$$

The velocity vector is continuous across the interface and approaches the applied flow far from the interface:

$$\llbracket \mathbf{u} \rrbracket = \mathbf{0}, \quad \mathbf{x} \in S, \quad (4.7)$$

and

$$\mathbf{u}(\mathbf{x}) \rightarrow \mathbf{u}^\infty(\mathbf{x}), \quad \text{as } z \rightarrow \pm\infty. \quad (4.8)$$

In the absence of Marangoni effects, the jump in hydrodynamic and electric tractions across the interface is balanced by capillary forces:

$$\llbracket \mathbf{f}^H \rrbracket + \llbracket \mathbf{f}^E \rrbracket = \gamma (\nabla_s \cdot \mathbf{n}) \mathbf{n}, \quad \mathbf{x} \in S, \quad (4.9)$$

with uniform surface tension  $\gamma$ . Hydrodynamic and electric tractions are expressed in terms of the Newtonian and Maxwell stress tensors, respectively:

$$\mathbf{f}^H = \mathbf{n} \cdot \mathbf{T}^H, \quad \mathbf{T}^H = -p\mathbf{I} + \mu(\nabla\mathbf{u} + \nabla\mathbf{u}^T), \quad (4.10)$$

$$\mathbf{f}^E = \mathbf{n} \cdot \mathbf{T}^E, \quad \mathbf{T}^E = \epsilon \left( \mathbf{E}\mathbf{E} - \frac{1}{2}E^2\mathbf{I} \right). \quad (4.11)$$

Finally, the interface evolves and deforms under the local velocity field as a material surface.

Defining the function  $g(\mathbf{x}, t) = z - \xi(x, t)$ , the kinematic boundary condition reads:

$$\frac{Dg}{Dt} = 0, \quad \mathbf{x} \in S, \quad (4.12)$$

leading to the condition

$$\partial_t \xi = -u \partial_x \xi + v, \quad (4.13)$$

where  $\mathbf{u} = (u, v)$  are the velocity components. We also note that the surface normal is given by  $\mathbf{n} = \nabla g / |\nabla g|$ .

Our focus is on analyzing the stability of the interface near a stagnation point, and to this end we choose the background flow  $\mathbf{u}^\infty = (u^\infty, v^\infty)$  to be extensional along the  $z$ -direction, compressional along the  $x$ -direction, with a stagnation point at the origin. The strength of the background flow is characterized by the local strain rate at the stagnation point, which is denoted by  $A = \partial_z v^\infty$  where  $A > 0$ . Three different types of background flows are used in this study and are illustrated in figure 4.3. The first type, depicted in figure 4.3(a), is simply the linear flow  $\mathbf{u}^\infty = (-Ax, Az)$ , which will be used in the development of the local linear theory of Sec. 4.4. The numerical scheme of Sec. 4.5, however, requires periodicity in the  $x$ -direction, and for this reason we will also consider two periodic flow fields. The first one is the Taylor-Green vortex [177] shown in figure 4.3(b) and defined as:

$$u^\infty = U^\infty \cos\left(ax - \frac{\pi}{2}\right) \sin\left(bz - \frac{\pi}{2}\right), \quad (4.14)$$

$$v^\infty = V^\infty \sin\left(ax - \frac{\pi}{2}\right) \cos\left(bz - \frac{\pi}{2}\right), \quad (4.15)$$

where

$$U^\infty a + V^\infty b = 0, \quad a = b = \frac{2\pi}{L_p}. \quad (4.16)$$

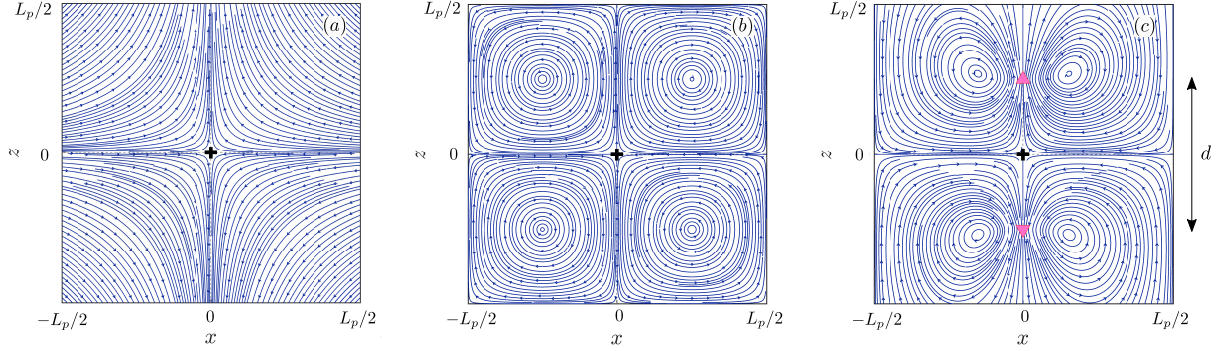


**Figure 4.3.** Streamlines of the various background flows used in this study: (a) linear planar extensional flow, (b) periodic Taylor-Green vortex, (c) periodic array of anti-parallel point forces separated by  $d$  and  $L_p$  along the  $z$ - and  $x$ -directions, respectively. The origin is marked with a “+”, the positions of the point forces are marked with triangles and the interface is located at  $z = 0$ .

The local strain rate at the stagnation point is then simply given by:

$$A = \partial_z v^\infty(0,0) = V_\infty b. \quad (4.17)$$

We also consider a second background flow shown in figure 4.3(c) and induced by a periodic array of anti-parallel point forces separated by distances  $L_p$  and  $d$  along the  $x$ - and  $z$ -directions, respectively:

$$\mathbf{u}^\infty = \frac{1}{4\pi} [\mathbf{G}^P(\mathbf{x}, \mathbf{x}_0^u) \cdot \mathbf{m} - \mathbf{G}^P(\mathbf{x}, \mathbf{x}_0^l) \cdot \mathbf{m}], \quad (4.18)$$

where  $\mathbf{m} = m\hat{\mathbf{e}}_z$  is the strength of the point forces,  $\mathbf{x}_0^u$  and  $\mathbf{x}_0^l$  are the locations of upper and lower point forces, respectively, and  $\mathbf{G}^P$  is the singly periodic Green’s function for the Stokes equations [125]. The local strain rate at the stagnation point is given by:

$$A = \partial_z v^\infty(0,0) = \frac{1}{8\pi} \left( \frac{mk_p^2 d}{\cosh(k_p d/2) - 1} \right), \quad (4.19)$$

where  $k_p = 2\pi/L_p$  is the wavenumber associated with the unit cell. In obtaining (4.19), it is assumed that  $x_0^u = x_0^l = 0$  and  $z_0^u = -z_0^l = d/2$ . Our numerical calculations produce identical linear stability results for a given local strain rate under the two periodic flow fields described by equations (4.15) and (4.18). In all transient nonlinear simulations, we use the periodic array of

point forces as background flow.

### 4.3 Non-dimensionalization

For the system presented above, dimensional analysis yields six non-dimensional groups, three of which characterize the mismatch in physical properties between the two layers:

$$\lambda = \frac{\mu_1}{\mu_2}, \quad R = \frac{\sigma_2}{\sigma_1}, \quad Q = \frac{\epsilon_1}{\epsilon_2}. \quad (4.20)$$

The other three parameters can be obtained as ratios of characteristic time scales in the problem. First, we note that free charges in the bulk fluids relax on a conduction time scale defined as

$$\tau_c = \frac{\epsilon}{\sigma}. \quad (4.21)$$

Note that the product  $RQ = \tau_{c,1}/\tau_{c,2}$  is the ratio of the charge relaxation time scales in the two liquid phases, and characterizes their responses to conduction. For instance,  $RQ > 1$  when the lower layer is less conductive. The time scale for the deformed interface to relax to its flat configuration under capillary effects can be defined as

$$\tau_\gamma = \frac{\mu_2(1+\lambda)}{k\gamma}, \quad (4.22)$$

where  $k^{-1}$  is the characteristic length scale associated with the deformation. In our periodic simulations and analysis, we use the length scale  $k_p^{-1} = L_p/2\pi$  based on the periodicity of the base flow, whereas  $k$  will be the wavenumber of the plane wave in the local stability theory of Sec. 4.4. The accumulation of free charges on the interface creates an electric force that can drive the fluid into motion. The time scale for deformations under this electrohydrodynamic flow is

inversely proportional to the magnitude of electric tractions on the interface:

$$\tau_{EHD} = \frac{\mu_2(1+\lambda)}{\epsilon_2 E_0^2}. \quad (4.23)$$

Finally, the characteristic time scale associated with the background flow is given by the inverse of the applied strain rate at the stagnation point:

$$\tau_f = A^{-1}. \quad (4.24)$$

Taking ratios of these time scales yields the three remaining dimensionless groups, which we define as

$$Ca_E = \frac{\tau_\gamma}{\tau_{EHD}} = \frac{\epsilon_2 E_0^2}{\gamma k}, \quad Re_E = \frac{\tau_{c,2}}{\tau_{EHD}} = \frac{\epsilon_2^2 E_0^2}{\mu_2(1+\lambda)\sigma_2}, \quad \hat{A} = \frac{\tau_{c,2}}{\tau_f} = \frac{\epsilon_2 A}{\sigma_2}. \quad (4.25)$$

The electric capillary number  $Ca_E$  compares electric to capillary forces, while the electric Reynolds number  $Re_E$  characterizes the importance of charge convection versus conduction, the two mechanisms responsible for the evolution of the interfacial charge distribution. Finally,  $\hat{A}$  is the dimensionless strain rate of the applied flow.

We scale the governing equations and boundary conditions using time scale  $\tau_{c,2}$ , length scale  $k^{-1}$ , pressure scale  $\epsilon_2 E_0^2$ , velocity scale  $(\tau_{EHD} k)^{-1}$ , and characteristic electric potential  $E_0 k^{-1}$ . The dimensionless Stokes equations read:

$$\nabla^2 \mathbf{u} - (1+\lambda) \nabla p = \mathbf{0}, \quad \mathbf{x} \in V_2, \quad (4.26)$$

$$\nabla^2 \mathbf{u} - (1+\lambda^{-1}) \nabla p = \mathbf{0}, \quad \mathbf{x} \in V_1. \quad (4.27)$$

The charge conservation equation (4.5) becomes:

$$\partial_t q + \mathbf{n} \cdot [\mathbf{E}_2 - R^{-1} \mathbf{E}_1] + Re_E \nabla_s \cdot (q \mathbf{u}) = 0, \quad \mathbf{x} \in S, \quad (4.28)$$

where

$$q = \mathbf{n} \cdot [\mathbf{E}_2 - Q\mathbf{E}_1]. \quad (4.29)$$

The stress balance at the interface is written:

$$\begin{aligned} \mathbf{n} \cdot \left[ -p_2 \mathbf{I} + (1 + \lambda)^{-1} (\nabla \mathbf{u}_2 + \nabla \mathbf{u}_2^T) + p_1 \mathbf{I} - (1 + \lambda^{-1})^{-1} (\nabla \mathbf{u}_1 + \nabla \mathbf{u}_1^T) \right] \\ + \mathbf{n} \cdot \left[ (\mathbf{E}_2 \mathbf{E}_2 - \frac{1}{2} E_2^2 \mathbf{I}) - Q (\mathbf{E}_1 \mathbf{E}_1 - \frac{1}{2} E_1^2 \mathbf{I}) \right] = C a_E^{-1} (\nabla_s \cdot \mathbf{n}) \mathbf{n}, \quad \mathbf{x} \in S. \end{aligned} \quad (4.30)$$

Finally, the kinematic boundary condition becomes

$$\partial_t \xi = Re_E (-u \partial_x \xi + v), \quad \text{for } \mathbf{x} \in S. \quad (4.31)$$

The remaining governing equations and boundary conditions in (4.1)–(4.3), (4.7) and (4.8) remain unchanged in their non-dimensional form, and hence are not repeated here. In the remainder of the paper, all equations and variables are presented in non-dimensional form.

## 4.4 Local linear stability theory

We first perform a linear stability analysis in the vicinity of the stagnation point, in the spirit of [189] who, following an approach previously proposed by [129], considered a similar problem with inertia but no electric field. In the base state (subscript 0), the interface is flat and uncharged:  $\xi_0(x) = 0$ ,  $q_0(x) = 0$ . The applied electric field generates a potential  $\varphi_0(x, z) = -x$  and results in a pressure jump  $[[p_0]] = (Q - 1)/2$  across the interface. The base flow is taken to be the planar extensional flow  $\mathbf{u}_0 = \mathbf{u}^\infty = (\hat{A}/Re_E)(-x, z)$ , which we represent in terms of the streamfunction  $\psi_0(x, z) = -(\hat{A}/Re_E)xz$  with the convention  $(u, v) = (\partial_z \psi, -\partial_x \psi)$ . The base state variables are perturbed as

$$\varphi = \varphi_0 + \varepsilon \tilde{\varphi}, \quad \psi = \psi_0 + \varepsilon \tilde{\psi}, \quad p = p_0 + \varepsilon \tilde{p}, \quad q = \varepsilon \tilde{q}, \quad \xi = \varepsilon \tilde{\xi}. \quad (4.32)$$

We substitute these expressions into the governing equations and boundary conditions and linearize with respect to  $\varepsilon$ . Following [189], we neglect all terms in the linearization that have non-constant coefficients, which restricts our analysis to the neighborhood of the stagnation point at  $(0, 0)$ ; the consequences of this approximation will be discussed in Sec. 4.6. The governing equations for the potential and streamfunction in the two regions are

$$\nabla^2 \tilde{\varphi} = 0, \quad \nabla^4 \tilde{\psi} = 0, \quad (4.33)$$

with jump conditions  $[[\tilde{\varphi}]] = [[\tilde{\psi}]] = [[\partial_z \tilde{\psi}]] = 0$  at the location of the linearized interface  $z = 0$ .

The charge conservation equation and Gauss's law read:

$$\partial_t \tilde{q} - \hat{A} \tilde{q} = \partial_z (\tilde{\varphi}_2 - R^{-1} \tilde{\varphi}_1) + (1 - R^{-1}) \partial_x \tilde{\xi}, \quad (4.34)$$

$$\tilde{q} = \partial_z (Q \tilde{\varphi}_1 - \tilde{\varphi}_2) + (Q - 1) \partial_x \tilde{\xi}, \quad (4.35)$$

while the kinematic and dynamic boundary conditions yield

$$\partial_t \tilde{\xi} = Re_E \partial_x \tilde{\psi}_2 + \hat{A} \tilde{\xi}, \quad (4.36)$$

$$Ca_E^{-1} \partial_{xx} \tilde{\xi} = \tilde{p}_2 - \tilde{p}_1 + (Q - 1) \partial_x \tilde{\varphi}_2 - 2 \left( \frac{1 - \lambda}{1 + \lambda} \right) \partial_{xz} \tilde{\psi}_2, \quad (4.37)$$

$$(1 + \lambda) \tilde{q} = (1 - \lambda) [\partial_{xx} \tilde{\psi}_2 + 4 \hat{A} Re_E^{-1} \partial_x \tilde{\xi}] + \partial_{zz} (\lambda \tilde{\psi}_1 - \tilde{\psi}_2). \quad (4.38)$$

(4.33)–(4.38) form a system of homogeneous constant-coefficient linear partial differential equations. Recall from Sec. 4.3 that in the present non-dimensionalization lengths have been scaled by  $k^{-1}$ , where  $k$  is the wavenumber of the perturbation. We therefore seek normal mode solutions of the form  $\tilde{\varphi}(x, z, t) = \hat{\varphi}(z) \exp(ix + st)$ , with similar expressions for all the variables. Equation (4.33), along with the decay properties as  $z \rightarrow \pm\infty$ , leads to

$$\hat{\varphi}_i = A_i e^{(-1)^{i-1} z}, \quad \hat{\psi}_i = (B_i + C_i z) e^{(-1)^{i-1} z} \quad \text{for } i = 1, 2. \quad (4.39)$$

Applying the boundary conditions yields an algebraic system for the unknown coefficients. Setting its determinant to zero provides the dispersion relation for the growth rate  $s$ :

$$s = \hat{A} - Re_E \left[ \frac{1}{2Ca_E} - \frac{(Q-1)}{2} \left\{ \frac{R-1 - (s-\hat{A})(Q-1)R}{R+1 + (s-\hat{A})(Q+1)R} \right\} \right], \quad (4.40)$$

where the dependence on wavenumber  $k$  is implicit via the electric capillary number defined in (4.25). The first term on the right-hand side of (4.40) shows that the background flow is destabilizing when  $\hat{A} > 0$ , i.e. when the interface is aligned with the compressional axis [189]. The second and third terms describe the effects of capillary and electric stresses, respectively. A more detailed discussion of this dispersion relation is deferred to Sec. 4.6.

## 4.5 Boundary element method and numerical stability

We complement the local linear analysis of Sec. 4.4 with numerical simulations and a numerical stability analysis. We first present in §4.5.1 a numerical method for the nonlinear solution of the system of governing equations (4.26)–(4.30) based on the boundary integral equations for the Laplace and Stokes equations in a periodic domain of period  $L_p$  along the  $x$ -direction. These simulations will provide insight into the dynamics of the system far from its base state. The methodology shares similarities with that of [40] for axisymmetric drops, but implements adaptive grid refinement to handle large local deformations and charge gradients in the nonlinear regime of growth. Subsequently in §4.5.2, we utilize the same boundary element method to perform a numerical normal-mode linear stability analysis by computing the Jacobian of the dynamical system and solving for its eigenspectrum to identify fundamental modes of instability.

### 4.5.1 Boundary element method

We formulate the electric problem using the boundary integral equation for Laplace's equation [157, 10, 90]:

$$\varphi_{1,2}(\mathbf{x}_0) = -\mathbf{x}_0 \cdot \mathbf{E}_0 - \int_S \mathbf{n}(\mathbf{x}) \cdot \llbracket \nabla \varphi(\mathbf{x}) \rrbracket \mathcal{G}^P(\mathbf{x}_0; \mathbf{x}) d\mathbf{l}(\mathbf{x}), \quad \text{for } \mathbf{x}_0 \in V, S, \quad (4.41)$$

where the evaluation point  $\mathbf{x}_0$  can be anywhere in space whereas  $\mathbf{x}$  denotes the integration point on the interface. The periodic Green's function for Laplace's equation,  $\mathcal{G}^P(\mathbf{x}_0; \mathbf{x})$ , represents the potential due to a periodic array of point sources with period  $L_p$  along the  $x$ -axis [126]. Taking the gradient of equation (4.41) with respect to  $\mathbf{x}_0$  and using Gauss's law (4.29), we can derive an integral equation for the jump in the normal electric field across the interface:

$$\int_S \llbracket E^n(\mathbf{x}) \rrbracket [\mathbf{n}(\mathbf{x}_0) \cdot \nabla_0 \mathcal{G}^P] d\mathbf{l}(\mathbf{x}) - \frac{1+Q}{2(1-Q)} \llbracket E^n(\mathbf{x}_0) \rrbracket = E_0^n(\mathbf{x}_0) - \frac{q(\mathbf{x}_0)}{1-Q}, \quad \text{for } \mathbf{x}_0 \in S. \quad (4.42)$$

Given the charge distribution  $q$ , equation (4.42) can be used to solve for  $\llbracket E^n \rrbracket$ , from which we obtain  $E_1^n$  and  $E_2^n$  as

$$E_1^n = \frac{q - \llbracket E^n \rrbracket}{1-Q}, \quad E_2^n = \frac{q - Q \llbracket E^n \rrbracket}{1-Q}. \quad (4.43)$$

The tangential electric field  $\mathbf{E}^t = -\nabla_s \varphi$  can then also be obtained by differentiating the electric potential in (4.41) in the direction tangential to the interface.

Similarly, the flow problem can be formulated in boundary integral form as [133, 125]:

$$\begin{aligned} \mathbf{u}(\mathbf{x}_0) = & \frac{2}{1+\lambda} \mathbf{u}^\infty(\mathbf{x}_0) - \frac{1}{2\pi} \int_S \llbracket \mathbf{f}^H(\mathbf{x}) \rrbracket \cdot \mathbf{G}^P(\mathbf{x}; \mathbf{x}_0) d\mathbf{l}(\mathbf{x}) \\ & + \frac{1-\lambda}{2\pi(1+\lambda)} \int_S \mathbf{u}(\mathbf{x}) \cdot \mathbf{T}^P(\mathbf{x}; \mathbf{x}_0) \cdot \mathbf{n}(\mathbf{x}) d\mathbf{l}(\mathbf{x}), \quad \text{for } \mathbf{x}_0 \in S, \end{aligned} \quad (4.44)$$

where the hydrodynamic traction jump  $\llbracket \mathbf{f}^H \rrbracket$  is obtained from the dynamic boundary condition (4.9). Here,  $\mathbf{G}^P$  is the singly periodic Green's function capturing the flow due to a periodic array of point forces separated by the distance  $L_p$  along the  $x$ -direction, and  $\mathbf{T}^P$  is the corresponding

stress tensor [125]. Note that, in the results shown below, we choose  $\lambda = 1$  and therefore the double-layer potential vanishes in (4.44). The single-layer potential exhibits a logarithmic singularity when  $\mathbf{x}$  approaches  $\mathbf{x}_0$ , which we isolate and treat separately with a quadrature designed for singular integrands [169]. Gauss-Legendre quadrature with 6 base points is used for non-singular elements.

The numerical algorithm for transient nonlinear simulations follows [40] and can be summarized as follows. At  $t = 0$ , the periodic flat interface is discretized into  $N$  elements using  $N$  grid points with locations  $\mathbf{x}_i(t)$  that move with the normal component of the interfacial velocity to satisfy the kinematic boundary condition. The interface shape is reconstructed using cubic splines based on the grid point locations, which allows for an accurate and convenient determination of geometric properties such as the normal and tangential vectors and surface curvature, and for the accurate evaluation of surface integrals. Considering the high-order of accuracy of cubic spline interpolations with a reasonable grid resolution, the most challenging errors are those incurred in the numerical integration, especially in the treatment of the singular terms. The asymptotic rate of convergence of our method is found to be between 1.5 and 2. More details on error analysis are presented in §4.6.1.

At every time iteration, we perform the following steps:

1. Given the current charge distribution  $q(\mathbf{x})$  and shape of the interface, compute  $\llbracket E^n(\mathbf{x}) \rrbracket$  by numerically inverting (4.42) using a GMRES solver [138, 59]. From  $\llbracket E^n(\mathbf{x}) \rrbracket$ , obtain  $E_1^n$  and  $E_2^n$  via (4.43).
2. Determine the potential  $\varphi$  along the interface by evaluating (4.41).
3. Differentiate the surface potential numerically along the interface in order to obtain the tangential electric field  $\mathbf{E}^t = -\nabla_s \varphi$ .
4. Knowing both components of the electric field, determine the jump in the electric traction  $\llbracket \mathbf{f}^E \rrbracket$  and use it to obtain  $\llbracket \mathbf{f}^H \rrbracket$  using (4.9).

5. Solve for the interfacial velocity using the Stokes boundary integral equation (4.44).
6. Compute  $\partial_t q$  via (4.5) and update the charge distribution using a second-order Runge-Kutta scheme.
7. Update the position of the interface by advecting the grid with the normal component of the interfacial velocity:  $\dot{\mathbf{x}}_i(t) = (\mathbf{u} \cdot \mathbf{n})\mathbf{n}$ . Refine the grid locally if either the curvature of the interface, magnitude of charge gradient, or length of the element exceeds a certain threshold. Typical grids used in the simulations have  $N \sim 1000$  elements.

### 4.5.2 Numerical linear stability analysis

We also perform a numerical normal-mode linear stability analysis based on the full system of equations and boundary conditions, following a method proposed by [128] for the stability of pendant drops. We analyze the stability of the base state of a flat interface with zero charge, which allows us to parametrize the interface as  $z = \xi(x, t)$ . The system of governing equations can be viewed as a dynamical system for the surface charge density  $q(x, t)$  and interface deflection  $\xi(x, t)$ , which evolve according to equations (4.28) and (4.12), or

$$\partial_t \begin{bmatrix} q(x, t) \\ \xi(x, t) \end{bmatrix} = \begin{bmatrix} -\mathbf{n} \cdot [\mathbf{E}_2 - R^{-1} \mathbf{E}_1] - Re_E \nabla_s \cdot (q\mathbf{u}) \\ Re_E(-u\partial_x \xi + v) \end{bmatrix} = \begin{bmatrix} \mathcal{Q}(q, \xi) \\ \mathcal{Z}(q, \xi) \end{bmatrix}, \quad (4.45)$$

where the electric field  $\mathbf{E}$  and velocity  $\mathbf{u}$  are solutions of the boundary integral equations (4.42) and (4.44). The right-hand side in (4.45) is evaluated on the interface. It can be viewed as a nonlinear functional of the two variables  $(q, \xi)$  and can be calculated numerically using the algorithm of Sec. 4.5.1. The flat configuration with zero charge, given by  $q(x, t) = \xi(x, t) = 0$ , is an equilibrium solution.

The numerical linear stability analysis is performed in a periodic domain of period  $L_p$ . After spatial discretization of the unit period using  $N$  grid points, the dynamical system (4.45)

yields a system of coupled ordinary differential equations of the form

$$\partial_t \mathbf{Y} = \mathbf{J}(\mathbf{Y}), \quad (4.46)$$

where  $\mathbf{Y}$  and  $\mathbf{J}$  are vectors of length  $2N$  containing the values of the variables at the grid points:

$$\mathbf{Y} = (q^1, q^2, \dots, q^N, \xi^1, \xi^2, \dots, \xi^N), \quad (4.47)$$

and

$$\mathbf{J} = (\mathcal{Q}^1, \mathcal{Q}^2, \dots, \mathcal{Q}^N, \mathcal{Z}^1, \mathcal{Z}^2, \dots, \mathcal{Z}^N). \quad (4.48)$$

The linear stability of the equilibrium solution  $\mathbf{Y} = \mathbf{0}$  is studied by perturbing the system as  $\mathbf{Y}(t) = \varepsilon \hat{\mathbf{Y}} e^{st}$ . At linear order in  $\varepsilon \ll 1$ , we obtain a linear eigenvalue problem

$$\mathcal{J} \cdot \hat{\mathbf{Y}} = s \hat{\mathbf{Y}}, \quad (4.49)$$

where

$$\mathcal{J}_{ik} = \frac{\partial J_k}{\partial Y_i}(\mathbf{Y} = \mathbf{0}) \quad (4.50)$$

is the Jacobian of the system. The components of the Jacobian are calculated numerically using a second-order central finite difference scheme:

$$\mathcal{J}_{ik} \approx \frac{J_k(+\delta Y_i) - J_k(-\delta Y_i)}{2\delta Y_i}, \quad (4.51)$$

where each variable  $Y_i$  is successively perturbed by a small amount  $\pm\delta Y_i$  (corresponding to a small perturbation of charge  $\pm\delta q$  for  $i = 1, \dots, N$  or of shape  $\pm\delta\xi$  for  $i = N + 1, \dots, 2N$ ), and where  $J_k(\pm\delta Y_i)$  at the numerator is obtained using the boundary integral method. Once  $\mathcal{J}$  is known, its eigenvalues  $s$  provide the growth rates of the perturbation, while its eigenvectors  $\hat{\mathbf{Y}}$  capture the corresponding eigenmodes of charge and shape.

## 4.6 Results and discussion

We present results on the stability of the system by comparing predictions from the local linear theory (LT) of Sec. 4.4 and from the numerical linear stability analysis (Num-LSA) of Sec. 4.5.2. Nonlinear dynamics are also explored in transient simulations (TS) using the boundary element method of Sec. 4.5.1. We discuss our results in the following order: first, we analyze the behavior of the system subject to a tangential electric field in the absence of any background flow in Sec. 4.6.1. Next, in Sec. 4.6.2, we study the effect of an extensional background flow when there is no electric field. Finally, we characterize in Sec. 4.6.3 the interplay between field and flow when both are applied to the system simultaneously.

### 4.6.1 Effect of tangential electric field

We first consider the case where a tangential electric field is applied to the interface in the absence of any background flow. In this case, results from the local linear theory and numerical linear stability analysis are expected to match, as the approximations of the local theory only affect terms involving the applied flow. Since the base flow is stationary and the interfacial charge is zero in the equilibrium state, the effects of charge convection only arise at quadratic order and therefore have no effect on the linear stability. The growth rate predicted by LT in this case is given by:

$$s = -Re_E \left[ \frac{1}{2Ca_E} - \frac{(Q-1)}{2} \left\{ \frac{R-1-s(Q-1)R}{R+1+s(Q+1)R} \right\} \right]. \quad (4.52)$$

Note that the dependence on wavenumber  $k$  is through the electric capillary number, with  $Ca_E^{-1} \propto k$ . Equation (4.52) is consistent with the results of [104] in the limit of zero inertia.

In the limit of instantaneous charge relaxation (i.e., considering only Ohmic terms in

equation (4.5)), the growth rate further simplifies to:

$$s = -Re_E \left[ \frac{1}{2Ca_E} - \frac{(Q-1)(R-1)}{2(R+1)} \right]. \quad (4.53)$$

The first term on the right-hand side is always negative and captures the stabilizing effect of capillary stresses. It is proportional to  $k$ , indicating that surface tension preferentially stabilizes high wavenumbers. The last term in (4.53) captures the effect of electric stresses and can be of either sign. For the system to be electrically unstable, the following condition must be met:

$$(Q-1)(R-1) > 0, \quad (4.54)$$

which means either  $R > 1$ ,  $Q > 1$  or  $R < 1$ ,  $Q < 1$ . Setting  $s = 0$  in (4.53) also provides a critical electric capillary number for instability:

$$Ca_{E,c} = \frac{R+1}{(Q-1)(R-1)}. \quad (4.55)$$

The system is unstable for  $Ca_E \geq Ca_{E,c}$  (long waves), and it is stable otherwise. The maximum growth rate is reached at zero wavenumber or under vanishing surface tension ( $Ca_E \rightarrow \infty$ ) and is given by

$$s_{max} = Re_E \frac{(Q-1)(R-1)}{2(R+1)}. \quad (4.56)$$

In the case of finite charge relaxation, the dispersion relation (4.52) is a quadratic equation for the growth rate  $s$ . The roots can be shown to be imaginary only when

$$(QR-1)(Q-1) < 0, \quad (4.57)$$

which is incompatible with the condition of equation (4.54) for instability, so that the growth rate is always real in electrically unstable systems.

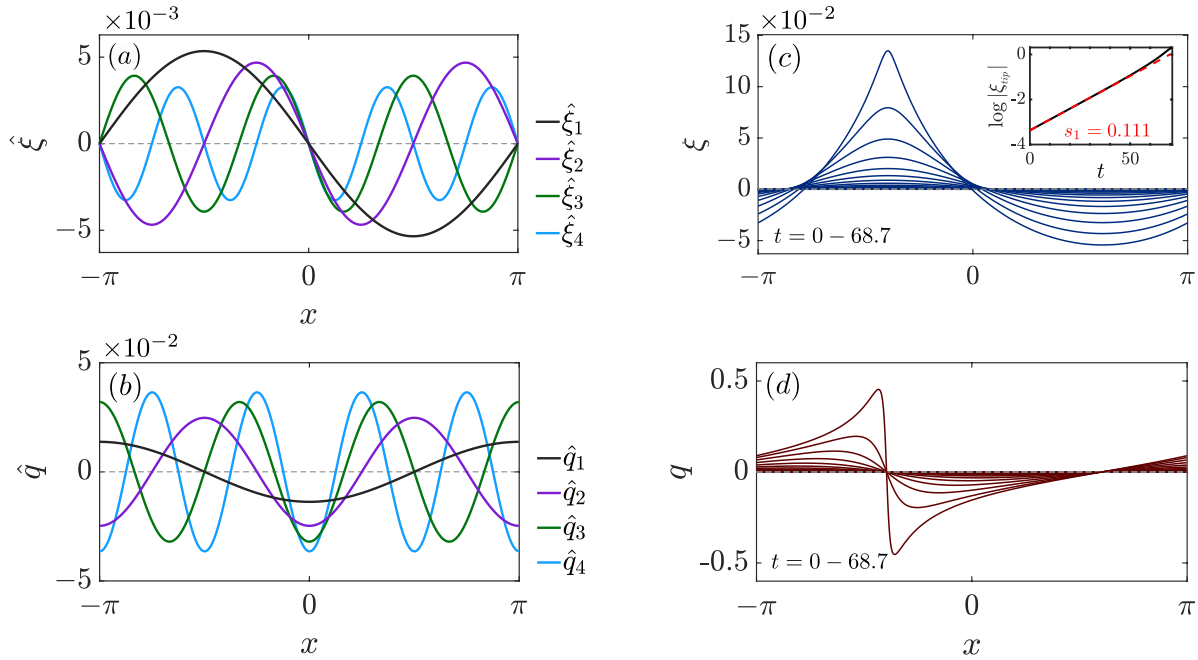


**Figure 4.4.** Effect of tangential electric field: dominant eigenmodes of (a) deformation  $\hat{\xi}$ , and (b) interfacial charge  $\hat{q}$ , obtained via Num-LSA for  $(R, Q, \lambda, Re_E, Ca_E) = (2, 3, 1, 1, 15.92)$ . The corresponding growth rate values are  $(s_1, s_2, s_3, s_4) = (0.111, 0.098, 0.085, 0.073)$ . (c, d) Time evolution of the interface shape and charge distribution in a transient simulation with an initial condition given  $(\hat{\xi}_1, \hat{q}_1)$ . Inset: black curve shows the location of the tip of the interface (maximum deflection) over time while the red line shows the growth rate predicted by Num-LSA. Also see video in Supplementary Material.

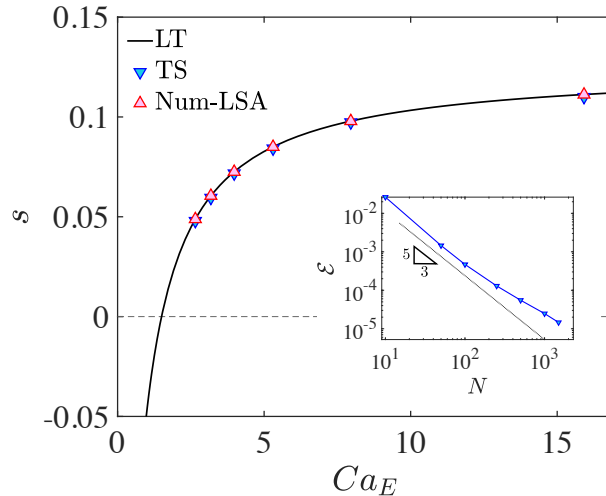


**Figure 4.5.** Growth rate  $s$  as a function of  $Ca_E$  obtained by Num-LSA, LT and TS for  $(R, Q, \lambda, Re_E) = (2, 3, 1, 1)$ . Inset shows the decay of the numerical error  $\mathcal{E}$  with the grid size  $N$  for  $Ca_E = 7.96$ .

Figure 4.4(*a,b*) shows the dominant unstable modes of deformation and charge distribution obtained via Num-LSA. It is evident that all the modes are sinusoidal as expected in the absence of flow, and the fastest-growing mode,  $\hat{\xi}_1$ , has the largest possible wavelength permitted by the computational domain. This is indeed expected based on LT. For comparison, we also calculate the growth rate of various eigenmodes numerically by performing short-time transient simulations. The growth rate  $s$  obtained from LT, Num-LSA and TS is plotted as a function of electric capillary number  $Ca_E$  in figure 4.5. The results from Num-LSA and TS are in close agreement with the ones predicted by (4.52), which provides validation of our numerical schemes. The numerical error  $\mathcal{E} = |(s - s_{LT})/s_{LT}|$  decays with the grid size  $N$  at a rate between 1.5 and 2 according to the inset of figure 4.5. Consequently, we dwell on numerical errors of the order  $O(10^{-5})$  with a grid size  $N \sim 1000$ .

The nonlinear evolution of the interface shape and charge distribution is illustrated in figure 4.4(*c,d*) (also see video in Supplementary Material), showing a representative transient simulation where the interface shape and charge distribution were initially perturbed by the dominant unstable eigenmode with a small amplitude. At short times, the sinusoidal modes amplify as the surface deflection grows and charge is brought to the interface via Ohmic conduction. As nonlinear effects become significant, the interface deflection becomes asymmetric. Electric stresses on the interface drive a flow which tends to further sweep opposite charges towards the interface tip, leading to the development of sharp charge gradients and of a pointed tip with high curvature. The tip grows unboundedly with an increasing curvature until it eventually causes our numerical method to break down. One should note that the eigenmodes have up-down mirror symmetry, meaning that both  $(\hat{\xi}, \hat{q})$  and  $(-\hat{\xi}, -\hat{q})$  have identical growth rates and exhibit similar dynamics at short times. This is in contrast to the nonlinear regime of evolution where the shape and charge distributions become asymmetric as evident in figure 4.4.

## 4.6.2 Effect of stagnation-point flow

Next, we consider the stability of the interface under the applied flow only, with no electric field. Since there is no applied field, the interfacial charge remains zero and the fate of the system is entirely determined by the balance of viscous and capillary stresses. Consequently, the only two time scales in the problem are  $\tau_\gamma$  and  $\tau_f$ , previously defined in (4.22) and (4.24), respectively. The local linear theory yields the following expression for the growth rate:

$$s_{LT}^* = 1 - \frac{1}{2Ca}, \quad (4.58)$$

where  $s_{LT}^*$  has been scaled by  $\tau_f^{-1}$  instead of  $\tau_{c,2}^{-1}$ , and where  $Ca = \tau_\gamma/\tau_f$  is the viscous capillary number and remains proportional to  $k_p^{-1}$ . This result is consistent with the analysis of [189] in the limit of zero inertia.

Figure 4.6(a) shows the most unstable modes of deformation obtained via Num-LSA. The modes are clearly non-sinusoidal in this case, with deflections from the flat base state occurring primarily in the neighborhood of the stagnation point. The dominant mode  $\hat{\xi}_1$  resembles a Gaussian centered around the origin, and higher-order modes involve shapes with increasing numbers of oscillations, all concentrated near  $x = 0$ . Since the modes are non-sinusoidal, the growth rate of the fastest-growing mode differs from the local prediction of equation (4.58). This is confirmed in figure 4.6(c) where the growth rates from LT and Num-LSA are compared as a function of  $Ca$ . Both methods provide similar growth rates at high capillary numbers (long wavelengths), but their predictions diverge at small values of  $Ca$ : while the local theory shows a stabilization of the system below a critical capillary number, the numerical stability analysis predict that the system is always unstable.

The nonlinear evolution of the interface shape is illustrated in figure 4.6(b) (also see video in Supplementary Material), showing a transient simulation in which the interface shape was perturbed at  $t = 0$  by the dominant unstable eigenmode of shape. The interface deflection increases with time, and as non-linear effects become significant the dimple in the interface

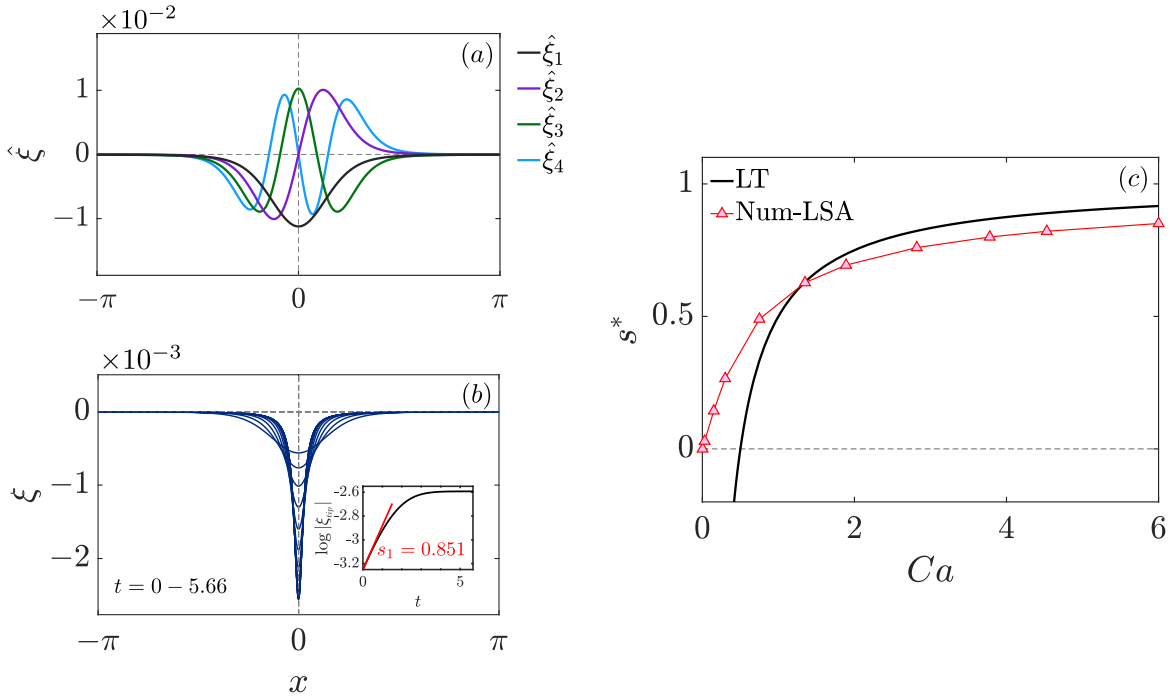


**Figure 4.6.** Effect of applied stagnation-point flow: (a) dominant eigenmodes of deformation  $\hat{\xi}$  obtained via Num-LSA for a system with  $(\lambda, Ca) = (1, 6)$ . The corresponding growth rates are  $(s_1^*, s_2^*, s_3^*, s_4^*) = (0.851, 0.650, 0.517, 0.393)$ . (b) Time evolution of the interface shape in a transient simulation with an initial condition given by  $\hat{\xi}_1$ . Inset: black line shows the location of the tip of the interface (maximum deflection) over time while the red curve shows the growth rate predicted by Num-LSA. Also see video in Supplementary Material. (c) Growth rate  $s^*$  as a function of  $Ca$  obtained via Num-LSA and LT.

narrows while the curvature at the tip increases, leading to an increase in capillary stresses which tend to resist further deformation. As shown in the inset of figure 4.6(b), this causes the interface deflection to saturate and reach a steady profile where capillary stresses balance viscous stresses arising from the applied flow. This is unlike the case of figure 4.4 for the electric field only, where the tip deformation did not saturate.

### 4.6.3 Combined effects of electric field and flow

We now turn to the general case where the system is subject to both a tangential electric field and a stagnation point flow. In this case, the local linear theory with finite charge relaxation and charge convection by the flow yields the dispersion relation of (4.40), with sinusoidal eigenmodes for all perturbation variables. It is clear, from the form of equation (4.40), that the applied flow and electric field contribute additively to the growth rate: the presence of the base flow simply shifts the growth rate of equation (4.53) for the electric problem by an amount of  $\hat{A}$ . In particular, an external flow with  $\hat{A} > 0$  always has a destabilizing effect under the local theory approximations. If charge convection is neglected in the theory, the effect of the background flow only affects the dynamics of the system through the kinematic boundary condition and the dispersion relation reduces to

$$s_{LT} = \hat{A} - Re_E \left[ \frac{1}{2Ca_E} - \frac{(Q-1)}{2} \left\{ \frac{R-1-s_{LT}(Q-1)R}{R+1+s_{LT}(Q+1)R} \right\} \right]. \quad (4.59)$$

As we show in figure 4.8 and discuss further below, this approximation results in a decrease in growth rate when compared to equation (4.40), suggesting that charge convection is destabilizing under the local theory.

The numerical linear stability analysis and transient simulations, however, paint a more complex picture. Recall that, in these two cases, the electric capillary number  $Ca_E$  is defined based on  $k_p = 2\pi L_p^{-1}$ , where  $L_p$  is the size of the periodic domain and sets the largest possible

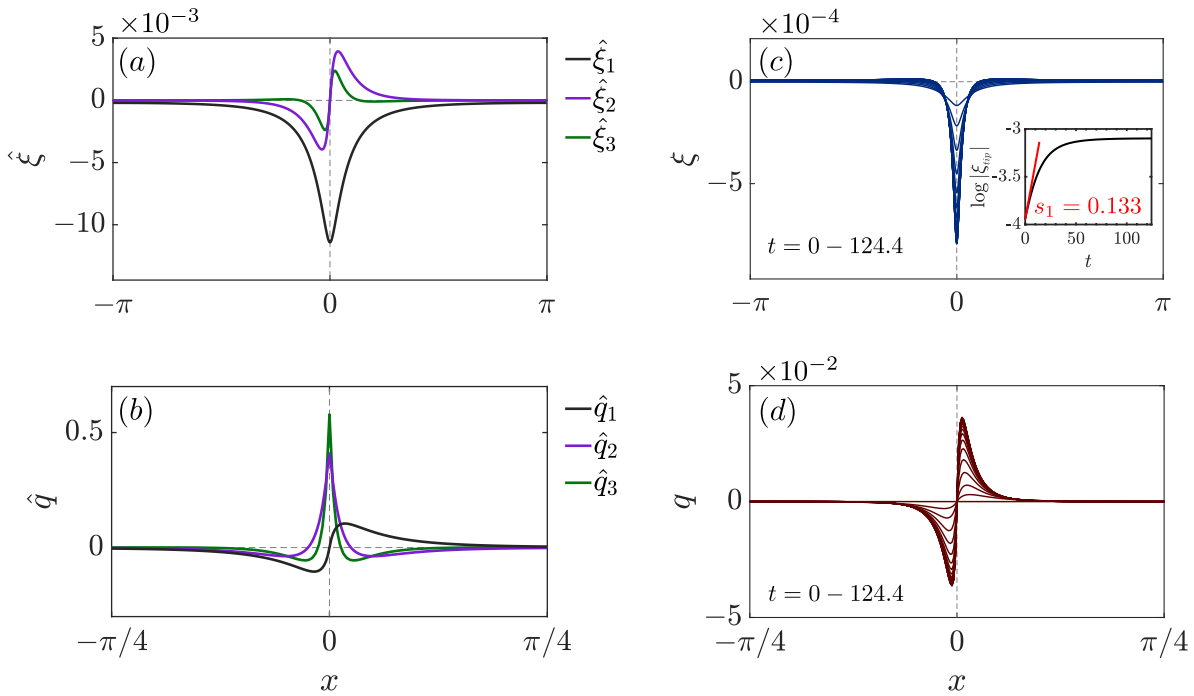


**Figure 4.7.** Combined effects of electric field and flow: (a, b) dominant eigenmodes of deformation  $\hat{\xi}$  and interfacial charge  $\hat{q}$  for a system with  $(R, Q, \lambda, Ca_E, Re_E, \hat{A}) = (2, 3, 1, 15.92, 1, 0.177)$ . (c, d) Time evolution of the interface shape and charge distribution in a transient simulation with initial condition given by  $(\hat{\xi}_1, \hat{q}_1)$ . Inset in (c): black line shows the location of the tip of the interface (maximum deflection) over time while the red curve shows the growth rate predicted by Num-LSA. Also see video in Supplementary Material. Note that (b) and (c) only show one quarter of the total domain, as interfacial charge variations are strongly localized near the origin.

length scale for the unstable eigenmodes. The dominant eigenmodes of shape and charge obtained by Num-LSA for a representative case are plotted in figure 4.7(*a,b*). Similar to the case of Sec. 4.6.2 with flow only, all the modes are non-sinusoidal and exhibit strong variations near the stagnation point. This is true especially of the eigenmodes of charge, which display shock-like structures at  $x = 0$ . These shocks result from the advection by the applied flow of surface charges of opposite sign on each side of the stagnation point. They are reminiscent of the nonlinear shapes of figure 4.4, but are even more strongly concentrated near the origin (note the different scales in figure 4.7(*a*) and (*b*)). Note that the charge conservation equation (4.5) does not account for surface diffusion of charge, which, if included, may regularize the profiles. These sharp gradients seen in the linear eigenmodes are yet further amplified in the nonlinear regime, as we show by performing transient simulations with a condition given by the first unstable eigenmode with a small amplitude. The evolution of the shape and charge profiles is shown in figure 4.7(*c,d*) (also see video in Supplementary Materials): the interface deflection sharpens rapidly as charges accumulate on each side of the stagnation point, leading ultimately to failure of our numerical method. The emergence of shocks in the charge distribution has also been observed in related configurations, such as in liquid drops under applied electric fields [92, 39, 40]. There, the quadrupolar Taylor flow generated by tangential electric stresses at the drop interface sweeps surface charges from the poles towards the equator, resulting in sharp gradients at that location.

To further understand the interaction between the background flow and the electric field, we study the behavior of the system as a function of local strain rate  $\hat{A}$  in figure 4.8, in a case where the interface is electrically unstable. As already discussed above, the local theory (LT) predicts that the applied flow is always destabilizing, especially in the presence of charge convection. The behavior is more complex according to the numerical linear stability analysis, showing that the background flow in fact has a stabilizing effect for  $0 < \hat{A} < \hat{A}_c$  ( $\hat{A}_c \approx 0.118$ ), as the growth rate decreases from its value at  $\hat{A} = 0$ . Beyond  $\hat{A} \geq \hat{A}_c$ , the background flow becomes destabilizing even in the presence of charge convection. However, the growth rate is always smaller when charge convection is included in the model. Interestingly, the growth rates predicted by LT and

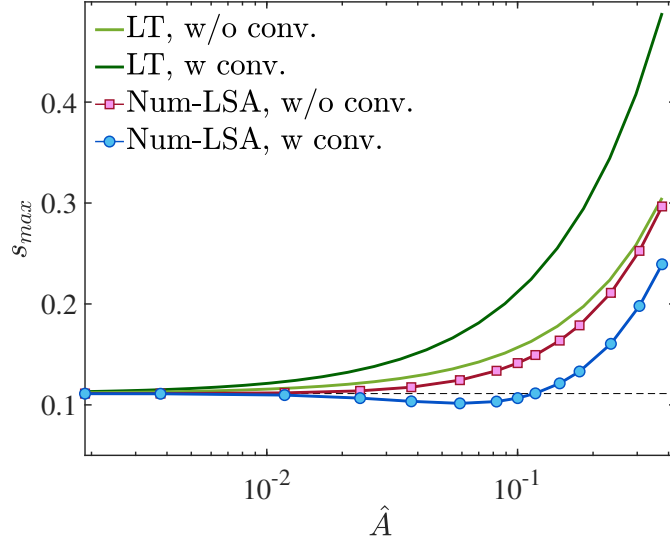


**Figure 4.8.** Maximum growth rate as a function of local strain rate  $\hat{A}$  in a system with  $(R, Q, \lambda, Re_E, Ca_E) = (2, 3, 1, 1, 15.92)$ . The blue and red curves show results of Num-LSA with and without charge convection, while the light and dark green curves show the predictions of LT with and without charge convection, respectively.

Num-LSA are in close agreement in the absence of charge convection. We discuss in §4.6.4 the mechanism for these trends, which involves the subtle interplay of convection with Ohmic conduction.

The effect of the conductivity ratio  $R$  and permittivity ratio  $Q$  on the stability of the system is studied in figure 4.9. Although both LT and Num-LSA yield qualitatively similar trends with respect to  $R$  and  $Q$ , the maximum growth rates obtained by the two methods differ significantly, and predict opposite effects of charge convection as already observed in figure 4.8. Another significant difference is that according to LT the interface is only unstable above critical values of  $R, Q \sim O(1)$ , whereas it is unstable for all values of  $R$  and  $Q$  according to the numerical stability. The evident discrepancy between the results of the two methods is attributed to the local approximation made in LT, where linear terms in  $x$  were neglected in the charge conservation equation. As demonstrated by Num-LSA, these coupling terms with non-constant coefficients result in very efficient charge transport towards the stagnation point, leading to strongly localized eigenmodes unlike the Fourier modes assumed by LT.

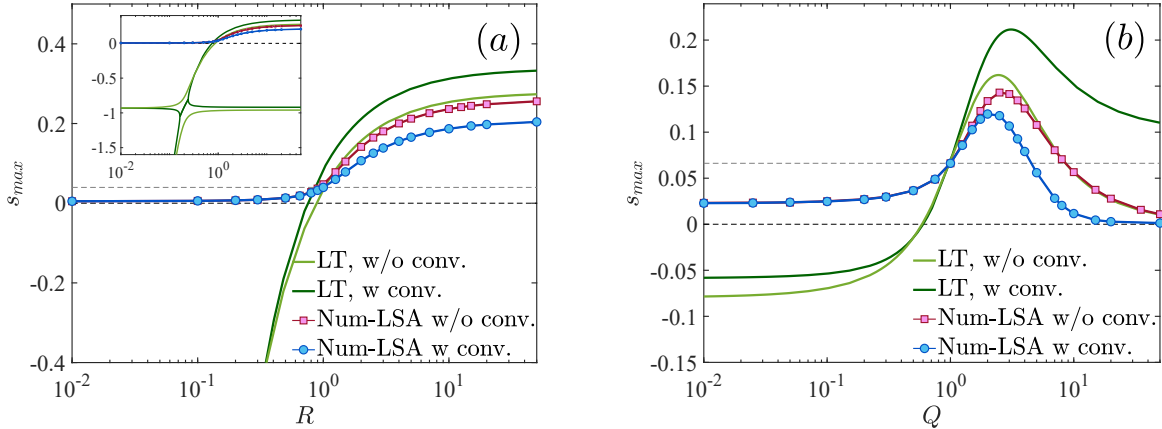


**Figure 4.9.** Maximum growth rate as a function of: (a) conductivity ratio  $R$  with  $Q = 3$ , and (b) permittivity ratio  $Q$  with  $R = 2$ . The remaining parameters are  $(\lambda, Re_E, Ca_E, \hat{A}) = (1, 1, 15.92, 0.1)$  in both cases. Inset in (a) shows a longer range for the vertical axis, highlighting additional stable eigenmodes.

#### 4.6.4 Mechanisms of charge transport in the dominant mode of instability

In order to explain the non-monotonic role of charge convection seen in figure 4.9, we further analyze the various mechanisms of charge transport in the dominant mode of instability. We define the Ohmic and convective fluxes as

$$\dot{q}_{ohm} = \mathbf{n} \cdot [R^{-1} \mathbf{E}_1 - \mathbf{E}_2], \quad (4.60)$$

$$\dot{q}_{conv} = -Re_E \nabla_s \cdot (q\mathbf{u}), \quad (4.61)$$

so that the charge conservation equation reads  $\partial_t q = \dot{q}_{ohm} + \dot{q}_{conv}$ . Figure 4.10(a) shows the profiles of  $\dot{q}_{ohm}$  and  $\dot{q}_{conv}$  for the most unstable eigenmode in a system with  $(R, Q, Ca_E, Re_E, \hat{A}) = (2, 3, 15.92, 1, 0.177)$ . It is evident that Ohmic conduction and charge convection oppose each other in the dominant mode as they have opposite signs over most of the domain. According to figure 4.10(a), charge convection is dominant in the vicinity of the stagnation point, whereas

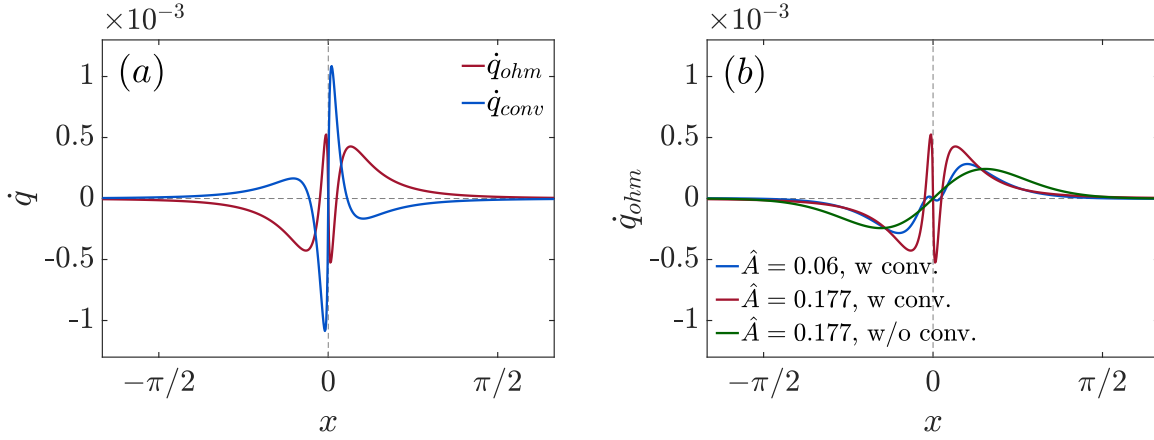


**Figure 4.10.** (a) Ohmic flux and convective flux, defined in equations (4.60)–(4.61), in the dominant mode of instability for a system with  $(R, Q, Ca_E, Re_E, \hat{A}) = (2, 3, 15.92, 1, 0.177)$ . (b) Ohmic flux in the dominant mode of instability for two different values of  $\hat{A}$ , with and without charge convection.

conduction takes over further away from the origin. Close to the stagnation point,  $\dot{q}_{ohm}$  exhibits oscillations, which are stronger with increasing  $\hat{A}$  as shown in figure 4.10(b) but are suppressed when charge convection is neglected.

To elucidate the underlying mechanisms for this behavior, we analyze the respective roles of interface deflections and charge perturbations in driving Ohmic currents in the dominant eigenmode. Recall that the eigenmodes obtained by Num-LSA involve both perturbations in shape  $\hat{\xi}$  and charge  $\hat{q}$ . Here we estimate the Ohmic current induced by these eigenmodes in the linear regime:

$$\hat{q}_{ohm} = R^{-1} \hat{E}_1^n - \hat{E}_2^n. \quad (4.62)$$

To express  $\hat{E}_1^n$  and  $\hat{E}_2^n$  in terms of  $(\hat{q}, \hat{\xi})$ , we linearize the boundary integral equation (4.42) to find:

$$-\frac{1+Q}{2(1-Q)}(\hat{E}_2^n - \hat{E}_1^n) = \hat{n}_x - \frac{\hat{q}}{1-Q}, \quad (4.63)$$

where  $\hat{n}_x = \partial_x \hat{\xi}$  is the  $x$  component of the surface normal. Gauss's law also provides

$$\hat{E}_2^n - Q\hat{E}_1^n = \hat{q}. \quad (4.64)$$

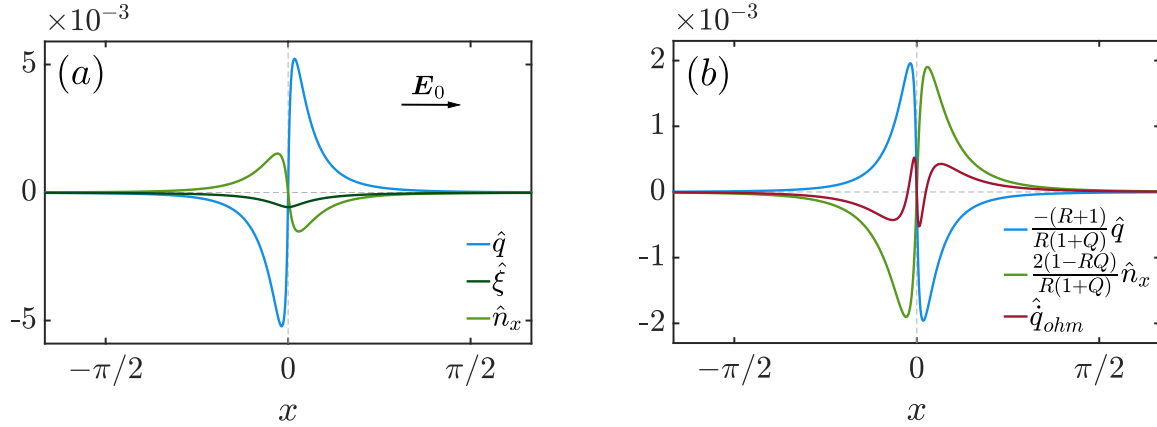


**Figure 4.11.** (a) Eigenmodes of charge  $\hat{q}$ , interfacial deflection  $\hat{\xi}$ , and horizontal component of the unit normal vector  $\hat{n}_x$  in the dominant mode of instability for a system with  $(R, Q, \lambda, Re_E, \hat{A}, Ca_E) = (2, 3, 1, 1, 0.177, 15.92)$ . (b) Resulting Ohmic currents induced by perturbations in the charge distribution (blue), interfacial shape (green), and their net distribution (red); see equation (4.65) for details.

Eliminating  $\hat{E}_1^n$  and  $\hat{E}_2^n$  using equations (4.63) and (4.64) yields the following expression for the charge conduction flux:

$$\hat{q}_{ohm} = 2 \frac{(1-RQ)}{R(1+Q)} \hat{n}_x - \frac{R+1}{R(1+Q)} \hat{q}, \quad (4.65)$$

which captures the conduction response of the system to small perturbations. The first term on the right-hand side represents the Ohmic flux induced by perturbing the shape while the second term is the flux induced by the charge perturbation. Figure 4.11 shows the profile of the perturbation in the dominant eigenmode along with the resulting Ohmic fluxes for the same set of parameters as used in figure 4.10. It is evident from figure 4.11(b) that the Ohmic currents induced by the applied deformation and charge distribution have opposite signs over the entire domain, and thus work against each other. This explains the oscillations in  $\hat{q}_{ohm}$  observed near the stagnation point in figure 4.10(a), and it is this complex Ohmic response that opposes charge convection in the dominant eigenmode, leading to the stabilizing effect of convection seen in figures 4.8 and 4.9. One should note that this behavior is independent of the sign of  $(1-RQ)$  since there is no preferred order to the arrangement of the fluid layers in the linear

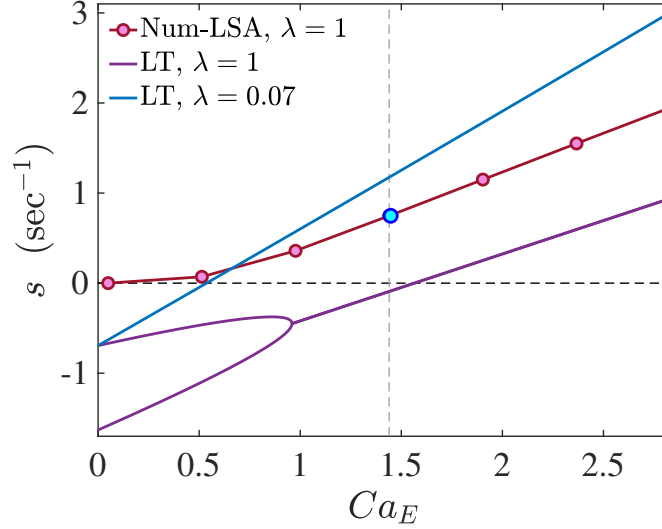


**Figure 4.12.** Growth rate  $s$  as a function of  $Ca_E$  obtained via Num-LSA and LT for a system with  $(R, Q) = (31.4, 0.6)$  characteristic of the EHD flow in a droplet.  $Re_E$  and  $\hat{A}$  are linearly proportional to  $Ca_E$  in that case, and the blue marker  $(\lambda, Re_E, \hat{A}, Ca_E) = (1, 4.37, 1.19, 1.45)$  is the reference point based on the experiments. Purple and blue lines show the predictions by LT for  $\lambda = 1$  and  $0.07$  respectively.

regime. In other words, two systems characterized by  $RQ$  and  $(RQ)^{-1}$  are dynamically equivalent.

## 4.7 Relevance to the equatorial streaming instability

Brosseau and Vlahovska reported streaming from the equator of a drop placed in a uniform electric field. In the experimental system,  $RQ > 1$  and the EHD flow driven by electric shear stresses on the drop interface converges at the equator (see figure 4.1) [20]. At the equator the applied electric field is also parallel to the drop interface. Thus, the configuration resembles the set-up considered in our theoretical study. Here, we use the LT and Num-LSA analyses to gain insight into the interface destabilization at the stagnation line of the electrohydrodynamic flow.

The LT of a fluid interface subject to a convergent flow predicts that the interface is always unstable [189]. However, the LT for a fluid interface subjected to a tangentially applied DC uniform field is stable for the experimental conditions according to equation (4.52). In the

experiments the streaming was only observed at sufficiently high electric fields,  $Ca_E \sim O(1)$ , which is likely due to the competition of the destabilizing and stabilizing actions of the field-driven flow and of the electric field.

Figure 4.12 shows the theoretical prediction for the growth rate of the instability. The strain rate of the convergent flow can be estimated from the EHD flow at the equator of the drop based on Taylor's classic solution [176]:

$$A = \frac{9}{5} \frac{R(RQ-1)}{(2R+1)^2} \tau_{EHD}^{-1} \quad \text{with} \quad \tau_{EHD} = \frac{\mu_2(1+\lambda)}{\epsilon_2 E_0^2}, \quad (4.66)$$

where fluids 1 and 2 represent the drop and the suspending liquid, respectively. We obtain  $A \approx 2.22 \text{ s}^{-1}$  using the experimental parameters for the drop of silicon oil ( $\rho_1 = 960 \text{ kg m}^{-3}$ ,  $\epsilon_1/\epsilon_0 = 2.8$ ,  $\sigma_1 = 1.4 \times 10^{-12} \text{ S m}$ ,  $\mu_1 = 0.048 \text{ Pas}$ ) suspended in castor oil ( $\rho_2 = 961 \text{ kg m}^{-3}$ ,  $\epsilon_2/\epsilon_0 = 4.6$ ,  $\sigma_2 = 4.4 \times 10^{-11} \text{ S m}$ ,  $\mu_2 = 0.69 \text{ Pas}$ ) under an electric field of  $E_0 = 4 \text{ kV cm}^{-1}$  and a surface tension  $\gamma = 4.5 \text{ mN m}^{-1}$ .

The LT does predict a threshold  $Ca_E$ , which increases with viscosity ratio. According to the Num-LSA, which can be only performed for  $\lambda = 1$ , the interface is always unstable. However, the growth rate is vanishingly small at low  $Ca_E$  and the instability may not develop on the time-scale of the experiment, which is on the order of 1 s. Indeed, only above  $Ca_E \sim 1$  does the instability grow at rate faster than  $1 \text{ s}^{-1}$ . Increasing the viscosity ratio further slows down the growth of the instability, and suggests that streaming would not be observed for viscosity ratios greater than one, in qualitative agreement with the experiment. Finally, we note that while the present study focuses on planar interfaces, the equatorial streaming instability in drops occurs on a curved surface and the effects of base-state interfacial curvature on the instability remain unknown.

## 4.8 Conclusions

We have presented a theoretical and numerical model in two dimensions to study the dynamics of an interface separating two immiscible fluid layers subject to a tangential electric field and a stagnation point flow. We performed a local linear stability analysis in the vicinity of the stagnation point, which was able to recover the previous results of [104] in the absence of the background flow, and of [189] in the absence of the electric field and in the limit of zero inertia. Our local theory was complemented by a numerical analysis using the boundary element method, which was also used to perform a numerical normal-mode linear stability analysis based on the complete Melcher-Taylor leaky dielectric model including charge convection. Our results show that charge convection plays a significant role in determining the dynamics of the system by altering the dominant unstable mode, in which it was shown to have a stabilizing effect. Further, we explored the dynamics of the system far from equilibrium using transient nonlinear numerical simulations and demonstrated how the coupling of flow and interfacial charge dynamics in the dominant unstable mode gives rise to strongly nonlinear effects such as the formation of high-curvature tips and of charge density shocks.

In this study, the convergent flow and the electric field were assumed to be independently applied. This differs from the case of the equatorial EHD instability in drops [20, 194], where the flow is also generated by the electric field. In spite of this simplification, our analysis provides valuable insights into the underlying mechanisms responsible for the EHD equatorial streaming such as the evolution of the convergent line instability and the emergence of strong charge gradients. A more detailed discussion of the relevance of the present work to describe equatorial instabilities in liquid drops is provided in Appendix 4.7. Extensions of the present study could include considering the effect of the viscosity contrast ( $\lambda \neq 1$ ) and of equilibrium surface curvature on the behavior of the system. Further attempts to improve the accuracy of the numerical simulations may involve implementation of shock capturing schemes for the solution of the charge conservation equation, as well as surface reparametrization schemes for handling

extreme local deformations.

## **4.9 Acknowledgements**

Chapter 4 is primarily based on the material published in *Journal of Fluid Mechanics*, authored by Mohammadhossein Firouznia, Michael J. Miksis, Petia M. Vlahovska and David Saintillan [57]. The dissertation author was the primary researcher and author of this paper and performed numerical simulations and worked on theoretical modeling.

The authors gratefully acknowledge funding from National Science Foundation Grants CBET-1704996 (P.V. and M.M.) and CBET-1705377 (D.S.).

## Chapter 5

# Electrohydrodynamic flows in viscous drops

A weakly conducting liquid droplet immersed in another leaky dielectric liquid can exhibit rich dynamical behaviors under the effect of an applied electric field. Depending on material properties and field strength, the nonlinear coupling of interfacial charge transport and fluid flow can trigger electrohydrodynamic instabilities that lead to shape deformations and complex dynamics. We present a spectral boundary integral method to simulate droplet electrohydrodynamics in a uniform electric field. All physical variables, such as drop shape and interfacial charge density, are represented using spherical harmonic expansions. In addition to its exponential accuracy, the spectral representation affords a nondissipative dealiasing method required for numerical stability. A comprehensive charge transport model, valid under a wide range of electric field strengths, accounts for charge relaxation, Ohmic conduction, and surface charge convection by the flow. A shape reparametrization technique enables the exploration of significant droplet deformation regimes. For low-viscosity drops, the convection by the flow drives steep interfacial charge gradients near the drop equator. This introduces numerical ringing artifacts that we treat via a weighted spherical harmonic expansion, resulting in solution convergence. The method and simulations are validated against experimental data and analytical predictions in the axisymmetric Taylor and Quincke electroration regimes.

## 5.1 Introduction

A wide range of engineering applications involve liquid drops immersed in another fluid while subject to an applied electric field. Some examples include ink-jet printing [8], electrospraying [52], and microfluidic devices and pumps [93]. These systems exhibit rich dynamics due to the electric field and fluid flow coupling. When an interface separating two immiscible fluids is subject to an otherwise uniform electric field, the electric field undergoes a jump across the interface due to the mismatch in material properties. This discontinuity in the electric field induces electric stresses that can deform the interface and drive the fluid into motion.

We are interested in leaky dielectric liquids such as oils, which serve as poor conductors. Unlike electrolyte solutions where diffuse Debye layers affect the system's dynamics, leaky dielectrics are characterized by the absence of diffuse Debye layers [143]. The free charges instead concentrate on the interfaces between different phases in the system. Consequently, the electric field acting on the interfacial charge creates electric stresses along the normal and tangential directions, which cause deformations and fluid motion. Surface tension has a stabilizing effect in general, trying to restore the equilibrium shape. Melcher and Taylor developed a framework for studying electrohydrodynamic phenomena in leaky dielectric systems, known as the leaky dielectric model (LDM) [103]. Central to their work is a charge conservation model that describes a balance between Ohmic fluxes from the bulk, interfacial charge convection, and finite charge relaxation. It was previously shown that LDM can be derived asymptotically from electrokinetic models in the limit of strong electric fields and thin Debye layers [148, 112].

This work focuses on the dynamics of a leaky dielectric drop immersed in another dielectric fluid under a uniform DC electric field. This canonical problem has been a long-standing research problem in electrohydrodynamics. In his pioneering work, Taylor [176] formulated a small-deformation theory for an isolated drop based on LDM and could predict oblate and prolate steady shapes depending on the material properties. While Taylor's theory

shows good agreement with experimental data in the limit of vanishing electric capillary number  $Ca_E$  (ratio of electric to capillary forces), the discrepancy is significant at larger values of  $Ca_E$ . Therefore, other researchers attempted to extend Taylor's work by accounting for second-order effects in  $Ca_E$  [2], considering spheroidal drops [201, 205], including inertial effects [91] and interfacial charge convection [158, 50, 76, 40].

A variety of computational models have been developed to study drop dynamics under strong electric fields at finite deformations, a problem untractable using analytical theories. In the limit of negligible inertia, boundary integral equations can be used to formulate and solve the coupled electrohydrodynamic problem. Sherwood was the first to develop a boundary element method for an axisymmetric drop in an equiviscous system and applied it to capture breakup modes in prolate drops [157]. His original work was subsequently extended to study drop pair interaction [10] and to cover a wider range of fluid and electric parameters [90]. These earlier attempts used a simplified boundary condition for the electric problem, which neglected transient charge relaxation and interfacial charge convection by the flow. These two effects have recently been shown to play a significant role in drop dynamics and deformations [40]. Lanauze et al. [92] and Das and Saintillan [39] recently addressed this problem and developed axisymmetric and three-dimensional boundary element methods based on the full Melcher-Taylor LDM. The effect of charge convection was specifically addressed in [39], where it was shown to be responsible for Quincke electroration. These methods, however, were found to lack accuracy and stability in the regime of strong electric fields. Other numerical approaches have been used to study drop electrohydrodynamics, including immersed boundary [79], level set [15, 180], and finite element methods [51, 49, 171]. More recently, finite element simulations [34, 195] were also used to investigate electrohydrodynamic instabilities such as tip and equatorial streaming in drops under strong electric fields. These latter techniques all include finite fluid inertia and, with few exceptions [180], do not treat the drop surface as a sharp interface.

Improved accuracy within the boundary integral framework can be achieved using spectral methods, which rely on expansions of the shape and interfacial variables based on spherical

harmonics. Such methods were recently developed to simulate electrohydrodynamics of lipid vesicles [191] and also extended to the case of individual drops and drop pairs [165, 163, 166]. These studies, however, all neglected charge relaxation and charge convection and were thus restricted to weak electric fields. Accurately capturing charge convection is especially challenging as it nonlinearly couples fluid flow and charge transport on a deformed interface. It can result in spurious aliasing errors with negative consequences for accuracy and stability. This work addresses this challenge and presents a spectral boundary integral method for the electrohydrodynamics of deformable liquid drops based on the complete Melcher–Taylor LDM. Interfacial charge convection is rigorously accounted for, and dealiasing and reparametrization techniques are implemented to improve accuracy and stability and enable long-time simulations.

The chapter is organized as follows. We define the problem and discuss the governing equations and boundary conditions in Sec. 5.2.1, along with their non-dimensionalization in Sec. 5.2.2. Sec. 5.2.3 presents the integral form of the governing equations and boundary conditions used in developing the boundary integral method. We discuss different aspects of the numerical method in Sec. 5.3: the spectral representation of all variables in terms of spherical harmonics is discussed in 5.3.1, followed by details of the dealiasing method in Sec. 5.3.2. Next, in Sec. 5.3.3, we summarize the numerical integration methods used in this study and correction methods to ensure charge neutrality and incompressibility in Sec. 5.3.4. As explained in Sec. 5.3.5, we also use a reparametrization method to improve the numerical stability in simulations where the drop undergoes significant deformations. In Sec. 5.3.6, we discuss the overall convergence of our numerical method as well as the limitations of the time step size. We test and validate our computational model by applying it to a wide range of dynamical behaviors, such as the axisymmetric Taylor regime under weak electric fields in Sec. 5.4.1, and Quincke electrorotation under stronger electric fields in Sec. 5.4.2. We also investigate the dynamics of low-viscosity drops in Sec. 5.4.3, where charge convection plays an important role. Finally, we discuss our conclusions and possible extensions of our work in Sec. 5.5.

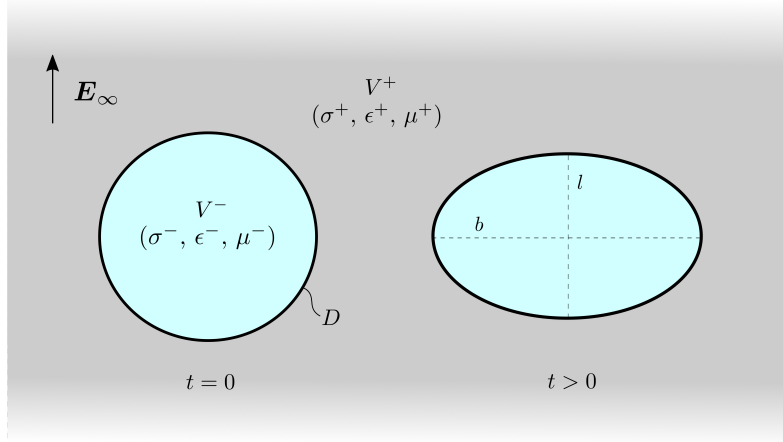


**Figure 5.1.** Problem definition: a leaky dielectric drop with  $(\sigma^-, \epsilon^-, \mu^-)$  is suspended in another leaky dielectric fluid with  $(\sigma^+, \epsilon^+, \mu^+)$  and subject to an external electric field  $\mathbf{E}_\infty$ . The drop deforms and diverges from its initially spherical shape.

## 5.2 Problem definition

### 5.2.1 Governing equations

We consider a neutrally buoyant drop of a fluid occupying volume  $V^-$  immersed in an infinite body of another fluid  $V^+$  while subject to a uniform electric field  $\mathbf{E}_\infty = E_\infty \hat{\mathbf{e}}_z$  as depicted schematically in Fig. 5.1. The interface  $D$  separates the two fluid media, and the surface unit normal  $\mathbf{n}(\mathbf{x})$  is pointed towards the suspending fluid. Initially, the drop is uncharged and spherical with radius  $r_0$ . The material properties, namely the dielectric permittivities, electric conductivities, and dynamic viscosities, are denoted by  $(\epsilon^\pm, \sigma^\pm, \mu^\pm)$  inside and outside the drop, respectively. Under the Taylor–Melcher leaky dielectric model [176], any net charge in the system appears on the interface  $D$ , and the bulk of the fluids remain electroneutral. Therefore, the electric potential is harmonic in the bulk:

$$\nabla^2 \varphi^\pm(\mathbf{x}) = 0, \quad \mathbf{x} \in V^\pm. \quad (5.1)$$

Far away from the interface, the electric field  $\mathbf{E} = -\nabla\varphi$  tends to the applied electric field:

$$\mathbf{E}^+ \rightarrow \mathbf{E}_\infty = E_\infty \hat{\mathbf{e}}_z, \quad \text{as } |\mathbf{x}| \rightarrow \pm\infty. \quad (5.2)$$

While the tangential component of the electric field is continuous across the interface, its normal component undergoes a jump due to the mismatch in material properties:

$$\mathbf{n} \times \llbracket \mathbf{E} \rrbracket = \mathbf{0}, \quad \mathbf{x} \in D. \quad (5.3)$$

We define the operator  $\llbracket \mathcal{F} \rrbracket := \mathcal{F}^+ - \mathcal{F}^-$  as the jump in any variable  $\mathcal{F}$  across the interface  $D$ . A surface charge density develops at the interface and follows Gauss's law,

$$q(\mathbf{x}) = \mathbf{n} \cdot \llbracket \epsilon \mathbf{E} \rrbracket, \quad \mathbf{x} \in D. \quad (5.4)$$

The surface charge evolves due to Ohmic currents from the bulk and convective currents on the interface. Consequently, it satisfies the conservation equation:

$$\partial_t q + \mathbf{n} \cdot \llbracket \sigma \mathbf{E} \rrbracket + \nabla_s \cdot (q\mathbf{u}) = 0, \quad \mathbf{x} \in D, \quad (5.5)$$

where  $\nabla_s = (\mathbf{I} - \mathbf{nn}) \cdot \nabla$  is the surface gradient operator and  $\mathbf{u}$  is the fluid velocity.

Neglecting the effect of inertia and gravity, the velocity and pressure fields satisfy the Stokes and continuity equations:

$$\mu^\pm \nabla^2 \mathbf{u}^\pm - \nabla p^\pm = \mathbf{0}, \quad \nabla \cdot \mathbf{u}^\pm = 0, \quad \mathbf{x} \in V^\pm. \quad (5.6)$$

The velocity vector is continuous across the interface and vanishes far from it:

$$\llbracket \mathbf{u}(\mathbf{x}) \rrbracket = \mathbf{0}, \quad \mathbf{x} \in D, \quad (5.7)$$

$$\mathbf{u}^+(\mathbf{x}) \rightarrow \mathbf{0}, \quad \text{as } |\mathbf{x}| \rightarrow \infty. \quad (5.8)$$

The balance of interfacial forces requires that the jump in hydrodynamic and electric tractions across the interface balance capillary forces:

$$\llbracket \mathbf{f}^H \rrbracket + \llbracket \mathbf{f}^E \rrbracket = \gamma(\nabla_s \cdot \mathbf{n})\mathbf{n}, \quad \mathbf{x} \in D. \quad (5.9)$$

We neglect Marangoni effects due to variations in surface tension,  $\nabla_s \gamma = \mathbf{0}$ . Hydrodynamic and electric tractions are expressed in terms of the Newtonian and Maxwell stress tensors, respectively:

$$\mathbf{f}^H = \mathbf{n} \cdot \mathbf{T}^H, \quad \mathbf{T}^H = -p\mathbf{I} + \mu(\nabla\mathbf{u} + \nabla\mathbf{u}^T), \quad (5.10)$$

$$\mathbf{f}^E = \mathbf{n} \cdot \mathbf{T}^E, \quad \mathbf{T}^E = \epsilon(\mathbf{E}\mathbf{E} - \frac{1}{2}E^2\mathbf{I}). \quad (5.11)$$

The jump in electric tractions can be decomposed into tangential and normal components as

$$\llbracket \mathbf{f}^E \rrbracket = \llbracket \epsilon E^n \rrbracket \mathbf{E}^t + \frac{1}{2} \llbracket \epsilon(E^{n2} - E^{t2}) \rrbracket \mathbf{n} = q\mathbf{E}^t + \llbracket p^E \rrbracket \mathbf{n}, \quad (5.12)$$

where  $p^E = \epsilon(E^{n2} - E^{t2})/2$  is the electric pressure [90]. The first term on the right-hand side represents the tangential electric stresses in leaky dielectrics, and it vanishes when both fluids are either perfect dielectrics or perfect conductors.

## 5.2.2 Non-dimensionalization

For the system described above, a dimensional analysis yields five dimensionless groups, three of which characterize the mismatch of material properties in the drop and the suspending fluid:

$$R = \frac{\sigma^+}{\sigma^-}, \quad Q = \frac{\epsilon^-}{\epsilon^+}, \quad \lambda = \frac{\mu^-}{\mu^+}. \quad (5.13)$$

The limits of  $\lambda \rightarrow 0$  and  $\infty$  correspond to a bubble and a rigid particle, respectively. The remaining dimensionless groups describe the system's dynamics and can be obtained by comparing the characteristic time scales in the problem. First, note that the response of each fluid phase to Ohmic conduction is characterized by the charge relaxation time:

$$\tau_c^\pm = \frac{\epsilon^\pm}{\sigma^\pm}. \quad (5.14)$$

The product  $RQ = \tau^-/\tau^+$  is the ratio of the charge relaxation times in the two fluids and plays an important role in the dynamics of the drop [39]. The polarization time for a rigid sphere under an applied electric field is the Maxwell–Wagner relaxation time

$$\tau_{\text{MW}} = \frac{\epsilon^- + 2\epsilon^+}{\sigma^- + 2\sigma^+} = \frac{R(Q+2)}{1+2R} \tau_c^+, \quad (5.15)$$

which provides an approximate timescale for polarization of the drop. The accumulation of free charges on the interface creates electric forces that drive the fluid into motion on the electrohydrodynamic time scale

$$\tau_{\text{EHD}} = \frac{\mu^+}{\epsilon^+ E_\infty^2}. \quad (5.16)$$

Deformations away from the equilibrium spherical shape relax under the effect of surface tension on the capillary time scale

$$\tau_\gamma = \frac{\mu^+ r_0}{\gamma}. \quad (5.17)$$

By taking the ratios of these time scales, the two remaining dimensionless groups can be defined as

$$\text{Ca}_E = \frac{\tau_\gamma}{\tau_{\text{EHD}}} = \frac{\epsilon E_\infty^2 r_0}{\gamma}, \quad \text{Ma} = \frac{\tau_{\text{EHD}}}{\tau_{\text{MW}}} = \frac{\mu^+}{\tau_{\text{MW}} \epsilon^+ E_\infty^2}. \quad (5.18)$$

The electric capillary number  $\text{Ca}_E$  compares electric forces versus capillary forces, while the Mason number  $\text{Ma}$  characterizes the importance of charge conduction against surface charge convection. Alternatively, we can combine  $\text{Ca}_E$  and  $\text{Ma}$  to construct a third dimensionless group  $\text{Ca}_{\text{MW}}$  to be independent of the electric field:

$$\text{Ca}_{\text{MW}} = \frac{\tau_\gamma}{\tau_{\text{MW}}} = \frac{\mu^+(1+\lambda)r_0}{\gamma\tau_{\text{MW}}} = (1+\lambda)\text{Ca}_E\text{Ma}. \quad (5.19)$$

For a given set of material properties, changing  $\text{Ca}_{\text{MW}}$  corresponds to varying the drop radius  $r_0$ .

We scale the governing equations and boundary conditions using length scale  $r_0$ , time scale  $\tau_{\text{MW}}$ , pressure scale  $\epsilon^+ E_\infty^2$ , and the characteristic electric potential  $E_\infty r_0$ . In the remainder of this manuscript, all governing equations and boundary conditions are dimensionless, and results are presented in terms of the corresponding dimensionless variables.

### 5.2.3 Boundary integral formulation

The electric problem is formulated in integral form based on the solution to Laplace's equation as [157, 10, 90]

$$\varphi(\mathbf{x}_0) = -\mathbf{x}_0 \cdot \mathbf{E}_\infty - \int_D \mathbf{n} \cdot \llbracket \nabla \varphi(\mathbf{x}) \rrbracket \mathcal{G}(\mathbf{x}_0; \mathbf{x}) \, ds(\mathbf{x}), \quad \text{for } \mathbf{x}_0 \in V^\pm, D, \quad (5.20)$$

where the evaluation point  $\mathbf{x}_0$  can be anywhere in space, and  $\mathbf{x}$  denotes the integration point on the interface. The free-space Green's function for Laplace's equation,  $\mathcal{G}(\mathbf{x}_0; \mathbf{x})$ , captures the

electric potential due to a point charge in an unbounded domain as

$$\mathcal{G}(\mathbf{x}_0; \mathbf{x}) = \frac{1}{4\pi r}, \quad \text{where } \mathbf{r} = \mathbf{x}_0 - \mathbf{x}, \quad r = |\mathbf{r}|. \quad (5.21)$$

Taking the gradient of Eq. (5.20) with respect to  $\mathbf{x}_0$  and using Gauss's law (5.4), we derive an integral equation for the jump in the normal electric field as a function of the surface charge distribution:

$$\int_D \llbracket E^n(\mathbf{x}) \rrbracket [\mathbf{n}(\mathbf{x}_0) \cdot \nabla_0 \mathcal{G}] ds(\mathbf{x}) - \frac{1+Q}{2(1-Q)} \llbracket E^n(\mathbf{x}_0) \rrbracket = E_\infty^n(\mathbf{x}_0) - \frac{q(\mathbf{x}_0)}{1-Q}, \quad \text{for } \mathbf{x}_0 \in D. \quad (5.22)$$

For a given charge distribution  $q(\mathbf{x})$ , Eq. (5.22) can determine  $\llbracket E^n(\mathbf{x}) \rrbracket$ , from which  $E^{n+}$  and  $E^{n-}$  follow as

$$E^{n+}(\mathbf{x}) = \frac{q(\mathbf{x}) - Q \llbracket E^n(\mathbf{x}) \rrbracket}{1-Q}, \quad E^{n-}(\mathbf{x}) = \frac{q(\mathbf{x}) - \llbracket E^n(\mathbf{x}) \rrbracket}{1-Q}. \quad (5.23)$$

The tangential electric field  $\mathbf{E}^t(\mathbf{x}) = -\nabla_s \varphi(\mathbf{x})$  can be computed by differentiation of the electric potential (5.20) along the tangential direction. The interfacial jump in electric tractions  $\llbracket \mathbf{f}^E \rrbracket$  follows from Eq. (5.12) based on the tangential and normal electric fields calculated at every point on the interface. This can be used to determine the jump in hydrodynamic tractions  $\llbracket \mathbf{f}^H \rrbracket$  using the dynamic boundary condition (5.9) as

$$\llbracket \mathbf{f}^H \rrbracket = -\llbracket \mathbf{f}^E \rrbracket + \text{Ca}_E^{-1} (\nabla_s \cdot \mathbf{n}) \mathbf{n}, \quad (5.24)$$

which enters the calculation of the velocity field, as explained next.

The flow problem is also recast into a boundary integral form as [133, 125]

$$\begin{aligned} \mathbf{u}(\mathbf{x}_0) = & -\frac{1}{4\pi \text{Ma}(1+\lambda)} \int_D \llbracket \mathbf{f}^H(\mathbf{x}) \rrbracket \cdot \mathbf{G}(\mathbf{x}_0; \mathbf{x}) ds(\mathbf{x}) \\ & + \frac{1-\lambda}{4\pi(1+\lambda)} \int_D \mathbf{u}(\mathbf{x}) \cdot \mathbf{T}(\mathbf{x}_0; \mathbf{x}) \cdot \mathbf{n}(\mathbf{x}) ds(\mathbf{x}), \quad \text{for } \mathbf{x}_0 \in D. \end{aligned} \quad (5.25)$$

Here,  $\mathbf{G}$  is the free-space Green's function for the Stokeslet or flow due to a unit point force in an unbounded domain, and  $\mathbf{T}$  is the corresponding stress tensor:

$$\mathbf{G}(\mathbf{x}_0; \mathbf{x}) = \frac{\mathbf{I}}{r} + \frac{\mathbf{r}\mathbf{r}}{r^3}, \quad \mathbf{T}(\mathbf{x}_0; \mathbf{x}) = 6\frac{\mathbf{r}\mathbf{r}\mathbf{r}}{r^5}. \quad (5.26)$$

Note that the integral equations (5.20), (5.22) and (5.25) exhibit singular behaviors of different orders as  $\mathbf{x}$  approaches  $\mathbf{x}_0$ . This is due to the singularity of the Green's function for Laplace's (5.21) and Stokes equations (5.26). Conventional quadrature schemes have poor accuracy in the presence of singular integrands and may not converge by increasing the level of discretization. Therefore, accurate numerical integration requires special treatment of the singularities, which we will discuss in Sec. 5.3.3.

### 5.3 Numerical methods

We solve Eqs. (5.22) and (5.25) by building upon a spectral boundary integral method introduced by [207]. This method was also previously applied to study vesicle dynamics under shear and extensional flows [22, 24] as well as flows of confined red blood cells [25, 23, 60]. All variables, including the interfacial shape, velocity, and charge, are represented using truncated series of spherical harmonic expansions as discussed in Sec. 5.3.1. Nonlinear operations, geometrical quantities (such as mean curvature), and spatial derivatives are computed accurately using a nondissipative dealiasing method discussed in Sec. 5.3.2. The boundary integrals are computed using a quadrature scheme for the surface collocation points, with a special treatment for the singular integrands, as summarized in Sec. 5.3.3. Any changes to the volume and net charge of the drop due to numerical errors are corrected as explained in Sec. 5.3.4 to ensure numerical stability over long simulation times. In addition, we adopt a reparameterization technique in Sec. 5.3.5 to minimize the high-frequency component of the interfacial shape, which improves the stability of the numerical method for cases with significant deformations. We

provide a convergence analysis for our numerical method in Sec. 5.3.6 and discuss the time step size restrictions for our time marching scheme. The code associated with the methods and simulations in this article is publicly available at [https://github.com/mfirouzn/EHD\\_Drop\\_3D](https://github.com/mfirouzn/EHD_Drop_3D) [55].

At  $t = 0$ , the drop is uncharged with a spherical shape. The numerical algorithm used in this study follows that of [39], [58], and [57]. We perform the following steps at every time iteration:

1. Given the current charge distribution  $q(\mathbf{x})$  and shape of the interface, compute  $\llbracket E^n(\mathbf{x}) \rrbracket$  by numerically inverting (5.22) using GMRES [138]. From  $\llbracket E^n(\mathbf{x}) \rrbracket$ , we obtain  $E^{n+}(\mathbf{x})$  and  $E^{n-}(\mathbf{x})$  via (5.23).
2. Determine the potential  $\varphi$  along the interface by evaluating (5.20).
3. Differentiate the surface potential numerically along the interface in order to obtain the tangential electric field  $\mathbf{E}^t = -\nabla_s \varphi$ .
4. Knowing both components of the electric field, determine the jump in the electric traction  $\llbracket \mathbf{f}^E \rrbracket$  and use it to obtain  $\llbracket \mathbf{f}^H \rrbracket$  using (5.24).
5. Solve for the interfacial velocity using the Stokes boundary integral equation (5.25).
6. Compute  $\partial_t q$  via (5.5) and update the charge distribution.
7. Update the position of the interface by advecting the grid with the normal component of the interfacial velocity:  $\partial_t \mathbf{x} = (\mathbf{u} \cdot \mathbf{n})\mathbf{n}$ .
8. Apply corrections to the shape and charge distribution to ensure incompressibility and charge neutrality, as discussed in Sec. 5.3.4.
9. Reparametrize the interfacial shape following the method discussed in Sec. 5.3.5 to minimize high-frequency components in the spherical harmonic expansion.

The algorithm above describes a single time-marching step. In practice, we use a second-order Runge-Kutta method as discussed in Sec. 5.3.6.

### 5.3.1 Surface representation

The shape of the drop is assumed to be smooth and of spherical topology. Therefore, the surface is parameterized by a truncated series of spherical harmonic expansion from a rectangular domain  $\mathbb{S}^2 = \{(\theta, \phi) | \theta \in (0, \pi), \phi \in [0, 2\pi)\}$  to  $\mathbb{R}^3$ :

$$\mathbf{x}(\theta, \phi) = \sum_{n=0}^{N-1} \sum_{m=0}^n \bar{P}_n^m(\cos \theta) (\mathbf{a}_{nm} \cos m\phi + \mathbf{b}_{nm} \sin m\phi), \quad (5.27)$$

where  $\theta$  and  $\phi$  are the latitude and longitude angles, and  $\mathbf{s} = \{\mathbf{a}_{nm}, \mathbf{b}_{nm}\}$  are the coefficients of the expansion in a compact form [17]. The representation above yields  $N^2$  spherical harmonic modes per each component of  $\mathbf{x}$  (total of  $3N^2$  modes). The normalized associated Legendre polynomials of degree  $n$  ( $n = 0, 1, 2, \dots$ ) and order  $m$  ( $m \leq n$ ) are defined as

$$\bar{P}_n^m(\eta) = \frac{1}{2^n n!} \sqrt{\frac{(2n+1)(n-m)!}{2(n+m)!}} (1-\eta^2)^{m/2} \frac{d^{n+m}}{d\eta^{n+m}} (\eta^2-1)^n, \quad (5.28)$$

and satisfy the orthogonality condition

$$\int_{-1}^1 \bar{P}_n^m(\eta) \bar{P}_{n'}^m(\eta) d\eta = \delta_{nn'}. \quad (5.29)$$

Similarly, the surface charge distribution is represented as

$$q(\theta, \phi) = \sum_{n=0}^{N-1} \sum_{m=0}^n \bar{P}_n^m(\cos \theta) (\tilde{a}_{nm} \cos m\phi + \tilde{b}_{nm} \sin m\phi). \quad (5.30)$$

The rectangular domain  $\mathbb{S}^2$  is discretized based on the roots of the Legendre polynomial  $P_N(\cos \theta)$  along  $\theta$ , and uniformly along  $\phi$ . Forward and backward transformations are performed using

the SPHEREPACK library [1, 172]. Partial derivatives of a given distribution can be computed using recurrence relations for the derivatives of the associated Legendre polynomials [1, 132]. Besides the spectral accuracy, the spherical harmonic representation allows for nondissipative dealiasing, which improves the numerical stability of the simulations [207].

A local coordinate system is constructed at every point  $\mathbf{x}(\theta, \phi)$  on the surface of the drop, using two tangent vectors  $\mathbf{a}_{1,2}$  and the unit normal  $\mathbf{a}_3$ :

$$\mathbf{a}_1 = \partial_\theta \mathbf{x}, \quad \mathbf{a}_2 = \partial_\phi \mathbf{x}, \quad \mathbf{a}_3 = \mathbf{n} = \frac{\mathbf{a}_1 \times \mathbf{a}_2}{|\mathbf{a}_1 \times \mathbf{a}_2|}. \quad (5.31)$$

Consequently, the first and second fundamental forms of the drop surface have the following components:

$$L_{ij} = \mathbf{a}_i \cdot \mathbf{a}_j, \quad \text{and} \quad B_{ij} = \mathbf{a}_{i,j} \cdot \mathbf{n}, \quad (i, j = 1, 2), \quad (5.32)$$

which will be used in the subsequent derivations. Given a scalar function  $f(\theta, \phi)$  on the surface  $D$  defined by the parameterization introduced in (5.27), the surface gradient  $\nabla_s f$  is

$$\nabla_s f = \left( \frac{L_{22} \mathbf{a}_1 - L_{12} \mathbf{a}_2}{W^2} \right) \partial_\theta f + \left( \frac{L_{11} \mathbf{a}_2 - L_{12} \mathbf{a}_1}{W^2} \right) \partial_\phi f, \quad (5.33)$$

where  $W = (\det \mathbf{L})^{1/2}$  is the area element. Similarly, the surface divergence of a vector field  $\mathbf{v}(\theta, \phi)$  can be expressed as

$$\nabla_s \cdot \mathbf{v} = \left( \frac{L_{22} \mathbf{a}_1 - L_{12} \mathbf{a}_2}{W^2} \right) \cdot \partial_\theta \mathbf{v} + \left( \frac{L_{11} \mathbf{a}_2 - L_{12} \mathbf{a}_1}{W^2} \right) \cdot \partial_\phi \mathbf{v}. \quad (5.34)$$

In this study, we consider a drop of an incompressible fluid. In the absence of Marangoni effects, the capillary stress is a function of the mean curvature  $H$ :

$$H = \frac{1}{2} \text{Tr}(\mathbf{L}^{-1} \mathbf{B}) = \frac{1}{2} \left( \frac{L_{22} B_{11} - 2L_{12} B_{12} + L_{11} B_{22}}{W^2} \right). \quad (5.35)$$

### 5.3.2 Aliasing errors

Samples of different functions may become indistinguishable on a discrete grid by so-called aliasing [28]. This means, for instance, that a high-frequency spherical harmonic basis function may be aliased to lower frequencies and cause numerical instability in the simulations. Nonlinear operations and differentiation broaden the deformation and charge distribution spectra on a drop. As a result, the energy is moved to frequencies not resolved by the grid resolution and may alias to the resolved frequencies [28]. Therefore, it is physically consistent with the discretization level to remove the corresponding energy from the solution.

Nonlinear operations that are susceptible to aliasing in our simulations include the calculation of mean curvature, electrical stress, convective charge flux, and quadrature. We use a mesh with finer resolution  $M > N$  in the simulations to prevent aliasing errors and filter the solution following any nonlinear manipulation [207]. Our numerical experiments show that  $M/N = 2$  is sufficient for lower-order and polynomial nonlinearities. For higher-order and non-polynomial nonlinear manipulations such as those incurred in calculating mean curvature and charge convection, we use an adaptive algorithm that follows [132]. Given a function  $\mathbf{f}^M$  sampled over an  $M$ -grid ( $2M^2$  points in physical space and  $M^2$  spherical harmonic modes), one can interpolate the distribution on a finer  $P$ -grid ( $P/M = u_f > 1$ ) by upsampling:

$$\mathbf{s}^P = \{\mathbf{a}_{nm}, \mathbf{b}_{nm}\}^P = \begin{cases} \{\mathbf{a}_{nm}, \mathbf{b}_{nm}\}^M, & \text{for } n \leq M \text{ and } 0 \leq m \leq n, \\ 0, & \text{for } n > M. \end{cases}$$

The upsampling factor  $u_f$  can be determined based on the desired tolerance. Fig. 5.2 shows how the error in the mean curvature decays as a function of the finer grid resolution  $P$  for oblate and prolate spheroids representing typical drop shapes subject to an electric field.

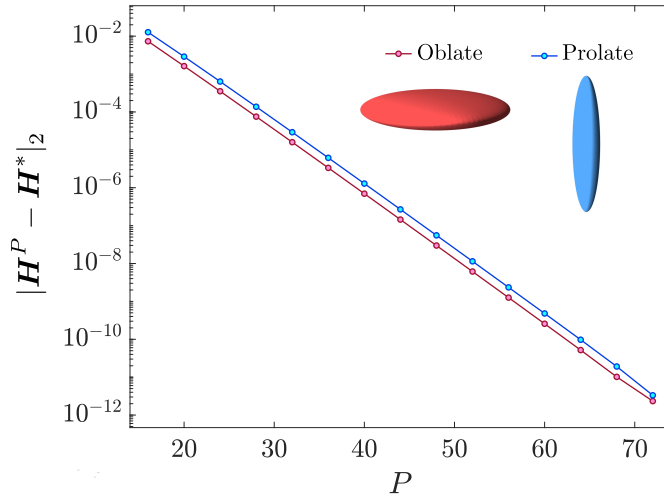


**Figure 5.2.** Error in the mean curvature as a function of the number of modes used in the upsampled  $P$ -space. Two ellipsoids with  $l/b = 5$  (prolate) and  $l/b = 0.2$  (oblate) are investigated, representing the typical shapes of a drop due to EHD flows with large deformations.  $H^*$  is the mean curvature computed on the finest upsampled grid and is chosen as a surrogate for the exact curvature values.

### 5.3.3 Numerical integration

This section summarizes the numerical integration scheme used in this study, which follows that used by [207]. The boundary integrals in (5.20), (5.22), and (5.25) can be written in the general form

$$I(\mathbf{x}_0) = \int_D K(\mathbf{x}, \mathbf{x}_0) f(\mathbf{x}) ds(\mathbf{x}) = \int_{\mathbb{S}^2} K(\mathbf{x}(\theta, \phi), \mathbf{x}_0) f(\mathbf{x}(\theta, \phi)) J(\mathbf{x}(\theta, \phi)) \sin \theta d\theta d\phi, \quad (5.36)$$

where  $f(\theta, \phi)$  is a smooth scalar function over surface  $D$ , and  $K$  is the kernel containing the Green's function for Stokes or Laplace's equations.

The approximate spacing of a mesh with  $N \times 2N$  points is  $h = \sqrt{A/2N^2}$ , where  $A$  is the drop surface area. Due to the singular behavior of  $K$  as  $\mathbf{x}_0 \rightarrow \mathbf{x}$ , the drop surface  $D$  is divided into two regions where the integral  $I$  has different behaviors. Following the method of floating partition of unity [21, 200, 207], a local polar patch is considered centered around  $\mathbf{x}_0$ . For any point  $\mathbf{x}$  on  $D$ ,  $\rho(\mathbf{x}, \mathbf{x}_0)$  is defined as the distance along the great circle that connects  $\mathbf{x}$  to  $\mathbf{x}_0$  on  $\mathbb{S}^2$ .

In the next step, a mask function is defined based on this coordinate as

$$\eta(\rho) = \begin{cases} \exp\left(\frac{2e^{-1/t}}{t-1}\right), & \text{for } t = \rho/\rho_1 < 1, \\ 0 & \text{for } \rho \geq \rho_1, \end{cases}$$

where  $\rho_1$  is the cutoff radius. This representation allows for accurate calculation of the integral (5.36) as  $\eta$  is a smooth function.

Next, the surface integral (5.36) is split into two parts:

$$I = I_1 + I_2 = \int_D K(\mathbf{x}, \mathbf{x}_0) \eta(\rho(\mathbf{x}, \mathbf{x}_0)) f(\mathbf{x}) ds(\mathbf{x}) + \int_D K(\mathbf{x}, \mathbf{x}_0) [1 - \eta(\rho(\mathbf{x}, \mathbf{x}_0))] f(\mathbf{x}) ds(\mathbf{x}). \quad (5.37)$$

The integrand of  $I_1$  has support only inside the patch.

Using a transformation to the local polar coordinate system  $(\rho, \varphi)$ , we write:

$$I_1 = \int_0^{2\pi} \int_0^{\rho_1} K(\mathbf{x}, \mathbf{x}_0) \eta(\rho) f(\rho, \varphi) \sin \rho d\rho d\varphi, \quad (5.38)$$

where the integrand is finite and periodic in  $\varphi$ . The integral (5.38) is computed using Gauss quadrature along  $\rho$  from 0 to  $\rho_1$ , with a uniform mesh in  $\varphi$  from 0 to  $2\pi$ . We set the patch radius on the reference sphere to  $\rho_1 = \pi/\sqrt{N}$ , which means the patch radius is  $O(h^{1/2})$  in  $\mathbb{S}^3$ . Inside the patch,  $\sqrt{N}$  points are considered along  $\rho$ , and  $2\sqrt{N}$  points along  $\varphi$ . We note that the quadrature points inside the patch do not coincide with the surface mesh points. Therefore, bi-cubic spline interpolation is used to evaluate the coordinates and other functions at quadrature points of  $I_1$ . The error of singular integration with the mentioned choice of patch size is  $O(h^3)$  [200]. Higher-order accuracy can be achieved using a larger patch size at the expense of computational cost.

The second part of integral (5.37) is  $I_2$ , which has a smooth integrand. Therefore, it is

computed accurately as:

$$I_2 \approx \sum_{i=1}^N \sum_{j=1}^{2N} K(\mathbf{x}_{ij}, \mathbf{x}_0) \eta(\rho(\mathbf{x}_{ij}, \mathbf{x}_0)) f_{ij} J_{ij} w_{ij}, \quad (5.39)$$

where  $\mathbf{x}_{ij} = \mathbf{x}(\theta_i, \phi_j)$  are the quadrature points,  $w_{ij}$  are the corresponding weights and  $J_{ij}$  is the Jacobian of the transformation from  $\mathbb{S}^2$  to  $\mathbb{R}^3$ . The quadrature (5.39) converges exponentially with the mesh size  $h$ , using quadrature points with Gaussian and uniform distributions along the  $\theta$  and  $\phi$  directions, respectively. Further details on the numerical integration scheme can be found in [207].

### 5.3.4 Incompressibility and charge neutrality

We expect no change in the drop volume, as both fluid phases are incompressible. However, small changes in the volume occur due to numerical errors, which we correct by adjusting the shape of the drop along the normal direction [207]. In the reported simulations, the magnitude of these adjustments is smaller than  $10^{-8}r_0$  at every time step, where  $r_0$  is the initial drop radius. Similarly, the net charge (less than  $10^{-17}\epsilon E_0$ ) is subtracted from the surface charge distribution at every time step to ensure charge neutrality throughout the simulations. The mentioned corrections are especially important for long simulation times.

### 5.3.5 Reparametrization

The fluid-fluid interface of the drop evolves and deforms. During this process, there is no physical mechanism to inhibit in-plane distortions of the grid (i.e., depletion, aggregation, and skewness) since there is no bending rigidity, in-plane shear resistance, or surface inextensibility. High-frequency components of the spherical harmonic expansions thus grow, exacerbating aliasing errors and resulting in numerical instability. In addition to correcting aliasing errors, as explained in Sec. 5.3.2, one must develop a reparameterization strategy that ensures stable and

accurate simulations over long simulation times. Here, we use an algorithm that minimizes the high-frequency components in the spherical harmonic expansion of the surface parametrization. This method was introduced by Veerapenani et al. [192, 132] and improved by [164].

Consider an implicit representation of the interface as a smooth function  $F : \mathbb{R}^3 \mapsto \mathbb{R}$  such that  $F(\mathbf{x}) = 0$  for all  $\mathbf{x} \in D$  where  $D$  is the drop surface. The unit normal vector can be expressed as  $\mathbf{n} = \nabla F / |\nabla F|$  at every point on the surface. We define a quality metric  $E : \mathcal{X} \mapsto \mathbb{R}$  where  $\mathcal{X}$  is the space of smooth functions defined over  $D$ . Now, we can view the reparameterization problem as a minimization of  $E(\mathbf{x})$  subject to the constraint  $F(\mathbf{x}) = 0$  as

$$\min_{\mathbf{x} \in D} \{E(\mathbf{x})\} \text{ subject to } F(\mathbf{x}) = 0. \quad (5.40)$$

It can be shown that the solution to the problem above is

$$(\mathbf{I} - \mathbf{n}(\mathbf{x})\mathbf{n}(\mathbf{x})) \cdot \nabla E(\mathbf{x}) = \mathbf{0}, \quad \text{and } F(\mathbf{x}) = 0. \quad (5.41)$$

The choice of quality metric  $E(\mathbf{x})$  is not unique and could vary depending on the reparameterization strategy. [192] proposed an equivalent of the following quality metric:

$$E(\mathbf{x}) = \sum_{n=0}^{N-1} \sum_{m=0}^n \alpha_{nm} \left( |\mathbf{a}_{nm}|_2^2 + |\mathbf{b}_{nm}|_2^2 \right), \quad (5.42)$$

where  $|\mathbf{y}|_2$  is the  $L^2$  norm of vector  $\mathbf{y}$ , and  $\alpha_{nm}$  is the weight for  $(n, m)$ -th spherical harmonic.  $E$ , as defined in (5.42), can be viewed as the spectral energy of the parametrization. We aim to minimize the high-frequency part of  $\mathbf{x}$ . Therefore, the weights  $\alpha_{nm}$  must be small for low frequencies and larger for high frequencies. Here, we use the following perfect low-pass filter

$$\alpha_{nm} = \begin{cases} 1, & \text{for } n > N_{\text{cutoff}}, \\ 0, & \text{for } n \leq N_{\text{cutoff}}. \end{cases}$$

that was used [192, 164] to simulate vesicles and surfactant-laden drops and improved long-time simulations.  $N_{\text{cutoff}}$  is the cutoff frequency and is chosen adaptively based on the energy spectrum as

$$N_{\text{cutoff}} = \min\{k \in \mathbb{N}, 1 \leq k \leq N-1 \mid E_k/E_1 \leq P_{\text{cutoff}}\}, \quad (5.43)$$

where  $E_k = \sum_{n=k}^{N-1} \sum_{m=0}^n \alpha_{nm} (|\mathbf{a}_{nm}|_2^2 + |\mathbf{b}_{nm}|_2^2)$  and  $P_{\text{cutoff}}$  determines the fraction of modes we penalize ( $P_{\text{cutoff}} = 0.2$  in our simulations) [164].

We solve (5.41) by marching in pseudo-time  $\tau$  along the tangential direction at every point:

$$\partial_\tau \mathbf{x} + (\mathbf{I} - \mathbf{n}(\mathbf{x})\mathbf{n}(\mathbf{x})) \cdot \nabla E(\mathbf{x}) = \mathbf{0}, \quad \text{with } \mathbf{x}(\tau = 0) = \mathbf{x}_0. \quad (5.44)$$

However, following (5.44) the volume is not necessarily conserved. In addition, the charge distribution is distorted and hence not spectrally accurate. We use the method of [164] to address these challenges. We project the linear pseudo-velocity  $\partial_\tau \mathbf{x}$  along the latitudinal and longitudinal directions to obtain the angular pseudo-velocity  $(\partial_\tau \theta, \partial_\tau \phi)$ . This strategy comprises updates of the angular coordinates  $(\theta, \phi)$  for every point and uses the original spherical harmonic expansions for the shape and charge distribution to interpolate the updated distributions. Using the chain rule,

$$\partial_\tau \mathbf{x} = \frac{\partial \mathbf{x}}{\partial \theta} \frac{\partial \theta}{\partial \tau} + \frac{\partial \mathbf{x}}{\partial \phi} \frac{\partial \phi}{\partial \tau} = \mathbf{a}_1 \partial_\tau \theta + \mathbf{a}_2 \partial_\tau \phi. \quad (5.45)$$

Next, we project  $\partial_\tau \mathbf{x}$  along the tangential directions by taking inner products with  $\mathbf{a}_1$  and  $\mathbf{a}_2$ :

$$\partial_\tau \mathbf{x} \cdot \mathbf{a}_1 = |\mathbf{a}_1|^2 \partial_\tau \theta + \mathbf{a}_1 \cdot \mathbf{a}_2 \partial_\tau \phi, \quad (5.46)$$

$$\partial_\tau \mathbf{x} \cdot \mathbf{a}_2 = \mathbf{a}_1 \cdot \mathbf{a}_2 \partial_\tau \theta + |\mathbf{a}_2|^2 \partial_\tau \phi. \quad (5.47)$$

The solution to (5.46) and (5.47) is

$$\partial_\tau \boldsymbol{\theta} = \mathbf{L}^{-1} \mathbf{w}, \quad (5.48)$$

where  $\partial_\tau \boldsymbol{\theta} = \{\partial_\tau \theta, \partial_\tau \phi\}^T$  and  $\mathbf{w} = \{\partial_\tau \mathbf{x} \cdot \mathbf{a}_1, \partial_\tau \mathbf{x} \cdot \mathbf{a}_2\}^T$ , and  $\mathbf{L}$  is the surface metric defined

in (5.32). We update the angular coordinates of every grid point by marching explicitly in pseudo-time to obtain new angles  $(\theta^*, \phi^*)$ . Using the new angular coordinates, we interpolate the position and surface charge at every point based on the spherical harmonic expansions of the grid before reparametrization (at  $\tau = 0$ ):

$$\mathbf{x}^*(\theta^*, \phi^*) = \sum_{n=0}^{N-1} \sum_{m=0}^n \bar{P}_n^m(\cos \theta^*) \left( \mathbf{a}_{nm}^0 \cos m\phi^* + \mathbf{b}_{nm}^0 \sin m\phi^* \right), \quad (5.49)$$

$$q^*(\theta^*, \phi^*) = \sum_{n=0}^{N-1} \sum_{m=0}^n \bar{P}_n^m(\cos \theta^*) \left( \tilde{a}_{nm}^0 \cos m\phi^* + \tilde{b}_{nm}^0 \sin m\phi^* \right). \quad (5.50)$$

Finally, a forward (FSHT) and backward (BSHT) spherical harmonic transformation of  $\mathbf{x}^*$  and  $q^*$  yields distributions on a standard grid that is spaced uniformly along  $\phi$  and Gaussian along  $\theta$ :

$$\mathbf{x}^* \xrightarrow{\text{FSHT}} \{\mathbf{a}_{nm}, \mathbf{b}_{nm}\} \xrightarrow{\text{BSHT}} \mathbf{x}, \quad (5.51)$$

$$q^* \xrightarrow{\text{FSHT}} \{\tilde{a}_{nm}, \tilde{b}_{nm}\} \xrightarrow{\text{BSHT}} q. \quad (5.52)$$

Figure 5.3 shows the effect of reparametrization when a drop of system **S5** (see Table 5.1 for material properties) undergoes large prolate deformations when subject to  $(\text{Ca}_E, \text{Ma}) = (0.35, 5.75)$ . In the absence of reparametrization, the grid quality decreases, especially near the drop poles where the grid points are depleted. This results in an inaccurate prediction of the overall behavior of this system, especially considering the fact that the charge concentration is maximum around the poles. We note that this system was previously studied by Lac and Homsy [90] using an axisymmetric model and a simplified charge conservation equation that only accounted for Ohmic conduction. We observe that including interfacial charge convection amplifies the deformation and has a quantitative effect on the behavior of the system, consistent with previous studies on the dynamics of prolate drops [49, 92].

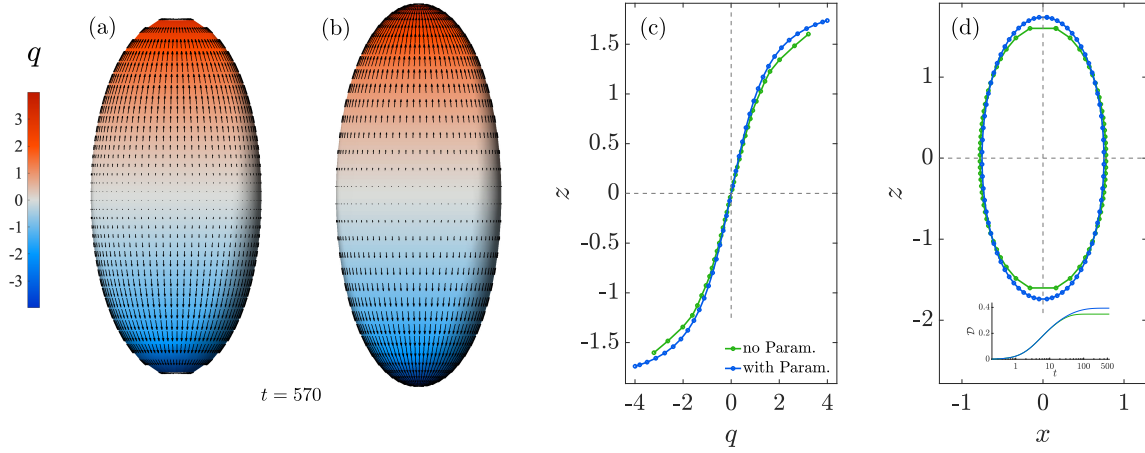


**Figure 5.3.** (a) Large deformations and strong flow degrade the grid when a drop of system **S5** is subject to  $(Ca_E, Ma) = (0.35, 5.75)$  without reparametrization. (b) Using reparametrization for the same system maintains the quality of the grid towards the steady state ( $P_{\text{cutoff}} = 0.2$ ,  $\tau = 1.0$ ). Both simulations are performed with  $N = 18$  and  $M = 2N$ . The steady charge profiles and shapes are compared between the two cases in (c) and (d), respectively. Inset of (d) shows the evolution of deformation parameter  $\mathcal{D}$ .

### 5.3.6 Convergence analysis and time step restriction

We study the overall convergence of our numerical method in Fig. 5.4(a) for model system **S2**, which reaches a steady state. For the purpose of estimating errors, we take the numerical solution on the finest grid,  $N^* = 32$ , as a surrogate for the exact solution. We plot in Fig. 5.4(a) the relative  $L_2$  errors in the steady-state charge density distribution, surface velocity field, and drop shape. Convergence of these fields is observed with a rate  $\sim O(N^{-\alpha})$  where  $4.11 \leq \alpha \leq 5.44$ . The relative error plotted in Fig. 5.4(a) is defined as:

$$e_{\mathbf{g}} = \frac{\sqrt{\int_D |\mathbf{g} - \mathbf{g}^*|^2 ds}}{\sqrt{\int_D |\mathbf{g}^*|^2 ds}}, \quad \text{where } \mathbf{g} \in \{q, \mathbf{v}, \mathbf{x}\}. \quad (5.53)$$

An efficient time marching scheme needs to strike a balance between computational costs and mitigating numerical errors in the charge density distribution and drop shape. The most computationally expensive part of our numerical method is the solution of the Stokes and

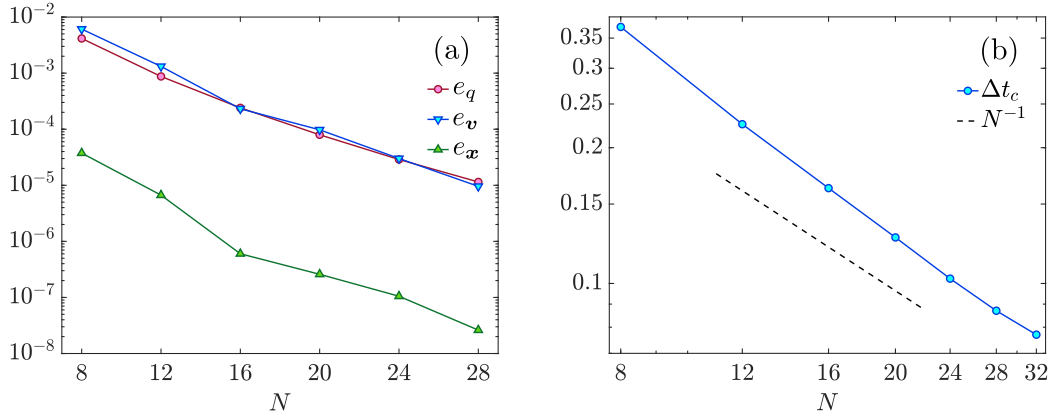


**Figure 5.4.** (a) Numerical convergence for drop shape, charge density distribution, and the velocity field. The numerical solution with  $N^* = 32$  is considered as the reference. The plot shows the relative error for each field, defined in Eq. (5.53), as a function of grid resolution  $N$ . (b) Critically stable time step size  $\Delta t_c$  as a function of  $N$ . The dashed line represents a first-order variation  $O(N^{-1})$ . A drop of system **S2** is considered in both cases, with  $M = 2N$  and  $(\text{Ca}_E, \text{Ma}) = (0.2, 2.44)$ .

Laplace’s integral equations, which we limit to twice per time step. Our numerical experiments show that an explicit second-order Runge-Kutta scheme performs sufficiently well in most cases, and all simulations shown in the paper were performed using that scheme.

Figure 5.4(b) shows the critical time step size for numerical stability,  $\Delta t_c$ , as a function of resolution  $N$  for the same model system **S2**. We determine  $\Delta t_c$  using the bisection method by starting from a large time step value. A time horizon of  $T = 40$  (in units of  $\tau_{\text{MW}}$ ) is chosen such that the system reaches steady state. If the simulation is found to be numerically unstable, we divide the time step size in half and repeat the process until we reach the maximum time step size required for stability,  $\Delta t_c$ . As shown in Fig. 5.4(b), our method shows first-order behavior with  $\Delta t_c \sim O(N^{-1})$ . Numerical tests further show that increasing the electric capillary number up to moderate values  $\text{Ca}_E \leq 0.5$  only reduces  $\Delta t_c$  by a small amount (less than 3%).

**Table 5.1.** Systems studied using simulations and their dimensional and non-dimensional parameters. We use  $\mu^+ = 0.69 \text{ Pa}\cdot\text{s}$ ,  $\gamma = 4.5 \text{ mN}\cdot\text{m}^{-1}$ ,  $\sigma^0 = 10^{-11} \text{ S}\cdot\text{m}^{-1}$ , and  $\epsilon^0 = 8.8542 \times 10^{-12} \text{ F}\cdot\text{m}^{-1}$  denotes the permittivity of vacuum.

system	Q	R	$\lambda$	$\text{Ca}_E$	Ma	$\sigma^+/\sigma^0$	$\epsilon^+/\epsilon^0$	$r_0$ (mm)
<b>S1</b>	0.57	36.59	1.41	0.05 – 0.75	0.21 – 3.25	4.5	5.3	0.7
<b>S2</b>	0.57	36.59	1.41	0.05 – 0.75	0.65 – 9.75	4.5	5.3	2.1
<b>S3</b>	0.57	36.59	14.12	0.01 – 1.44	0.28 – 5.0	4.5	5.3	0.25 : 0.5 : 1.75
<b>S4</b>	0.60	10.56	0.07	0.15 – 1.0	0.43 – 2.86	3.8	4.7	1.9
<b>S5</b>	1.37	0.1	1.0	0.35	5.75	4.5	5.3	1.37

## 5.4 Numerical results

In this section, we compare the results of our numerical method with existing theoretical solutions and previous computational and experimental studies on electrohydrodynamic flows in drops. In all simulations, the drop is initially uncharged ( $q = 0$ ) and spherical. Table 5.1 lists all physical systems considered in this study, including their dimensional and non-dimensional parameters.

### 5.4.1 Axisymmetric regime

Under weak electric fields ( $\text{Ca}_E \ll 1$ ), the drop adopts a steady axisymmetric shape and charge distribution, as shown in Fig. 5.5. Following the pioneering work of Taylor [176], various analytical models have been proposed to improve the predictions of the steady shape of a drop subject to weak electric fields and small deformations [133, 40]. We characterize the deviation from the spherical shape using Taylor’s deformation parameter  $\mathcal{D}$  defined as

$$\mathcal{D} = \frac{l-b}{l+b}, \quad (5.54)$$

where  $l$  and  $b$  are the lengths of the major axes of the drop in the directions parallel and perpendicular to the applied electric field (see Fig. 5.1). Figure 5.6 shows the steady-state deformation  $\mathcal{D}$  from our simulations compared to the predictions of different small-deformation

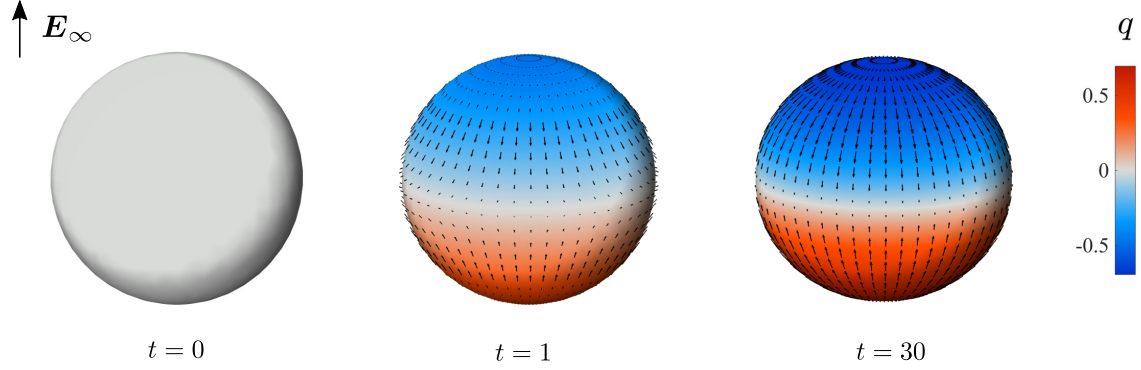


**Figure 5.5.** Axisymmetric regime: evolution of a drop of system **S2** subject to a uniform electric field with  $Ca_E = 0.2$  ( $N = 8$ ,  $M = 3N$ ). Colors show the interfacial charge density  $q$ , while arrows show the interfacial fluid velocity. Also see the corresponding video in the Supplemental Material.

theories (SDT), prior numerical simulations, as well as experimental data. As shown in Fig. 5.6, our simulation results closely match the experimental data and past predictions. In agreement with past studies [92, 40, 39], interfacial charge convection by the fluid flow plays a significant role in the dynamics and tends to weaken drop deformations.

## 5.4.2 Quincke regime

Upon increasing the intensity of the electric field, the drop can undergo a symmetry-breaking bifurcation to a dynamical regime characterized by a rotational component to the EHD flow, as shown in Fig. 5.7 [74, 142, 141]. When  $RQ > 1$ , the induced flow is from the poles to the equator, and the induced electric dipole is anti-parallel to the applied electric field. This condition is unfavorable for stability as perturbations to the system result in a destabilizing electric torque that can drive spontaneous rotation beyond a critical electric field strength  $E_c$ . Quincke first observed a similar phenomenon in solid spheres subject to uniform electric fields [131]. In solid spheres, the threshold for Quincke electrorotation is given by [82]

$$E_c = \sqrt{\frac{2\mu^+}{3\epsilon^+ \tau_{MW} (\bar{\epsilon} - \bar{\sigma})}}, \quad \text{where} \quad \bar{\sigma} = \frac{\sigma^- - \sigma^+}{\sigma^- + 2\sigma^+}, \quad \bar{\epsilon} = \frac{\epsilon^- - \epsilon^+}{\epsilon^- + 2\epsilon^+}. \quad (5.55)$$

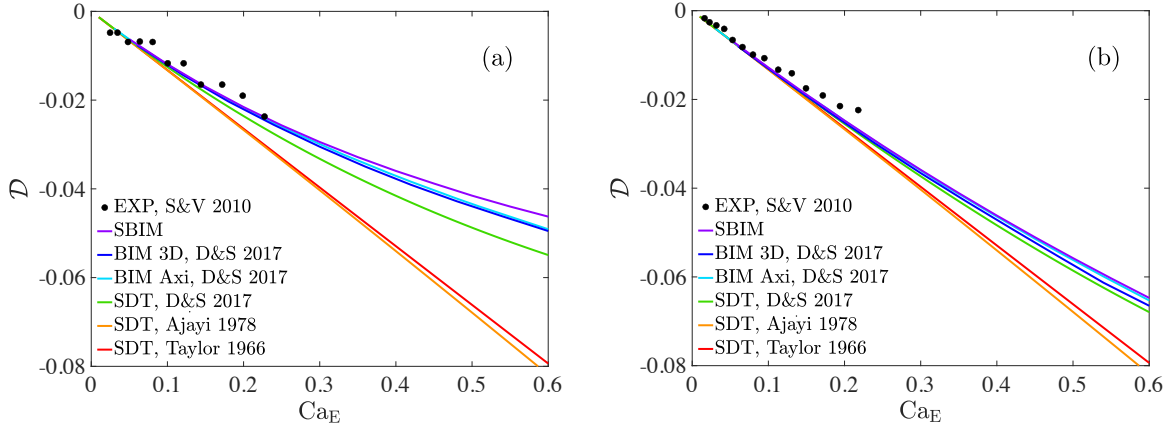


**Figure 5.6.** Steady drop deformation as a function of electric capillary number  $Ca_E$  for systems **S1** in (a) and **S2** in (b). Results from our spectral boundary integral method (SBIM) are compared with the experimental data (EXP) of [141], along with axisymmetric and three-dimensional boundary integral simulations (BIM) by Das and Saintillan [39, 40] and various small-deformation theories (SDT) [176, 2, 40]. We use  $N = 8$  and  $M = 3N$  in the simulations shown here.

Figure 5.7 shows the velocity field and charge distribution in a leaky dielectric drop during Quincke electroration. Following the onset of instability, the drop tilts away from its initial orientation. The tilt angle  $\alpha$  and deformation oscillate until they reach their steady-state values. Figure 5.8 shows the steady-state tilt angle and deformation as a function of the applied electric field  $E_\infty/E_c$  for a drop of the system **S3**. For a given set of material properties, different values of  $Ca_{MW}$  correspond to different drop sizes, and the effect of capillary forces is stronger for smaller drops (small  $Ca_{MW}$ ). Therefore, we expect the drop tilt angle  $\alpha$  to approach that of a solid sphere  $\beta$  [82, 141]:

$$\beta = \frac{\pi}{2} - \arctan\left(\frac{E_\infty^2}{E_c^2} - 1\right)^{-\frac{1}{2}}, \quad \text{for } E_\infty \geq E_c, \quad (5.56)$$

for sufficiently large  $\lambda$  and small  $Ca_{MW}$ . This is verified in Fig. 5.8(a), where the green curve for  $Ca_{MW} = 0.44$  closely follows the black line corresponding to  $\beta$ .

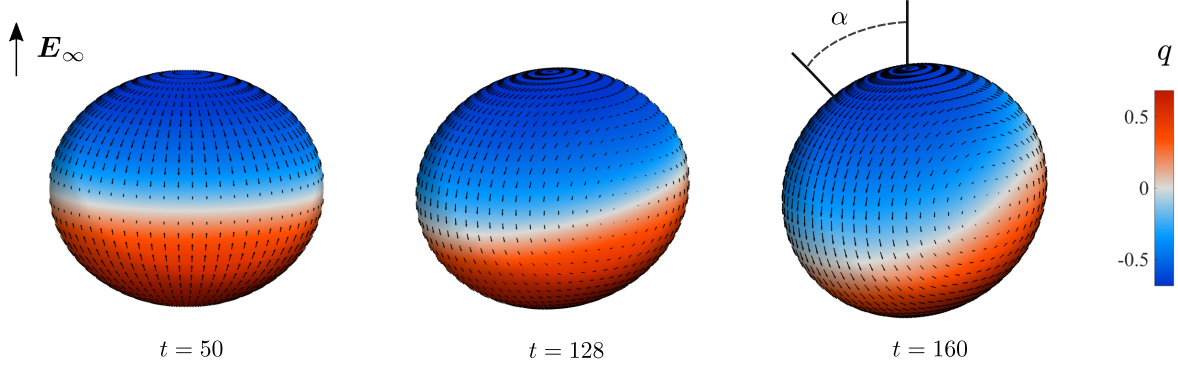


**Figure 5.7.** Quincke regime: spontaneous rotation and tilt of a drop of system **S3** subject to an applied electric field with  $E_\infty/E_c = 1$  and  $\text{Ca}_{\text{MW}} = 1.32$  ( $N = 10$ ,  $M = 3N$ ). The tilt angle  $\alpha$  is measured from the initial orientation of the drop as depicted. See the Supplemental Material for the corresponding video showing the evolution of the drop in the Quincke regime.

### 5.4.3 Low-viscosity drops

When a leaky dielectric drop with  $\text{RQ} < 1$  is subject to a uniform electric field, it compresses along the field direction. The induced quadrupolar flow is from the poles to the equator at the interface. Under weak electric fields, the characteristic interfacial velocity is:

$$u_{\text{T}} = \frac{9}{10} \frac{\text{R}(\text{RQ} - 1)}{(2\text{R} + 1)^2 (1 + \lambda)} r_0 \tau_{\text{EHD}}^{-1} \quad (5.57)$$

based on Taylor's classic solution [176]. According to Eq. (5.57), we expect the EHD flow to be stronger in low-viscosity drops ( $\lambda < 1$ ) as  $u_{\text{T}} \propto (1 + \lambda)^{-1}$ . As we increase the intensity of the applied electric field, low-viscosity drops may undergo different types of EHD instabilities, such as dimpling, equatorial streaming, or Quincke rotation, depending on their material properties [20]. In other experiments, colloidal particles adsorbed on a drop interface were observed to accumulate at the equator and form a belt, which broke into vortices of particles [45, 117]. In this section, we study the dynamics of an oblate drop with a small viscosity ratio  $\lambda < 0.1$ , represented by **S4**, which is similar to the systems studied in [117].

Our results show that charge convection significantly affects the system's dynamics in this regime. As a result of the nonlinear coupling between the flow and charge dynamics, strong

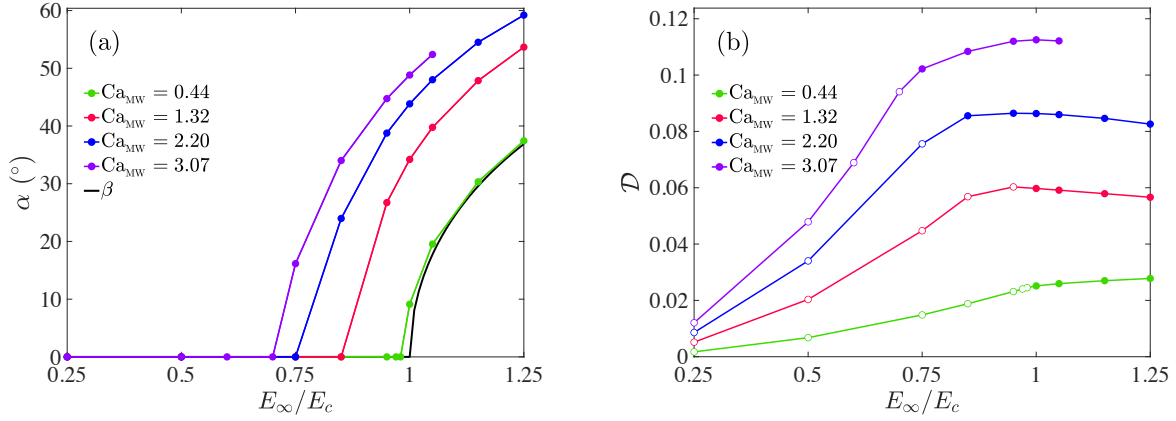


**Figure 5.8.** Steady tilt angle  $\alpha$  (a), and deformation  $\mathcal{D}$  (b) as functions of the applied electric field  $E_\infty/E_c$  for different values of  $Ca_{MW}$  (different  $r_0$ ) for system **S3**. The solid black line in (a) shows the tilt angle  $\beta$  of a rigid sphere. Filled markers in (b) show cases where Quincke electroration occurs. We used  $N = 10$  and  $M = 3N$  in all simulations.

charge gradients build up around the equator, as shown in Fig. 5.9. The nonlinear steepening disappears when we switch off the convective term in the charge conservation equation (5.5). Therefore, we can conclude that the charge convection is responsible for the nonlinear behavior mentioned. This can be verified in Fig. 5.9(c) by comparing the charge profiles for simulations with and without convection. The convergent EHD flow sweeps charges of opposite signs towards the equator, which is the stagnation line of the flow where the electric field is locally tangent to the interface. It has been shown that in systems where an interface is subject to a tangential electric field and a converging flow, strong charge gradients develop around the stagnation line due to the effect of charge convection [57].

The emergence of sharp local features in the charge profile poses a fundamental challenge for our numerical method, as spectral methods are most efficient for smooth field variables. It is known that large gradients or discontinuities in a function result in Gibbs phenomenon or ringing artifacts in its spherical harmonic representation [65]. Following the emergence of ringing artifacts, spurious oscillations cannot be contained locally as spherical harmonics are global basis functions. This phenomenon occurs due to the inability of the finite spherical harmonic expansions to properly represent the infinite (or very large) derivatives in the sharp regions of a

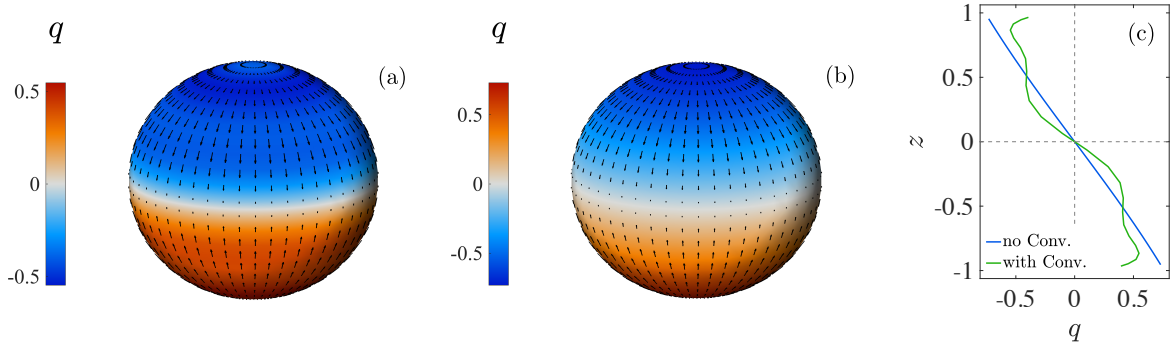


**Figure 5.9.** Charge dynamics in a low-viscosity drop of  $S4$  with  $(Ca_E, Ma) = (0.3, 1.43)$ : steady-state velocity and charge density fields in the presence of charge convection (a), and with no convection (b), and the corresponding charge profiles along the direction of the applied electric field (c). We used  $N = 8$ ,  $M = 3N$  in both simulations.

discontinuous (or nearly discontinuous) function.

For relatively small electric capillary numbers  $Ca_E < 0.2$ , we can suppress ringing artifacts by using a finer mesh corresponding to a larger number of spherical harmonics modes, a more restricted time step size, and, therefore, a higher computational cost. However, due to the stronger effect of charge convection at larger values of  $Ca_E$ , refining the resolution is insufficient to remove the ringing artifacts when  $Ca_E$  is increased.

To resolve this problem, we propose a weighted spherical harmonic expansion (WSH) for the charge density distribution, where the contribution from high-frequency components is exponentially relaxed [32]. For a given charge density distribution  $q(\theta, \phi)$ , the spherical harmonic expansion (5.30) gives coefficients  $\tilde{s} = \{\tilde{a}_{nm}, \tilde{b}_{nm}\}$  where  $n = 0, 1, 2, \dots, N-1$  and  $m \leq n$ . Accordingly, we define WSH:  $q \mapsto q_{\text{WSH}}$  as:

$$q_{\text{WSH}}(\theta, \phi) = \sum_{n=0}^{N-1} \sum_{m=0}^n e^{-n(n+1)\delta} (\tilde{a}_{nm} \cos m\phi + \tilde{b}_{nm} \sin m\phi) \bar{P}_n^m(\cos \theta), \quad (5.58)$$

where  $\delta$  is the relaxation factor. Based on (5.58), we note that WSH does not affect the mean, and  $q_{\text{WSH}}$  converges to  $q$  in the limit of  $\delta \rightarrow 0$ . In Fig. 5.10(a), we demonstrate that increasing the mesh resolution at a fixed value of  $\delta$  eliminates the ringing artifacts. In addition,

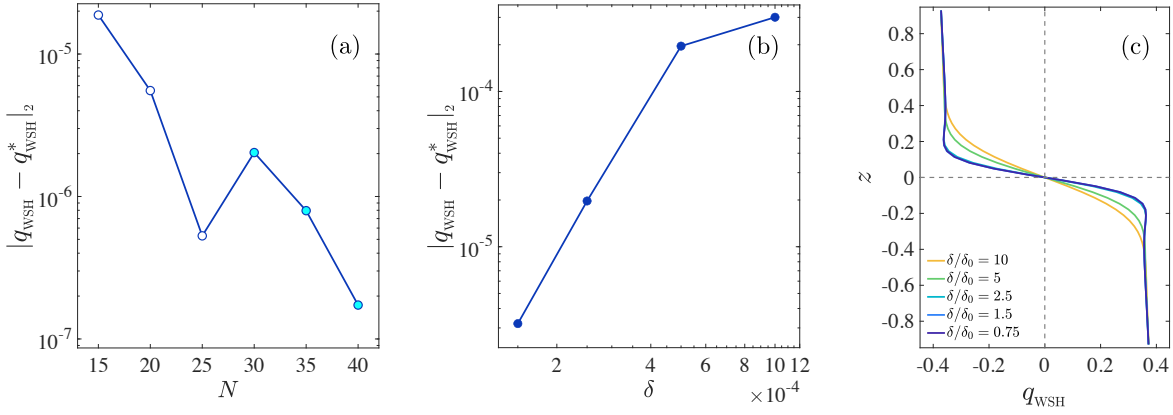


**Figure 5.10.** WSH convergence study on a drop of **S4** with  $(\text{Ca}_E, \text{Ma}) = (1.0, 0.43)$ : (a) Error in the steady-state charge density distribution as a function of mesh resolution  $N$  for a fixed value of  $\delta = 10^{-3}$  ( $N^* = 42$ ). Open markers correspond to cases with ringing artifacts. (b) Error in the steady-state charge density distribution as a function of relaxation factor  $\delta$  ( $N^* = 80$ ,  $\delta/\delta_0 = 0.75$  and  $\delta_0 = 10^{-4}$  for  $q_{\text{WSH}}^*$ ). (c) Interfacial charge profiles corresponding to (b). See the simulation video for  $N^* = 80$ ,  $\delta/\delta_0 = 0.75$  and  $\delta_0 = 10^{-4}$  in the Supplemental Material.

Fig. 5.10(b) shows that the steady-state charge profile at a fixed resolution converges as the relaxation factor  $\delta$  decreases. We combine both approaches and increase  $N$  while decreasing  $\delta$  to refine the numerical solution while avoiding the emergence of ringing artifacts. The numerical solution with the finest resolution,  $N^* = \max(N)$ , is then chosen as a surrogate to the exact solution in Fig. 5.10(a,b). To compare the charge profiles computed on different mesh resolutions, we upsample them to a fine grid with  $N^u > N^*$ . Convergence of the charge profile is illustrated in Fig. 5.10(c), where the coupling of the flow and charge dynamics is found to result in the formation of strong gradients in the charge density profile near the equator, consistent with previous studies [40]. We note that our simulations for system **S4** under electric capillary numbers of up to  $\text{Ca}_E \sim O(1)$  reach a steady axisymmetric profile and do not exhibit any electrohydrodynamic instability, suggesting that the equatorial vortices observed by [117] could be a consequence of the colloidal particles present at the interface in their experiments.

## 5.5 Conclusions

We developed a spectral boundary integral method for simulating electrohydrodynamic flows in leaky dielectric viscous drops. The drop surface, charge density, and all other variables are represented using truncated series of spherical harmonic expansions. In addition to the excellent accuracy of the spectral representation, it enables us to develop a nondissipative dealiasing method required for numerical stability. The charge transport is modeled using a conservation equation for Ohmic conduction from the bulk and surface charge convection by the flow and finite charge relaxation. We employ a reparametrization technique which allows us to explore regimes where drops undergo significant deformations. Our results closely match the existing experimental data and analytical predictions in the axisymmetric Taylor and Quincke electroration regimes. The code used in this article is publicly available at [https://github.com/mfirouzn/EHD\\_Drop\\_3D](https://github.com/mfirouzn/EHD_Drop_3D) [55].

Moreover, our simulations confirmed that the dynamics of low-viscosity drops are strongly influenced by interfacial charge convection. In this regime, the interplay between the flow and charge dynamics results in steep gradients in the interfacial charge density. The development of these sharp features in the charge density profile results in the formation of ringing artifacts due to the Gibbs phenomenon. Increasing the mesh resolution would eliminate the Gibbs phenomenon under relatively small electric capillary numbers  $Ca_E < 0.2$ . However, the effect of nonlinear steepening by the flow is sufficiently strong at larger  $Ca_E$  that increasing the resolution does not prevent ringing. To solve this problem, we introduced a weighted spherical harmonic transformation that serves as a relaxation method to exponentially damp high-wave-number coefficients. The convergence of our numerical solution with decreasing level of relaxation shows that it provides a close approximation to the true solution in this regime. Further characterizing the system's dynamics in this regime will require more sophisticated numerical methods for solutions containing discontinuities.

## 5.6 Acknowledgements

Chapter 5 is primarily based on the material published in *Journal of Computational Physics*, authored by Mohammadhossein Firouznia, Spencer H. Bryngelson and David Saintillan [56]. The dissertation author was the primary researcher and author of this paper.

The authors gratefully acknowledge funding from the US National Science Foundation under Grant No. CBET-1705377.

## Chapter 6

# Viscous drops with interfacial nematic activity

Biological surfaces are usually driven by chemical reactions at microscopic scales. In addition, they often possess an in-plane order (such as nematic or polar) that allows for large-scale hydrodynamic interactions and self-organized behavior. The interplay between the mechanics of the surface, activity due to chemical reactions, hydrodynamic interactions of the in-plane order, and the fluid flow leads to complex dynamics which is essential in various biological processes such as cell division and tissue morphogenesis. We consider a viscous drop suspended in another immiscible fluid with a surface nematic activity that drives the system out of equilibrium. This system serves as a simplified model for understanding complex active living systems, such as cells. Using a spectral boundary integral solver for Stokes flow coupled with a hydrodynamic evolution equation for the nematic tensor, we reveal the intricate interplay between flow, nematic order, and interface mechanics, leading to self-organized behaviors and symmetry-breaking phenomena, consistent with experimental observations. Diverse dynamical behaviors are observed, from periodic braiding motion of topological defects to chaotic creation and annihilation of defects under high activity levels. Our study provides valuable insights into emergent dynamics in biological and biomimetic systems with active fluid surfaces.

## 6.1 Introduction

Living materials are characterized by their ability to continuously transform chemical energy into mechanical work at the single particle level. When confined to deformable surfaces, these active materials demonstrate a myriad of dynamic behaviors. Biological surfaces often exhibit intrinsic degrees of freedom that correspond to in-plane order (such as nematic or polar), which facilitate long-range hydrodynamic interactions, resulting in the emergence of self-organized spatiotemporal patterns. This is a fundamental aspect of various biological systems, including the cell cortex, and confluent eukaryotic cells, and plays a crucial role in their functional properties. Here, we focus on systems that exhibit nematic symmetry. Experimental observations indicate the emergence of nematic order during cytokinesis [167, 134]. Nematic alignment has also been evidenced in different stages of tissue morphogenesis when individual cells exhibit a unidirectional axis of elongation [72, 144, 46].

The central motif of these biological systems has been utilized to create synthetic soft active materials [86, 73, 196]. In their pioneering work, Keber and coworkers assembled a shape-shifting lipid vesicle by encapsulating a film of microtubules and kinesin motors to its inner surface [86]. Understanding the interplay between the orientational order, activity-induced flow, and substrate geometry has been the subject of subsequent studies thereafter. Different topological confinements have been studied including spherical and toroidal systems, probing the effect of substrate curvature on the dynamics of topological defects [206, 155, 69, 115, 123].

Biological processes on subcellular and multicellular scales often occur on self-deforming surfaces with different mechanical properties. Examples include shape changes during polarization, migration, and division in cells and apical constrictions in epithelial morphogenesis [139, 101, 100]. Therefore, understanding their morphological dynamics necessitates theoretical models that account for the three-way coupling between surface deformations, in-plane order, and flow [109, 140, 3]. More recently, axisymmetric and 3D numerical simulations have been used to investigate the mechanisms responsible for fundamental shape changes observed in cells

and epithelial tissues [106, 137, 87].

This study focuses on the self-organized dynamics of a viscous drop with surface nematic activity. We use a spectral boundary integral method to simulate the flow coupled with a hydrodynamic evolution equation for the nematic tensor. We demonstrate how the interplay between flow, nematic order, and interface mechanics, leads to self-organized behaviors and symmetry-breaking phenomena, consistent with experimental observations across different regimes. In Sec. 6.2, we formally introduce the problem and present the governing equations in detail. Additionally, we discuss the relevant non-dimensional groups in Sec. 6.3. Next, in Sec. 6.4, we describe our numerical methods and introduce the braiding analysis, which plays a crucial role in analyzing our simulations. The results are presented and discussed in Sec. 6.5, where we explore two distinct limits: small and finite deformations. These findings are compared with experimental observations in each limit, further confirming the validity of our results. Finally, we summarize our conclusions and discuss potential extensions of this work in Sec. 6.6.

## 6.2 Problem definition and governing equations

We consider a viscous drop occupying volume  $V^-$  that is suspended in another viscous fluid  $V^+$  as shown in Fig. 6.1. The interface  $\partial V$  is defined by a smooth surface  $\mathbf{x} = \mathbf{x}(s^1, s^2)$  embedded in  $\mathbb{R}^3$  and parameterized by coordinates  $(s^1, s^2)$ . Tangent vectors  $\mathbf{g}_i = \partial_i \mathbf{r}$  ( $i = 1, 2$ ) along with the unit normal vector  $\mathbf{v} = (\mathbf{g}_1 \times \mathbf{g}_2) / |\mathbf{g}_1 \times \mathbf{g}_2|$  form a local coordinate system with the surface metric tensor given by  $g_{ij} = \mathbf{g}_i \cdot \mathbf{g}_j$ . The drop is initially spherical with radius  $R$ . A monolayer of active nematic particles is constrained to the interface of the drop. The interfacial nematic activity drives the system out of equilibrium by inducing flows inside and outside of the drop and by causing deformations. We use a coarse-grained representation of the nematic field using  $\mathbf{Q}$  tensor,  $\mathbf{Q} = Q^{ij} \mathbf{g}_i \mathbf{g}_j$  where  $Q^{ij} = S(n^i n^j - g^{ij}/2)$ .  $\mathbf{n} = n^i \mathbf{g}_i$  denotes the local average nematic director such that  $n^i n_i = 1$ , and  $S$  ( $0 \leq S \leq 1$ ) is the scalar order parameter showing the

strength of local alignment in the nematic monolayer. We note that  $\mathbf{Q}$  is symmetric and trace-free by construction.

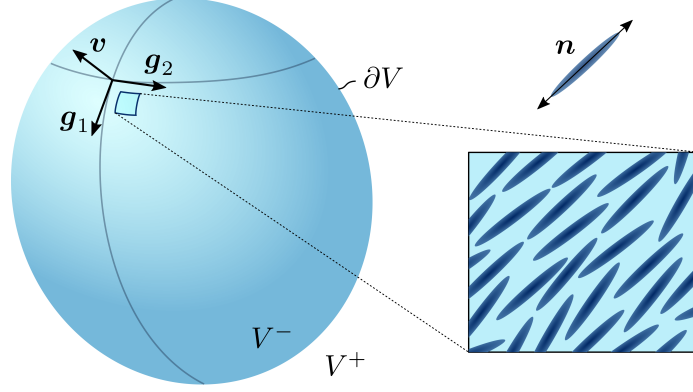


**Figure 6.1.** A viscous drop with interfacial nematic activity. The director field  $\mathbf{n}$  represents the average orientation of the nematic particles at every point on the interface.

Neglecting inertial effects and gravity, the flow is governed by Stokes and continuity equations:

$$\mu^\pm \nabla^2 \mathbf{u}^\pm - \nabla p^\pm = \mathbf{0}, \quad \nabla \cdot \mathbf{u}^\pm = 0, \quad \mathbf{x} \in V^\pm. \quad (6.1)$$

The velocity vector remains continuous across the interface and vanishes far from the drop. The evolution of nematic tensor is described by the hydrodynamic equations of an active nematic [66, 123, 140]:

$$D_t Q^{ij} = \frac{1}{\Gamma} H^{ij} + \zeta \tilde{U}^{ij}, \quad \mathbf{x} \in \partial V. \quad (6.2)$$

The term on the left-hand side denotes a co-rotational material derivative that embodies the advection and rotation of the nematic field by the flow:

$$\begin{aligned} D_t Q^{ij} = & \partial_t Q^{ij} + u^k \nabla_k Q^{ij} + u_n (C_k^j Q^{ik} + C_k^i Q^{kj}) \\ & + w_n (\epsilon^{ik} Q_k^j + \epsilon^{jk} Q_k^i), \end{aligned} \quad (6.3)$$

where  $\nabla_k$  is the covariant derivative with respect to  $s^k$ ,  $C_{ij} = -\partial_j \partial_i \mathbf{x} \cdot \mathbf{n}$  is the curvature tensor,

$w_n = \frac{1}{2}\epsilon_{ij}\nabla_i u_j$  is the normal vorticity, and  $\epsilon^{ij} = \mathbf{v} \cdot (\mathbf{g}^i \times \mathbf{g}^j)$  is the Levi-Civita tensor. The first term on the right-hand side of Eq. 6.2 represents the orientational relaxation governed by the molecular tensor  $H^{ij} = -\delta F/\delta Q^{ij}$ , and  $\Gamma$  is the rotational viscosity. We express the free energy  $F$  as:

$$F = \frac{1}{2} \int_{\partial V} dA \left( k_s \left[ \left( a + \frac{b}{3}S + \frac{c}{6}S^2 \right) Q_{ij} Q^{ij} + c(Q_{ij} Q^{ij})^2 \right] + k_e \left[ \nabla_i Q_{jk} \nabla^i Q^{jk} \right] \right), \quad (6.4)$$

by accounting for short-range and elastic interactions in the nematic monolayer [116, 88].  $k_s$  and  $k_e$  are steric and elastic phenomenological constants and  $a$ ,  $b$  and  $c$  are normalized thermotropic parameters. We assume that the characteristic length of an individual nematic particle is relatively small compared to the characteristic radius of curvature. Therefore, we do not consider any explicit coupling between the extrinsic curvature and the nematic tensor in Eq. 6.4. Finally, the alignment by the flow is represented by  $\zeta \tilde{U}^{ij}$  where  $\zeta$  is the flow alignment parameter, and  $\tilde{U}^{ij}$  is the trace-less part of the strain-rate tensor:

$$\tilde{U}^{ij} = U^{ij} - \frac{1}{2} U_k^k g^{ij}, \quad U^{ij} = \frac{1}{2} (\nabla^i u^j + \nabla^j u^i) + C^{ij} u_n. \quad (6.5)$$

We note that the velocity vector can be decomposed into tangential and normal components as  $\mathbf{u} = u^i \mathbf{g}_i + u_n \mathbf{v}$  at any point on the interface.

Nematic particles exert active stress  $\mathbf{T}^a = \xi \mathbf{Q}$  on their surrounding which drags the fluid into motion and causes deformations. The constant  $\xi$  represents the biochemical activity level. We consider extensile activity  $\xi < 0$ , motivated by the experiments of Keber and coworkers [86]. The local force balance along the tangential and normal directions reads

$$f^{H,j} + \xi \nabla_i Q^{ij} = 0, \quad \mathbf{x} \in \partial V, \quad (6.6)$$

$$f_n^H - \gamma C_k^k - \xi C_{ij} Q^{ij} = 0, \quad \mathbf{x} \in \partial V, \quad (6.7)$$

where  $\gamma$  is the surface tension.  $\mathbf{f}^H = \mathbf{v} \cdot [\mathbf{T}^{H+} - \mathbf{T}^{H-}]$  is the jump in the hydrodynamic tractions across interface and  $\mathbf{T}^{H\pm} = -p^\pm \mathbf{I} + \mu^\pm (\nabla \mathbf{u}^\pm + \nabla \mathbf{u}^{\pm T})$  is the Newtonian stress tensor.

### 6.3 Non-dimensional groups

To make the governing equations dimensionless, we use  $R$ ,  $\Gamma$ , and  $R|\xi|/\mu^+$  as the characteristic scales for length, time, and velocity respectively. The dimensional analysis yields four nondimensional groups in addition to the flow alignment parameter  $\zeta$ :

$$\text{Ca} = |\xi| R/\gamma, \quad \text{Pe} = |\xi| \Gamma/\mu^+, \quad l_c = R^{-1} \sqrt{k_e/k_s}, \quad \lambda = \mu^-/\mu^+. \quad (6.8)$$

Due to the effect of active stresses on the interface, the drop deviates from its initial spherical shape. The capillary number  $\text{Ca} = |\xi| R/\gamma$  compares the strength of active stresses to surface tension. Next, we define the Peclet number  $\text{Pe} = |\xi| \Gamma/\mu^+$  which characterizes the strength of convective fluxes of the  $\mathbf{Q}$  tensor versus its relaxational fluxes in Eq. 6.2. The balance between the short-range and the elastic interactions in the nematic monolayer defines a coherence length  $l_c = R^{-1} \sqrt{k_e/k_s}$  which can be considered as an effective distance over which a topological defect affects its surrounding nematic field. Finally, the viscosity ratio between the drop and the outer fluid is given by  $\lambda = \mu^-/\mu^+$ . All of the results presented in this work are for equiviscous systems  $\lambda = 1$ . We found that changing  $\lambda$  does not alter the overall dynamics of the system significantly. Table C.1 lists all the non-dimensional parameters we used in our simulations.

Using the scaling described above, the Stokes equations can be expressed in dimensionless form as:

$$\lambda \nabla^2 \mathbf{u}^- - \nabla p^- = \mathbf{0}, \quad \mathbf{x} \in V^-, \quad (6.9)$$

$$\nabla^2 \mathbf{u}^+ - \nabla p^+ = \mathbf{0}, \quad \mathbf{x} \in V^+, \quad (6.10)$$

inside and outside of the drop, respectively. The hydrodynamic evolution equation for the nematic tensor in Eq.6.2 becomes:

$$\partial_t Q^{ij} + \text{Pe} \mathcal{J}_c^{ij} = H^{ij} + \zeta \text{Pe} \tilde{U}^{ij}, \quad \mathbf{x} \in \partial V, \quad (6.11)$$

$$\mathcal{J}_c^{ij} = u^k \nabla_k Q^{ij} + u_n (C_k^j Q^{ik} + C_k^i Q^{kj}) + w_n (\epsilon^{ik} Q_k^j + \epsilon^{jk} Q_k^i). \quad (6.12)$$

Finally, the force balance equations in (6.6) and (6.7), take the following form:

$$f^{H,j} + \nabla_i Q^{ij} = 0, \quad \mathbf{x} \in \partial V, \quad (6.13)$$

$$f_n^H - \text{Ca}^{-1} C_k^k - C_{ij} Q^{ij} = 0, \quad \mathbf{x} \in \partial V. \quad (6.14)$$

## 6.4 Methods

### 6.4.1 Boundary integral method

To solve Eqs. 6.9- 6.14 numerically, we use a spectral boundary integral solver that we developed previously, for simulating electrohydrodynamic flows in viscous drops in Ch.5 [55, 56]. The flow problem is reformulated into a boundary integral form as [133, 125]:

$$\begin{aligned} \mathbf{u}(\mathbf{x}_0) = & -\frac{1}{4\pi(1+\lambda)} \int_D \mathbf{f}^H(\mathbf{x}) \cdot \mathbf{G}(\mathbf{x}_0; \mathbf{x}) \, ds(\mathbf{x}) \\ & + \frac{1-\lambda}{4\pi(1+\lambda)} \int_D \mathbf{u}(\mathbf{x}) \cdot \mathbf{T}(\mathbf{x}_0; \mathbf{x}) \cdot \mathbf{n}(\mathbf{x}) \, ds(\mathbf{x}), \quad \text{for } \mathbf{x}_0 \in \partial V, \end{aligned} \quad (6.15)$$

where  $\mathbf{r} = \mathbf{x}_0 - \mathbf{x}$ ,  $r = |\mathbf{r}|$ . Here,  $\mathbf{G}$  is the free-space Green's function for the Stokeslet or flow due to a unit point force in an unbounded domain, and  $\mathbf{T}$  is the corresponding stress tensor:

$$\mathbf{G}(\mathbf{x}_0; \mathbf{x}) = \frac{\mathbf{I}}{r} + \frac{\mathbf{r}\mathbf{r}}{r^3}, \quad \mathbf{T}(\mathbf{x}_0; \mathbf{x}) = 6 \frac{\mathbf{r}\mathbf{r}\mathbf{r}}{r^5}. \quad (6.16)$$

All physical variables on the interface, including the interfacial shape, velocity, and the nematic tensor are expressed in terms of truncated series of spherical harmonic expansions. Specifically, the interfacial shape and the nematic tensor are expressed, respectively as:

$$\mathbf{x}(\theta, \phi) = \sum_{n=0}^{N-1} \sum_{m=0}^n \bar{P}_n^m(\cos \theta) (\mathbf{a}_{nm} \cos m\phi + \mathbf{b}_{nm} \sin m\phi), \quad (6.17)$$

$$\mathbf{Q}(\theta, \phi) = \sum_{n=0}^{N-1} \sum_{m=0}^n \bar{P}_n^m(\cos \theta) (\mathbf{A}_{nm} \cos m\phi + \mathbf{B}_{nm} \sin m\phi), \quad (6.18)$$

where  $0 < \theta < \pi$  and  $0 \leq \phi < 2\pi$  are the latitude and longitude angles, and  $\{\mathbf{a}_{nm}, \mathbf{b}_{nm}\}$  and  $\{\mathbf{A}_{nm}, \mathbf{B}_{nm}\}$  are the corresponding coefficients of the expansion in a compact form.  $\bar{P}_n^m(\eta)$  is the normalized associated Legendre polynomial of degree  $n$  ( $n = 0, 1, 2, \dots$ ) and order  $m$  ( $m \leq n$ ) defined as:

$$\bar{P}_n^m(\eta) = \frac{1}{2^n n!} \sqrt{\frac{(2n+1)(n-m)!}{2(n+m)!}} (1-\eta^2)^{m/2} \frac{d^{n+m}}{dx^{n+m}} (\eta^2 - 1)^n, \quad (6.19)$$

and satisfies the orthogonality condition

$$\int_{-1}^1 \bar{P}_n^m(\eta) \bar{P}_{n'}^m(\eta) d\eta = \delta_{nn'}. \quad (6.20)$$

We note that the components of  $\mathbf{Q}$  tensor in the Cartesian coordinate system vary more smoothly over the poles ( $\theta = 0, \pi$ ), compared to its covariant components. Therefore, the Cartesian representation of  $\mathbf{Q}$  is used to perform spherical harmonic transformation. In addition to its exponential accuracy, the spectral representation affords a non-dissipative dealiasing method that effectively eliminates high-frequency components of the solution that exceed the limit of discretization, ensuring numerical stability throughout the simulations. Furthermore, we implement a shape reparametrization technique, which enables us to explore regimes with significant droplet deformations. A more comprehensive discussion about our numerical method is provided in Sec.5.3, as well as in the publication by Firouznia et al. [56].

In our simulations, the drop is initially spherical and the nematic field has four +1/2

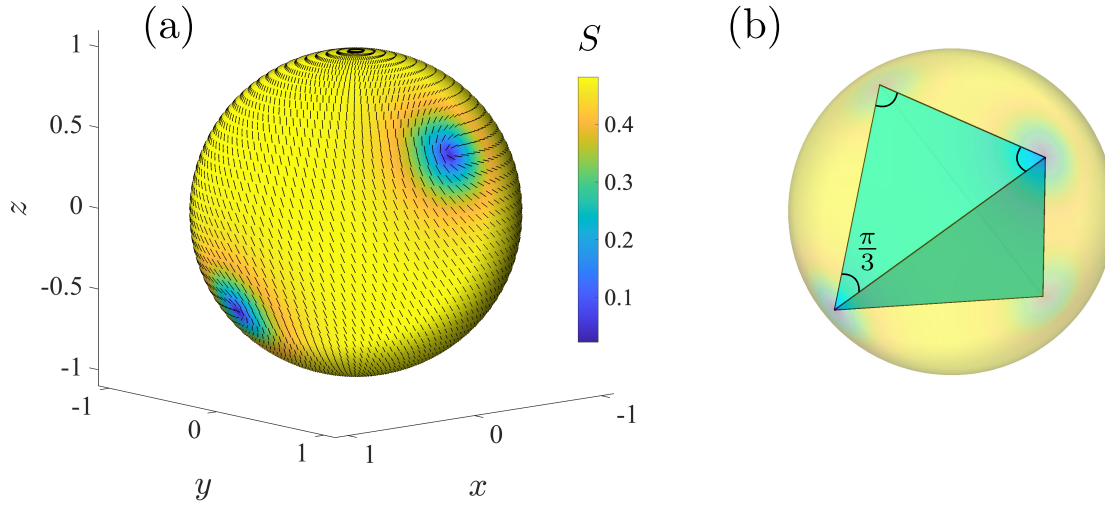


**Figure 6.2.** (a) Initial configuration depicting the director field and the surface distribution of the scalar order parameter. (b) The spatial arrangement of four defects positioned at the vertices of a symmetric tetrahedron.

defects arranged on the vertices of a symmetric tetrahedron. This initial configuration, as shown in Fig. 6.2, is obtained by numerically solving for the steady state solution of the nematodynamic equation (6.2) on a rigid sphere under a stationary velocity. The total topological charge of the nematic field is +2, which is determined by the system's topology. It is known that defects with the same-sign charge repel each other, and the energy associated with a defect is proportional to the square of its charge [98]. As a result, +1/2 defects are energetically more favorable and less costly compared to +1 defects. In the equilibrium state, the four defects are separated by maximal distances from each other, forming a symmetric tetrahedral arrangement.

Starting from the initial condition as described above, we perform the following steps at every time iteration:

1. Given the current nematic field  $\mathbf{Q}(\mathbf{x})$  and shape of the interface, determine active and capillary interfacial forces based on (6.13) and (6.14).
2. Determine the jump in the hydrodynamic traction  $\mathbf{f}^H$ , and use it to solve for the interfacial velocity using the Stokes boundary integral equation (6.15).

3. Compute the molecular tensor  $H^{ij} = -\delta F / \delta Q^{ij}$  by taking a variational derivative from the free energy given in (6.4).
4. Compute all convective fluxes of  $\mathbf{Q}$  in (6.3), and the flow alignment term  $\zeta \text{Pe} \tilde{U}^{ij}$ , based on the strain-rate tensor (6.5).
5. Compute  $\partial_t \mathbf{Q}$  via (6.11) and update the nematic tensor.
6. Update the position of the interface by advecting the grid with the normal component of the interfacial velocity:  $\partial_t \mathbf{x} = (\mathbf{u} \cdot \mathbf{v}) \mathbf{v}$ .
7. Apply corrections to the shape to ensure incompressibility, as discussed in Sec. 5.3.4.
8. Reparametrize the interfacial shape following the method discussed in Sec. 5.3.5 to minimize high-frequency components in the spherical harmonic expansion.

## 6.4.2 Identification of topological defects

One important feature of nematic systems is the existence of singular points called topological defects at which the scalar order parameter vanishes,  $S = 0$ . These defects are distinguished by their topological charge which represents the number of rotations of the director field,  $\mathbf{n}$ , around the defect (also known as the winding number). The total topological charge of the system is determined by the system's topology through the Poincaré–Hopf theorem. In the case of a nematic field confined to the surface of a spheroidal drop, the total charge is known to be +2 [98].

Topological defects play a crucial role in the dynamics of nematic materials. In our simulations, the precise location of these defects is determined through post-processing of the nematic tensor field. Due to the discretization of the grid, the defects may not fall exactly on the grid points. To accurately determine the location of a defect, we utilize spherical harmonic

expansions to interpolate its exact position. This approach allows us to obtain smooth and accurate spatiotemporal trajectories for each defect.

A defect can be understood as a local minimum of the scalar order parameter  $S$ , where  $S = 0$ :

$$(\mathbf{I} - \mathbf{v}(\mathbf{x})\mathbf{v}(\mathbf{x})) \cdot \nabla S(\mathbf{x}) = \mathbf{0}, \quad \text{with } S(\mathbf{x}) = 0. \quad (6.21)$$

Motivated by this expression, we have developed an algorithm based on the steepest descent method. In this algorithm, we iteratively march in pseudo time  $\tau$  to search for the minima of the scalar order parameter  $S$ . During each step of the simulation, we follow these steps:

1. Identify grid points where the scalar order parameter is below a cut-off value,  $I_0 = \{\mathbf{x} \in \partial V \mid S(\mathbf{x}) < S_{\text{ctf}}\}$ . In this study, the cut-off value is set to  $S_{\text{ctf}} = 0.2$ .
2. Determine the spherical harmonic expansion for  $S$ :

$$S(\theta, \phi) = \sum_{n=0}^{N-1} \sum_{m=0}^n \bar{P}_n^m(\cos \theta^*) \left( a_{nm}^0 \cos m\phi^* + b_{nm}^0 \sin m\phi^* \right). \quad (6.22)$$

3. Compute the pseudo-velocity  $\partial_\tau \mathbf{x}$  at the grid points identified in step 1:

$$\partial_\tau \mathbf{x} + (\mathbf{I} - \mathbf{v}(\mathbf{x})\mathbf{v}(\mathbf{x})) \cdot \nabla S(\mathbf{x}) = \mathbf{0}, \quad \text{with } \mathbf{x}(\tau = 0) \in I_0. \quad (6.23)$$

4. Project the linear pseudo-velocity along surface coordinates  $s^1$  and  $s^2$  (corresponding to  $\theta$  and  $\phi$  directions) to obtain the pseudo-angular velocity  $\partial_\tau \boldsymbol{\theta} = \{\partial_\tau \theta, \partial_\tau \phi\}^T$ :

$$(\partial_\tau x)_j = \partial_\tau \mathbf{x} \cdot \mathbf{g}_j, \quad (6.24)$$

$$(\partial_\tau x)^i = (\partial_\tau x)_j g^{ji}, \quad (6.25)$$

where

$$\partial_\tau \theta = (\partial_\tau x)^1, \quad \partial_\tau \phi = (\partial_\tau x)^2. \quad (6.26)$$

5. March explicitly in pseudo-time  $\tau$  to obtain the new angles  $(\theta^*, \phi^*)$ .
6. Determine the scalar order parameter  $S$  at  $(\theta^*, \phi^*)$  using the initial spherical harmonic expansions from step 2:

$$S^*(\theta^*, \phi^*) = \sum_{n=0}^{N-1} \sum_{m=0}^n \bar{P}_n^m(\cos \theta^*) \left( a_{nm}^0 \cos m\phi^* + b_{nm}^0 \sin m\phi^* \right). \quad (6.27)$$

7. Repeat steps 3 to 6 to converge to topological defects with a desired tolerance. Only retain distinct minima, as different starting points  $\mathbf{x}_0$  may converge to similar minima.
8. Determine the topological charge based on the total number of rotations of the director field  $\mathbf{n}$  on a closed path encircling the defect in a clockwise direction (also known as the winding number).

### 6.4.3 Braiding dynamics of topological defects

We observe that under low to moderate levels of activity, the topological defects exhibit braiding motion around the drop. To characterize these braiding patterns and quantify their complexity, we use a topological approach. This approach was pioneered by Boyland et al. [18] to characterize mixing in fluids, and used by others for various applications [37, 53, 182, 186, 54]. More recently, this approach has been adopted to characterize the dynamics of topological defects in active materials [174, 97, 161].

In our case, the motion of defects is confined to the interface,  $\partial V$  which is a two-dimensional spherical surface. Their trajectories in space and time can be viewed as intertwined strands or *braids*, as illustrated in Fig. 6.3(a). To map the defect trajectories from the spherical surface of the drop to a planar surface, we utilize stereographic projection. This mapping transforms the three-dimensional coordinates  $\mathbf{x} = (x, y, z)$  to the two-dimensional mid-plane ( $z = 0$ ) of the sphere, represented by  $\mathbf{X} = (X, Y)$ .

It is important to note that a spherical geometry differs from a planar disk in that a sphere does not have a boundary. To address this difference, we designate one trajectory as the reference trajectory, which is then mapped to the boundary at infinity [47, 14]. At any given time, the drop is rotated so that the reference defect is located at the north pole of the sphere, effectively mapping it to  $|\mathbf{X}| \rightarrow \infty$ . The remaining trajectories are ordered from left to right along a projection line as shown in Fig. 6.3(a,b). A crossing occurs when two defects interchange their order along the projection line. During a crossing, one trajectory either goes over or under the other trajectory. In other words, the direction of the crossing can be clockwise (over) or counterclockwise (under) on the projection line.

A sequence of crossings of defect trajectories can be represented by a braid  $\mathbf{b} = b_1 b_2 \dots b_k$ , where each  $b_j$ ,  $j = \{1, \dots, k\}$  represents a crossing event. Each crossing can be represented in terms of elementary generators  $\sigma_i$ ,  $i \in \{1, \dots, n-1\}$  of the  $n$ -particle braid group  $B_n$  [184]. The generator  $\sigma_i$  represents the clockwise exchange of defect  $i$  with defect  $i+1$  on the projection line, while  $\sigma_i^{-1}$  corresponds to their counterclockwise exchange. We utilize `braidlab`, a freely available MATLAB package, to construct braids from defect trajectories and to analyze their topological entropy [185]. Figure 6.3(c) shows the braid diagram corresponding to defects trajectories in Fig. 6.3(a,b).

To characterize the complexity of defect dynamics we adopt a topological approach. Each defect can be considered as a stirrer rod in the  $X - Y$  plane. Consider idealized material loops as tight rubber bands wrapped around these stirrer rods. These material loops are dragged by the trajectories and stretched due to their braiding motion. The braid entropy measures the exponential growth of these loops and provides a lower bound for the stretching of all material lines in the corresponding flow [48, 18, 68, 186]. For periodic trajectories, the braid entropy  $h(\mathbf{b})$  can be computed by evaluating the repeated action of braid  $\mathbf{b}$  on material loops. It is defined as:

$$h(\mathbf{b}) = \lim_{N \rightarrow \infty} \frac{1}{N} \log \left| \frac{\mathbf{b}^N l_E}{l_E} \right|, \quad (6.28)$$

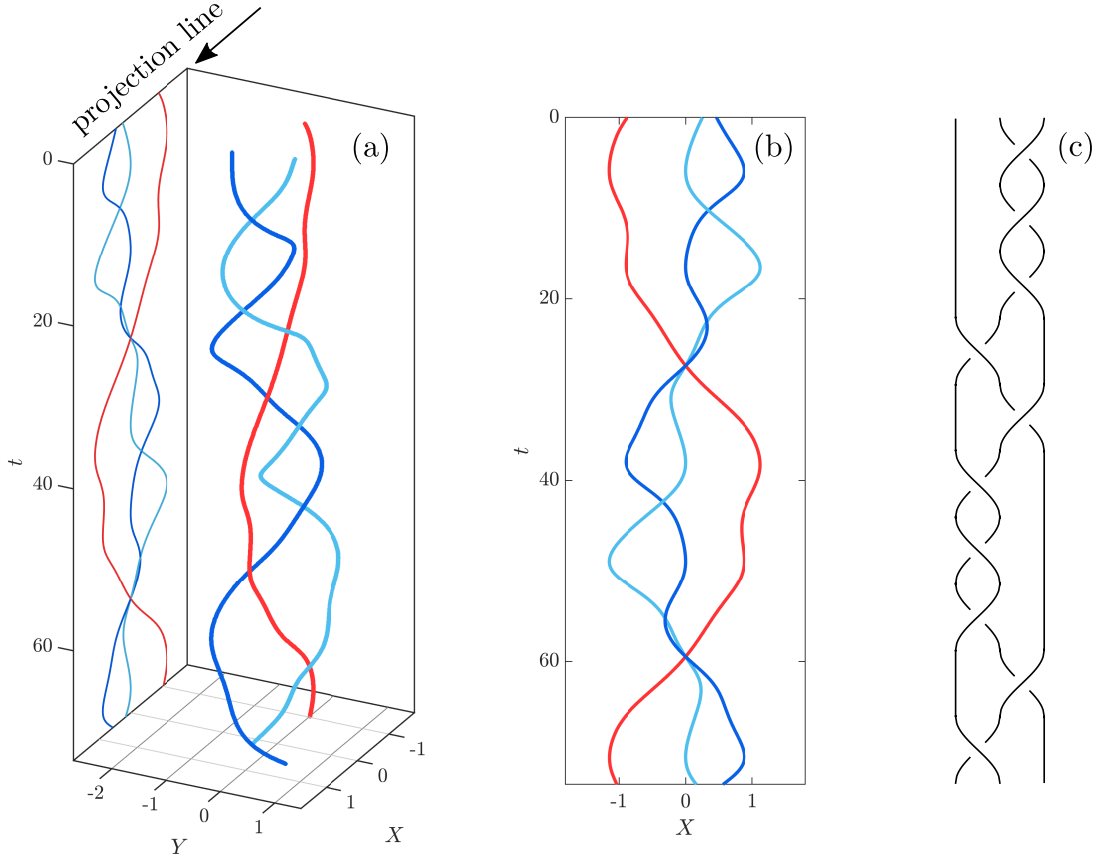


**Figure 6.3.** (a) Trajectories of three defects in the  $X - Y$  plane over time  $t$  on an active drop with  $(Ca, Pe, l_c) = (0.01, 0.2, 0.16)$ . At any given time, the reference defect is positioned at the north pole of the sphere which corresponds to  $|\mathbf{X}| \rightarrow \infty$ . (b) The projection of particle trajectories on the  $X$ -axis, and (c) the diagram for the corresponding braid,  $\mathbf{b} = \sigma_2^{-1} \sigma_2^{-1} \sigma_2 \sigma_1 \sigma_2^{-1} \sigma_1 \sigma_1 \sigma_1^{-1} \sigma_2^{-1} \sigma_1$ .

where  $l_E$  represents the generating set for the fundamental group on the  $n$ -punctured disk [113].

For systems with aperiodic trajectories, the finite-time braiding exponent (FTBE) was introduced by Budišić and Thiffeault as [26]:

$$\text{FTBE}(\mathbf{b}) = \frac{1}{T} \log \left| \frac{\mathbf{b} l_E}{l_E} \right|, \quad (6.29)$$

where  $T$  is the time interval between the first and last crossings. The FTBE measures the average expansion of material loops subjected to the braiding motion of defect trajectories. It is shown that for sufficiently long trajectories, the FTBE is independent of the projection angle, initial

configuration, and the length of trajectories [26]. We use `braidl` to compute the braid entropy and FTBE for our system.

## 6.5 Results and discussion

In this section, we analyze the behavior of an active drop as a function of controlling parameters and compare our simulations with the experimental observations by Keber et al. [86]. We start by investigating the regime of small deformations in Sec.6.5.1, where the drop retains its nearly spherical shape. Then, we explore the effect of finite deformations on the dynamics of the system in Sec.6.5.2.

### 6.5.1 Small deformations

We examine the regime of small capillary numbers ( $Ca \ll 1$ ) to isolate the effect of deformations. In this regime, the behavior of the system is primarily governed by two parameters: the activity level represented by  $Pe$ , and the nematic elasticity represented by  $l_c$ . The active stresses drive the system out of equilibrium while the nematic elasticity stabilizes the system. The strength of the elastic effects in the nematic monolayer is reflected in the coherence length  $l_c$ , which is the characteristic length over which the defects interact. As the nematic elasticity becomes stronger, the coherence length increases, resulting in a more constrained arrangement of the defects that repel one another. By systematically varying the values of  $Pe$  and  $l_c$ , we explore and analyze the intricate interplay between these effects, shedding light on the underlying dynamics of the system.

Each defect is propelled into motion by the activity-induced flow, which, in turn, influences the nematic field. We observe that the arrangement of defects oscillates between tetrahedral and planar configurations, as illustrated in Fig. 6.4, resembling the experimental observations by Keber et al. [86]. The angle between two defects  $i$  and  $j$  is denoted by  $\alpha_{ij}$ . We define  $\alpha$  as the

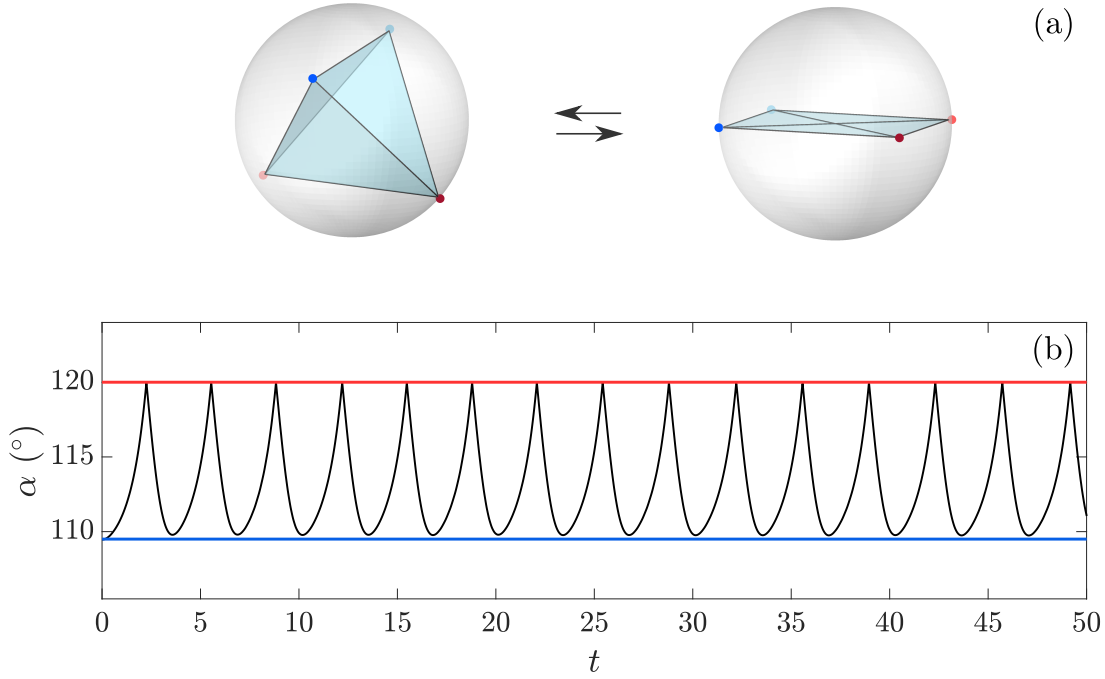


**Figure 6.4.** (a) The arrangements of defects oscillates between tetrahedral (left) and planar (right) configurations. (b) The average angle  $\alpha$  over time for a system with  $(Ca, Pe, l_c) = (0.01, 1.2, 0.32)$ , illustrating the oscillatory behavior between  $120^\circ$  (red) in the planar configuration, and  $109.5^\circ$  (blue) in the symmetric tetrahedral configuration.

average of all pairwise angles between the four defects:

$$\alpha = \frac{1}{6} \sum_{i < j}^4 \alpha_{ij}. \quad (6.30)$$

Figure 6.4(b) depicts the oscillatory behavior of the average angle  $\alpha$ , between  $120^\circ$  for the planar configuration, and  $109.5^\circ$  for the symmetric tetrahedral configuration.

Under small activity levels, the defects remain stationary. As the activity level surpasses a critical value  $Pe_c$ , the system undergoes a transition from a stationary to an unsteady regime characterized by the periodic braiding motion of defects. For activity levels close to  $Pe_c$  within the unsteady regime, the periodic motion of defects can be described by a single characteristic time scale. This is evident from the fast Fourier transform (FFT) of the average angle  $\alpha$ , which exhibits a single peak in this regime (see appendix C.2 for more information). The defect trajectories

follow a specific pattern known as the *golden braid*<sup>1</sup>, represented by the braid  $\mathbf{B}_1 = (\mathbf{b}_1)^k$ , where:

$$\mathbf{b}_1 = \sigma_1 \sigma_2^{-1} \sigma_1 \sigma_1 \sigma_2 \sigma_1^{-1} \sigma_2^{-1} \sigma_2^{-1}. \quad (6.31)$$

This name is derived from the fact that the topological entropy of  $\mathbf{b}_1$  is an integer multiple of  $\log \phi_1$ , where  $\phi_1 = (1 + \sqrt{5})/2$  is the golden ratio [37]:

$$h(\mathbf{b}_1) = 6 \log \phi_1 \approx 2.8873. \quad (6.32)$$

As the Peclet number is further increased, the nonlinear hydrodynamic effects become more pronounced, leading to the emergence of a second time scale. This is manifested in the FFT spectrum of  $\alpha$ , which exhibits two distinct peaks (Fig. C.2 in appendix C.2). Eventually, the braiding pattern undergoes a transition from the golden braid to the *silver braid*<sup>2</sup> represented by  $\mathbf{B}_2 = (\mathbf{b}_2)^k$ , where:

$$\mathbf{b}_2 = \sigma_1 \sigma_2 \sigma_1^{-1} \sigma_2^{-1} \sigma_1 \sigma_2^{-1}. \quad (6.33)$$

Similarly, the entropy of  $\mathbf{b}_2$  is a multiple of  $\log \phi_2$ , where  $\phi_2 = 1 + \sqrt{2}$  is the silver ratio [54]:

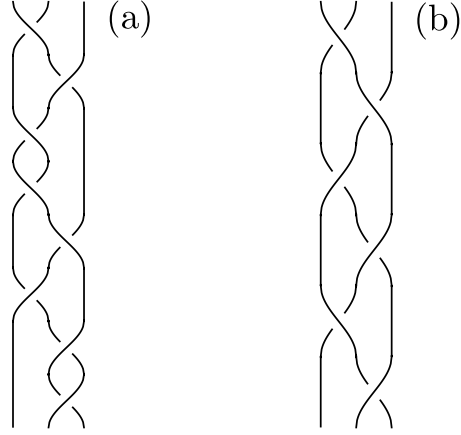
$$h(\mathbf{b}_2) = 2 \log \phi_2 \approx 1.7627. \quad (6.34)$$

Figure 6.5 depicts the diagrams of the golden and silver braids. The efficiency of a braiding pattern in increasing entropy can be assessed by comparing the topological entropy per generator (TEPG). Comparing the TEPG values of two braids shows that  $\text{TEPG}(\mathbf{b}_1)$  is approximately 1.23 times larger than  $\text{TEPG}(\mathbf{b}_2)$ . A higher TEPG value means that the golden braiding pattern is more effective in maximizing entropy. However, it is important to note that this increased

---

<sup>1</sup>We note that  $\mathbf{b}_1$  and  $(\sigma_1^{-1} \sigma_2)^3$  are conjugate braids which implies that they have the same topological entropy [19, 183]. The braid  $\sigma_1^{-1} \sigma_2$  is commonly known as the golden braid for  $n = 3$  [37]. Two braids are said to be conjugate if they represent the same permutation of strands but in a different ordering. In other words, they can be continuously deformed into each other without any self-intersections or changes in the linking of the strands [85].

<sup>2</sup> $\mathbf{b}_2$  is conjugate to  $\sigma_1^2 \sigma_2^{-2}$  which is referred to as the silver braid for  $n = 3$  in [54].



**Figure 6.5.** Diagram of (a) the golden braid  $\mathbf{b}_1$ , and (b) the silver braid  $\mathbf{b}_2$ .

efficiency comes at a higher energetic cost. In other words, the golden braid requires more energy to operate compared to the silver braid. We note that in our system with  $n = 3$ , the TEPG and the topological entropy per operation (TEPO) introduced in [54] are equivalent.

The active power for the drop is defined as:

$$P_a(t) = \int_{\partial V} \mathbf{f}^a \cdot \mathbf{u} \, ds, \quad (6.35)$$

where  $\mathbf{f}^a = \xi \nabla_i Q^{ij} \mathbf{g}_j - \xi C_{ij} Q^{ij} \mathbf{v}$  is the interfacial active force, and  $\mathbf{u}$  is the fluid velocity. The time-average active power is denoted by  $\bar{P}_a = \langle P_a \rangle_t$ . During the transition from the golden to silver braiding pattern, we observe a sudden decrease in the average active power  $\bar{P}_a$  as shown in Fig. 6.6(b). It is important to note that in the small deformations limit, the energy introduced to the system by interfacial activity gets dissipated through viscous effects in the bulk (proof provided in appendix C.3). Consequently, a higher active power corresponds to increased viscous dissipation in this regime. More significantly, our findings lead to the conclusion that operating the golden braiding pattern incurs higher energy costs compared to the silver braiding pattern.

As the activity level is further increased, the nonlinear hydrodynamic effects become even stronger, leading to a transition from periodic to aperiodic dynamics. This regime, referred to as the *mix braiding* phase, is characterized by the absence of a specific braiding pattern, with

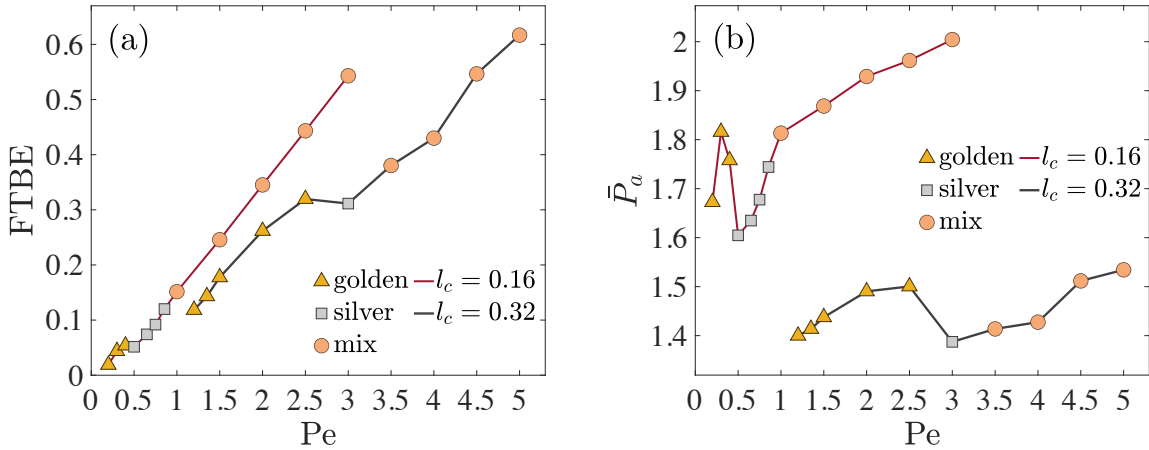


**Figure 6.6.** (a) Finite-Time Braiding Exponent (FTBE) of defect trajectories, and (b) the average active power  $\bar{P}_a$  of a spherical active drop as a function of Pe and  $l_c$ . The markers (golden, silver, and mix) represent different dynamical phases characterized by distinct braiding patterns. The capillary number is  $Ca = 0.01$  for all cases studied here. The defects remain stationary when  $Pe < 0.2$  for  $l_c = 0.16$ , and when  $Pe < 1.2$  for  $l_c = 0.32$ .

defect trajectories displaying irregular and chaotic behavior. The FFT spectrum of  $\alpha$  shows multiple time scales in this regime, indicating complex and highly nonlinear dynamics (Fig. C.3 in appendix C.2). Figure 6.7 presents three-dimensional defect trajectories in active drops with golden, silver, and mix braiding patterns, providing visual evidence of the increasing complexity with higher activity levels.

We compared the FTBE of defect trajectories as a function of Pe and  $l_c$  in Fig. 6.6(a). It is evident that the FTBE is an ascending function of Pe, indicating that higher activity levels lead to more complex and nonlinear dynamics. Furthermore, the transition from golden to silver braiding patterns is accompanied by a decrease in the FTBE, which can be attributed to the lower topological entropy observed in the silver braid compared to the golden braid.

It is important to highlight that increasing the coherence length has a stabilizing influence on the system's dynamics. Specifically, the critical Peclet number  $Pe_c$ , which signifies the transition from the stationary phase to the braiding motion of defects, rises significantly from  $Pe_c \approx 0.2$  for  $l_c = 0.16$  to  $Pe_c \approx 1.2$  for  $l_c = 0.32$ . We also observe that the onset of aperiodic defect motions (mix braiding phase) is delayed under larger coherence lengths. According to

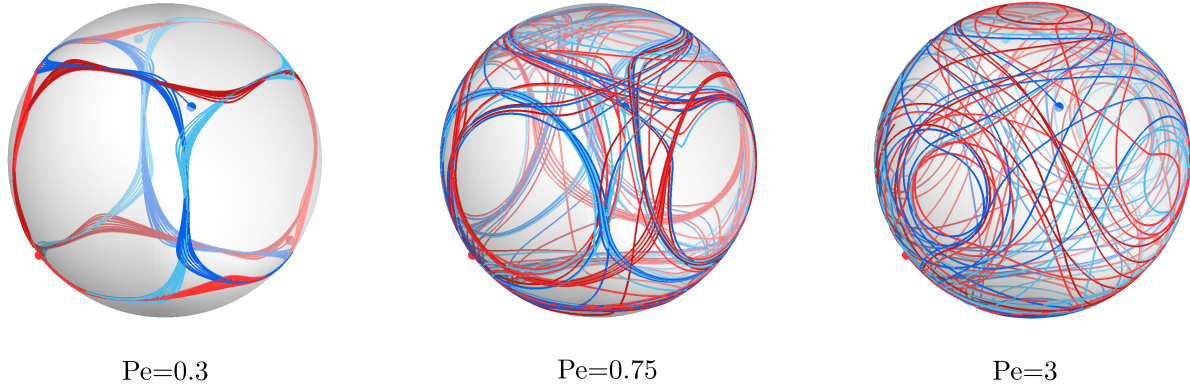


**Figure 6.7.** Defect trajectories in active drops with golden (left), silver (middle), and mix (right) braiding patterns, at different values of  $Pe$ . The initial positions of defects are indicated by circular markers. The time interval between the first and last data points is set to  $\Delta t = 50/f_1$ , where  $f_1$  corresponds to the peak frequency obtained from the FFT analysis of the average angle  $\alpha$ . All simulations are performed with  $(Ca, l_c) = (0.01, 0.16)$ .

Fig. 6.6(a,b), for a given Peclet number, the FTBE and the active power consistently decrease as the coherence length increases. These observations suggest that nematic elasticity plays a crucial role in stabilizing the system and maintaining more organized and constrained dynamical behavior. Moreover, these results highlight the significance of coherence length in modulating the behavior of the active drop and its transition to chaotic dynamics, providing insights into the interplay between nematic elasticity and the nonlinear hydrodynamic effects.

## 6.5.2 Finite deformations

Allowing for finite deformations (equivalently finite  $Ca$ ) significantly increases the complexity of the system's dynamics. In this regime, the active drop undergoes spontaneous deformations as the defects move around its surface. These deformations, in turn, impact the nematic field, establishing a three-way feedback loop involving the shape, nematic field, and flow. Notably, we find that the critical Peclet number,  $Pe_c$  increases at higher capillary numbers. This observation suggests that higher levels of activity are necessary for defects to overcome the energy barriers induced by deformations.

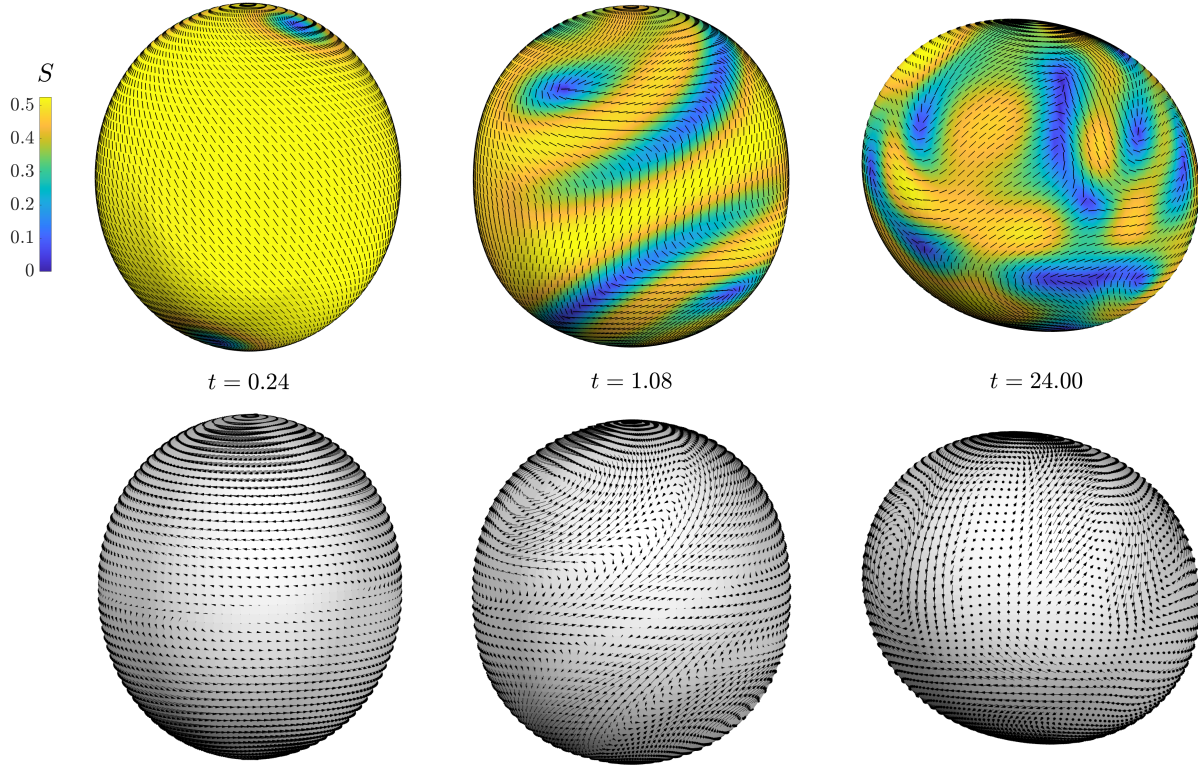


**Figure 6.8.** Chaotic regime: snapshots of the director field (first row) and the scalar order parameter represented as the colormap, along with the corresponding interfacial velocity field (second row). The simulations is conducted for a system with  $(Ca, l_c, Pe) = (0.5, 0.16, 10)$ .

For the smaller coherence length  $l_c = 0.16$ , we observe that under moderate values of  $Pe > Pe_c$ , the defects exhibit braiding motion similar to the behavior observed in the small deformations limit. Concurrently, the shape of the drop undergoes spontaneous changes due to the influence of active stresses. We find that the drop eventually reaches an equilibrium state at long times, for Peclet numbers up to  $Pe_{eq} > Pe_c$ . The time horizon to reach equilibrium typically varies from  $T \approx 75$  to 350 (in units of  $\Gamma$ ) in our simulations. It is important to acknowledge that these large time scales might not be readily achievable in experimental settings. Nonetheless, our simulations of active drops under finite deformations closely resemble the qualitative experimental observations reported by Keber et al. in [86].

The nonlinearity introduced by finite deformations amplifies the asymmetry in the nematic field and, consequently, in the defect configurations. As a result, a translational component

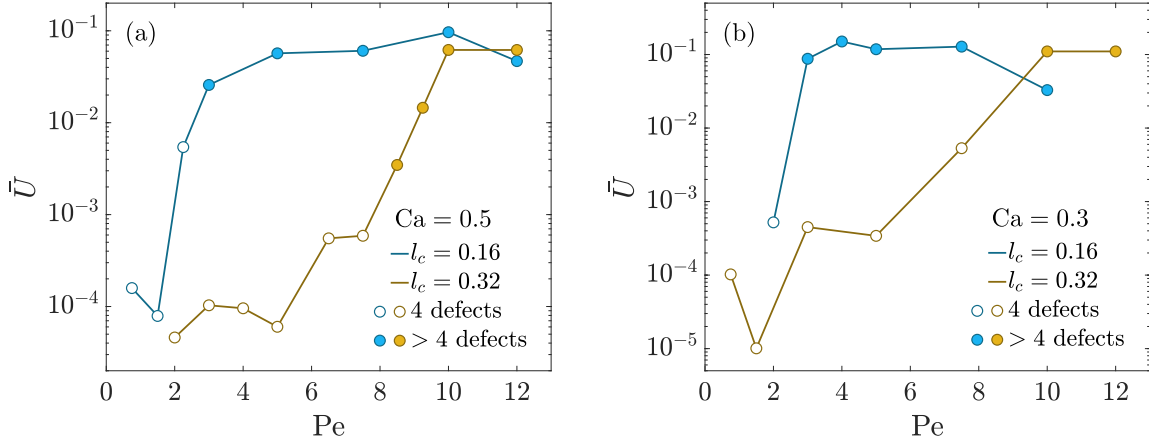


**Figure 6.9.** Time-average translational velocity as a function of  $Pe$ , under finite deformations: (a)  $Ca = 0.5$ , and (b)  $Ca = 0.3$ . Blue and brown lines correspond to  $l_c = 0.16$  and  $0.32$ , respectively. Filled markers indicate cases where more than four defects were observed during the evolution of the active drop.

emerges in the velocity field. The volume-average velocity of the drop can be expressed as a surface integral using the divergence theorem:

$$\mathbf{U}(t) = \frac{1}{V_d} \int_V \mathbf{u} \, dv = \frac{1}{V_d} \int_V \nabla \cdot (\mathbf{u} \mathbf{x}) \, dv = \frac{1}{V_d} \int_{\partial V} \mathbf{x} (\mathbf{n} \cdot \mathbf{u}) \, ds, \quad (6.36)$$

where  $V_d = \int_V dv$  represents the volume of the drop. The time-average velocity of the drop and its magnitude is denoted by  $\bar{\mathbf{U}} = \langle \mathbf{U} \rangle_t$  and  $\bar{U} = |\bar{\mathbf{U}}|$ , respectively. We observe that the translational velocity is orders of magnitude larger compared to the regime of  $Ca \ll 1$ . This highlights the effect of deformations on inducing symmetry-breaking behaviors in the system. With increasing  $Pe$ , the system transitions to a chaotic regime characterized by the creation and annihilation of defects. The newly formed defects emerge as pairs with  $\pm 1/2$  topological charges, maintaining the net topological charge of the system constant. Figure 6.8 shows snapshots of the drop during the chaotic regime (see appendix C.4 for more information).

Figure 6.9 shows the time-average translational velocity  $\bar{U}$  as a function of  $Pe$  under finite deformations. For the smaller coherence length  $l_c = 0.16$ ,  $\bar{U}$  exhibits an initial increase with  $Pe$ , indicating stronger nonlinear hydrodynamic effects at higher activity levels. However, as  $Pe$

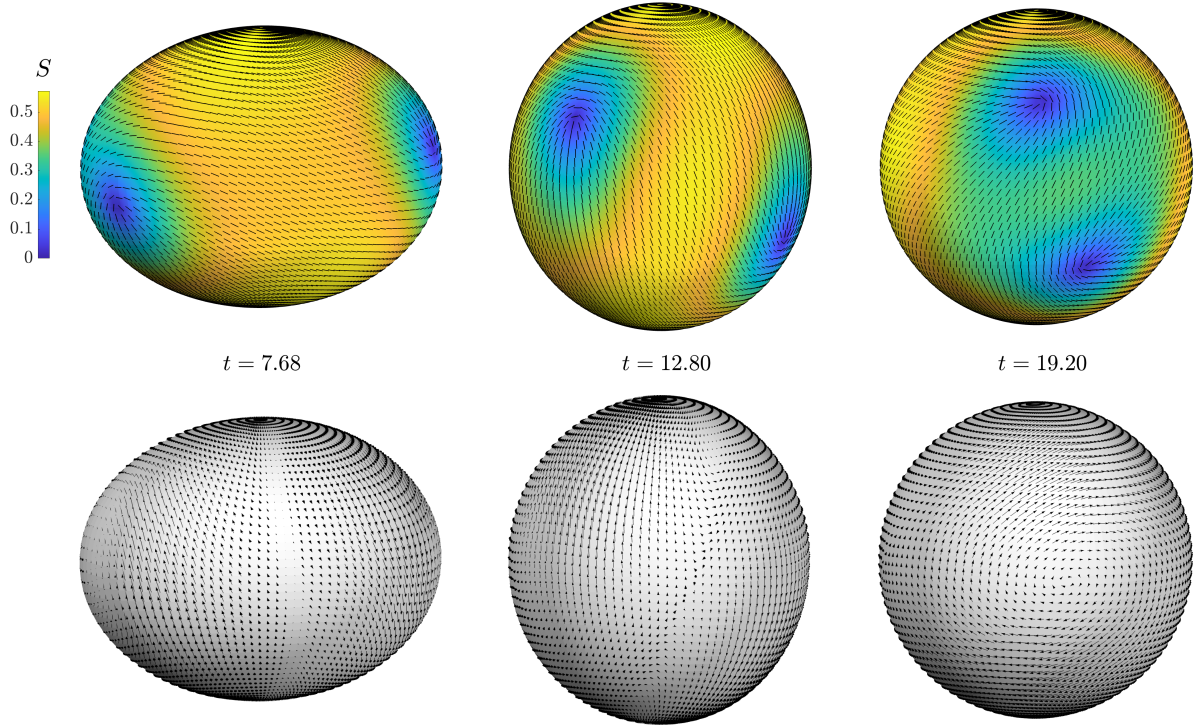


**Figure 6.10.** Shape-shifting active drop: snapshots of the director field (first row) and the scalar order parameter represented as the colormap, along with the corresponding interfacial velocity field (second row). The simulations is conducted for a system with  $(Ca, l_c, Pe) = (0.5, 0.32, 5)$ .

is further increased, the translational velocity reaches a plateau followed by a decrease. This behavior is observed in the chaotic regime, where the rapid creation and annihilation of defects around the drop lead to a more symmetric dynamical state. Consequently, increasing the activity has the opposite effect on  $\bar{U}$  in this regime.

For the larger coherence length  $l_c = 0.32$ , we observe that the system reaches equilibrium at long times, for all values of the Peclet number studied here ( $0 < Pe < 12$ ). Figure 6.10 shows snapshots of a shape-shifting active drop at a moderate activity level, where the defects undergo braiding motion. At high activity levels, the dynamical behavior of the drop is characterized by the braiding motion of defects and spontaneous deformations, followed by the creation and annihilation of defects, leading to an equilibrium state with an asymmetric arrangement of defects around the drop. This asymmetric configuration results in a translational velocity that increases with  $Pe$ , as depicted in Fig. 6.9(a,b). Notably,  $\bar{U}$  is consistently stronger under the smaller

coherence length, except in the chaotic regime, as evident from Fig. 6.9(a,b). This behavior can be attributed to the effect of nematic elasticity, which promotes ordered dynamical behavior and leads to more symmetric shapes of the active drops.

## 6.6 Conclusions

In this study, we investigated the behavior of a viscous drop suspended in another immiscible fluid with a surface nematic activity, driving the system out of equilibrium. To model this system, we employed a spectral boundary integral solver for Stokes flow coupled with a hydrodynamic evolution equation for the surface nematic tensor. Our simulations revealed the intricate interplay between flow, nematic order, and interface mechanics, leading to self-organized behaviors and symmetry-breaking phenomena. Notably, our results captured the qualitative behaviors observed in experiments, both in the small and finite deformation regimes [86].

In the small deformation regime, the topological defects move around the drop due to the hydrodynamic interaction between the activity-induced flow, and the nematic field. The arrangement of the defects oscillates between the planar and tetrahedral configurations consistent with the experimental observations. Using the dynamics of braids, we characterized the topological pattern of defect trajectories as a function of activity level and coherence length. Remarkably, we found that weak activity led to periodic braiding patterns following the golden braid, known for maximizing the topological entropy per generator (TEPG). As the activity is increased, the braiding pattern transitions to the silver braid, which exhibits lower TEPG and incurs less energetic cost to operate. At higher activity, the defect trajectories become aperiodic due to strong nonlinear effects. By analyzing the finite-time braiding exponent (FTBE), we compared the complexity associated with defect dynamics among different braiding patterns. Notably, we demonstrated that nematic elasticity, as indicated by the coherence length, promoted more ordered dynamical behavior and counteracted active effects.

In the presence of finite deformations, the system exhibits a more complex behavior. At sufficiently high activity levels, defects exhibit braiding motion while the shape of the drop spontaneously changes due to active stresses. This behavior closely resembles experimental observations in this regime. At even higher activity levels, the system transitions to a chaotic regime characterized by continuous creation and annihilation of new defects. The nonlinear effects introduced by deformations give rise to a translational component in the velocity field, characterized as a function of Peclet number and coherence length. We observed opposing effects of nematic elasticity and activity, where higher nematic elasticity stabilized the dynamics.

While our study focuses on a synthetic system where activity is considered uniform around the drop, it is important to note that living active systems, such as cells, exhibit more intricate dynamics. Chemical cues have been demonstrated to play a crucial role in biological processes, such as cell division [181, 136]. Therefore, exploring the impact of chemical cues on emergent behaviors in such systems is of great interest and represents a promising direction for future research. Overall, our work provides valuable insights into the emergent dynamics of active fluid surfaces with in-plane order, both in biological and biomimetic systems.

## **6.7 Acknowledgements**

Chapter 6 is a manuscript in preparation authored by Mohammadhossein Firouznia and David Saintillan. The dissertation author was the primary researcher and author of this paper.

# Chapter 7

## Conclusions and directions for future work

### 7.1 Conclusions

In this thesis, we studied interfacially driven flows in various fluid-fluid systems. A common thread among all systems studied here is the three-way coupling between the flow in the bulk of fluids, interfacial transport of a surface property (scalar or a higher order tensor), and the mechanics of a deforming surface. Despite the linear governing equations in the bulk, such as Laplace's and Stokes equations, these systems exhibit interfacial instabilities and nonlinear phenomena due to boundary effects. The nonlinear coupling of different physical effects takes place at a deforming boundary which is the interface. Consequently, studying the dynamics of these systems presents inherent challenges for analytic methods and numerical simulations. To address these complexities, we employed high-fidelity computational methods to study the intricate dynamics of these systems and carefully compared our results with available experimental studies. Our numerical simulations were complemented by analytic solutions, scaling analyses, and reduced-order models that capture the underlying physical mechanisms at play.

In Ch. 3, we investigated interfacial instabilities and nonlinear patterning in a freely suspended film of leaky dielectric fluid under a uniform electric field. We identified different modes of instability through theoretical analysis, and characterized the behavior of the system in each mode, as a function of different nondimensional groups of the problem. Using boundary

element simulations, we explored the dynamics of the system far from equilibrium where the coupling of the flow, charge dynamics, and deformations gives rise to nonlinear phenomena such as tip streaming jets and pinching of the film into droplets. Our study offers valuable insights into nonlinear patterning in electrified viscous films, with significant implications for engineering applications, particularly in microfluidics.

In Ch. 4, we studied electrohydrodynamics instabilities occurring at a planar interface subjected to a stagnation point flow and a tangential electric field. This configuration is inspired by the equatorial streaming observed in oblate drops under strong electric fields. Through a local theoretical analysis and numerical linear stability analysis, we unveiled the crucial and nontrivial impact of charge convection on the system's dynamics. Using stability analyses along with numerical simulations far from equilibrium, we elucidated the underlying mechanisms driving electrohydrodynamic (EHD) equatorial streaming in droplets. Specifically, we demonstrated the emergence of a convergent line instability at the stagnation point, where nonlinear steepening by the flow generates large gradients in the charge density distribution.

In Ch. 5, we developed a spectral boundary integral method for simulating electrohydrodynamic flows in viscous drops. We used a comprehensive charge transport model valid under a wide range of electric field strengths. Different mechanisms are accounted for, including Ohmic conduction, surface charge convection, and finite charge relaxation. All physical quantities including the shape of the droplet and the interfacial charge density, are represented using spherical harmonic expansions. The adoption of a spectral representation offers exponential accuracy and allows for a non-dissipative dealiasing method, required for numerical stability. To avoid grid distortions in the presence of large deformations, we employed a reparametrization technique by minimizing the high-frequency components of the shape, thereby improving the numerical stability of our method.

Our methodology was validated against experimental data and analytical solutions in the axisymmetric Taylor and Quincke electrorotation regimes. This serves as an assessment of the accuracy and reliability of our method. In the case of low-viscosity droplets, strong charge

convection leads to steep interfacial charge gradients which can be challenging for numerical simulations. To address this issue, we adopted a weighted spherical harmonic expansion approach, which enables convergent solutions. Our primary objective in Ch. 5 was to create a robust and versatile numerical solver applicable to interfacially driven flows in drops, including those in electrohydrodynamics.

In Ch. 6, we studied morphological dynamics in a freely-suspended viscous drop with surface nematic activity, inducing non-equilibrium behavior. Nematic order has been observed to play a key role in the development of important biological processes such as cytokinesis and tissue morphogenesis. The system we studied in this chapter serves as a simplified model for understanding complex active living systems, such as cells. Leveraging the computational tools developed in Ch. 5, we employed a spectral boundary integral solver for Stokes flow coupled with a hydrodynamic evolution equation for the nematic tensor to model the complex dynamics of the system. Our study uncovered the intricate interplay between flow, nematic order, and interface mechanics in these systems, leading to self-organized behaviors and symmetry-breaking phenomena, consistent with experimental observations. We observed a diverse range of dynamical behaviors, from periodic braiding motion of topological defects to chaotic creation and annihilation of defects under high activity levels. Our study provides valuable insights into emergent dynamics in biological and biomimetic systems with active fluid surfaces.

## 7.2 Directions for future work

Our research has opened up a number of promising avenues for future investigations. In the following, we outline these directions:

- *EHD interaction of drops with walls:* In an unbounded domain, a leaky dielectric drop immersed in another leaky dielectric fluid exhibits axisymmetric flow when subjected to weak uniform electric fields. However, when a nearby boundary, such as a plane wall, is introduced, the system's symmetry is broken, resulting in a net motion of the drop relative

to the wall. This flow configuration closely resembles various microfluidic applications, such as flow sorting, where electric effects are utilized to manipulate the flow and its inclusions [44]. Additionally, understanding the electric-induced migration is crucial to characterize the flows and rheology of emulsions under external electric fields [160].

Theoretical analysis reveals that the disturbance flow far away from a drop near a wall can be represented by the flow due to a stresslet flow singularity [160]. In the case of an oblate drop, the interaction with the wall is repulsive. Our research focuses on studying the EHD migration of drops in the presence of an insulating wall under an applied tangential electric field. We utilize the computational tools developed in Chapter 5, combined with theoretical analysis and experiments. Our investigation aims to characterize the system's behavior for various viscosity ratios between the drop and the medium, as well as different electrical material properties.

- *Mechanochemical effects in active drops:* In Ch. 6, we studied self-organized behaviors in active drops, focusing on a synthetic active system with uniform activity around the drop. However, living active systems, such as cells, exhibit more complex dynamics. It has been evidenced that chemical cues play a crucial role in biological processes such as cell division [181, 136]. Therefore, exploring the impact of chemical cues on emergent behaviors in these systems is of great interest.

To address this, a theoretical and computational framework is needed, considering a four-way coupling between the transport of chemical species, induced flow in the bulk, orientational order, and the mechanics of the interface. However, tackling such problems is fundamentally challenging due to the nonlinear coupling of different effects and the presence of deforming boundaries.

- *Lagrangian coherent structures in active drops:* In Ch. 6, we employed a topological approach to analyze the behavior of active drops by using braid dynamics. While this method efficiently characterized the topological complexity associated with defect trajectories,

it does not provide further insight into the organization of the induced flows. To gain a better understanding of the flow patterns and their organizing structures, we propose the analysis of the Lagrangian coherent structures (LCSs). LCSs are spatiotemporal organizing structures in the flow, which can be classified as repellers or attractors.

Recent research has applied finite-time Lyapunov exponent (FTLE) analysis to determine and characterize LCSs during the development of chick and *Drosophila* embryos [154]. The collective motion of cells during embryogenesis, occurring over extended time scales, can be effectively modeled as the flow of an active fluid. Notably, it has been discovered that  $+1/2$  defects play a significant role in influencing the motion and deformation of LCSs, making them crucial for controlling the system [152, 159]. Our understanding of LCSs in active drops provides a novel perspective to describe and potentially control their self-organized behavior, with promising applications in the context of biological and biomimetic systems.

# Appendix A

## Electrified liquid films

### A.1 Linear stability analysis

In the base state, all liquid layers are at rest, both interfaces have flat shapes,  $\tilde{\xi}_u = -\tilde{\xi}_l = 1$ , and the electric potential field in each layer reads:

$$\tilde{\varphi}_u(z) = -z + (1 - R), \quad z \geq 1, \quad (\text{A.1})$$

$$\tilde{\varphi}_m(z) = -Rz, \quad -1 \leq z \leq 1, \quad (\text{A.2})$$

$$\tilde{\varphi}_l(z) = -z - (1 - R), \quad z \leq -1, \quad (\text{A.3})$$

for which

$$\tilde{\mathbf{E}}_l = \tilde{\mathbf{E}}_u = R^{-1} \tilde{\mathbf{E}}_m = (0, 1), \quad (\text{A.4})$$

$$\tilde{q}_u = -\tilde{q}_l = (1 - RQ), \quad (\text{A.5})$$

$$\tilde{p}_u - \tilde{p}_m = \tilde{p}_l - \tilde{p}_m = (1 - QR^2)/2. \quad (\text{A.6})$$

After perturbing the base state, we linearize the governing equations and boundary conditions. Next, we seek normal-mode solutions of the form  $\varphi'(x, z, t) = \Re\{\hat{\varphi}(z) \exp(st + ikx)\}$ , with similar expressions for all the variables. Substituting the normal-modes into the governing equations and using the decay properties as  $z \rightarrow \pm\infty$  provides the amplitude of the normal modes

as:

$$\hat{\phi}_u(z) = A_u e^{-kz}, \quad z \geq 1, \quad (\text{A.7})$$

$$\hat{\phi}_m(z) = A_{m1} e^{-kz} + A_{m2} e^{kz}, \quad -1 \leq z \leq 1, \quad (\text{A.8})$$

$$\hat{\phi}_l(z) = A_l e^{kz}, \quad z \leq -1, \quad (\text{A.9})$$

$$\hat{p}_u(z) = B_u e^{-kz}, \quad z \geq 1, \quad (\text{A.10})$$

$$\hat{p}_m(z) = B_{m1} e^{-kz} + B_{m2} e^{kz}, \quad -1 \leq z \leq 1, \quad (\text{A.11})$$

$$\hat{p}_l(z) = B_l e^{kz}, \quad z \leq -1, \quad (\text{A.12})$$

$$\hat{u}_u(z) = C_u e^{-kz} - iB_u \left(\frac{1+\lambda}{2}\right) z e^{-kz}, \quad z \geq 1, \quad (\text{A.13})$$

$$\hat{u}_m(z) = C_{m1} e^{-kz} + C_{m2} e^{kz} - iB_{m1} \left(\frac{1+\lambda^{-1}}{2}\right) z e^{-kz} + iB_{m2} \left(\frac{1+\lambda^{-1}}{2}\right) z e^{kz}, \quad -1 \leq z \leq 1, \quad (\text{A.14})$$

$$\hat{u}_l(z) = C_l e^{kz} + iB_l \left(\frac{1+\lambda}{2}\right) z e^{kz}, \quad z \leq -1, \quad (\text{A.15})$$

$$\hat{w}_u(z) = D_u e^{-kz} + B_u \left(\frac{1+\lambda}{2}\right) z e^{-kz}, \quad z \geq 1, \quad (\text{A.16})$$

$$\hat{w}_m(z) = D_{m1} e^{-kz} + D_{m2} e^{kz} + B_{m1} \left(\frac{1+\lambda^{-1}}{2}\right) z e^{-kz} + B_{m2} \left(\frac{1+\lambda^{-1}}{2}\right) z e^{kz}, \quad -1 \leq z \leq 1, \quad (\text{A.17})$$

$$\hat{w}_l(z) = D_l e^{kz} + B_l \left(\frac{1+\lambda}{2}\right) z e^{kz}, \quad z \leq -1, \quad (\text{A.18})$$

where

$$D_u = iC_u + B_u(1+\lambda)(2k)^{-1}, \quad D_l = -iC_l - B_l(1+\lambda)(2k)^{-1}, \quad (\text{A.19})$$

$$D_{m1} = iC_{m1} + B_{m1}(1+\lambda^{-1})(2k)^{-1}, \quad D_{m2} = -iC_{m2} - B_{m2}(1+\lambda^{-1})(2k)^{-1}. \quad (\text{A.20})$$

Applying the boundary conditions for the perturbation variables results in a linear algebraic

system for the unknown coefficients  $A_j$ ,  $B_j$ ,  $C_j$  and  $D_j$  where  $j \in \{l, m1, m2, u\}$ . Finally, we obtain the dispersion relation by setting the determinant of the algebraic system to zero.

## A.2 Fastest growing mode

The maximum growth rate and the corresponding wavenumber in each mode are defined respectively as  $s_{max}$  and  $k_{max}$ . Figures A.1 and A.2 show how the non-dimensional parameters governing the system affect  $k_{max}$  in each mode.

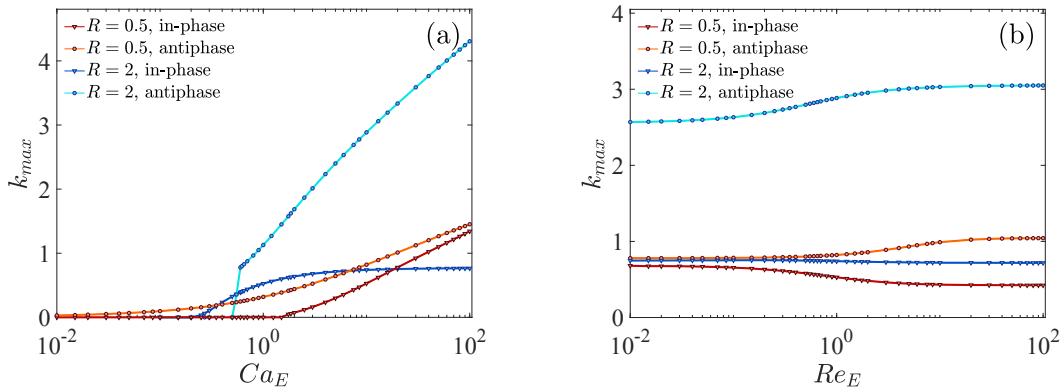


**Figure A.1.** Fastest-growing wavenumber in each mode of instability as a function of: (a) electric capillary number, and (b) electric Reynolds number for two different systems with  $R = 0.5$  and  $R = 2$  with  $(Q, \lambda) = (1, 1)$ .  $Re_E = 1$  in (a) and  $Ca_E = 10$  in (b).

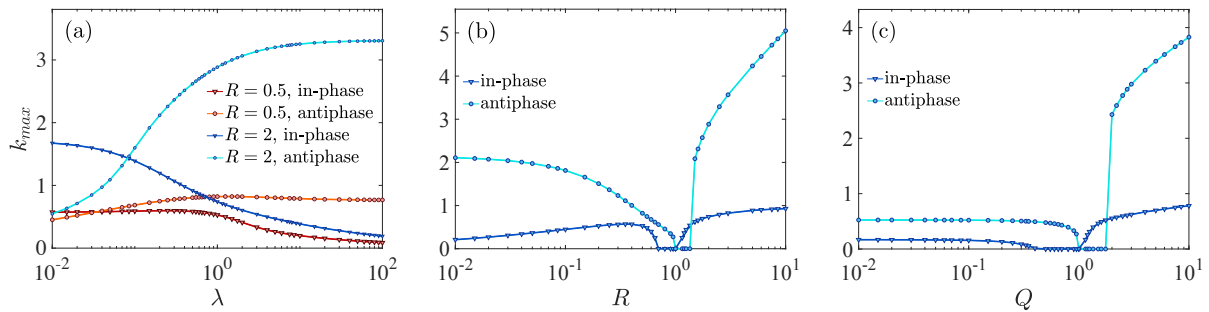


**Figure A.2.** Fastest-growing wavenumber in each mode of instability as a function of: (a) viscosity ratio  $\lambda$  for two different systems with  $R = 0.5$  and  $R = 2$ , (b) conductivity ratio  $R$ , and (c) permittivity ratio  $Q$ . The permittivity ratio is set to  $Q = 1$  in (a,b), the conductivity ratio is  $R = 1$  in (c) and  $\lambda = 1$  in (b,c). In all systems  $(Ca_E, Re_E) = (10, 1)$ .

### **A.3 Nonlinear regime**

The development of the flow and charge dynamics in antiphase instabilities gives rise to the formation of tip streaming jets during the nonlinear regime. On the other hand, during in-phase instability, we observe inward and outward jets that intrude the film and the suspending phase, respectively. Figures A.3 and A.4 show the effect of the mismatch in the different material properties on the evolution of the emerging jets in each mode.

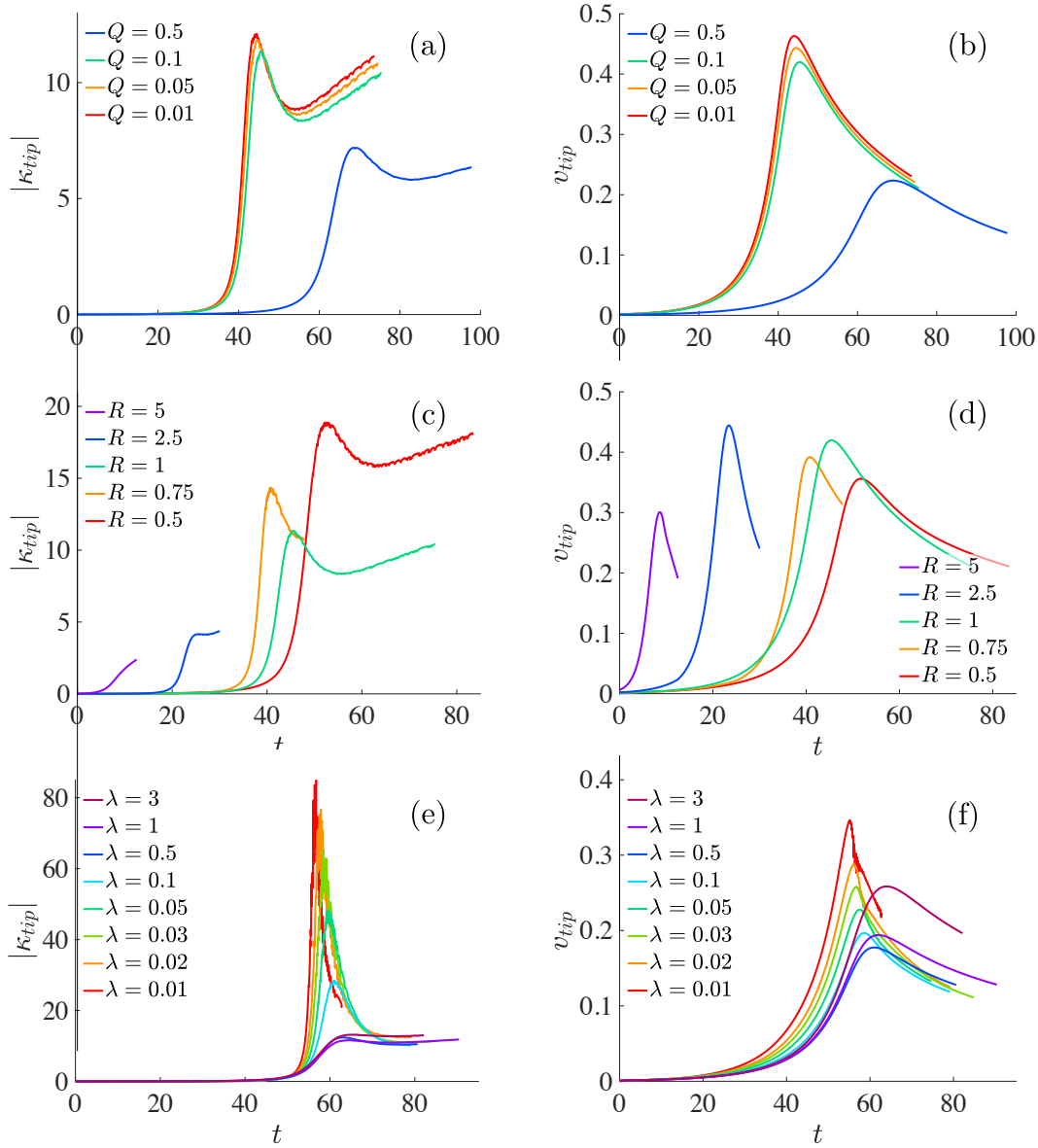


**Figure A.3.** Evolution of the tip streaming jets during antiphase instability as a function of: (a,b) permittivity ratio in system **S4**, (c,d) conductivity ratio in system **S3**, and (e,f) viscosity ratio in system **S5**. Left and right columns show the evolution of the tip curvature and vertical tip velocity, respectively.

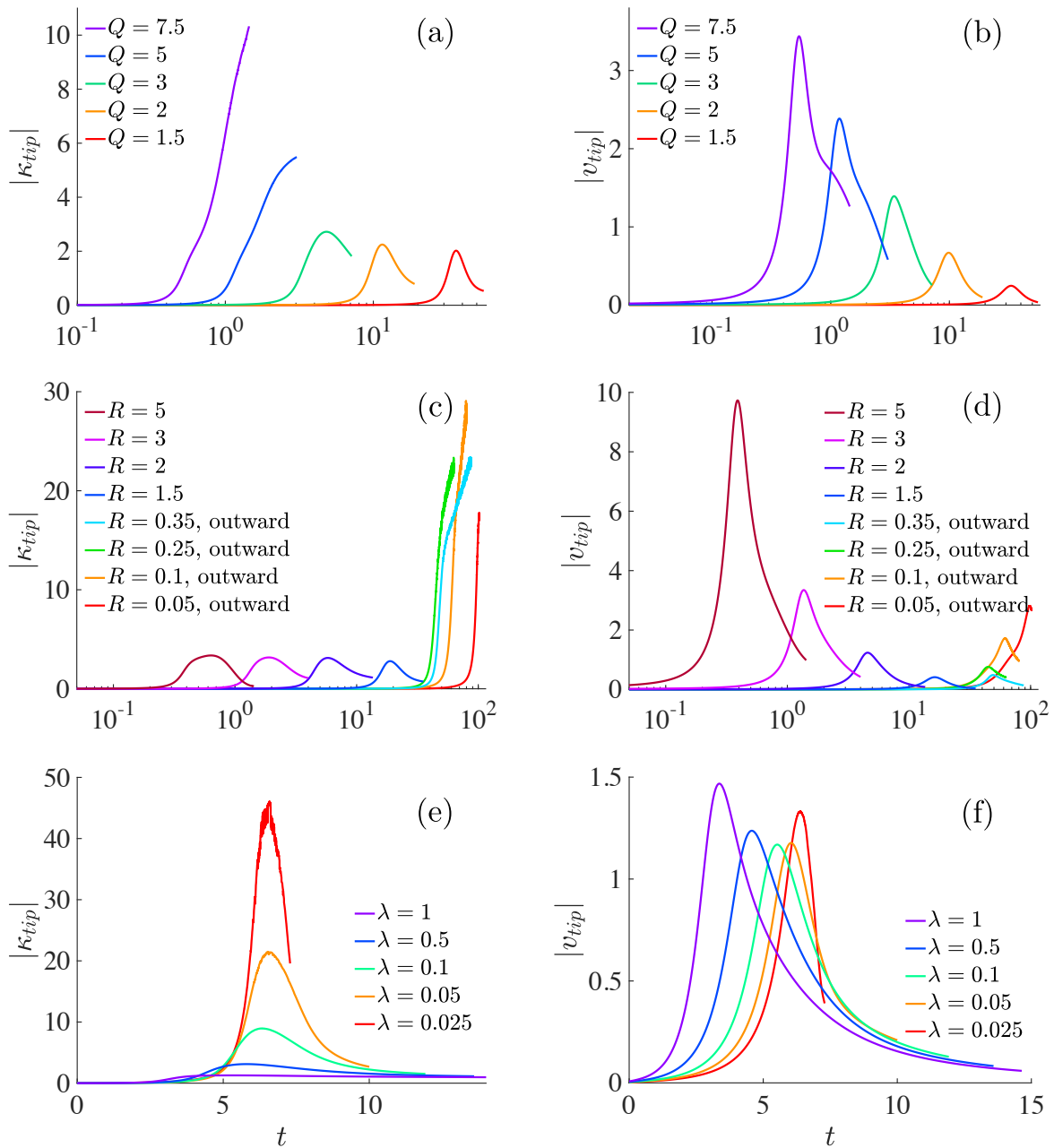


**Figure A.4.** Evolution of the inward and outward jets during in-phase instability as a function of: (a,b) permittivity ratio in system **S4**, (c,d) conductivity ratio in system **S6**, and (e,f) viscosity ratio in system **S7**. Left and right columns show the evolution of the tip curvature and vertical tip velocity, respectively.

# Appendix B

## Differential geometry of curved surfaces

In this section, we provide a summary of the notations and relationships used in the differential geometry of curved surfaces. Let us consider a two-dimensional surface embedded in  $\mathbb{R}^3$  and described by the position vector  $\mathbf{r} = \mathbf{r}(s^1, s^2)$  in terms of two surface coordinates  $s^1$  and  $s^2$ . In this context, Latin indices (e.g.,  $i, j, k, \dots$ ) correspond to surface coordinates, meaning that they can take values of 1 or 2. It is important to note that we will use the Einstein summation convention throughout our derivations.

The local tangent vectors, and the unit normal vector are respectively given as:

$$\mathbf{g}_i = \frac{\partial \mathbf{r}}{\partial s^i} = \partial_i \mathbf{r}, \quad (\text{B.1})$$

$$\mathbf{v} = \frac{\mathbf{g}_1 \times \mathbf{g}_2}{|\mathbf{g}_1 \times \mathbf{g}_2|}, \quad (\text{B.2})$$

where  $\partial_i$  denotes the partial derivative with respect to  $s^i$ . The associated covariant surface metric, and the curvature tensor are defined as:

$$g_{ij} = \mathbf{g}_i \cdot \mathbf{g}_j, \quad (\text{B.3})$$

$$C_{ij} = -\partial_i \partial_j \mathbf{r} \cdot \mathbf{v} = \partial_j \mathbf{r} \cdot \partial_i \mathbf{v}. \quad (\text{B.4})$$

The determinant of the metric  $g = \det g_{ij}$  is proportional to the area of the local surface element via  $dA = \sqrt{g} ds^1 ds^2$ . The inverse of the metric is denoted by  $g^{ij}$ , and is defined as  $g^{ik} g_{kj} = \delta_j^i$ ,

where  $\delta_j^i$  represents the Kronecker delta. Furthermore, the contravariant tangent basis  $(\mathbf{g}^1, \mathbf{g}^2)$  is defined as:

$$\mathbf{g}^i \cdot \mathbf{g}_j = \delta_j^i. \quad (\text{B.5})$$

The Levi-Civita tensor of the curved surface is defined as:

$$\epsilon_{ij} = \mathbf{v} \cdot (\mathbf{g}_i \times \mathbf{g}_j), \quad (\text{B.6})$$

and has skew-symmetric property. It satisfies the following identity:

$$\epsilon_{ij} \epsilon^{jk} = -\delta_i^k. \quad (\text{B.7})$$

and is used to express vectorial products of the basis vectors:

$$\mathbf{g}_i \times \mathbf{g}_j = \epsilon_{ij} \mathbf{n}, \quad (\text{B.8})$$

$$\mathbf{n} \times \mathbf{g}_i = \epsilon_i^j \mathbf{g}_j. \quad (\text{B.9})$$

Using the local tangent basis, we can express vector  $\mathbf{a}$ , or tensor  $\mathbf{T}$  in terms of their components:

$$\mathbf{a} = a^i \mathbf{g}_i = a^j \mathbf{g}_j, \quad (\text{B.10})$$

$$\mathbf{T} = T^{ij} \mathbf{g}_i \mathbf{g}_j = T_{ij} \mathbf{g}^i \mathbf{g}^j. \quad (\text{B.11})$$

*Index Juggling*, or the operation of lowering or raising indices are performed using metric tensors:

$$a^i = a_j g^{ji}, \quad (\text{B.12})$$

$$a_i = a^j g_{ji}, \quad (\text{B.13})$$

$$T^{ij} = T_{kl} g^{ki} g^{lj}, \quad (\text{B.14})$$

$$T_j^i = T^{ik} g_{kj}, \quad (\text{B.15})$$

$$\partial^j = g^{ji} \partial_i. \quad (\text{B.16})$$

We note that the partial derivative of a tensor is not a tensor itself. Therefore, one must use the *covariant derivative* to obtain a tensor. For a general surface tensor  $T_j^i$ , the covariant derivative  $\nabla_k$  is defined as:

$$\nabla_k T_j^i = \partial_k T_j^i + \Gamma_{kl}^i T_j^l - \Gamma_{kj}^l T_l^i, \quad (\text{B.17})$$

The first term on the right-hand side represents the rate of change in the component  $T_j^i$  while the last two terms take into account the change of basis. The Christoffel symbols  $\Gamma_{kl}^i$  and  $\Gamma_{kj}^l$  used in (B.17) are defined as:

$$\Gamma_{jk}^i = \mathbf{g}_i \cdot \partial_k \mathbf{g}_j. \quad (\text{B.18})$$

More comprehensive discussions and derivations related to the geometry of curved surfaces can be found in [71, 114], as well as other textbooks that cover similar topics in differential geometry.

# Appendix C

## Active drops

### C.1 Simulation parameters

Below is the list of all parameters used in our simulations. We observed that changing the viscosity ratio does not affect the overall behavior of the system.

**Table C.1.** Non-dimensional parameters used in the simulations of active drops.

$l_c$	$a$	$b$	$c$	$\zeta$	$\lambda$	Pe	Ca
0.16	-1.33	-1	2	0.5	1	variable	variable
0.32	-1.33	-1	1.67	0.5	1	variable	variable

### C.2 Defect dynamics in spherical active drops

In Sec. 6.5.1, we discussed that the topological defects undergo braiding motion beyond a critical Peclet number  $Pe_c$ . During the braiding motion, the average angle  $\alpha$  exhibits oscillations between  $109.5^\circ$  and  $120^\circ$ , corresponding to symmetric tetrahedral and planar configurations, respectively. For relatively small values of  $Pe > Pe_c$ , the fast-Fourier transform (FFT) of  $\alpha$  exhibits a single peak, as shown in Fig. C.1. However, as we increase  $Pe$ , a second peak emerges as depicted in Fig. C.2. This indicates the presence of two important time scales in the system dynamics. At even larger values of  $Pe$ , a range of time scales is observed, as illustrated in Fig. C.3, suggesting highly nonlinear and complex behavior in the active drop. We denote the two most dominant frequencies obtained by FFT as  $f_1$  and  $f_2$ , with  $f_1$  being the most dominant. Figure

C.4 presents the variations of  $f_1$  and  $f_2$  as functions of  $Pe$ .

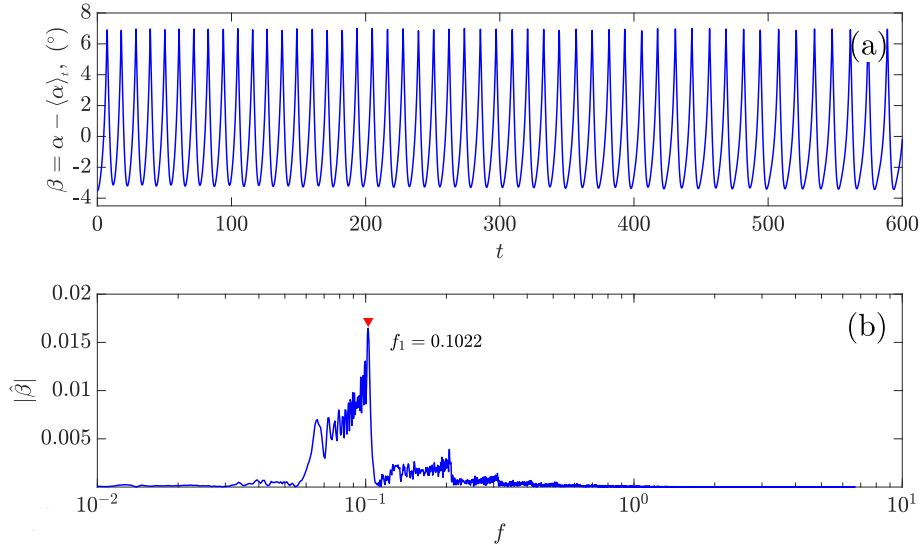


**Figure C.1.** (a) Zero-mean oscillations of the average angle,  $\beta = \alpha - \langle \alpha \rangle_t$  (in degrees  $^\circ$ ), for an active drop with  $(Ca, l_c, Pe) = (0.01, 0.16, 0.3)$ . Only 38% of the time series is displayed for better visualization. (b) Corresponding FFT spectrum displaying a single peak frequency  $f_1$ , indicated by a triangle.

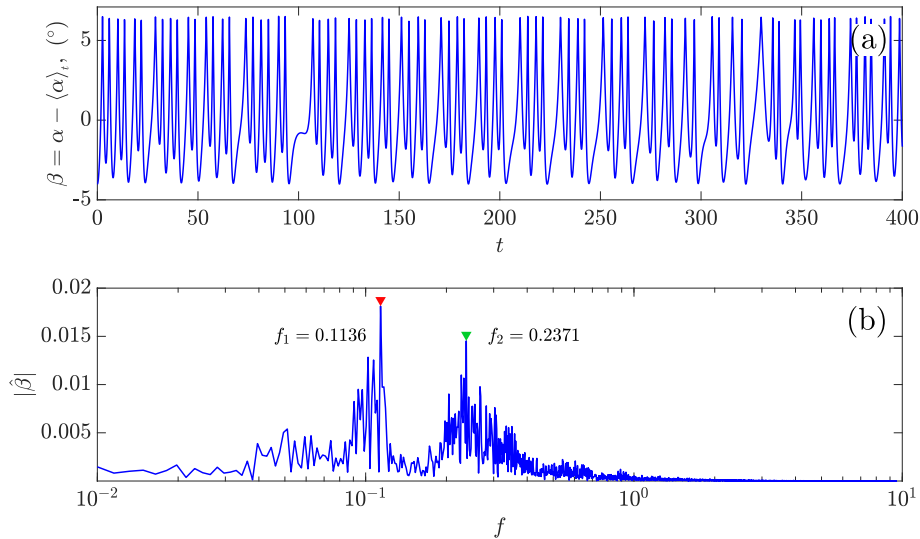


**Figure C.2.** (a) Zero-mean oscillations of the average angle,  $\beta = \alpha - \langle \alpha \rangle_t$  (in degrees  $^\circ$ ), for an active drop with  $(Ca, l_c, Pe) = (0.01, 0.16, 0.75)$ . Only 46% of the time series is displayed for better visualization. (b) The corresponding FFT spectrum displays two peaks, indicated by red ( $f_1$ ) and green ( $f_2$ ) triangles.

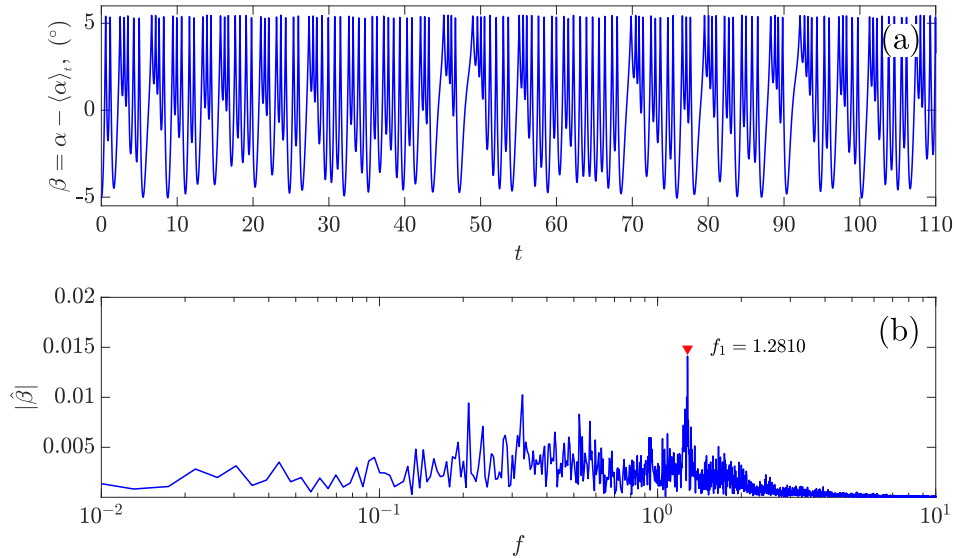


**Figure C.3.** (a) Zero-mean oscillations of the average angle,  $\beta = \alpha - \langle \alpha \rangle_t$  (in degrees  $^\circ$ ), for an active drop with  $(Ca, l_c, Pe) = (0.01, 0.16, 3)$ . Only 47% of the time series is displayed for better visualization. (b) The corresponding FFT spectrum showing a range of important time scales. The most dominant frequency  $f_1$  is marked by a triangle.

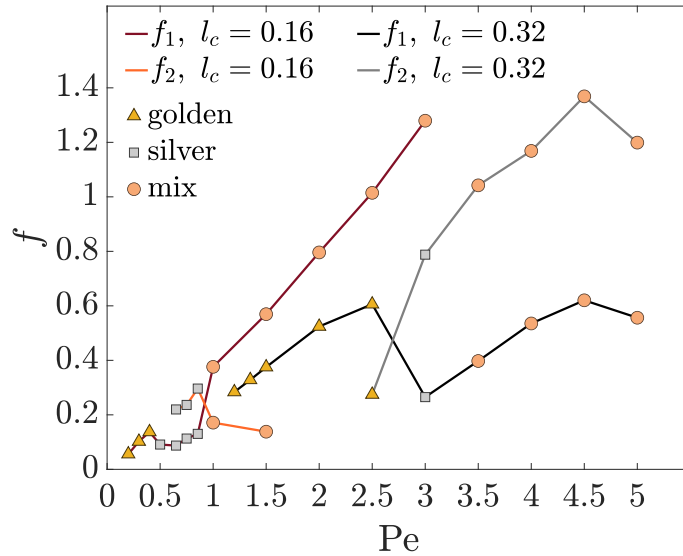


**Figure C.4.** The first and second most dominant frequencies ( $f_1$  and  $f_2$ ) derived from the FFT analysis of the average angle  $\alpha$  as a function of  $Pe$  and  $l_c$ , for an active drop with  $Ca = 0.01$ . Each marker represents a distinct dynamical phase characterized by a specific braiding pattern: golden (triangle), silver (square), and mix (circle).

### C.3 Energy conservation in a an active drop

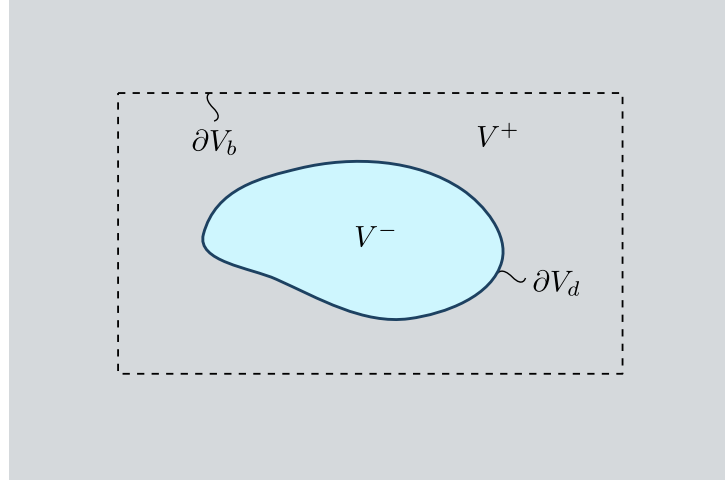


**Figure C.5.** An immersed drop with interfacial activity.

Consider a drop immersed in an immiscible fluid with interfacial activity, as discussed in Sec. 6.2. The schematic of the problem is depicted in Figure C.5. The total viscous dissipation in an imaginary box represented by  $\partial V_b$  is given by:

$$P_v(t) = \int_{V^+ \cup V^-} E_{jk} \tau_{kj} \, d\nu = \int_{V^+} 2\mu^+ E_{jk} E_{kj} \, d\nu + \int_{V^-} 2\mu^- E_{jk} E_{kj} \, d\nu, \quad (\text{C.1})$$

where  $E_{jk} = \frac{1}{2} \left( \frac{\partial u_j}{\partial x_k} + \frac{\partial u_k}{\partial x_j} \right)$  is the strain rate tensor and  $\tau_{jk} = 2\mu E_{jk}$  is the Newtonian viscous stress tensor. By expanding  $\mu^\pm E_{jk} E_{kj}$  and simplifying the results using Stokes equation and incompressibility, we obtain:

$$\mu^\pm E_{jk} E_{kj} = \frac{\mu^\pm}{2} \left[ \frac{\partial u_j}{\partial x_k} \frac{\partial u_j}{\partial x_k} + \frac{\partial u_k}{\partial x_j} \frac{\partial u_j}{\partial x_k} \right] \quad (\text{C.2})$$

$$= \frac{\mu^\pm}{2} \left[ \frac{\partial}{\partial x_k} \left( u_j \frac{\partial u_j}{\partial x_k} \right) - u_j \frac{\partial^2 u_j}{\partial x_k^2} + \frac{\partial}{\partial x_k} \left( u_j \frac{\partial u_k}{\partial x_j} \right) - u_j \frac{\partial}{\partial x_j} \left( \frac{\partial u_k}{\partial x_k} \right) \right] \quad (\text{C.3})$$

$$= \frac{\mu^\pm}{2} \left[ \frac{\partial}{\partial x_k} \left( u_j \frac{\partial u_j}{\partial x_k} \right) + \frac{\partial}{\partial x_k} \left( u_j \frac{\partial u_k}{\partial x_j} \right) \right] - u_j \frac{\partial p}{\partial x_j}. \quad (\text{C.4})$$

Substituting (C.4) into (C.1) and applying the divergence theorem, we get:

$$P_v(t) = \int_{\partial V_b} n_k \left[ \mu^+ \left( \frac{\partial u_j}{\partial x_k} + \frac{\partial u_k}{\partial x_j} \right) - p \delta_{kj} \right] u_j ds + \int_{\partial V_d} n_k \left[ \mu^+ \left( \frac{\partial u_j}{\partial x_k} + \frac{\partial u_k}{\partial x_j} \right) - p \delta_{kj} \right] u_j ds \quad (\text{C.5})$$

$$- \int_{\partial V_d} n_k \left[ \mu^- \left( \frac{\partial u_j}{\partial x_k} + \frac{\partial u_k}{\partial x_j} \right) - p \delta_{kj} \right] u_j ds, \quad (\text{C.6})$$

where  $n_k$  is the unit normal vector pointing to  $V^+$ . Taking the limit of  $\partial V_b \rightarrow \infty$  enables us to determine the total viscous dissipation in space. In this limit, the contribution from the first integral of (C.5) vanishes, leading us to the following equation:

$$P_v(t) = \int_{\partial V_d} n_k \left[ \left[ \mu^+ \left( \frac{\partial u_j}{\partial x_k} + \frac{\partial u_k}{\partial x_j} \right) - p \delta_{kj} \right] - \left[ \mu^- \left( \frac{\partial u_j}{\partial x_k} + \frac{\partial u_k}{\partial x_j} \right) - p \delta_{kj} \right] \right] u_j ds. \quad (\text{C.7})$$

Finally, we write (C.7) in terms of the jump in the hydrodynamic traction  $\mathbf{f}^H$  as:

$$P_v(t) = \int_{\partial V_d} f_j^H u_j ds = \int E_{jk} \tau_{kj} dv. \quad (\text{C.8})$$

The significance of (C.8) lies in its representation of the total viscous dissipation in space as an integral over the surface of the drop. Combining (C.8) with the force balance equations (6.6) and (6.7), we obtain the relationships for  $P_a(t)$  and  $P_c(t)$ , which represent active and capillary powers, respectively:

$$P_v(t) + P_a(t) + P_c(t) = 0, \quad (\text{C.9})$$

$$P_v(t) = \int_{\partial V_d} \mathbf{f}^H \cdot \mathbf{u} ds, \quad (\text{C.10})$$

$$P_a(t) = \int_{\partial V_d} \mathbf{f}^a \cdot \mathbf{u} ds, \quad (\text{C.11})$$

$$P_c(t) = \int_{\partial V_d} -(\gamma 2H \mathbf{n}) \cdot \mathbf{u} ds. \quad (\text{C.12})$$

In (C.12)  $H$  is the mean curvature and  $\gamma$  is the surface tension. In the limit of small deformations, the drop maintains its spherical shape, and the velocity field remains tangential all over the drop

interface, indicating that  $\mathbf{n} \cdot \mathbf{u} = 0$ . As a result, we can conclude that  $P_c(t) = 0$ , resulting in the following relationship:

$$P_v(t) + P_a(t) = 0. \quad (\text{C.13})$$

This relationship means that the active power injected into the system at the interface is dissipated by viscous effects in the bulk. It is important to note that under finite deformations, the capillary power  $P_c$  is generally nonzero and could take positive or negative values.

## C.4 Active drops under finite deformations

As discussed in Sec. 6.5.2, the active drop reaches an equilibrium state for Peclet numbers up to  $Pe_{eq}$ , under finite capillary numbers. Specifically, we observed that for  $l_c = 0.16$ , the values of  $Pe_{eq}$  are approximately 5 and 4 under  $Ca = 0.3$  and  $0.5$ , respectively. On the other hand, for  $l_c = 0.32$ , the system reaches a steady state for all Peclet number values studied, i.e.,  $0 < Pe < 12$ .

With increasing  $Pe$ , the system transitions to a chaotic regime characterized by the creation and annihilation of defects. Figure C.6 displays snapshots of the nematic field on the drop surface, during the chaotic regime. We note that Fig. C.6 corresponds to the same system studied in Fig. 6.8, featuring more time steps for more detailed visualization.

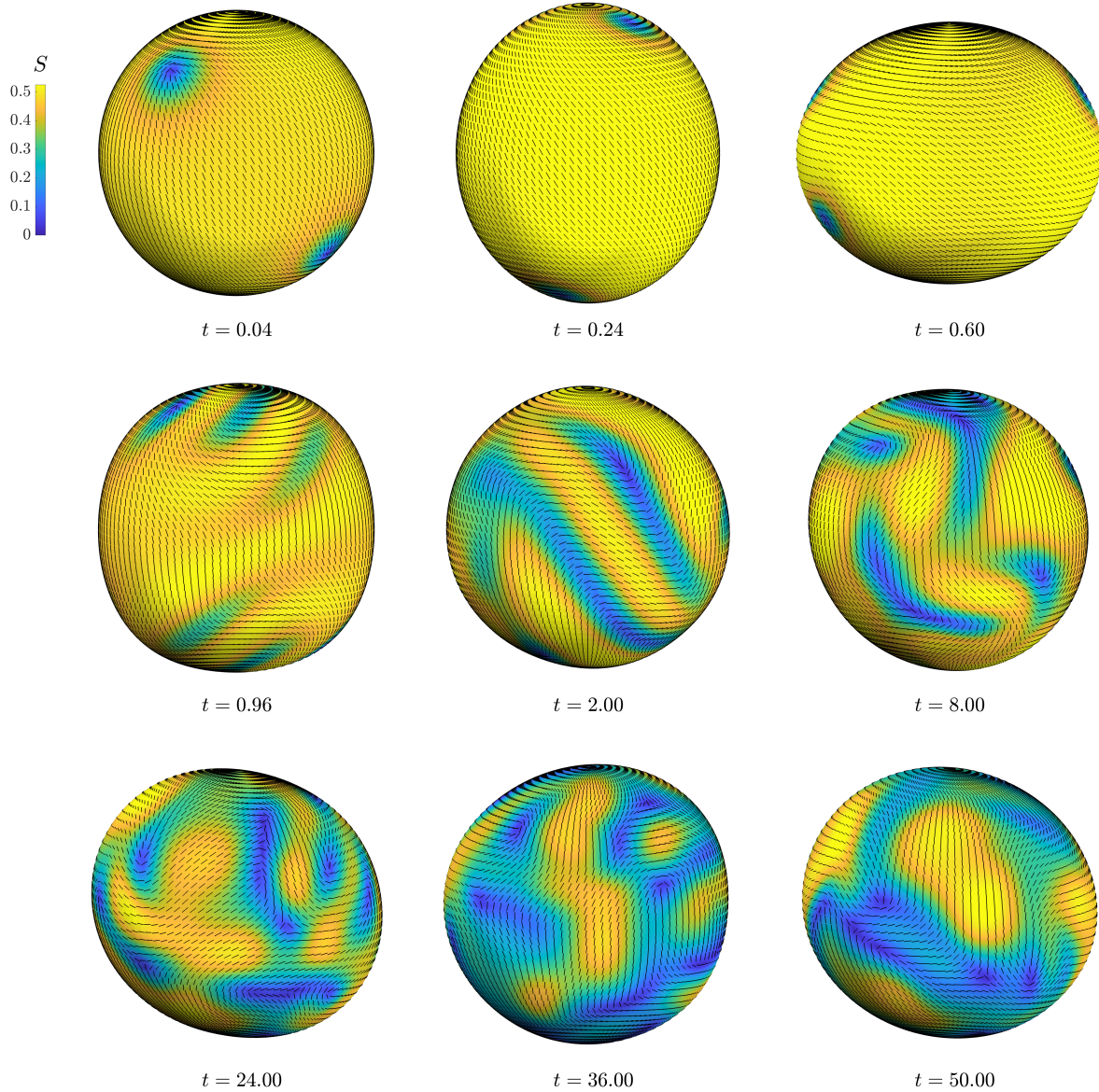


**Figure C.6.** Snapshots of an active drop displaying chaotic behavior under a strong activity and finite deformations. In this regime, new pairs of  $\pm 1/2$  defects are continuously created and annihilated. The director field is depicted along with the scalar order parameter as the colormap for an active drop with  $(Ca, l_c, Pe) = (0.5, 0.16, 10)$ .

# Bibliography

- [1] J. C. Adams and P. Swarztrauber. Spherepack 3.0: A model development facility. *Mon. Wea. Rev.*, 127(8):1872–1878, 1999.
- [2] O. O. Ajayi. A note on Taylor’s electrohydrodynamic theory. *Proc. R. Soc. A*, 364(1719):499–507, 1978.
- [3] S. C. Al-Izzi and R. G. Morris. Morphodynamics of active nematic fluid surfaces. *J. Fluid Mech.*, 957:A4, 2023.
- [4] J. L. Anderson. Colloid transport by interfacial forces. *Annu. Rev. Fluid Mech.*, 21(1):61–99, 1989.
- [5] S. L. Anna. Droplets and bubbles in microfluidic devices. *Annu. Rev. Fluid Mech.*, 48:285–309, 2016.
- [6] A. Barrero and I. G. Loscertales. Micro- and nanoparticles via capillary flows. *Annu. Rev. Fluid Mech.*, 39:89–106, 2007.
- [7] S. F. Bart, L. S. Tavrow, M. Mehregany, and J. H. Lang. Microfabricated electrohydrodynamic pumps. *Sens. Actuator A Phys.*, 21(1-3):193–197, 1990.
- [8] O. A. Basaran, H. Gao, and P. P. Bhat. Nonstandard inkjets. *Annu. Rev. Fluid Mech.*, 45:85–113, 2013.
- [9] T. Baumgart, S. T. Hess, and W. W. Webb. Imaging coexisting fluid domains in biomembrane models coupling curvature and line tension. *Nature*, 425(6960):821–824, 2003.
- [10] J. C. Baygents, N. J. Rivette, and H. A. Stone. Electrohydrodynamic deformation and interaction of drop pairs. *J. Fluid Mech.*, 368:359–375, 1998.
- [11] J. C. Baygents and D. A. Saville. Electrophoresis of drops and bubbles. *J. Chem. Soc., Faraday trans.*, 87(12):1883–1898, 1991.
- [12] M. Z. Bazant. Electrokinetics meets electrohydrodynamics. *J. Fluid Mech.*, 782:1–4, 2015.
- [13] M. Z. Bazant and T. M. Squires. Induced-charge electrokinetic phenomena. *Curr. Opin. Colloid Interface Sci.*, 15(3):203–213, 2010.

- [14] J. S. Birman. *Braids, links, and mapping class groups*. Number 82. Princeton University Press, 1974.
- [15] E. Bjørklund. The level-set method applied to droplet dynamics in the presence of an electric field. *Comput. Fluids*, 38(2):358–369, 2009.
- [16] M. G. Blyth and C. Pozrikidis. Stagnation-point flow against a liquid film on a plane wall. *Acta Mech.*, 180:203–219, 2005.
- [17] J. P. Boyd. *Chebyshev and Fourier spectral methods*. Courier Corporation, 2001.
- [18] P. L. Boyland, H. Aref, and M. A. Stremler. Topological fluid mechanics of stirring. *J. Fluid Mech.*, 403:277–304, 2000.
- [19] P. L. Boyland, M. Stremler, and H. Aref. Topological fluid mechanics of point vortex motions. *Phys. D: Nonlinear Phenom.*, 175(1-2):69–95, 2003.
- [20] Q. Brosseau and P. M. Vlahovska. Streaming from the equator of a drop in an external electric field. *Phys. Rev. Lett.*, 119:034501, 2017.
- [21] O. P. Bruno and L. A. Kunyansky. A fast, high-order algorithm for the solution of surface scattering problems: basic implementation, tests, and applications. *J. Comput. Phys.*, 169(1):80–110, 2001.
- [22] S. H. Bryngelson and J. B. Freund. Floquet stability analysis of capsules in viscous shear flow. *J. Fluid Mech.*, 852:663–677, 2018.
- [23] S. H. Bryngelson and J. B. Freund. Global stability of flowing red blood cell trains. *Phys. Rev. Fluids*, 3:073101, 2018.
- [24] S. H. Bryngelson and J. B. Freund. Non-modal Floquet stability of a capsule in large amplitude oscillatory extension. *Eur. J. Mech. B Fluids.*, 77:171–176, 2019.
- [25] S. H. Bryngelson, F. Guéniat, and J. B. Freund. Irregular dynamics of cellular blood flow in a model microvessel. *Phys. Rev. E*, 100:012203, 2019.
- [26] M. Budišić and J.-L. Thiffeault. Finite-time braiding exponents. *Chaos*, 25(8), 2015.
- [27] A. C. Callan-Jones, V. Ruprecht, S. Wieser, C. P. Heisenberg, and R. Voituriez. Cortical flow-driven shapes of nonadherent cells. *Phys. Rev. Lett.*, 116(2):028102, 2016.
- [28] C. Canuto, M. Y. Hussaini, A. Quarteroni, and T. A. Thomas. *Spectral methods in fluid dynamics*. Springer, 2012.
- [29] K. J. Chalut and E. K. Paluch. The actin cortex: a bridge between cell shape and function. *Dev. Cell*, 38(6):571–573, 2016.
- [30] L. T. Cherney. Electrohydrodynamics of electrified liquid menisci and emitted jets. *J. Aerosol Sci.*, 30(7):851–862, 1999.

- [31] S. Y. Chou and L. Zhuang. Lithographically induced self-assembly of periodic polymer micropillar arrays. *J. Vac. Sci. Technol. B: Nanotechnol. Microelectron.*, 17(6):3197–3202, 1999.
- [32] M. K. Chung, S. M. Robbins, K. M. Dalton, R. J. Davidson, A. L. Alexander, and A. C. Evans. Cortical thickness analysis in autism with heat kernel smoothing. *NeuroImage*, 25(4):1256–1265, 2005.
- [33] R. T. Collins, J. J. Jones, M. T. Harris, and O. A. Basaran. Electrohydrodynamic tip streaming and emission of charged drops from liquid cones. *Nat. Phys.*, 4(2):149–154, 2008.
- [34] R. T. Collins, K. Sambath, M. T. Harris, and O. A. Basaran. Universal scaling laws for the disintegration of electrified drops. *Proc. Natl. Acad. Sci. U.S.A.*, 110:4905–4910, 2013.
- [35] R. V. Craster and O. K. Matar. Electrically induced pattern formation in thin leaky dielectric films. *Phys. Fluids*, 17(3):032104, 2005.
- [36] H. B. da Rocha, J. Bleyer, and H. Turlier. A viscous active shell theory of the cell cortex. *J. Mech. Phys. Solids*, 164:104876, 2022.
- [37] D. D’Alessandro, M. Dahleh, and I. Mezic. Control of mixing in fluid flow: A maximum entropy approach. *IEEE Trans. Autom. Control*, 44(10):1852–1863, 1999.
- [38] J. Darabi, M. M. Ohadi, and D. DeVoe. An electrohydrodynamic polarization micropump for electronic cooling. *J. Microelectromech. Syst.*, 10(1):98–106, 2001.
- [39] D. Das and D. Saintillan. Electrohydrodynamics of viscous drops in strong electric fields: numerical simulations. *J. Fluid Mech.*, 829:127–152, 2017.
- [40] D. Das and D. Saintillan. A nonlinear small-deformation theory for transient droplet electrohydrodynamics. *J. Fluid Mech.*, 810:225–253, 2017.
- [41] C. de Boor. *A Practical Guide to Splines*. Springer-Verlag New York, 1978.
- [42] P.-G. De Gennes and J. Prost. *The physics of liquid crystals*. Number 83. Oxford university press, 1993.
- [43] D. Dell’Arciprete, M. L. Blow, A. T. Brown, F. D. C. Farrell, J. S. Lintuvuori, A. F. McVey, D. Marenduzzo, and W. C. K. Poon. A growing bacterial colony in two dimensions as an active nematic. *Nat. Commun.*, 9(1):4190, 2018.
- [44] I. Doh and Y.-H. Cho. A continuous cell separation chip using hydrodynamic dielectrophoresis (dep) process. *Sensors and Actuators A: Physical*, 121(1):59–65, 2005.
- [45] P. Dommersnes, Z. Rozynek, A. Mikkelsen, R. Castberg, K. Kjerstad, K. Hersvik, and J. Otto Fossum. Active structuring of colloidal armour on liquid drops. *Nat. Commun.*, 4(1):1–8, 2013.

- [46] G. Duclos, C. Erlenkämper, J.-F. Joanny, and P. Silberzan. Topological defects in confined populations of spindle-shaped cells. *Nat. Phys.*, 13(1):58–62, 2017.
- [47] E. Fadell and J. Van Buskirk. On the braid groups of  $e_2$  and  $s_2$ . *Bull. Amer. Math. Soc.*, 67:211–213, 1961.
- [48] A. Fathi. Travaux de thurston sur les surfaces. *Seminaire Orsay, Asterisque, Soc. Math. France, Paris, 1979*, pages 66–67, 1979.
- [49] J. Q. Feng. Electrohydrodynamic behaviour of a drop subjected to a steady uniform electric field at finite electric Reynolds number. *Proc. R. Soc. A*, 455(1986):2245–2269, 1999.
- [50] J. Q. Feng. A 2D electrohydrodynamic model for electrorotation of fluid drops. *J. Colloid Interface Sci.*, 246(1):112–121, 2002.
- [51] J. Q. Feng and T. C. Scott. A computational analysis of electrohydrodynamics of a leaky dielectric drop in an electric field. *J. Fluid Mech.*, 311:289–326, 1996.
- [52] J. Fernández de La Mora. The fluid dynamics of Taylor cones. *Annu. Rev. Fluid Mech.*, 39:217–243, 2007.
- [53] M. D. Finn, S. M. Cox, and H. M. Byrne. Topological chaos in inviscid and viscous mixers. *J. Fluid Mech.*, 493:345–361, 2003.
- [54] M. D. Finn and J.-L. Thiffeault. Topological optimization of rod-stirring devices. *SIAM review*, 53(4):723–743, 2011.
- [55] M. Firouznia, S. H. Bryngelson, and D. Saintillan. Spectral Boundary Integral Solver for Electrohydrodynamic Flows in Viscous Drops, October 2022. Version 1.0.
- [56] M. Firouznia, S. H. Bryngelson, and D. Saintillan. A spectral boundary integral method for simulating electrohydrodynamic flows in viscous drops. *J. Comput. Phys.*, 489:112248, 2023.
- [57] M. Firouznia, M. J. Miksis, P. M. Vlahovska, and D. Saintillan. Instability of a planar fluid interface under a tangential electric field in a stagnation point flow. *J. Fluid Mech.*, 931:A25, 2022.
- [58] M. Firouznia and D. Saintillan. Electrohydrodynamic instabilities in freely suspended viscous films under normal electric fields. *Phys. Rev. Fluids*, 6(10):103703, 2021.
- [59] V. Frayssé, L. Giraud, S. Gratton, and J. Langou. Algorithm 842: A set of GMRES routines for real and complex arithmetics on high performance computers. *ACM Trans. Math. Software*, 31:228–238, 2005.
- [60] J. B. Freund. The flow of red blood cells through a narrow spleen-like slit. *Phys. Fluids*, 25(11):110807, 2013.

- [61] A. M. Ganan-Calvo, J. Davila, and A. Barrero. Current and droplet size in the electro-spraying of liquids. Scaling laws. *J. Aerosol Sci.*, 28(2):249–275, 1997.
- [62] A. M. Ganan-Calvo, J. M. López-Herrera, M. A. Herrada, A. Ramos, and J. M. Montanero. Review on the physics of electrospray: From electrokinetics to the operating conditions of single and coaxial Taylor cone-jets, and ac electrospray. *J. Aerosol Sci.*, 125:32–56, 2018.
- [63] A. M. Ganan-Calvo, J. M. López-Herrera, N. Rebollo-Munoz, and J. M. Montanero. The onset of electrospray: the universal scaling laws of the first ejection. *Sci. Rep.*, 6:32357, SEP 1 2016.
- [64] A. M. Ganan-Calvo and J. M. Montanero. Revision of capillary cone-jet physics: Electrospray and flow focusing. *Phys. Rev. E*, 79:066305, JUN 2009.
- [65] A. Gelb. The resolution of the Gibbs phenomenon for spherical harmonics. *Math. Comput.*, 66(218):699–717, 1997.
- [66] L. Giomi. Geometry and topology of turbulence in active nematics. *Phys. Rev. X*, 5(3):031003, 2015.
- [67] N. W. Goehring, Ph. K. Trong, J. S. Bois, D. Chowdhury, E. M. Nicola, A. A. Hyman, and S. W. Grill. Polarization of par proteins by advective triggering of a pattern-forming system. *Science*, 334(6059):1137–1141, 2011.
- [68] E. Guillard, J.-L. Thiffeault, and M. D. Finn. Topological mixing with ghost rods. *Phys. Rev. E*, 73(3):036311, 2006.
- [69] R. Green, J. Toner, and V. Vitelli. Geometry of thresholdless active flow in nematic microfluidics. *Phys. Rev. Fluids*, 2(10):104201, 2017.
- [70] E. M. Griffing, S. G. Bankoff, M. J. Miksis, and R. A. Schluter. Electrohydrodynamics of thin flowing films. *J. Fluid Eng.*, 128:276–283, 2006.
- [71] P. Grinfeld. *Introduction to tensor analysis and the calculus of moving surfaces*. Springer, 2013.
- [72] P. Guillamat, C. Blanch-Mercader, G. Pernellet, K. Kruse, and A. Roux. Integer topological defects organize stresses driving tissue morphogenesis. *Nat. Mater.*, 21(5):588–597, 2022.
- [73] P. Guillamat, Z. Kos, J. Hardouin, J. Ignés-Mullol, M. Ravnik, and F. Sagués. Active nematic emulsions. *Sci. Adv.*, 4(4):eaao1470, 2018.
- [74] J. W. Ha and S. M. Yang. Electrohydrodynamics and electrorotation of a drop with fluid less conductive than that of the ambient fluid. *Phys. Fluids*, 12(4):764–772, 2000.
- [75] R. J. Hawkins, R. Poincloux, O. Bénichou, M. Piel, P. Chavrier, and R. Voituriez. Spontaneous contractility-mediated cortical flow generates cell migration in three-dimensional environments. *Biophys. J.*, 101(5):1041–1045, 2011.

- [76] H. He, P. F. Salipante, and P. M. Vlahovska. Electrorotation of a viscous droplet in a uniform direct current electric field. *Phys. Fluids*, 25(3):032106, 2013.
- [77] M. A. Herrada, J. M. López-Herrera, A. M. Gañán Calvo, E. J. Vega, J. M. Montanero, and S. Popinet. Numerical simulation of electrospray in the cone-jet mode. *Phys. Rev. E*, 86:026305, Aug 2012.
- [78] L. A. Hoffmann, L. Nicola Carenza, J. Eckert, and L. Giomi. Theory of defect-mediated morphogenesis. *Sci. Adv.*, 8(15):eabk2712, 2022.
- [79] W. F. Hu, M. C. Lai, and Y. N. Young. A hybrid immersed boundary and immersed interface method for electrohydrodynamic simulations. *J. Comput. Phys.*, 282:47–61, 2015.
- [80] X. Hu, P. H. Bessette, J. Qian, C. D. Meinhart, P. S. Daugherty, and H. T. Soh. Marker-specific sorting of rare cells using dielectrophoresis. *PNAS*, 102(44):15757–15761, 2005.
- [81] J. D. Jackson. *Classical electrodynamics*, 1999.
- [82] T. B. Jones. Quincke rotation of spheres. *IEEE Trans. Ind. Appl.*, IA-20(4):845–849, 1984.
- [83] N. Kahya, D. Scherfeld, K. Bacia, and P. Schwille. Lipid domain formation and dynamics in giant unilamellar vesicles explored by fluorescence correlation spectroscopy. *J. Struct. Biol.*, 147(1):77–89, 2004.
- [84] R. B. Karyappa, S. D. Deshmukh, and R. M. Thaokar. Breakup of a conducting drop in a uniform electric field. *J. Fluid Mech.*, 754:550–589, 2014.
- [85] C. Kassel and V. Turaev. *Braid groups*, volume 247. Springer Science & Business Media, 2008.
- [86] F. C. Keber, E. Loiseau, T. Sanchez, S. J. DeCamp, L. Giomi, M. J. Bowick, M. C. Marchetti, Z. Dogic, and A. R. Bausch. Topology and dynamics of active nematic vesicles. *Science*, 345(6201):1135–1139, 2014.
- [87] D. Khoromskaia and G. Salbreux. Active morphogenesis of patterned epithelial shells. *eLife*, 12:e75878, 2023.
- [88] S. Kralj, R. Rosso, and E. G. Virga. Curvature control of valence on nematic shells. *Soft Matter*, 7(2):670–683, 2011.
- [89] K. Kruse, J.-F. Joanny, F. Jülicher, J. Prost, and K. Sekimoto. Generic theory of active polar gels: a paradigm for cytoskeletal dynamics. *EPJ E*, 16:5–16, 2005.
- [90] E. Lac and G. M. Homsy. Axisymmetric deformation and stability of a viscous drop in a steady electric field. *J. Fluid Mech.*, 590:239–264, 2007.

- [91] J. A. Lanauze, L. M. Walker, and A. S. Khair. The influence of inertia and charge relaxation on electrohydrodynamic drop deformation. *Phys. Fluids*, 25(11):112101, 2013.
- [92] J. A. Lanauze, L. M. Walker, and A. S. Khair. Nonlinear electrohydrodynamics of slightly deformed oblate drops. *J. Fluid Mech.*, 774:245–266, 2015.
- [93] D. J. Laser and J. G. Santiago. A review of micropumps. *J. Micromech. Microeng.*, 14(6):R35, 2004.
- [94] V. G. Levich and V. S. Krylov. Surface-tension-driven phenomena. *Annu. Rev. Fluid Mech.*, 1(1):293–316, 1969.
- [95] F. Li, O. Ozen, N. Aubry, D. T. Papageorgiou, and P. G. Petropoulos. Linear stability of a two-fluid interface for electrohydrodynamic mixing in a channel. *J. Fluid Mech.*, 583(July):347–377, 2007.
- [96] Z. Lin, T. Kerle, T. P. Russell, E. Schäffer, and U. Steiner. Structure formation at the interface of liquid/liquid bilayer in electric field. *Macromolecules*, 35(10):3971–3976, 2002.
- [97] J. Liu, J. F. Tetz, P. W. Miller, A. D. Hastewell, Y.-C. Chao, J. Dunkel, and N. Fakhri. Topological braiding and virtual particles on the cell membrane. *PNAS*, 118(34):e2104191118, 2021.
- [98] T. C. Lubensky and J. Prost. Orientational order and vesicle shape. *Journal de Physique II*, 2(3):371–382, 1992.
- [99] J. Lyklema, H.P. van Leeuwen, and A.M. Cazabat. *Fundamentals of Interface and Colloid Science: Fundamentals*. Fundamentals of Interface & Co. Elsevier Science, 1991.
- [100] Y. Maroudas-Sacks, L. Garion, L. Shani-Zerbib, A. Livshits, E. Braun, and K. Keren. Topological defects in the nematic order of actin fibres as organization centres of hydra morphogenesis. *Nat. Phys*, 17(2):251–259, 2021.
- [101] A. C. Martin and B. Goldstein. Apical constriction: themes and variations on a cellular mechanism driving morphogenesis. *J. Dev.*, 141(10):1987–1998, 2014.
- [102] M. Mayer, M. Depken, J. S. Bois, F. Jülicher, and S. W. Grill. Anisotropies in cortical tension reveal the physical basis of polarizing cortical flows. *Nature*, 467(7315):617–621, 2010.
- [103] J. R. Melcher. Electrohydrodynamics: a review of the role of interfacial shear stresses. *Annu. Rev. Fluid Mech.*, 1:111–146, 1969.
- [104] J. R. Melcher and W. J. Schwarz Jr. Interfacial relaxation overstability in a tangential electric field. *Phys. Fluids*, 11:2604–2616, 1968.
- [105] J. R. Melcher and C. V. Smith. Electrohydrodynamic charge relaxation and interfacial perpendicular-field instability. *Phys. Fluids*, 12(4):778–790, 1969.

- [106] L. Metselaar, J. M. Yeomans, and A. Doostmohammadi. Topology and morphology of self-deforming active shells. *PRL*, 123(20):208001, 2019.
- [107] D. H. Michael and M. E. O’Neill. Electrohydrodynamic instability in plane layers of fluid. *J. Fluid Mech.*, 41(3):571–580, 1970.
- [108] A. Mietke, V. Jemseena, K. V. Kumar, I. F. Sbalzarini, and F. Jülicher. Minimal model of cellular symmetry breaking. *Phys. Rev. Lett.*, 123(18):188101, 2019.
- [109] A. Mietke, F. Jülicher, and I. F. Sbalzarini. Self-organized shape dynamics of active surfaces. *PNAS*, 116(1):29–34, 2019.
- [110] A. S. Mohamed, J. M. Lopez-Herrera, M. A. Herrada, L. B. Modesto-Lopez, and A. M. Ganan-Calvo. Effect of a surrounding liquid environment on the electrical disruption of pendant droplets. *Langmuir*, 32:6815–6824, JUL 12 2016.
- [111] M. D. Morariu, N. E. Voicu, E. Schäffer, Z. Lin, T. P. Russell, and U. Steiner. Hierarchical structure formation and pattern replication induced by an electric field. *Nat. Mater.*, 2(1):48–52, 2003.
- [112] Y. Mori and Y. N. Young. From electrodiffusion theory to the electrohydrodynamics of leaky dielectrics through the weak electrolyte limit. *J. Fluid Mech.*, 855:67–130, 2018.
- [113] J.-O. Moussafir. On computing the entropy of braids. *Functional Analysis and Other Mathematics*, 1:37–46, 2006.
- [114] M. Nakahara. *Geometry, topology and physics*. CRC press, 2003.
- [115] I. Nitschke, M. Nestler, S. Praetorius, H. Löwen, and A. Voigt. Nematic liquid crystals on curved surfaces: a thin film limit. *Proc. R. Soc. A*, 474(2214):20170686, 2018.
- [116] I. Nitschke, S. Reuther, and A. Voigt. Liquid crystals on deformable surfaces. *Proc. R. Soc. A*, 476(2241):20200313, 2020.
- [117] M. Ouriemi and P. M. Vlahovska. Electrohydrodynamics of particle-covered drops. *J. Fluid Mech.*, 751:106–120, 2014.
- [118] D. T. Papageorgiou. Film flows in the presence of electric fields. *Annu. Rev. Fluid Mech.*, 51:155–187, 2019.
- [119] D. T. Papageorgiou and P. G. Petropoulos. Generation of interfacial instabilities in charged electrified viscous liquid films. *J. Eng. Math.*, 50(2-3):223–240, 2004.
- [120] J. S. Park and D. Saintillan. Electric-field-induced ordering and pattern formation in colloidal suspensions. *Phys. Rev. E*, 83(4):041409, 2011.
- [121] J. U. Park, M. Hardy, S. J. Kang, K. Barton, K. Adair, D. K. Mukhopadhyay, C. Y. Lee, M. S. Strano, A. G. Alleyne, J. G. Georgiadis, et al. High-resolution electrohydrodynamic jet printing. *Nat. Mater.*, 6(10):782–789, 2007.

- [122] A. J. Pascall, K. T. Sullivan, and J. D. Kuntz. Morphology of electrophoretically deposited films on electrode strips. *J. Phys. Chem. B*, 117(6):1702–1707, 2013.
- [123] D. J. G. Pearce, P. W. Ellis, A. Fernandez-Nieves, and L. Giomi. Geometrical control of active turbulence in curved topographies. *Phys. Rev. Lett.*, 122(16):168002, 2019.
- [124] L. F. Pease III and W. B. Russel. Linear stability analysis of thin leaky dielectric films subjected to electric fields. *J. Nonnewton. Fluid Mech.*, 102(2):233–250, 2002.
- [125] C. Pozrikidis. *Boundary Integral and Singularity Methods for Linearized Viscous Flow*. Cambridge University Press, 1992.
- [126] C. Pozrikidis. *A Practical Guide to Boundary Element Methods with the Software Library BEMLIB*. CRC Press, 2002.
- [127] C. Pozrikidis. *Introduction to Theoretical and Computational Fluid Dynamics*. Oxford University Press, 2011.
- [128] C. Pozrikidis. Stability of sessile and pendant liquid drops. *J. Eng. Math.*, 72:1–20, 2012.
- [129] C. Pozrikidis and M. G. Blyth. Effect of stretching on interfacial stability. *Acta Mech.*, 170:149–162, 2004.
- [130] J. Prost, F. Jülicher, and J. F. Joanny. Active gel physics. *Nat. Phys.*, 11(2):111–117, 2015.
- [131] G. Quincke. Ueber Rotationen im constanten electrischen Felde. *Annalen der Physik*, 295(11):417–486, 1896.
- [132] A. Rahimian, S. K. Veerapaneni, D. Zorin, and G. Biros. Boundary integral method for the flow of vesicles with viscosity contrast in three dimensions. *J. Comput. Phys.*, 298:766–786, 2015.
- [133] J. M. Rallison and A. Acrivos. A numerical study of the deformation and burst of a viscous drop in an extensional flow. *J. Fluid Mech.*, 89:191–200, 1978.
- [134] A.-C. Reymann, F. Staniscia, A. Erzberger, G. Salbreux, and S. W. Grill. Cortical flow aligns actin filaments to form a furrow. *Elife*, 5:e17807, 2016.
- [135] A. Richter and H. Sandmaier. An electrohydrodynamic micropump. In *IEEE Proceedings on Micro Electro Mechanical Systems, An Investigation of Micro Structures, Sensors, Actuators, Machines and Robots.*, pages 99–104. IEEE, 1990.
- [136] N. T. L. Rodrigues, S. Lekomtsev, S. Jananji, J. Kriston-Vizi, G. R. X. Hickson, and B. Baum. Kinetochore-localized pp1–sds22 couples chromosome segregation to polar relaxation. *Nature*, 524(7566):489–492, 2015.
- [137] L. J. Ruske and J. M. Yeomans. Morphology of active deformable 3d droplets. *Physical Review X*, 11(2):021001, 2021.

- [138] Y. Saad and M. H. Schultz. GMRES: A generalized minimal residual algorithm for solving nonsymmetric linear systems. *SIAM J. Sci. Comput.*, 7:856–869, 1986.
- [139] G. Salbreux, G. Charras, and E. Paluch. Actin cortex mechanics and cellular morphogenesis. *Trends Cell Biol.*, 22(10):536–545, 2012.
- [140] G. Salbreux, F. Jülicher, J. Prost, and A. Callan-Jones. Theory of nematic and polar active fluid surfaces. *Phys. Rev. Res.*, 4(3):033158, 2022.
- [141] P. F. Salipante and P. M. Vlahovska. Electrohydrodynamics of drops in strong uniform dc electric fields. *Phys. Fluids*, 22(11):112110, 2010.
- [142] H. Sato, N. Kaji, T. Mochizuki, and Y. H. Mori. Behavior of oblately deformed droplets in an immiscible dielectric liquid under a steady and uniform electric field. *Phys. Fluids*, 18(12):127101, 2006.
- [143] D. A. Saville. Electrohydrodynamics: the Taylor-Melcher leaky dielectric model. *Annu. Rev. Fluid Mech.*, 29(1):27–64, 1997.
- [144] T. B. Saw, A. Doostmohammadi, V. Nier, L. Kocgozlu, S. Thampi, Y. Toyama, P. Marcq, C. T. Lim, J. M. Yeomans, and B. Ladoux. Topological defects in epithelia govern cell death and extrusion. *Nature*, 544(7649):212–216, 2017.
- [145] T. B. Saw, W. Xi, B. Ladoux, and Ch. T. Lim. Biological tissues as active nematic liquid crystals. *Adv. Mater.*, 30(47):1802579, 2018.
- [146] E. Schäffer, T. Thurn-Albrecht, T. P. Russell, and U. Steiner. Electrically induced structure formation and pattern transfer. *Nature*, 403(6772):874–877, 2000.
- [147] E. Schäffer, T. Thurn-Albrecht, T. P. Russell, and U. Steiner. Electrohydrodynamic instabilities in polymer films. *EPL*, 53(4):518, 2001.
- [148] O. Schnitzer and E. Yariv. The Taylor–Melcher leaky dielectric model as a macroscale electrokinetic description. *J. Fluid Mech.*, 773:1–33, 2015.
- [149] J. Sedzinski, M. Biro, A. Oswald, J.-Y. Tinevez, G. Salbreux, and E. Paluch. Polar actomyosin contractility destabilizes the position of the cytokinetic furrow. *Nature*, 476(7361):462–466, 2011.
- [150] A. Sellier. On the computation of the derivatives of potentials on a boundary by using boundary-integral equations. *Comput. Methods Appl. Mech. Eng.*, 196(1-3):489–501, 2006.
- [151] R. Sengupta, L. M. Walker, and A. S. Khair. The role of surface charge convection in the electrohydrodynamics and breakup of prolate drops. *J. Fluid Mech.*, 833:29–53, DEC 25 2017.
- [152] M. Serra, L. Lemma, L. Giomi, Z. Dogic, and L. Mahadevan. Defect-mediated dynamics of coherent structures in active nematics. *Nat. Phys.*, pages 1–7, 2023.

- [153] M. Serra, G. S. Nájera, M. Chuai, V. Spandan, C. J. Weijer, and L. Mahadevan. A mechanochemical model recapitulates distinct vertebrate gastrulation modes. *bioRxiv*, pages 2021–10, 2021.
- [154] M. Serra, S. Streichan, M. Chuai, C. J. Weijer, and L. Mahadevan. Dynamic morphoskeletons in development. *PNAS*, 117(21):11444–11449, 2020.
- [155] S. Shankar, M. J. Bowick, and M. C. Marchetti. Topological sound and flocking on curved surfaces. *Phys. Rev. X.*, 7(3):031039, 2017.
- [156] V. Shankar and A. Sharma. Instability of the interface between thin fluid films subjected to electric fields. *J. Colloid Interface Sci.*, 274(1):294–308, 2004.
- [157] J. D. Sherwood. Breakup of fluid droplets in electric and magnetic fields. *J. Fluid Mech.*, 188:133–146, 1988.
- [158] V. Y. Shkadov and A. A. Shutov. Drop and bubble deformation in an electric field. *Fluid Dyn.*, 37(5):713–724, 2002.
- [159] C. Sinigaglia, F. Braghin, and M. Serra. Optimal control of short-time attractors in active fluid flows. *arXiv preprint arXiv:2305.00193*, 2023.
- [160] J. R. Smart and D. T. Leighton Jr. Measurement of the drift of a droplet due to the presence of a plane. *Phys. Fluids A*, 3(1):21–28, 1991.
- [161] S. A. Smith and R. Gong. Braiding dynamics in active nematics. *Front. Phys.*, page 530, 2022.
- [162] Y. S. Song, Y. H. Choi, et al. Microextraction in a tetrabutylammonium bromide/ammonium sulfate aqueous two-phase system and electrohydrodynamic generation of a micro-droplet. *J. Chromatogr. A*, 1162(2):180–186, 2007.
- [163] C. Sorentone, J. I. Kach, A. S. Khair, L. M. Walker, and P. M. Vlahovska. Numerical and asymptotic analysis of the three-dimensional electrohydrodynamic interactions of drop pairs. *J. Fluid Mech.*, 914:A24, 2021.
- [164] C. Sorentone and A. K. Tornberg. A highly accurate boundary integral equation method for surfactant-laden drops in 3D. *J. Comput. Phys.*, 360:167–191, 2018.
- [165] C. Sorentone, A. K. Tornberg, and P. M. Vlahovska. A 3D boundary integral method for the electrohydrodynamics of surfactant-covered drops. *J. Comput. Phys.*, 389:111–127, 2019.
- [166] C. Sorentone and P. M. Vlahovska. Tandem droplet locomotion in a uniform electric field. *J. Fluid Mech.*, 951:R2, 2022.

- [167] F. Spira, S. Cuylen-Haering, S. Mehta, M. Samwer, A. Reversat, A. Verma, R. Oldenbourg, M. Sixt, and D. W. Gerlich. Cytokinesis in vertebrate cells initiated by contraction of an equatorial actomyosin network composed of randomly oriented filaments. *Elife*, 6:e30867, 2017.
- [168] H. A. Stone. Dynamics of drop deformation and breakup in viscous fluids. *Annu. Rev. Fluid Mech.*, 26(1):65–102, 1994.
- [169] A. H. Stroud and D. Secrest. *Gaussian Quadrature Formulas*. Prentice-Hall, 1966.
- [170] L. Sui, S. Alt, M. Weigert, N. Dye, S. Eaton, F. Jug, E. W. Myers, F. Jülicher, G. Salbreux, and C. Dahmann. Differential lateral and basal tension drive folding of drosophila wing discs through two distinct mechanisms. *Nat. Commun.*, 9(1):4620, 2018.
- [171] G. Supeene, C. R. Koch, and S. Bhattacharjee. Deformation of a droplet in an electric field: Nonlinear transient response in perfect and leaky dielectric media. *J. Colloid Interface Sci.*, 318(2):463–476, 2008.
- [172] P. N. Swarztrauber and W. F. Spitz. Generalized discrete spherical harmonic transforms. *J. Comput. Phys.*, 159(2):213–230, 2000.
- [173] S. Takagi and Y. Matsumoto. Surfactant effects on bubble motion and bubbly flows. *Annu. Rev. Fluid Mech.*, 43:615–636, 2011.
- [174] A. J. Tan, E. Roberts, S. A. Smith, U. A. Olvera, J. Arteaga, S. Fortini, K. A. Mitchell, and L. S. Hirst. Topological chaos in active nematics. *Nat. Phys.*, 15(10):1033–1039, 2019.
- [175] G. I. Taylor. Disintegration of water drops in an electric field. *Proc. Royal Soc. Lond. A*, 280:383–397, 1964.
- [176] G. I. Taylor. Studies in electrohydrodynamics. I. The circulation produced in a drop by an electric field. *Proc. R. Soc. A*, 291(1425):159–166, 1966.
- [177] G. I. Taylor and A. E. Green. Mechanism of the production of small eddies from large ones. *Proc. R. Soc. Lond. A*, 158:499–521, 1937.
- [178] G. I. Taylor and A. D. McEwan. The stability of a horizontal fluid interface in a vertical electric field. *J. Fluid Mech.*, 22:1–15, 1965.
- [179] R. M. Thaokar and V. Kumaran. Electrohydrodynamic instability of the interface between two fluids confined in a channel. *Phys. Fluids*, 17(8):084104, 2005.
- [180] M. Theillard, F. Gibou, and D. Saintillan. Sharp numerical simulations of incompressible two-phase flows. *J. Comput. Phys.*, 391:91–118, 2019.
- [181] M. Théry, A. Jiménez-Dalmaroni, V. Racine, M. Bornens, and F. Jülicher. Experimental and theoretical study of mitotic spindle orientation. *Nature*, 447(7143):493–496, 2007.
- [182] J.-L. Thiffeault. Measuring topological chaos. *Phys. Rev. Lett.*, 94(8):084502, 2005.

- [183] J.-L. Thiffeault. Braids of entangled particle trajectories. *Chaos: An Interdisciplinary Journal of Nonlinear Science*, 20(1), 2010.
- [184] J.-L. Thiffeault. *Braids and Dynamics*, volume 9. Springer Nature, 2022.
- [185] J.-L. Thiffeault and M. Budišić. Braidlab: A software package for braids and loops, 2013–2021. Version 3.2.5.
- [186] J.-L. Thiffeault and M. D. Finn. Topology, braids and mixing in fluids. *Proc. R. Soc. A*, 364(1849):3251–3266, 2006.
- [187] J.-Y. Tinevez, U. Schulze, G. Salbreux, J. Roensch, J.-F. Joanny, and E. Paluch. Role of cortical tension in bleb growth. *PNAS*, 106(44):18581–18586, 2009.
- [188] S. Torza, R.G. Cox, and S.G. Mason. Electrohydrodynamic deformation and burst of liquid drops. *Phil. Trans. Royal Soc. A*, 269:295–319, 1971.
- [189] Y.-H. Tseng and A. Prosperetti. Local interfacial stability near a zero vorticity point. *J. Fluid Mech.*, 776:5, 2015.
- [190] A Kerem Uguz and N Aubry. Quantifying the linear stability of a flowing electrified two-fluid layer in a channel for fast electric times for normal and parallel electric fields. *Phys. Fluids*, 20(9):092103, 2008.
- [191] S. Veerapaneni. Integral equation methods for vesicle electrohydrodynamics in three dimensions. *J. Comput. Phys.*, 326:278–289, 2016.
- [192] S. K. Veerapaneni, A. Rahimian, G. Biros, and D. Zorin. A fast algorithm for simulating vesicle flows in three dimensions. *J. Comput. Phys.*, 230(14):5610–5634, 2011.
- [193] P. M. Vlahovska. Electrohydrodynamics of drops and vesicles. *Annu. Rev. Fluid Mech.*, 51:305–330, 2019.
- [194] B. W. Wagoner, P. M. Vlahovska, M. T. Harris, and O. A. Basaran. Electric-field-induced transitions from spherical to discocyte and lens-shaped drops. *J. Fluid Mech.*, 904, 2020.
- [195] B. W. Wagoner, P. M. Vlahovska, M. T. Harris, and O. A. Basaran. Electrohydrodynamics of lenticular drops and equatorial streaming. *J. Fluid Mech.*, 925:A36, 2021.
- [196] K. L. Weirich, K. Dasbiswas, T. A. Witten, S. Vaikuntanathan, and Margaret L. Gardel. Self-organizing motors divide active liquid droplets. *PNAS*, 116(23):11125–11130, 2019.
- [197] J. G. White and G. G. Borisy. On the mechanisms of cytokinesis in animal cells. *J. Theor. Biol.*, 101(2):289–316, 1983.
- [198] S. J. Williams, N. G. Kumar, A. and Green, and S. T. Wereley. Optically induced electrokinetic concentration and sorting of colloids. *JMM*, 20(1):015022, 2009.

- [199] N. Wu and W. B. Russel. Micro-and nano-patterns created via electrohydrodynamic instabilities. *Nano Today*, 4:180–192, 2009.
- [200] L. Ying, G. Biros, and D. Zorin. A high-order 3D boundary integral equation solver for elliptic PDEs in smooth domains. *J. Comput. Phys.*, 219(1):247–275, 2006.
- [201] M. Zabarankin. A liquid spheroidal drop in a viscous incompressible fluid under a steady electric field. *SIAM J. Appl. Math.*, 73(2):677–699, 2013.
- [202] J. D. Zahn and V. Reddy. Two phase micromixing and analysis using electrohydrodynamic instabilities. *Microfluid. Nanofluidics*, 2(5):399–415, 2006.
- [203] J. Zeleny. Instability of electrified liquid surfaces. *Phys. Rev.*, 10:1–6, Jul 1917.
- [204] J. Zhang, J. D. Zahn, and H. Lin. A general analysis for the electrohydrodynamic instability of stratified immiscible fluids. *J. Fluid Mech.*, 681:293–310, 2011.
- [205] J. Zhang, J. D. Zahn, and H. Lin. Transient solution for droplet deformation under electric fields. *Phys. Rev. E*, 87(4):043008, 2013.
- [206] R. Zhang, Y. Zhou, M. Rahimi, and J. J. De Pablo. Dynamic structure of active nematic shells. *Nat. Commun.*, 7(1):13483, 2016.
- [207] H. Zhao, A. H. G. Isfahani, L. N. Olson, and J. B. Freund. A spectral boundary integral method for flowing blood cells. *J. Comput. Phys.*, 229(10):3726–3744, 2010.
- [208] N. M. Zubarev. Formation of conic cusps at the surface of liquid metal in electric field. *J. Exp. Theor. Phys.*, 73(10):544–548, 2001.
- [209] N. M. Zubarev. Self-similar solutions for conic cusps formation at the surface of dielectric liquids in electric field. *Phys. Rev. E*, 65(5):055301, 2002.